2013

An in Silico Liver: Model of Gluconeogenesis

Elie R. Chalhoub
Cleveland State University

AN *IN SILICO* LIVER: MODEL OF GLUCONEOGENSIS

ELIE CHALHOUB

Bachelor of Science in Chemistry

Lebanese University

July, 1998

Master of Science in Chemical Engineering

Cleveland State University

July, 2004

submitted in partial fulfillment of requirements for the degree

DOCTOR OF ENGINEERING IN APPLIED BIOMEDICAL ENGINEERING

at

CLEVELAND STATE UNIVERSITY

March 2013

This thesis has been approved

for the Department of Chemical and Biomedical Engineering

and the College of Graduate Studies by

_____

Committee Chairperson, Joanne M. Belovich, Ph.D Date
Chemical and Biomedical Engineering

_____

George P. Chatzimavroudis, Ph.D. Date
Chemical and Biomedical Engineering

_____

Jorge E. Gatica, Ph.D. Date
Chemical and Biomedical Engineering

_____

Richard W. Hanson, Ph.D. Date
Biochemistry, Case Western Reserve University

_____

Nolan Holland, Ph.D. Date
Chemical and Biomedical Engineering

Dedication

This thesis is dedicated to the loving memory of my mother, Noha Chalhoub. She planted in me the seeds for hard work and the desire to always aim for higher goals in life through higher education. Her endurance and acceptance of her suffering were my biggest inspiration to fully dedicate myself to this work.

I owe my deepest gratitude first and foremost to my parents and brother Nour. This work would not have seen the light at the end of the tunnel if it were not for your unwavering support, vision, and prayers. You always pushed me and encouraged me to take on the hurdles during this journey, and you were always there to lift me up when the work pressure took a toll on me. Your words of wisdom were the best cure for my soul and this work is the fruit of your love and generosity.

I would like also to dedicate this work to the love of my life Samar Ghanem as she accompanied me through the late phase of this work with the warmest and unconditional love and support. I hope with the closure of this work I will always make you proud of me.

ACKNOWLEDGEMENTS

I would like to express the deepest appreciation to my advisor Dr. Joanne Belovich. She continually conveyed a spirit of engagement in regard to research and academic formation. I was greatly influenced by her professionalism, integrity, and outmost dedication and attention to details in regard to research and scientific findings. Her persistence and guidance has made this a rewarding journey and without her valuable input this dissertation would not have been possible.

I am indebted to Dr. Richard Hanson, whose vast and deep knowledge in biochemistry and metabolism was essential in advancing and cementing my research work. His permanent smile and enthusiasm for sharing and passing on the information left an unforgettable touch on my research and my personal life and for that I am forever grateful.

I would like to thank Dr. Jorge Gatica, for his immense contribution in shaping my academic formation and for his intellectual and crucial help, especially in assisting me with the numerical methods throughout this research work.

In addition I would like to thank the committee members, Dr. George Chatzimavroudis and Dr. Nolan Holland for their support over the last four years of my research and for their valuable advice as I moved through this work from an initial idea to a completed study.

I cannot find words to express my gratitude to our beloved administrative secretary Becky Laird. Thank you for your constant encouragement, over the years you helped me

find my voice and get to the point. Your personal advice helped a great deal in shaping my professional and academic character and for pointing me in the right direction.

Becky Laird and Darlene Montgomery, I am so thankful for your friendship and for putting me up and putting up with me when I needed a break from my dissertation work. I am also deeply indebted to my many colleagues and labmates who assisted and supported me through this thesis work (Parang Pande, Zhawoei Wang, Smruta Koppaka).

I would like also to thank my uncle Boutros Chalhoub, his wife, and my cousin Rami Chalhoub, for the extensive support that has been ever present during this time of my life, for which I am grateful.

Last but not least I would like to express my sincere gratitude to the Haddad family; I would not have been able to complete this journey if it was not for your ultimate care and support. You were like a second family to me; you treated me like a son and brother and shared with me all my complaints and this had a lasting touch.

An *In Silico* Liver: Model of Gluconeogenesis

Elie Chalhoub

Abstract

An *in silico* liver was developed in attempt to represent the *in vivo* state of the fasted liver. It featured two conceptual models. The first one represented carbohydrate metabolism of the human liver, which included the heterogeneous nature of the liver by incorporating spatial variation of key enzyme activities. This model was able to predict the overall fluxes in tissue and the effect of high intensity exercise on the various hepatic fluxes. A second model of hepatic metabolism was developed to represent the complex interplay between gluconeogenesis, lipid metabolism, and alcohol metabolism in the fasted rat liver. Biochemical pathways are represented by key kinetic reactions that include allosteric and substrates effectors, and phosphorylation/dephosphorylation enzymes regulation. The model also incorporates the compartmentation and inter-compartmental transports between the cytosol and the mitochondria, and transport of metabolites between blood compartment and the tissue. The model is based on the experimental set-up of fasted perfused rat livers. The model was used to simulate the effects of the two main gluconeogenic substrates available during the fasting state--lactate and pyruvate--along with the addition of fatty acids and/or ethanol. The model predicts successfully the rates of glucose and ketone production, substrate uptake, and citric acid cycle. Parameter estimations were performed in order to obtain a set of physiological parameters capable of representing the liver under various combinations of nutrients. Parameter sensitivity analysis was generated to quantify the contribution of

each parameter to the model output. The model was validated with data available in the published literature from *ex vivo* studies.

The *in silico* liver constitutes a tool that can be used to predict the effect of physiological stimuli on flux and concentration distributions. This will provide an increase in the understanding of such effects and to determine what parameters, enzymes, and fluxes are responsible for a particular perturbation. These findings can prove critical in determining the causes of various liver-related diseases, therefore offering more possibilities for diagnosis and testing new therapeutic agents.

TABLE OF CONTENTS

Page

LIST OF TABLES

LIST OF FIGURES

CHAPTER I

INTRODUCTION

1.1 Problem Statement and Specific Aims

The liver is a complex organ, with disparate functions of maintaining glucose homeostasis, toxin clearance, and bile secretion. To accomplish these objectives, the liver makes use of comprehensive metabolic network, further complicated by a non-uniform distribution of enzyme activities along the billion sinusoids within the tissue. An *in silico* liver can be a tool to better advance the understanding of normal metabolic processes and their abnormalities, as well as to test the efficacy of new drugs used in the treatment of life threatening diseases such as type II diabetes and fatty liver disease. The overall goal of this study is to develop a model of an *in silico* liver that can accurately represent the *in vivo* state of a fasted rat liver by accurately predicting the reaction and transport flux distributions and species concentrations under various nutritional and hormonal changes. This process can be achieved by implementing biochemical reactions that represent the key metabolic pathways in the liver. These reactions reflect short term enzyme regulation such as allosteric effectors, specific substrate interactions, and effects of

phosphorylation/dephosphorylation by using *in vitro* kinetic data and specific mechanisms. This work is divided into four specific aims, as described below.

Aim 1. **Develop a distributed model of carbohydrate transport and metabolism in the *in vivo* human liver during rest and high-intensity exercise.** A model of reaction and transport in the liver that describes the metabolite concentration and reaction flux dynamics separately within the tissue and blood domains was developed. The blood domain contains equations for convection, axial dispersion, and transport to the surrounding tissue; and the tissue domain consists of reactions representing key carbohydrate metabolic pathways. The tissue is modeled as a tubular reactor with axial concentration distributions. The model includes the metabolic heterogeneity of the liver by incorporating spatial variation of key enzymatic maximal activities. This model provides a framework for evaluating the relative importance to hepatic function of various phenomenological changes that occur during exercise. The model can also be used to assess the potential effect of metabolic heterogeneity on metabolism.

Aim 2. Develop a computer model of gluconeogenesis and lipid metabolism in the perfused rat liver A model of the perfused rat liver to predict intermediate metabolite concentrations and fluxes in response to changes in various substrate concentrations in the perfusion medium was developed. The blood and tissue compartments are each considered to be well-mixed. The model simulates gluconeogenesis in the liver perfused separately with lactate and pyruvate, and the combination of these substrates with fatty acids (specifically, oleate). The model consists of the key reactions representing

gluconeogenesis, glycolysis, fatty acid metabolism, the citric acid cycle, oxidative phosphorylation, and ketogenesis. Michaelis-Menten type kinetic expressions, with control by ATP/ADP, are used for most of the reactions. For key regulated reactions—FBPase, PFK, PC, PDC, and PK—rate expressions that incorporate allosteric effectors, specific substrate relationships (e.g. cooperative binding), and/or phosphorylation/dephosphorylation using *in vitro* enzyme activity data and knowledge of the specific mechanisms were developed. The model was validated by comparing model predictions to ten sets of experimental data from seven different published works, with no parameter adjustments. This model is a useful tool to analyze the complex relationships between carbohydrate and fat metabolism, with potential applications to many metabolic disorders.

Aim 3. Incorporation of cytsolic/mitochondrial compartmentation into the gluconeogenesis model for fasted perfused rat livers. The gluconeogenesis model developed in Aim 2 simulates the effects of fatty acid uptake on glucose production, ketogenesis, TCA cycle, and substrate uptake (lactate and pyruvate) in the perfused liver. Results obtained with gluconeogenesis from lactate showed good agreement with experimental data, specifically with respect to rates of glucose production and lactate uptake. Results from pyruvate were lower by 50% compared to experimental data. Moreover ketogenesis rates were overestimated in both cases. Therefore species compartmentation, inter-compartmental transport between mitochondria and cytosol and aspartate-malate shuttle were added to the model to ensure the right balance of $NADH/NAD^+$ between the cytosol and mitochondria. Detailed TCA cycle and anionic

transport mechanism across the mitochondrial membrane reactions were added to ensure better physiological representations of the redox ratio in the cytosolic and mitochondrial compartment, gluconeoenesis, TCA cycle and ketogenesis rates.

Aim 4. Development of a model for ethanol oxidation in fasted perfused rat liver.

The effects of ethanol on the redox ratio and various metabolic rates such as gluconeogenesis and ketogenesis was simulated through the addition of ethanol to liver perfused with lactate and pyruvate. Reactions involved in ethanol metabolism were added to the model developed in Aim 3.

1.2 Background

1.2.1 Liver Anatomy

The gross anatomy of the liver reveals the existence of two main lobes, the right and the left, shaped in the form of wedges. Each lobe is a cluster of thousands of uniform smaller functional units called lobules. The lobule measures about one millimeter in

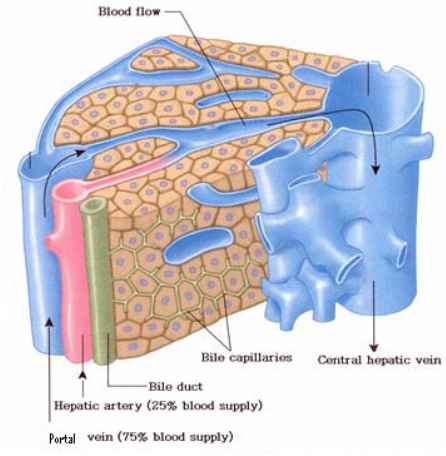

Fig. 1.1 Lobule structure of a liver
http://bh.knu.ac.kr/~sdsong/images/HB16-liver.gif

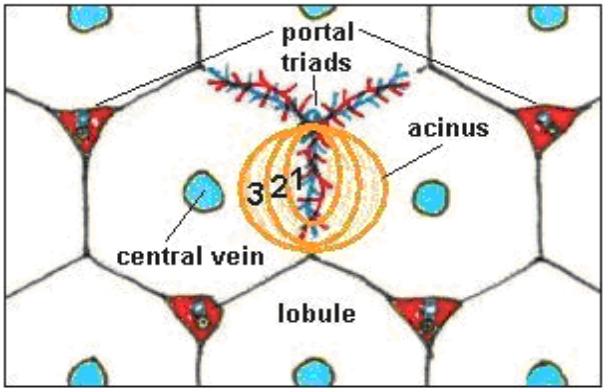

Fig 1.2. Schematic representation of an acinus representing the zonation areas of a lobule. Zone1:perivenous region ; zone2: transient zone ; zone3: pericentral region.
http://arbl.cvmbs.colostate.edu/hbooks/pathphys/digestion/liver/histo_acinus.html

diameter and consists of many cells called hepatocytes. It has a hexagonal shape with approximately six portal triads at the vertices and a central vein in the middle. The portal triad consists of a bile duct, a branch of the portal vein, and a branch of the hepatic artery. The liver receives its blood supply through two sources: the hepatic artery and the portal vein. The portal vein carries blood supplied with nutrients and digested substances absorbed from the small intestine. The portal vein provides 75% of the liver's blood supply while the remaining 25 % comes through the hepatic artery which carries blood rich in oxygen from the aorta as shown in Fig. 1.1.

The terminal branches of the hepatic artery and the portal vein of the portal triad empty its blood content into small channels called sinusoids Sinusoids are low-pressure vascular tunnels that carry blood from the portal triads toward the central vein. The lobule contains millions of sinusoids that are lined in parallel to groups of highly fenestrated endothelial cells and are surrounded circumferentially by plates of parenchymal cells-hepatocytes allowing the exchange of nutrients and oxygen between the blood and the hepatocytes. The space between the endothelial cells and the hepatocytes is known as the space of Disse which serves as a plasma filter collecting and providing the body's lymph. The lobule in Fig. 1.1 is considered to be the structural unit of the liver while the hepatic acinus (Rappaport 1960; Rappaport 1976) (Fig. 1.2), which is hard to visualize, is considered as the functional unit of the liver. The acinus is roughly divided into three zones depending on the distance of the hepatocytes from the portal tract. These zones are: the periportal region, the transitory zone, and the perivenous region. As blood flows through the liver it carries oxygen, substrates, and different hormones to the periportal region, whereas the perivenous region receives deoxygenated

blood enriched in CO_2, substrates, and hormones. Hepatocytes located along the length of the sinusoid process the blood flowing along it differently in different zones. The upstream hepatocytes (periportal) possess different enzyme activities and subcellular structures from the downstream cells (perivenous). These different functional characteristics of the hepatocytes are responsible for the phenomenon of "zonation". Gluconeogenesis, β-oxidation, and oxidative phosphorylation are predominant in the periportal zone since these cells are exposed to oxygenated blood; on the other hand glycolysis and lipogenesis are mostly located in the perivenous region.

The hepatocytes form the main functional unit of the liver by performing various metabolic, endocrine and secretory functions. They are capable of synthesizing different type of metabolites used by different organs to maintain the homeostasis of the whole organism. The liver is responsible for metabolic processes of carbohydrate, fat, and protein metabolism. The liver also plays a major role in bile secretion that is necessary in lipid digestion and in the clearance of toxins such as ammonia and drugs.

1.2.2 Liver Metabolism

The liver plays a central role in maintaining homeostasis by controlling the rate of uptake and release of glucose. During the absorptive phase the liver removes excess blood glucose by transforming it into a large glycogen--via the glycogenesis pathway, and then by transforming it into triglycerides through glycolysis and liponeogenesis. During the postabsorptive phase, the liver initially restores the normal blood glucose level by breaking down the glycogen stored in the liver via glycogenolysis. When the stored glycogen becomes scarce the hepatocytes respond by activating an alternate

metabolic pathway-gluconeogenesis. Gluconeogenesis is mainly concerned with synthesizing glucose from non-hexose precursors such as lactate, amino acids, and glycerol. The hepatocytes achieve these different metabolic functions by switching through a network with regulation by hormones and other effectors.

Gluconeogenesis. Gluconeogenesis is the major source of glucose during fasting. This pathway is achieved through a set of enzyme-catalyzed steps that are unique to gluconeogenesis and in part through steps common to both gluconeogenesis and glycolysis. The common steps are fully reversible whereas the unique steps are considered to bypass the irreversible steps of the glycolytic pathway, hence conserving energy. Two important futile cycles are active during gluconeogenesis and are involved in the regulation of the glucose production: the phosphoenolpyruvate/pyruvate cycle, and the fructose1,6 bisphosphate/fructose-6-phosphate cycle. These substrate cycles are important in determining the direction and the rate of the flux. Regulation of these rates can occur at the site of the enzyme reactions catalyzing these substrate cycle steps. Different types of regulation are involved in this process such as substrate effectors, covalent modification, and through phosphphorylation/dephosphorylation (by means of hormonal control) of the enzymes.

The bifunctional enzyme 6 phosphofructo-2-kinase/fructose-2,6bisphosphatase exerts a regulatory role on fructose 1,6 bisphosphatase (FBPase), and phosphofructokinase (PFK). Fructose 2,6 bisphosphate, a product of this bifunctional enzyme, is an allosteric activator for PFK and an inhibitor for fFBPase. PFK is also regulated by ATP, playing the role of an inhibitor while AMP acts as an activator. AMP ia also acts an uncompetitive inhibitor for the FBPase enzyme. Glucagon regulates FBPase by means of

phosphorylation and dephosphorylation through cyclic-AMP (cAMP) which activates Protein Kinase A. Pyruvate kinase (PK) is regulated by glucagon during fasting. Glucagon acts on the pyruvate kinase by phosphorylation through the protein kinase A (PKA) which is mediated by means of cAMP. ATP and alanine (Ala) act as an allosteric inhibitor of PK, whereas the F1,6BP product of PFK acts as an activator. Pyruvate carboxylase (PC) is another key enzyme in gluconeogenesis and is activated by acetyl-CoA (AcCoa), while ADP acts as an uncompetitive inhibitor to pyruvate and acts as a competitive inhibitor to ATP.

Protein Metabolism. The major aspects of protein metabolism in the liver consist of transamination of amino acids, urea synthesis, synthesis of plasma protein, and formation of heparin. During the early stages of starvation, protein degradation in muscle is high, providing the liver with the necessary supply of amino acids in order to support gluconeogenesis. These amino acids are transaminated in the liver through specific aminotransferases, the most dominant one being alanine aminotransferase and aspartate aminotransfease. Alanine is converted to pyruvate via alanine aminotransferase, providing an important precursor for gluconeogenesis during fasting.

The second important role of liver with respect to protein metabolism is the synthesis of urea. Ammonia accumulation is toxic since it can affect the central nervous system leading to encephalopathy. The liver acts rapidly and efficiently to remove the ammonia that is formed from amino acid catabolism by the urea cycle. In addition, the liver is responsible for synthesizing albumin, a major constituent of plasma protein.

Fatty acid metabolism and ketogenesis. Fatty acids taken up by the liver can either be esterified to produce phospholipid and triacyglycerol, or oxidized to produce acetyl-CoA. The break down of fatty acids starts with the activation of the fatty acids in the cytosol by addition of an acyl-CoA derivative before it gets transported into the mitochondria by specific transport sysytems. Once the fatty acids are inside the mitochondria they are oxidized via the β-oxidation to acetyl-CoA which can either enter the tri-carboxylic-acid (TCA) cycle for oxidation to CO_2, providing the necessary energy for the cell, or can be transformed into the ketone bodies, acetoacetate and hydroxybutyrate. Ketone bodies are released into the blood, where other tissues such as the brain and the muscle use them during the fasting state.

The rate of ketogenesis in the liver is mainly regulated by the level of fatty acids in the blood and by the availability of acetyl-CoA. The processing of the acetyl-CoA in the TCA cycle depends essentially on the availability of oxaloacetate for the citrate synthesis reaction and the rate of TCA cycle flux.

D-3- hydroxybutyrate dehydrogenase(BHBdh), a key enzyme of ketogenesis, reduces NADH and it is considered to reflect the ratio of free NAD/NADH in the mitochondria which is proportional to the ratio of acetoacetate (AcAc)/β-hydroxybutyrate (BHB). The ratio of NAD+/NADH is an indicator for the direction of this reaction; a low ratio will favor the formation of BHB while a higher rate will increase the AcAc concentration.

1.2.3 Mathematical Models of the Liver

Given the complexity of liver metabolism, it is important to understand the mechanisms and regulation behind these complex pathways not only in qualitative terms

but also in quantitative terms. Mathematical modeling represents a useful tool to test physiological hypotheses and can be a source for immeasurable parameters, intermediates, and fluxes. These estimations can be of great importance to understand metabolic and nutritional regulation. Various researchers and investigators have attempted to develop a mathematical model of the liver. These models were classified in two main categories: the lumped model and the distributed-in-space model.

The lumped model is based on the assumption that the liver is a well-mixed organ. Garfinkel and colleagues (Achs et al. 1971; Anderson et al. 1971) developed the first comprehensive model of liver metabolism by using the lumped model theory. In their work, they model the gluconeogenic pathway by setting a series of algebraic rate equations representing part of gluconeogenesis between phosphoenoyl-pyruvate (PEP) and glucose. The main purpose of their study was to obtain a set of enzymatic parameters which can be used to simulate the level of intermediates during gluconeogenesis. They used experimental measurements of gluconeogenic intermediates determined from previous studies by Williamson and colleagues who used perfused rat liver (Williamson et al. 1969). Each individual enzyme was optimized separately to match the expected steady state flux before all the kinetic reactions were combined. This model has some major simplifications. It focused more on the rate of conversion from PEP to glucose ignoring key dehydrogenase reactions such as lactate dehydrogenase and β-hydroxybutyrate dehydrogenase (responsible for the ketone body production). The author included the effects of the redox ratio of NADH/NAD+ and the ATP, ADP, AMP on some of the reactions by setting them as fixed concentrations, however the model lacks the necessary mass balances for the redox and the ATP and ADP. The PK reaction was

not introduced in this model, therefore ignoring another important potential futile cycle that is responsible for regulating the PEP supply. Other key reactions such as PC and phosphoenol-pyruvate carboxykinase (PEPCK) were omitted for simplicity, hence failing to represent the importance of acetyl CoA on activating these reactions during increased fatty acid supply. Garfinkel (1971a; 1971b) used a similar strategy in order to construct a model of the TCA cycle, by using experimental data from Williamson (Williamson et al. 1969). These models did not integrate all the major pathways (gluconeogenesis, TCA cycle, β-oxidation, and ketone metabolism) in the liver, which relate the effect of lipid metabolism on gluconeogenesis.

El-Refai and Bergman (1976) developed a mathematical model for glycogen metabolism. They simulated the dynamic interactions between hormones; specifically glucagon and insulin, on overall hepatic glucose production. Their rate expressions were represented by simple Michaelis-Menten kinetics, and the kinetics parameters were determined from *in vitro* published data. No kinetic expressions were used for the gluconeogenic pathway and it was lumped into a constant flux. The effect of insulin and glucagon were mediated through the level of cAMP, which was assumed to be directly proportional to the maximal velocity (Vmax) of the glycogen degradadtion. The model did not include the effect of cofactors such as ATP and UTP into their kinetics. A similar approach was used by Kurland and D'Argenio (1988) with the addition of dynamics of some gluconeogenic intermediates.

Bohnensack and Fritz (1991) developed a mathematical model for liver metabolism based on experimental data from a fasted rat liver perfused with a combination of ammonia, alanine and fatty acids. The model consisted of 13 kinetic reactions

representing the essential pathways through gluconeogenesis, alanine catabolism, and energy metabolism. The kinetic parameters of the model equations were estimated by fitting the model to the experimental data. The model is simple and many pathways were lumped. It lacks many adequate kinetic expressions. Five of the kinetic reactions were expressed by Michaelis-Menten equations, whereas the others were not represented by their own kinetics parameters, but as a function of other fluxes (e.g: glucose rate= ½(rate (PEPCK)–rate (PK))). The model equations did not include the ATP and ADP concentrations.

Calik and Akbay (2007) used a different approach to model human liver metabolism. Their study implemented the mass flux balance analysis by maximizing a selected objective function (palmitate synthesis), instead of relying on the reaction kinetics. The model assumed the intermediates to be in quasi-steady state. This model is very extensive and included all the major pathways in the liver (gluconeogenesis, glycolysis, pentose pathway, TCA cycle, catabolism and biosynthesis of the amino acids). The model consisted of 125 reaction fluxes and 83 metabolites. Glucose and amino acids uptake rates were used as inputs to calculate the flux distributions in the human liver. As a flux balance analysis model, it did not determine the intermediate concentrations found at steady state.

Recently, Nolan et al. (2006) developed a model by combining the metabolic flux analysis, Gibbs free energy balances and nested optimization. The only inputs to this model were in the form of experimental flux measurements and thermodynamic constraints, which were in the form of negative Gibbs free energy. Beard and Qian (2005) have also used the combination of flux balance (FBA) and the energy balance analyses

(EBA) and applied it to hepaticc glycogenesis and glycogenolysis. This work differs from the earlier cited ones in its ability to predict the intermediates or reactant concentrations at steady state. The introduction of EBA to the FBA enables these models to make physiological predictions. However, these models still suffer from their inability to provide accurate fluxes distributions.

The assumption of the liver as a well-mixed organ does not represent its true nature. Several researchers (Ahmad et al. 1983; Saville et al. 1992) have attempted to model the liver as a spatially distributed model due to the heterogeneous nature of the liver. The application of such models was limited mostly to pharmacokinetic representations, such as the clearance of hepatic drugs.

Bassingthwaite et al. (1970) developed a model that described the transport of oxygen between the capillary and the tissue. This model represents the capillary and the tissue in the form of a cylinder surrounded by a concentric tissue domain. The advantage of this model was that it represented the concentration of metabolites in both the blood compartment and the tissue. It also features the concentration in the blood along axial and radial directions.

These models lack the details and the complexity of the liver pathways thought to be a critical factor in modeling the *in silico* liver. In addition these models did not account for the zonation of hepatocytes.

1.3 Significance and Approach

The ultimate aim of any *in silico* model of a liver is to be able to represent the complex nature of the liver, including its structural heterogeneity, and its diverse

metabolic functions. The creation of such a model would reduce the need for physical testing and probably reduce the use of invasive treatments. Researchers as well as medical professionals would be able to have a tool at hand that can enable them to obtain a wide variety of steady state and dynamic data and perform different *in silico* experiments related to liver diseases such as type II diabetes, liver cancer, and fatty liver disease.

An *in silico* model would also offer an opportunity to scientists to develop and test various drugs in order to understand their effect on the liver metabolism. It is difficult to gain data from organs such as the liver *in vivo*, and therefore data acquisition in humans is limited to sampling from venous and arterial plasma and urine. Animals represent a slight advantage, since specific vessels such as hepatic vein and portal vein are accessible. This limitation to measurements in plasma can not give enough information regarding fluxes, such as endogenous production, storage and intermediate catabolism rates. The *in silico* liver plays an important role by estimating parameters and metabolic fluxes not available from direct measurement.

The *in silico* liver will help in understanding the effect of liver heterogeneity, and metabolic zonation on its metabolic function. The characteristics of an ultimate *in silico* liver mentioned above are a long term goal which requires an intense collaboration between computer modeling and physiology/biology. The model should be able, in the early stages, to accurately reflect the behavior of the normal liver and to predict its metabolic outcome under various in *vivo* nutritional states, and different hormonal stimulation, such as: glucagon, insulin, and catecholamine. The model should accurately predict the metabolic flux distributions (glucose production, fatty acid oxidation,

ketogenesis rate, TCA cycle, rate of uptake or release of different metabolites such as lactate, amino acids, glycerol) as well as intermediates (glucose, lactate, glycerol, alanine, pyruvate, acetylCoA, ATP, ketone bodies).

This primary goal can be achieved by building a model around a healthy liver. Experimental data from human subjects are not sufficient to examine the detailed process of liver function. Perfused rat liver offer a wealth of experimental data that are obtained under well-controlled experiments. These experiments also offer a possibility to validate the model predictions. While previous models were constructed for some specific pathways, they lack the integration of different pathways and the testing at various nutritional states.

The goal of this study is to achieve a more predictive and robust model. This can be achieved by incorporating a set of realistic and physiological kinetic expressions representing the different metabolic pathways and combining it with the physiological and anatomical heterogeneity of the organ.

This study aims at providing a tool to predict and evaluate the metabolic flux distributions during gluconeogenesis in the liver and to evaluate the complex interplay of gluconeogenesis and lipid metabolism, and the various factors controlling the interactions of these pathways in the liver. The liver is modeled essentially on the basis of two separate compartments: blood and tissue domain. The blood domain is represented mathematically by metabolite mass balance equations and transport reactions, while the tissue domain is also compartmentalized into the cytosol and mitochondria, consisting of mass balances and kinetic expressions representing principal reactions in glycolysis, gluconeogenesis, glycogenolysis, fatty acid metabolism, The TCA cycle, ketogenesis,

and the oxidative phosphorylation pathways. Simulations of the perfused rat livers were generated under conditions of infusion of various substrates. The model was validated using physiological data gathered from literature from perfused rat livers subjected to various substrate combinations and dietary conditions. The model was tested with combinations of gluconeogenic substrates, lactate and pyruvate, along with fatty acids and ethanol, in order to investigate the interrelationship between gluconeogenesis and lipid metabolism. Parameters were estimated based on sets of experimental data gathered from published literature. The model was also independently validated using different sets of experimental data from fasted rat liver perfused with combinations of substrates.

CHAPTER II

A DISTRIBUTED MODEL OF CARBOHYDRATE TRANSPORT AND METABOLISM IN THE LIVER DURING REST AND HIGH-INTENSITY EXERCISE

2.1 Introduction

Mathematical models of the liver can be divided into two broad categories: lumped models that consider the organ as well-mixed, and single-drug elimination models that consider the heterogeneous nature of the organ. Garfinkel (1971a,b) developed the first comprehensive model of liver metabolism using the lumped approach and detailed *in vitro*-based kinetic expressions. Other hepatic carbohydrate metabolism models based on the lumped model approach include that developed by El-Refai and Bergman (1976), who simulated glycogen metabolism, and Beard and Qian (2005), who developed a thermodynamic constraint-based model, among others. Numerous others have developed metabolic models that consider specific functions or pathways within the liver, again using the well-mixed approach. Rowland et al. (1983) used this approach to predict the elimination of drugs such as lignocaine and mepridine. In addition to liver models,

there is a very large body of work on models of complex metabolic systems (including other organ systems, cell lines, and single-celled organisms) that are based on the well-mixed approach.

While the well-mixed approach may be appropriate for single-celled organisms and cell lines, it is less appropriate for organs, such as the liver, that have a distributed-in-space organization. The human liver is constructed of about 1000 lobules, with each lobule consisting of about a million channels through which blood flows (the sinusoids), with each sinusoid surrounded by a layer of hepatocytes. The sinusoids are arranged roughly in parallel, and drain into a central vein. Models that consider this distributed-in-space nature have represented the liver by a system of parallel tubes in which blood flows through each tube with the same velocity. The elimination of drugs such as ethanol, galactose, and diazepam has been modeled using this approach (e.g. Saville et al., 1992). These models are mathematically simple—they do not include dispersion and usually consist of a single species mass balance and single reaction.

Roberts and Rowland (1985) proposed a dispersion model of the liver. As in the parallel tube approach, the dispersion model assumes that the liver is a tubular reactor. In addition, the model includes axial dispersion which is based on cumulative effects of radial variations in velocity, variations in length of the sinusoid, convective mixing in the flow direction of blood in the sinusoid, and diffusion. The model was applied to the drugs antipyrine, carbamazepine, and lignocaine. The model consists of a partial differential equation for the drug in one compartment (sinusoid) and a first order elimination rate

Gray and Tam (1986) have suggested a model that considers the liver as a series of compartments connected together. The model is based on the tanks-in-series model used

by chemical engineers. Each compartment is considered to be well mixed. The model does not differentiate the blood from the tissue compartments. Tsuji et al. (1983) developed a liver model consisting of mass balances for a single species (i.e. β-lactam antibiotics) in three compartments, representing the sinusoids, space of Disse and tissue.

Bassingthwaite et al. (1970) developed a model for capillary - tissue exchange that combined the Krogh's cylinder model from 1919 for the transport of oxygen from the capillary into tissue with the dispersion model. The model is of a single straight capillary surrounded by a concentric tissue compartment. The model had two sets of equations, one representing concentration in the capillary and the other in the tissue. This model was used to predict the concentration of a metabolite along the axial direction in a capillary, and along axial and radial directions in the tissue. This work was extended to represent parallel multi-capillary systems in King et al. (1996) and Deussen and Bassingthwaighte (1996).

None of these distributed-in-space models considered the complex network of metabolic pathways found in the liver, nor the unique feature of the liver, that is, the metabolic heterogeneity or zonation shown by the hepatocytes. Hepatocytes from the periportal zone of the liver have different enzyme activities from the perivenous zone (Jungermann et al. 1982). It has been shown that the periportal zone has a relatively high gluconeogenesis rate since the zone is rich in enzyme activities such as glucose-6-phosphatase, fructose 1,6 bisphosphatase and phosphoenol pyruvate carboxykinase, while the perivenous zone is rich in glycolytic enzyme activities such as pyruvate kinase and glucokinase. During the absorptive phase, the perivenous cells take up glucose from the blood and convert it into glycogen and lactate. The lactate is released into the blood

stream, and in combination with lactate released by the gut, is then absorbed by the periportal cells and converted to glycogen through gluconeogenesis. During the fasting phase, the periportal cells release glucose from the breakdown of glycogen and through gluconeogenesis, while the perivenous cells form lactate through glycogen breakdown.

We have combined the features of the detailed carbohydrate metabolism found in the lumped models with features of the dispersion, Krogh cylinder, and multi-capillary system approaches in order to represent carbohydrate metabolism as well as tissue heterogeneity and axial concentration gradients. The model of the single sinusoid considers two compartments: the blood compartment, with convection, axial dispersion, and transport to the surrounding tissue; and the tissue compartment, where reactions representing key processes of glycolysis, gluconeogenesis, glycogenolysis, tricarboxylic acid cycle, oxidative phosphorylation, and fatty acid degradation and synthesis take place. Each reaction is represented by Michaelis-Menten expressions with modulation by ADP/ATP and/or $NADH/NAD^+$, as appropriate, using an approach similar to that by Salem et al. (2002). The model includes the metabolic heterogeneity of the liver by incorporating spatial variation of key enzymatic activities. By means of this model one can predict gradients in reaction rates in the tissue, and determine whether these gradients result primarily from concentration gradients in the sinusoid or from zonation of enzyme activities. The results from the single sinusoid model are then scaled-up to provide values for total organ output fluxes and concentrations which are compared to experimental data.

This liver model was intended to be included in a whole-body model being developed by other members of the research team. One of the goals of the whole-body model

development was the integration of physiological data related to high-intensity exercise and an improved understanding of controlling factors underlying the physiological response to exercise. To this end, hepatic concentrations and fluxes during the fasted, high-intensity exercise state were calculated using the model presented here. These simulations allow one to determine the relative importance of various physiological changes that occur during exercise on hepatic glucose/lactate output, such as the increased arterial lactate concentration and the changes in enzymatic activities induced by glucagon secretion.

2.2 Model Development

2.2.1 Overall Liver Model

The human liver is known to have 1 million lobules, with each lobule containing about 1000 sinusoids. Each lobule is drained by a central vein, and the output from all lobules is collected in the hepatic vein. Blood flows roughly in parallel through all of the approximately 1 billion sinusoids. A schematic of the liver, which is the basis of the model presented here, is shown in Figure 2.1.

The net production rate of species *i* in sinusoid *j* (p_{ij}) is given by a mass balance over the entire sinusoid:

$$p_{i,j} = v_j A_{xs,j} (C_{i,blood,j}\big|_{x=L,j} - C^{\infty}{}_{i,blood}) \quad (2.1)$$

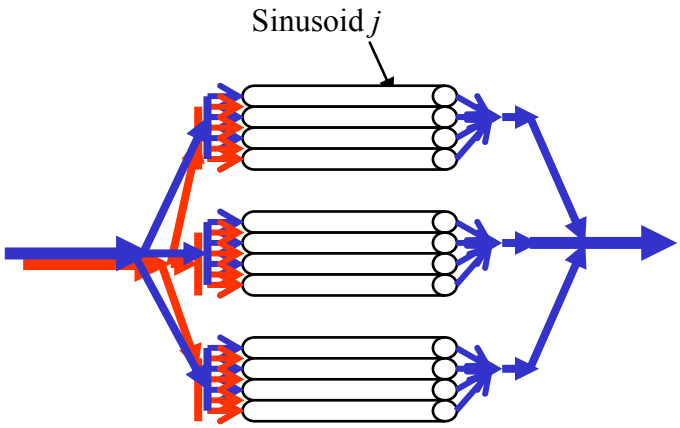

Figure 2.1. Schematic of the lobule structure within the liver.

where v_j is the blood velocity in sinusoid j, $A_{xs,j}$ is the cross-sectional area of each sinusoid calculated from the sinusoid diameter (d_s), $C^{\infty}{}_{i,blood}$ is the concentration of species i in the blood upstream of the sinusoid (i.e. mixture of the hepatic artery and portal vein), and $C_{i,blood}\big|_{x=L,j}$ is the concentration of species i at the outlet of each sinusoid j (i.e. the central vein). The net production from the entire liver is given by:

$$P_i = \sum_{j}^{n_{sinusoids}} p_{i,j} \quad (2.2)$$

All sinusoids are assumed to have the same length (L), blood velocity (v), and cross-sectional area. The sinusoid length has been reported to be 0.25 – 1 mm (Rappaport 1980; MacPhee et al. 1995; LeCouteur 2004). Blood velocity distributions have been reported to range from 0-400 μm/s (MacPhee et al. 1995), with means of 69 μm/s in mouse and 180 μm/s in rat, while Koo and Liang (1979) reported velocities of 150 – 250 μm/s in rat. The sinusoid diameter (d_s) is reported at values from 4 to 15 um, with the

diameter slightly increasing from periportal to perivenous ends (LeCouteur 2004; MacPhee et al. 1995; Rappaport 1980). The actual values used in the model (Table 2.1) were selected from within the reported ranges, with the criteria that they result in liver geometry that is consistent with macroscopic measurements of human liver. Using the equation for total liver blood flow rate, Q, and assuming that all the sinusoids have the same length and velocity (i.e., v_j=v):

$$Q = \sum_{j}^{n_{\text{sin usoids}}} v_j A_{xs,j}$$

results in Q=1.47 L/min blood flow (compared to 1.5 L/min as commonly reported), 83% liver mass equal to hepatocytes (compared to 80% as commonly reported), and residence time within a single sinusoid of 5 sec (compared to mean residence time of 4 sec, Goresky, 1980).

The concentration of each species at the outlet of each sinusoid ($C_{i,blood}\big|_{x=L,j}$) is obtained from the mass balances comprising the model of the individual sinusoid, given in the following section.

2.2.2 Single Sinusoid Model

Each sinusoid is lined with endothelial cells, which are separated from the single row of surrounding hepatocytes by the space of Disse (Figure 2.2). The endothelial cells contain fenestrae, or pores, that permit dissolved substances in the blood to enter the space of Disse, but prevent transport of large particles such as red blood cells.

Table 2.1 Model parameters.

Variable	Description	Value used in model	Additional information/reference
d_s	Diameter of sinusoid	5.7 μm	4 um (PP) and 5 um (PP) (LeCouteur 2004); 5.9 um (PP) and 7.3 um (PV) in mice (MacPhee et al. 1995); 7-15 um (Rappaport 1980)
d_t	½ of hepatocyte sheet thickness	5.5 μm	3.6 μm (calculated from Goresky et al. 1973); 6-12 um human hepatocyte radius, 2.5-8 um in other tissue (http://www.bartleby.com/107/pages/page1196.html)
d_{ed}	Endothelial cell thickness + space of Disse	1.8 μm	Calculated from Goresky et al.1973
L	Sinusoid length	1 mm	1 mm (LeCouteur 2004); .25 mm (Rappaport 1980); 0.3 mm, estimated from images (MacPhee et al. 1995) .
V_{tissue}	Volume of tissue surrounding a single sinusoid	9.5×10^{-8} cm^3	Calculated.
V_{blood}	Volume of blood within a single sinusoid plus the space of Disse.	4.42×10^{-8} cm^3	Calculated.
v	Velocity of blood in sinusoid	183 um/s ; yields τ=5.4 sec	Mean values: 69 um/s (mouse) and 180 um/s (rat), range: 0-400 um/s (MacPhee et al. 1995); 150, 250 um/s, rat (Koo and Liang 1979)
$n_{sinusoids}$	Number of sinusoids in the liver	5.23×10^9	
Q	Blood flow rate through liver	1.47 L/min	
D_G	Diffusivity of glucose in blood	5.46×10^{-4} cm^2/min	Renkin 1977
D_L	Diffusivity of lactate in blood	7.71×10^{-4} cm^2/min	Calculated using Renkin's model (Fournier et al. 1998). $1.013 \times 10^{-4} \times (MW)^{-0.46}$
$D_{a,G}$	Dispersion coefficient of glucose	5.50×10^{-4} cm^2/min	Calculated using Equation 2.4
$D_{a,L}$	Dispersion coefficient of lactate	7.74×10^{-4} cm^2/min	Calculated using Equation 2.4

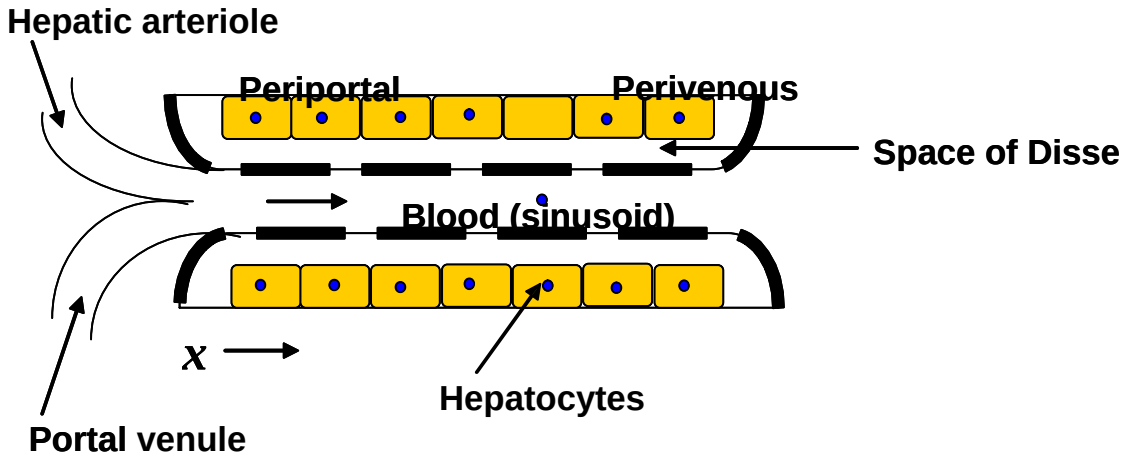

Figure 2.2. Schematic of a single sinusoid.

An idealized view of the sinusoid is used as the basis for the model (Fig. 2.3). The liver tissue is represented as a cylindrical region surrounding the sinusoid with a constant cross sectional area. The model can be considered to consist of three domains: the sinusoid, the space of Disse, and the tissue. Goresky et al. (1973) have shown through their tracer studies that species concentrations in the space of Disse equilibrate rapidly and are nearly equal to the species concentrations within the sinusoids. Moreover, convective transport within this region can be considered negligible. Therefore, mass balances are only written for the sinusoid and tissue domains, while the concentrations within the space of Disse are assumed to be equal to the concentrations at the corresponding axial position in the sinusoid.

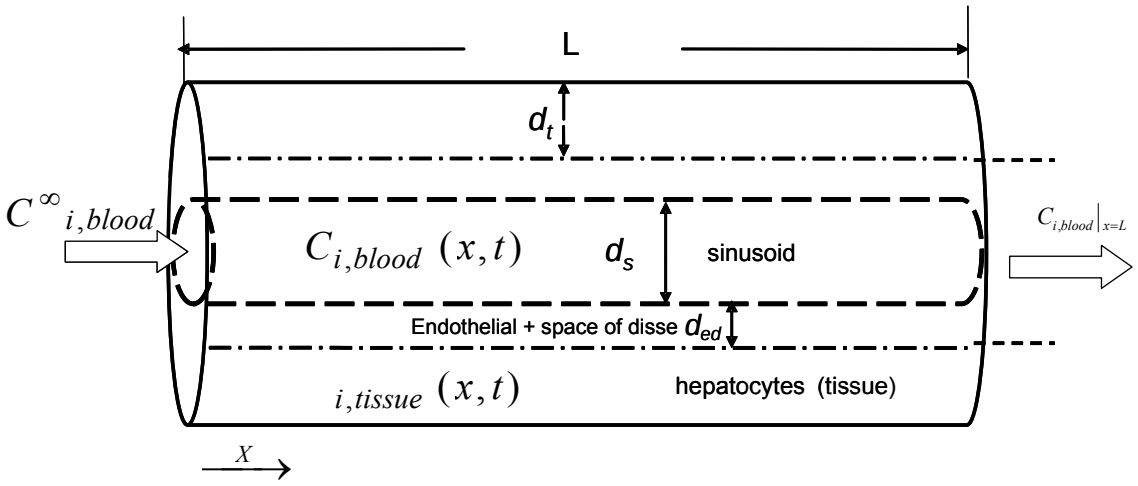

Figure 2.3. Schematic of a single idealized sinusoid as basis for the model. Large arrows represent the flow of blood within the sinusoid. d_s is the diameter of the sinusoid; d_t is the half-thickness of the hepatocyte layer; d_{ed} is the width of the endothelial cell layer plus the space of Disse; $C_{i,blood}$ is the concentration of species *i* within the sinusoid, as function of distance and time; $C_{i,tissue}$ is the concentration of species *i* within the tissue, as function of distance and time; L is the length of an average sinusoid; $C^{\infty}_{i,blood}$ is the concentration of species *i* entering the sinusoid from the portal artery and hepatic vein. Values of variables are given in Table 2.1.

2.2.3 Governing Equations

The mass balance for each species in the blood within a single sinusoid is based on the convective flow of blood through the sinusoid, the dispersion occurring due to the flow, and the transport of the metabolite from blood into the hepatocytes. The mass balance equation is given by Taylor's axial dispersion model (Fogler 2001), which describes an axial-dispersion model of a compound through a tubular reactor, with slight modification by including the transport of the species from blood into the tissue:

$$\frac{\partial C_{i,blood}}{\partial t} = -v\frac{\partial C_{i,blood}}{\partial x} + D_{a,i}\frac{\partial^2 C_{i,blood}}{\partial x^2} - J_{i,b-t}(x,t) \quad (2.3)$$

where C_i is the concentration of species i, t is time, x is axial distance along the sinusoid, $D_{a,i}$ is the dispersion coefficient, and $J_{i,b-t}$ is the transport flux from the blood into tissue. The kinetics for bi-directional carrier-mediated transport is given by the simplified expression:

$$J_{i,b-t} = \frac{V\max_i (C_{i,blood} - C_{i,tissue})}{Km_i + (C_{i,blood} + C_{i,tissue})}$$

The dispersion coefficients were calculated using the Aris–Taylor's relation (Fogler, 2001):

$$D_{a,i} = D_i + \frac{\left(\frac{vd_s}{2}\right)^2}{48D_i} \qquad (2.4)$$

where D_i is the diffusion coefficient of species i in blood.

The mass balance of each species in the tissue includes transport between the blood and tissue and reaction kinetics. Due to the relatively small tissue thickness, concentration gradients in the radial direction are neglected. Axial diffusion is also neglected. The tissue here is treated as a set of sub-compartments connected in parallel to the sinusoid domain, via the space of Disse domain. Since the concentrations in the space of Disse equilibrate rapidly with the concentrations in the corresponding position within the sinusoid, the radial flux can be considered to result from the concentration difference between each tissue sub-compartment and the corresponding region of the sinusoid. Reactions occur inside each tissue sub-compartment, and each sub-compartment is considered to be well-mixed. The concentration gradient in the tissue is

thus driven by different rates of transport into/out of each tissue sub-compartment, as well as different reaction rates in each sub-compartment. The general mass balance equation for each metabolite *i* in tissue is then:

$$\frac{\partial C_{i,tissue}(x,t)}{\partial t} = J'_{i,b-t}(x,t) - R_i(x,t) \quad (2.5)$$

where R_i = rate of reaction of each metabolite within each tissue sub-compartment.

The transport flux for the tissue equation is divided by the volume ratio (V_{ratio}) of tissue to blood to make the units consistent for the two compartments. By doing this, the units of the transport flux will be with respect to each compartmental volume:

$$J'_{b-t} = J_{b-t} * (\frac{1}{V_{ratio}})$$

where $V_{ratio} = \frac{V_{tissue}}{V_{blood}}$, V_{tissue} is the volume of tissue surrounding a single sinusoid, and V_{blood} is the total volume of blood within both a single sinusoid and the space of Disse.

Equations 2.3 and 2.5 are made dimensionless in the axial direction by defining the following variables:

$$\xi = \frac{x}{L}; \tau = L / v \qquad (2.6)$$

Using the above variables, Equation 2.3 can be written as follows:

$$\tau \frac{\partial C_{i,blood}}{\partial t} = -\frac{\partial C_{i,blood}}{\partial \xi} + \frac{1}{Pe_i}\frac{\partial^2 C_{i,blood}}{\partial \xi^2} - J_{i,b-t}\tau \qquad (2.7)$$

where Pe is the Peclet number which is defined as

$$Pe_i = \frac{vL}{D_{a,i}}$$

Using the parameter values given in Table 2.1, Pe_{GLC} and Pe_{LAC} are calculated to be 200 and 142 respectively.

The boundary conditions are obtained by assuming that the flow of blood is plug flow (i.e. no dispersion) before entering and after leaving the sinusoids. These are called Danckwert's boundary conditions and represent an open system. The corresponding boundary conditions are given by (Fogler 2001):

At x = 0:

$$C_{i,blood}\Big|_{x=0} = C^{\infty}{}_{i,blood} + \frac{D_{a,i}}{v}\frac{\partial C_i}{\partial x} \qquad (2.8)$$

At x = L:

$$\frac{\partial C_{i,blood}}{\partial x} = 0 \qquad (2.9)$$

The initial concentrations depend upon the physiological state and will be discussed in the Results section.

2.2.4 Metabolic Pathways

Simplified pathways representing glycolysis, gluconeogenesis, glycogenolysis, glycogen synthesis, citric acid cycle, oxidative phosphorylation, triglyceride breakdown, and fatty acid synthesis and degradation were included (Figure 2.4). Each of these pathways is represented by 1-3 key reactions. The name of the reaction either corresponds to the enzyme name (when representing a single reaction) or to the names of the substrate and product (when representing a series of reactions lumped together).

Kinetic expressions are given in Table 2.2. Reversible, near-equilibrium reactions ($R_{GAP \rightarrow PEP}$, $R_{LAC \rightarrow PYR}$) are represented by a simplified form of a reversible, ping-pong mechanism. All other reactions are assumed to be essentially irreversible and are represented by Michaelis-Menten kinetic expressions with modulation by C_{ADP}/C_{ATP} and C_{NADH}/C_{NAD+} as relevant. The flux through the citric acid cycle was assumed to exist in an additive "ping-pong" relationship (Salem et al. 2002).

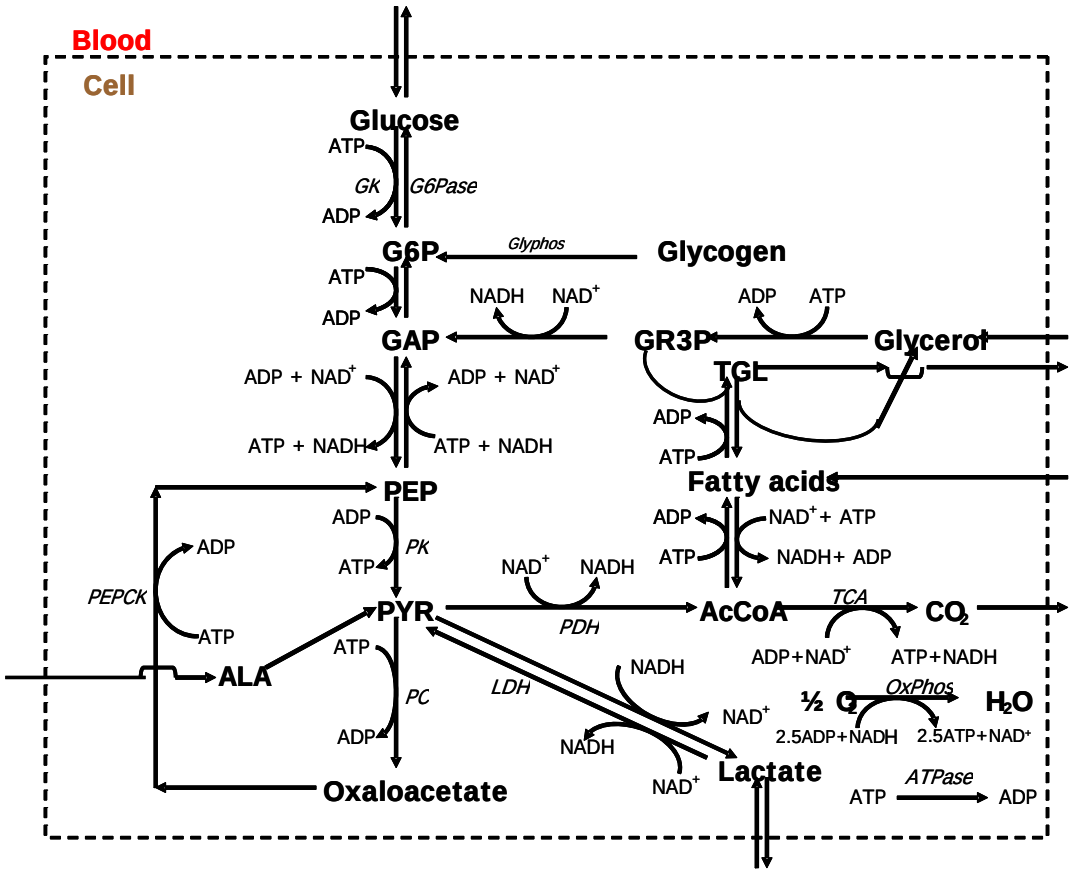

Figure 2.4. Reaction network considered in tissue model. Arrows without enzyme names indicate a series of reactions that have been lumped together. The ATPase reaction represents the total of all ATP-utilizing reactions that are not considered explicitly in the model. GK: glucokinase; G6Pase: glucose-6-phosphatase; Glyphos: glycogen phosphorylase; OxPhos: oxidative phosphorylation, PK: pyruvate kinase; PC: pyruvate carboxylase; PEPCK: phosphoenyl pyruvate carboxykinase; PDH: pyruvate dehydrogenase; LDH: lactate dehydrogenase; G6P: glucose-6-phosphate; GAP: glyceraldehyde-3-phosphate; GR3P: glycerol-3-phosphate; PEP: phosphoenyl pyruvate; AcCoA: acetyl CoA.

Kinetic parameters were estimated from concentration and flux data measured at the overnight fasted, resting state. The input and output fluxes at steady state were estimated from a combination of *in vivo* experiments on humans and dogs and internal fluxes were then calculated using flux balance analysis (FBA). Species concentrations were compiled mostly from experiments with overnight fasted rats. The set of experimental and calculated fluxes and concentrations are shown in Tables 2.2 and 2.3, respectively. In the case of irreversible reactions, the K_m in each reaction was set equal to the experimental substrate concentration at steady state, the K_m for C_{ADP}/C_{ATP}, represented by PS_i, was set equal to the steady state experimental C_{ADP}/C_{ATP} ratio, and the K_m for C_{NADH}/C_{NAD+}, represented by RS_i, was set equal to the experimental C_{NADH}/C_{NAD+} ratio, all measured in animals following an overnight fast. From these parameter values and concentration and flux values, the V_{max}'s were calculated uniquely using the kinetic expressions. Reversible reactions were handled differently. In general, the V_{max}'s and K_{eq}'s were determined from *in vitro* measurements, and then the K_m's were calculated such that the net flux through the reaction matched the experimental (or FBA-calculated) flux. The Haldane equation (relating kinetic parameter values at near-equilibrium) was used to reduce the number of unknown parameters and to ensure consistency with thermodynamic constraints. If no kinetic expression is given, then that flux was assigned a constant value in the model, given by either the measured or calculated flux.

Table 2.2. Fluxes, kinetic expressions and parameter values (PS=C_{ATP}/C_{ADP}; RS=C_{NAD+}/C_{NADH}). The fluxes used for parameter estimation are derived from either experimental data (with reference given), or calculated from flux balance analysis. Fluxes are in μmol substrate/gww hep/min, unless otherwise specified. ‡Some of the input/output fluxes used deviate somewhat from experimental reports. Since this model is to be used in a model of the whole body, the input and output fluxes were required to be consistent with the overall balances in the body for species such as FA, TGL, Glc, ALA, GLR, and LAC. GLR: glycerol; Glc: glucose; Gly: glycogen; LAC: lactate; OXA: oxaloacetate. *Value calculated via Flux Balance Analysis (FBA).

Rate	Flux used for parameter estimation	Flux calc. from simulation	Kinetic Expression	Parameter Values (V_{max} in μmol/gww/min; K_m in μmol/gww)
R_{GK}	0.136 (Miyoshi et al. 1988; Shulmanet al. 1985)	0.14	$\frac{V_{max,GK} C_{GLC\_t}}{K_{m,GK} + C_{GLC\_t}} \left(\frac{1/PS}{1/PS_i + 1/PS} \right)$	$V_{max,GK}$= 0.54 $K_{M,GK}$=3.61 PS_i=0.45
R_{G6Pase}	0.721*	0.717	$\frac{V_{max,G6Pase} C_{G6P}}{K_{m,G6Pase} + C_{G6P}}$	$V_{max,G6Pase}$=1.41 $K_{m,G6Pase}$=0.06
$R_{GlyPhos}$	0.304 μmole C6/gww/min (Petersen et al., 1996)			
$R_{G6P->GAP}$	0.136 μmole C6/gww/min (Miyoshi et al. 1988; Shulman et al. 1985)	0.134	$\frac{V_{max,G6P\_GAP} C_{G6P}}{K_{m,G6P\_GAP} + C_{G6P}} \left(\frac{1/PS}{1/PS_i + 1/PS} \right)$	$V_{max,G6P\_GAP}$=0.54 $K_{m,G6P\_GAP}$ =0.06
$R_{GAP->G6P}$	0.83 μmole C3/gww/min *	0.815	$\frac{V_{max,GAP\_G6P} C_{GAP}}{K_{m,GAP\_G6P} + C_{GAP}}$	V_{max,GAP_G6P}=1.60 K_{m,GAP_G6P}=0.0031
$R_{PEP->GAP,net}$	0.472*	0.458	$\frac{\frac{V_{max,PEP\_GAP}}{K_{m,PEP\_GAP}} \left(C_{PEP} C_{NADH} C_{ATP} - \frac{C_{GAP} C_{Pi} C_{NAD+} C_{ADP}}{K_{eq,PEP\_GAP}} \right)}{1 + \frac{C_{PEP} C_{NADH} C_{ATP}}{K_{m,PEP\_GAP}} + \frac{C_{GAP} C_{Pi} C_{NAD+} C_{ADP}}{K_{m,GAP\_PEP}}}$	V_{max,PEP_GAP}=94 (Diem and Lentner 1970) K_{m,PEP_GAP}= $2.7x10^{-4}$ K_{m,GAP_PEP}= $1.75x10^{-4}$ K_{eq,PEP_GAP}=4167 (Reich and Selkov 1981)
$R_{GR3P->GAP}$	0.0888*; (0.112 in Brundin and Wahren 1993)			
R_{PK}	0.94 *	0.931	$\frac{V_{max,pk} C_{PEP}}{K_{m,PK} + C_{PEP}} \left(\frac{PS}{PS_i + PS} \right)$	$V_{max,PK}$=3.78 $K_{m,PK}$=0.046

R_{PC}	1.416*	1.39	$\frac{V_{max,PC}C_{PYR}}{K_{m,PC}+C_{PYR}}\left(\frac{1/PS}{1/PS_i+1/PS}\right)$	$V_{max,PC}$=5.66 $K_{m,PC}$=0.059
R_{PEPCK}	1.416 (Jones et al. 1991)*	1.39	$\frac{V_{max,PEPCK}C_{OXA}}{K_{m,PEPCK}+C_{OXA}}\left(\frac{1/PS}{1/PS_i+1/PS}\right)$	$V_{max,PEPCK}$=5.66 $K_{m,PEPCK}$=0.0003
R_{PDH}	0.0 (Magnusson et al. 1991)			

Table 2.3. Species concentrations in liver tissue, at the overnight fasted state, used to estimate kinetic parameters.

Species	**Concentration used to estimate parameters (μmol gww^{-1} hep)**	**Reference**
Glc,tissue	3.61	Bergmeyer 1974
Glc,blood	3.5	Bergman and El-Refai 1975
G6P	0.06	Bergmeyer 1974
glycogen	391	Petersen et al. 1996
GAP	0.0031	Stubs et al. 1972
GR3P	0.281	Bergmeyer 1974
PEP	.046	Bergmeyer 1974
PYR	0.059	Stubbs et al. 1972
OXA	0.0003	Bergmeyer 1974
LAC,blood	1.2	Bergmeyer 1974
LAC,tissue	0.98	Krebs 1967
AcCoA	0.1	Bergmeyer 1974
Oxygen	7.33	Brundin and Wahren 1991
ATP	3.43	Gyorgy et al. 1995; Morikawa et al. 1998; Gannon et al. 2002; Hultman et al. 1975; Boesiger et al. 1994
NADH+NAD$^+$	1.22	Bergmeyer 1974
NADH/NAD$^+$	.0014	Stubbs et al. 1972
Pi	5.74	Morikawa et al. 1998; Bode et al. 1973

The zonation phenomenon is incorporated into the model by assuming either linear ($V_{max}= V_{o,l}+ a\cdot x/L$) or exponential ($V_{max}=V_{o,e}\cdot exp(b\cdot x/L)$ variations in maximal activities for the reactions for which the phenomenon has been observed. The parameter values in these functions were determined by assuming that the relative changes in maximal enzyme activities between the periportal and perivenous regions are similar to those reported in the literature (Table 2.4), and that the maximal activities at x/L=0.5 are given by the values in Table 2.2. The parameters used in the functions for V_{max} are given in

Table 2.4 and the functions are graphed in Figure 2.5. The use of exponential functions is based on the hypothesis that substrate concentration gradients along the sinusoid are most likely exponential (e.g. as measured for pO_2), which may influence the distribution of enzyme activity. There is clear literature support for the zonation of glucokinase (GK), glucose-6-phosphatase (G6Pase), fructose-1,6-bis-phosphatase (represented by $V_{max,GAP\rightarrow G6P}$), phosphoenolpyruvate carboxykinase (PEPCK), and pyruvate kinase (PK). Although zonation of pyruvate carboxylase (PC) has not been specifically reported, because of this enzyme's key role in gluconeogenesis, the zonation of $V_{max,PC}$ was included using a function similar to that used for $V_{max,PEPCK}$. Similarly, the results were calculated with zonation of phosphofructokinase (represented by $V_{max,G6P\rightarrow GAP}$) using a similar function to that of GK. The incorporation of zonation of $V_{max,G6P\rightarrow GAP}$ did not change any of the flux profiles, except for that of $V_{G6P\rightarrow GAP}$ itself (data not shown), and thus does not seem to be essential. Although zonation is also known to occur in lipid metabolism, this was not addressed in this work since detailed lipid metabolism kinetics are not included in the model.

Table 2.4. Literature sources for maximal enzyme activities in periportal and perivenous regions, and the parameters values used in the linear ($V_{max}= V_{o,l}+ a \cdot x/L$) or exponential ($V_{max}=V_{o,e} \cdot exp(b \cdot x/L)$ zonation functions.

Reaction	**Reference**	$V_{o,l}$ (μmol/g/min)	a (μmol/g/min)	$V_{o,e}$ (μmol/g/min)	b (μmol/g/min)
$V_{max,GK}$	Jungermann et al. 1982	0.17	0.74	0.27	1.39
$V_{max,G6Pase}$	Katz et al. 1977	1.87	-0.87	2.46	-1.07
$V_{max,GAP\rightarrow G6P}$	Matsumura et al. 1984	2.70	2.16	2.83	0.58
$V_{max,PK}$	Guder and Schmidt 1976; Jungermann 1988	2.33	-1.33	2.50	-0.81
$V_{max,PEPCK}$	Guder and Schmidt 1976; Matsumura et al. 1984	8.54	-5.76	9.52	-1.04
$V_{max,PC}$		8.54	-5.76	9.52	-1.04

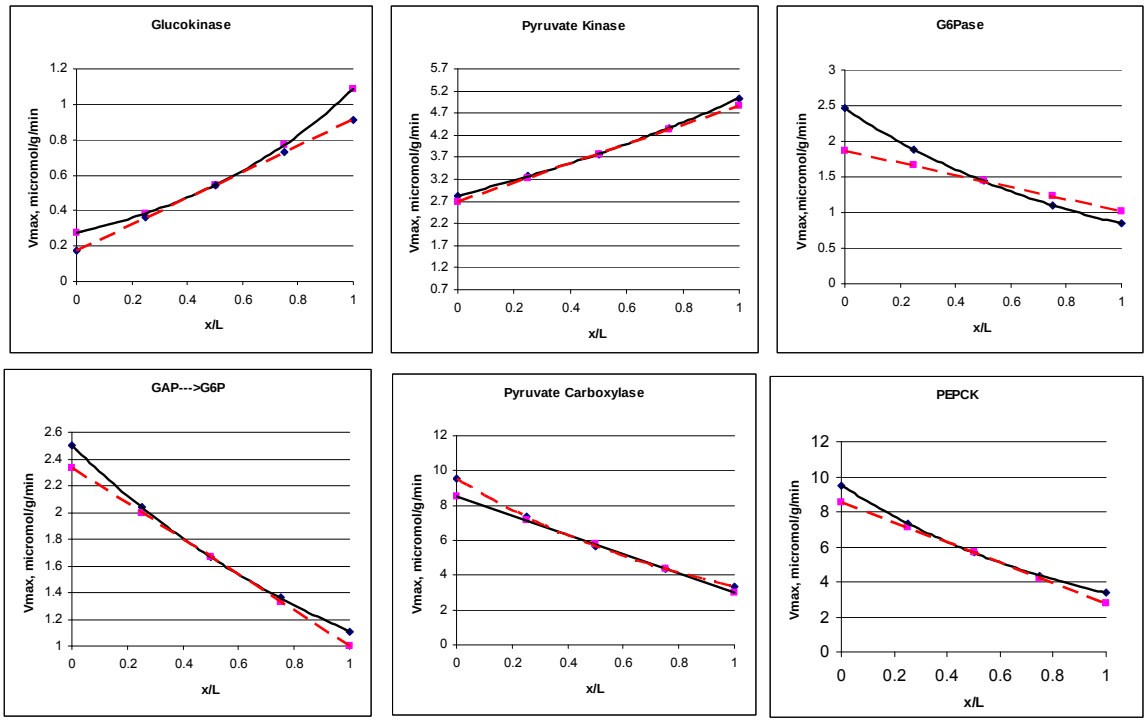

Figure 2.5. Linear and exponential functions of V_{max} as a function of distance along the sinusoid length. Functions are fitted by assuming that the V_{max} (given in Table 2.2) occurs at x/L=0.5, and using the ratio of maximal activities from periportal to perivenous, derived from data found in the references in Table 2.4. Function parameters are given in Table 2.4. The dashed line is a linear fit to the data, solid line is exponential fit.

The model consists of 13 mass balances: glucose in blood and tissue(GLC_b, GLC_t), lactate in blood and tissue (LAC_b, LAC_t), and in tissue only: glucose-6-phosphate(G6P), phosphoenolpyruvate (PEP), pyruvate (PYR), AcCoA, oxaloacetate (OXA), ATP, NADH, glycogen (GLY), glyceraldehyde-3-phosphate (GAP). The quantities $C_{NADH}+C_{NAD+}$, $C_{ATP}+C_{ADP}$, and C_{Pi} are assumed to be constant, with values given in Table 2.3.

The governing equations in the blood, which is a partial differential equation for each species in the blood, were converted to ordinary differential equations by means of the finite difference method using 200 grid points. The governing equations in the tissue were written for each species for each of the 200 grid points. All ODE's were then solved simultaneously using the FORTRAN routine LSODE.

The sensitivity coefficients of concentration of species *i* (C_i) and flux *i* (R_i) to parameter K_j are defined as:

$$S_{Ci,j} = \frac{\partial C_i / C_i}{\partial K_j / K_j}; \qquad S_{Ri,j} = \frac{\partial R_i / R_i}{\partial K_j / K_j} \qquad (2.10)$$

Partial derivatives were estimated by central finite differences.

2.3 Results

Simulations were first performed at the resting, overnight fasted state, without zonation, and with boundary conditions given by:

$$C^{\infty}_{GLC,blood} = 3.5 \ \ mM$$
$$C^{\infty}_{LAC,blood} = 1.2 \ \ mM$$

The resulting fluxes are nearly identical to the experimental (Table 2.2) and the calculated concentrations agree closely with the experimental concentrations (not shown). Since these fluxes and concentrations were used to estimate the kinetic parameters, these results indicate that the program and model are consistent and do not constitute independent verification of the model.

The total glucose output and lactate uptake by the liver in the fasted, resting state, calculated from Equation 2.2 and assuming constant V_{max}'s, are shown in Figure 2.6. The simulated values for both glucose output and lactate uptake are nearly identical to experimental values. The incorporation of zonation, whether linear or exponential, has no effect on the overall liver output, mainly because the functions used in zonation were based on setting the V_{max} (at x/L=0.5) equal to the constant V_{max} used in the "no zonation" simulation.

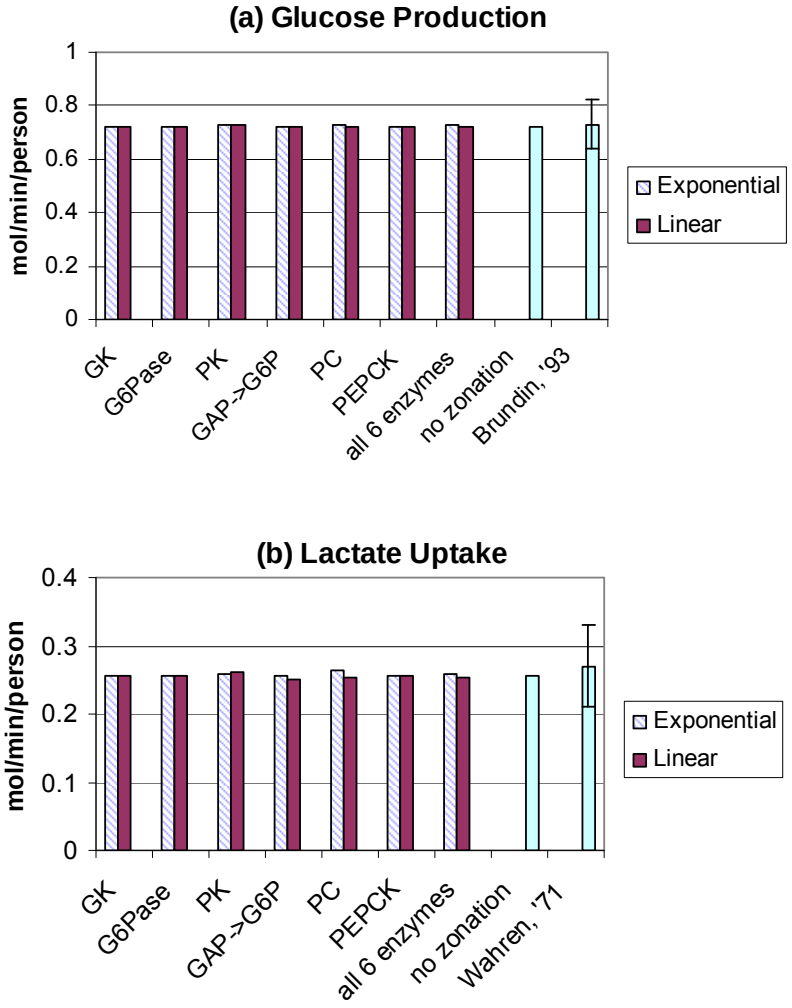

Figure 2.6. (a) Net glucose production by the liver and (b) net lactate uptake by the liver at the fasted, resting state, using blood flow = 1.47 L/min and parameters given in Tables 2.1 and 2.2. Results are shown for both exponential and linear zonation functions. Results were calculated using a single enzyme with a zonation function, then with zonation in all six enzymes simultaneously, and also with no zonation (i.e. constant V_{max}'s). Experimental data from the literature are shown for comparison.

The net glucose production and lactate uptake rates along the sinusoid length are shown in Figure 2.7. As shown in Figure 2.7a (with no zonation), the net glucose and lactate fluxes are essentially constant along the length of the sinusoid, indicating that at the relatively high blood velocities (and therefore Pe), the species concentration gradients in the axial direction are minimal, causing little variations in fluxes. Figures 2.7(b-g) show the results from simulations where a single enzyme has its V_{max} as a function of distance. These results indicate that PK, F1,6BPase (represented by GAP→G6P), and PC have the greatest influence on spatial variation in glucose and lactate fluxes. With zonation of all six reactions (Figure 2.7h), synergistic effects are observed with a 35% decrease in glucose production between periportal and perivenous regions, and with lactate flux changing from uptake (in periportal) to production in the perivenous region. Experimental values (Jungermann 1983) of net glucose production from microdissected liver tissue and from cultured hepatocytes stimulated to represent either periportal or perivenous cells are shown in Figure 2.7h. While the magnitude of change between periportal and perivenous was greater in the experiments than the simulations, the simulations do show the expected trend. Furthermore, there is significant uncertainty in the experimental data. For instance, the data from the liver tissue are actually calculated from measurements of maximal enzyme activities and substrate concentrations from the tissue extracts, and assuming Michaelis-Menten kinetics, so there is significant room for error there. Secondly, the cultured hepatocyte system is, at best, an approximation of the two regions of the liver parenchyma *in vivo*.

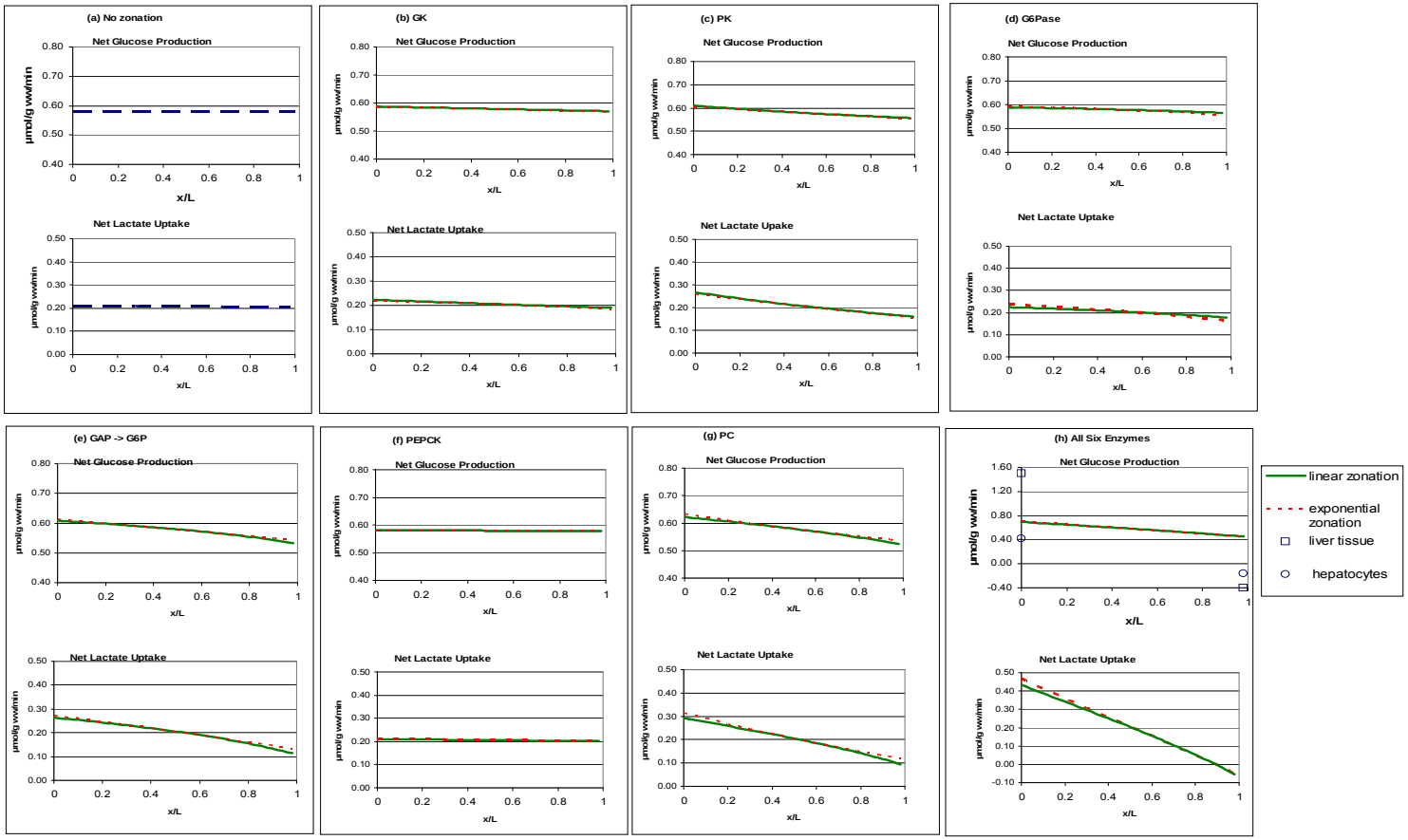

Figure 2.7. Net rates of glucose production, $J_{GLC,t\rightarrow b,net}$ and lactate uptake $J_{LAC,b\rightarrow t,net}$ by the tissue along the length of the sinusoid, in fasted, resting condition. (a) no zonation; (b) – (g) with zonation only for the enzyme indicated in the graph title, with all other enzymes having constant activity; solid line: linear zonation; dotted line: exponential zonation; (h) zonation of all six enzymes simultaneously, compared with experimental data from Jungermann, 1983; solid line: linear zonation function; dotted line: exponential zonation function; □: tissue extracts from periportal (shown at x/L=0) and perivenous (shown at x/L=1) zones of microdissected rat liver parenchyma, with fluxes calculated from measured local enzyme activities and substrate concentrations and assuming Michaelis-Menten kinetics; O: measured in cultured hepatocytes that have been stimulated to resemble either periportal (shown at x/L=0) or perivenous (shown at x/L=1) cells, and placed in media representing the fasted state,.

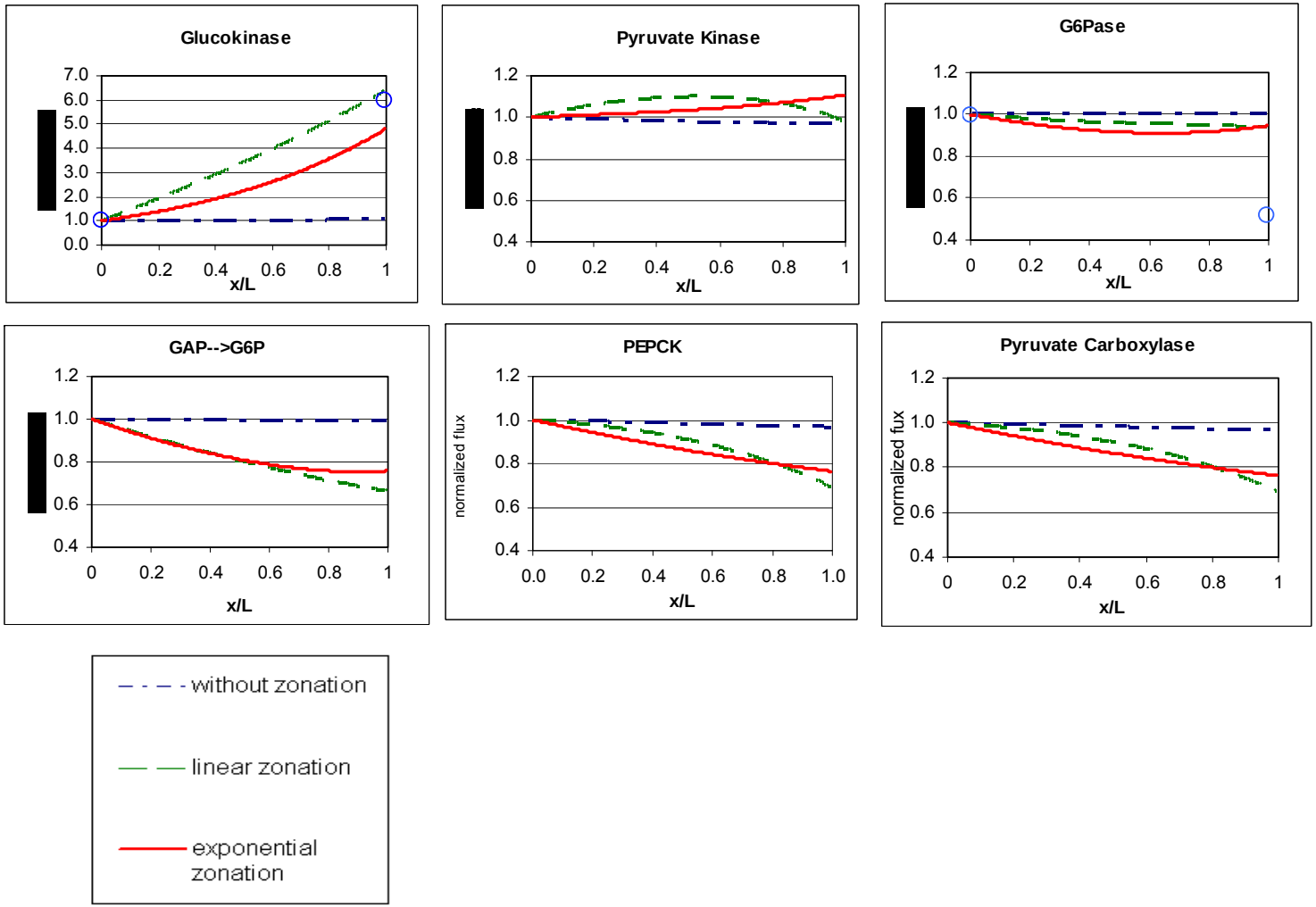

Figure 2.8. Reaction fluxes as a function of sinusoid length, during the fasted, resting state, with zonation of all six reactions, and without zonation. Fluxes are normalized to the flux value at x/L=0. Lines represent simulations, open circles represent experimental data from cultured hepatocytes, stimulated to resemble either periportal (shown at x/L=0) or perivenous (shown at x/L=1) cells, and placed in media representing the fasted state, from Jungerman 1983.

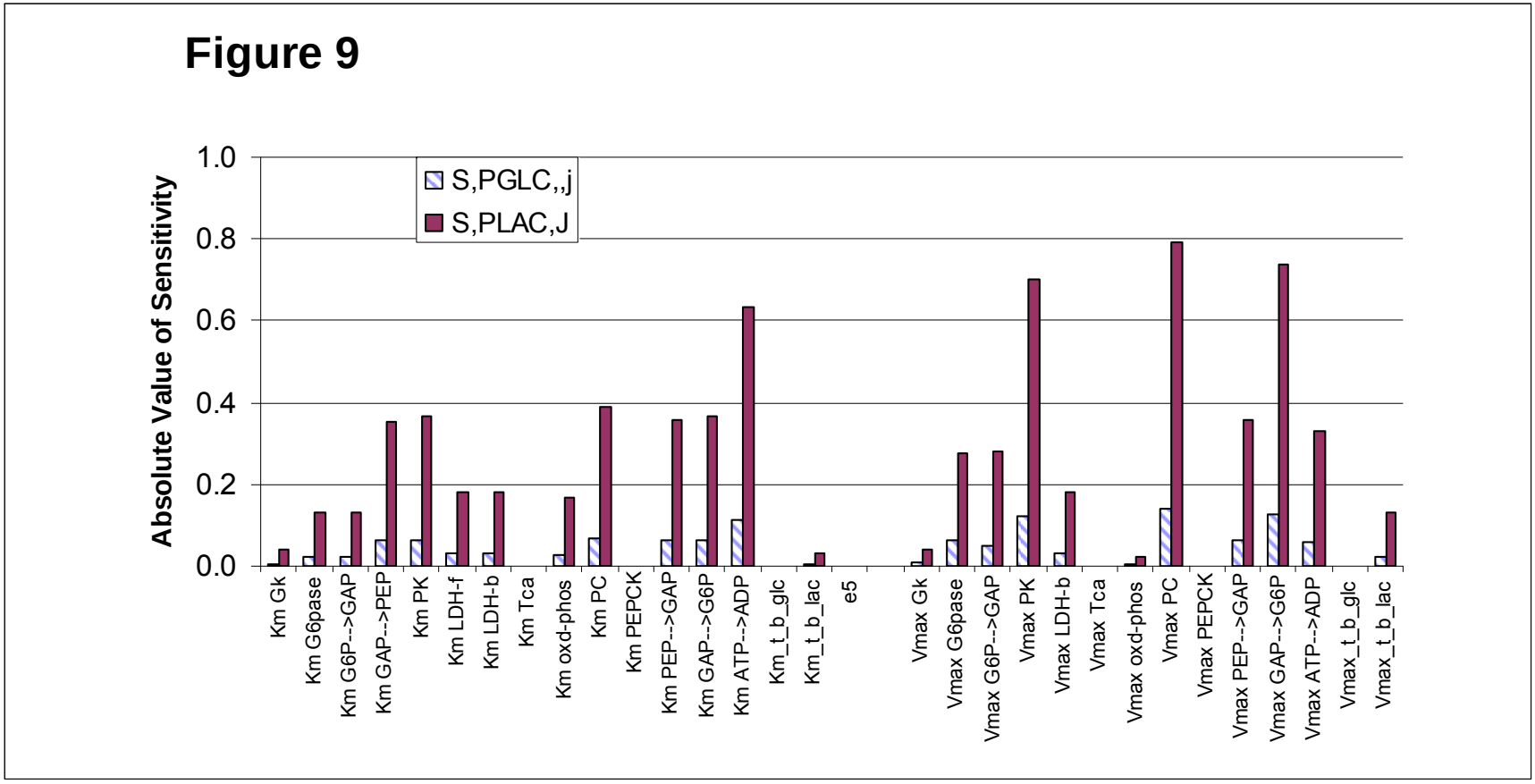

Figure 2.9. Absolute values of the sensitivities of net overall glucose production ($S_{PGLC,j}$) and lactate uptake ($S_{PLAC,j}$) to kinetic parameters j, given in the x-axis.

The fluxes through each of these six reactions (calculated with zonation in all six reactions, compared to no zonation) are shown in Figure 2.8, after normalization to the flux at x/L=0. Again, fluxes in each reaction are nearly constant along the length when there is no zonation, indicating that there is little effect of potential concentration gradients on flux distributions. The axial variations become much more significant with the incorporation of enzyme zonation, with the glycolytic fluxes (GK, PK) increasing with distance and the gluconeogenic fluxes (G6Pase, F1,6BPase, PEPCK, PC) decreasing. For example, the calculated glucokinase flux, with zonation, increases six-fold between periportal (x/L=0) and perivenous (x/L=1). This result is identical to the six-fold increase in glycolytic flux measured in periportal-like vs. perivenous-like hepatocytes (Jungermann 1983). On the other hand, the calculated G6Pase flux decreases between periportal and perivenous, but to a much lesser extent than that reported by Jungerman (5% decrease in calculated value, compared to 48% decrease in measured gluconeogenic flux). The G6Pase reaction flux does not change as significantly as the maximal activity for G6Pase (Figure 2.5), since the flux is tempered by the substrate concentration and the relatively large blood flow rate in the liver.

The parametric sensitivity coefficients were calculated using the model without zonation representing the fasted, resting state. The sensitivities of overall glucose production (P_{GLC}) and lactate uptake (P_{LAC}) relative to the kinetic parameters are shown in Figure 2.9. The lactate uptake is much more sensitive to parameters than the glucose output, since the glucose output is a function of both glycogen degradation (which is set to a constant) as well as the lactate uptake and intermediary reactions. Not surprisingly, the fluxes are most sensitive to parameters in some of the key regulatory reactions, such

as PK, PC, and F1,6BPase (represented by GAP→G6P). Also note that the sensitivity to the parameters related to nonspecific ATP demand is also relatively high. But for all parameters, the sensitivities of overall glucose output and lactate uptake are less than one, indicating that the results are stable and that no single parameter has an amplification effect on the overall fluxes.

The sensitivities for all internal fluxes and species concentrations are shown in Tables 2.5 and 2.6. In general, concentrations and fluxes were more sensitive to V_{max}'s than to K_m's, indicating the importance of having good estimates especially for the V_{max}'s. The V_{max}'s corresponding to gluconeogenic reactions were most influential, i.e. G6Pase, PC, GAP→G6P, and PK (which affects the amount of cycling during gluconeogenesis). The most influential K_m is K_{m,ATP_ADP}, which appears in the nonspecific ATP usage kinetic expression. This parameter does not have direct physiological significance, and thus an experimental value is unavailable. The transport parameters had relatively little effect on the results, indicating that the system is more metabolically driven rather than transport driven.

The sensitivities of all the fluxes to all the parameters are all less than one, indicating that there were no cases of disproportionate effects of parameters on flux distributions. On the other hand, the OXA concentration was hypersensitive to $V_{max,PEPCK}$, $V_{max,PC}$, V_{max,ATP_ADP}, and to a less extent, $V_{max,OxPhos}$. This results from the low *in vivo* concentration of OXA (0.0003 μmol/g/ww).

Table 2.5 Sensitivity coefficients to Km's, defined by Eq. 2.10. Values in boldface have magnitude greater than 0.50.

	$K_{m,GK}$	$K_{m,G6pase}$	$K_{m,G6P\_GAP}$	K_{m,GAP_PEP}	$K_{m,PK}$	K_{m,LAC_PYR}	K_{m,PYR_LAC}	$K_{m,OxPhos}$	$K_{m,PC}$	$K_{m,PEPCK}$	K_{m,PEP_GAP}	K_{m,GAP_G6P}	K_{m,ATP_ADP}	K_{m,Glc,b_t}	K_{m,LAC,b_t}	e5
Glc_{blood}	4.9E-04	-1.7E-03	1.7E-03	4.5E-03	4.7E-03	2.3E-03	-2.3E-03	-2.0E-03	-4.9E-03	0.0E+00	-4.5E-03	-4.7E-03	8.4E-03	-5.3E-06	-4.1E-04	0.0E+00
Glc_{tissue}	6.9E-04	-2.3E-03	2.3E-03	6.3E-03	6.5E-03	3.2E-03	-3.2E-03	-2.8E-03	-6.9E-03	0.0E+00	-6.3E-03	-6.5E-03	1.2E-02	9.5E-03	-5.8E-04	0.0E+00
LAC_{blood}	-3.4E-03	1.1E-02	-1.1E-02	-3.1E-02	-3.2E-02	-1.6E-02	1.6E-02	1.4E-02	3.3E-02	0.0E+00	3.1E-02	3.2E-02	-5.7E-02	3.6E-05	2.8E-03	0.0E+00
LAC_{tissue}	-1.2E-02	3.9E-02	-3.9E-02	-1.1E-01	-1.1E-01	-5.5E-02	5.5E-02	5.0E-02	1.2E-01	-7.4E-07	1.1E-01	1.1E-01	-2.0E-01	1.3E-04	-6.7E-02	0.0E+00
G6P	-1.5E-01	**9.5E-01**	4.0E-02	1.0E-01	1.1E-01	3.9E-02	-3.9E-02	-1.0E-02	-8.3E-02	-1.1E-06	-1.0E-01	-1.1E-01	3.4E-01	1.6E-03	-7.1E-03	0.0E+00
GLY	0.0E+00	0.0E+00	0.0E+00	0.0E+00	0.0E+00	0.0E+00	0.0E+00	0.0E+00	0.0E+00	0.0E+00	0.0E+00	0.0E+00	0.0E+00	0.0E+00	0.0E+00	0.0E+00
ATP	5.4E-03	-5.4E-03	5.4E-03	3.0E-03	3.1E-03	-2.0E-02	2.0E-02	5.7E-02	4.2E-02	0.0E+00	-3.0E-03	-3.1E-03	2.8E-01	-5.9E-05	3.6E-03	0.0E+00
NADH	1.7E-02	-1.7E-02	1.7E-02	9.4E-03	9.8E-03	-6.4E-02	6.4E-02	2.9E+00	1.4E-01	0.0E+00	-9.5E-03	-9.7E-03	**2.5E+00**	-1.8E-04	1.2E-02	0.0E+00
PYR	-4.7E-02	1.2E-01	-1.2E-01	-2.9E-01	-3.0E-01	3.4E-01	-3.4E-01	-1.0E+00	1.7E-01	-1.2E-06	2.9E-01	3.0E-01	**-2.0E+00**	5.0E-04	-6.3E-02	0.0E+00
AcCoA	8.6E-03	-8.6E-03	8.6E-03	4.7E-03	4.9E-03	-3.2E-02	3.2E-02	**8.4E-01**	6.8E-02	0.0E+00	-4.7E-03	-4.9E-03	**1.0E+00**	-9.1E-05	5.8E-03	-1.7E-04
PEP	-4.3E-02	1.9E-01	-1.9E-01	-5.7E-01	3.6E-01	2.8E-01	-2.8E-01	-1.1E+00	**-6.1E-01**	-1.5E-06	**5.7E-01**	**5.9E-01**	**-5.4E-01**	4.6E-04	-5.1E-02	0.0E+00
OXA	-4.7E-02	1.2E-01	-1.2E-01	-2.9E-01	-3.0E-01	3.4E-01	-3.4E-01	-1.0E+00	**-8.1E-01**	1.0E+00	2.9E-01	3.0E-01	**-2.0E+00**	5.0E-04	-6.3E-02	0.0E+00
GAP	-2.5E-02	2.1E-01	-2.1E-01	2.1E-01	2.2E-01	7.9E-02	-7.9E-02	-2.2E-02	-1.7E-01	0.0E+00	-2.1E-01	**7.5E-01**	**6.8E-01**	2.7E-04	-1.4E-02	0.0E+00
GK	-4.2E-01	-9.9E-03	9.9E-03	7.9E-03	8.2E-03	-3.1E-02	3.1E-02	9.3E-02	6.5E-02	-4.8E-06	-7.9E-03	-8.1E-03	4.7E-01	4.5E-03	5.6E-03	0.0E+00
PK	-3.1E-02	1.0E-01	-1.0E-01	-2.8E-01	-2.9E-01	1.8E-01	-1.8E-01	**-7.6E-01**	-3.7E-01	7.2E-06	2.8E-01	2.9E-01	**-7.4E-01**	3.3E-04	-3.2E-02	2.9E-06
G6Pase	-7.6E-02	-2.0E-02	2.0E-02	5.1E-02	5.3E-02	2.0E-02	-2.0E-02	-5.2E-03	-4.2E-02	9.3E-07	-5.1E-02	-5.3E-02	1.8E-01	8.2E-04	-3.6E-03	0.0E+00
TCA	0.0E+00	0.0E+00	0.0E+00	0.0E+00	0.0E+00	0.0E+00	0.0E+00	-6.0E-06	0.0E+00	0.0E+00	0.0E+00	0.0E+00	-6.2E-05	0.0E+00	0.0E+00	0.0E+00
OxPhos	0.0E+00	0.0E+00	0.0E+00	0.0E+00	0.0E+00	0.0E+00	0.0E+00	-3.2E-06	0.0E+00	0.0E+00	0.0E+00	0.0E+00	-4.4E-05	0.0E+00	0.0E+00	0.0E+00
LDH	3.9E-02	-1.3E-01	1.3E-01	3.5E-01	3.7E-01	1.8E-01	-1.8E-01	-1.7E-01	-3.9E-01	3.3E-06	-3.6E-01	-3.7E-01	**6.4E-01**	-4.1E-04	-3.3E-02	0.0E+00
PC	-1.5E-02	5.1E-02	-5.1E-02	-1.4E-01	-1.4E-01	1.4E-01	-1.4E-01	**-5.3E-01**	-3.1E-01	4.8E-06	1.4E-01	1.4E-01	-4.0E-01	1.6E-04	-2.6E-02	0.0E+00
PEPCK	-1.5E-02	5.1E-02	-5.1E-02	-1.4E-01	-1.4E-01	1.4E-01	-1.4E-01	**-5.3E-01**	-3.1E-01	4.8E-06	1.4E-01	1.4E-01	-4.0E-01	1.6E-04	-2.6E-02	0.0E+00
G6P_GAP	-6.8E-02	4.2E-01	-4.2E-01	5.6E-02	5.8E-02	-1.3E-02	1.3E-02	8.8E-02	2.6E-02	0.0E+00	-5.6E-02	-5.8E-02	**6.4E-01**	7.2E-04	2.3E-03	0.0E+00
GAP_G6P	-1.3E-02	1.1E-01	-1.1E-01	1.1E-01	1.1E-01	4.1E-02	-4.1E-02	-1.2E-02	-8.7E-02	1.6E-06	-1.1E-01	-1.1E-01	3.7E-01	1.4E-04	-7.4E-03	8.2E-07
PEP_GAP	1.7E-02	-5.7E-02	5.7E-02	1.6E-01	1.6E-01	8.0E-02	-8.0E-02	-7.3E-02	-1.7E-01	2.9E-06	-1.6E-01	-1.6E-01	2.8E-01	-1.8E-04	-1.5E-02	1.5E-06
ATPase	8.8E-03	-8.8E-03	8.8E-03	4.8E-03	5.0E-03	-3.2E-02	3.2E-02	9.4E-02	6.8E-02	-8.0E-07	-4.9E-03	-5.0E-03	1.9E-02	-9.6E-05	5.9E-03	0.0E+00
Glc,b_t_net	6.7E-03	-2.3E-02	2.3E-02	6.2E-02	6.4E-02	3.2E-02	-3.2E-02	-2.9E-02	-6.8E-02	-2.0E-05	-6.2E-02	-6.4E-02	1.1E-01	-5.8E-05	-5.8E-03	-2.3E-06
LAC,b_t,net	3.8E-02	-1.3E-01	1.3E-01	3.5E-01	3.7E-01	1.8E-01	-1.8E-01	-1.7E-01	-3.9E-01	-5.0E-05	-3.6E-01	-3.7E-01	**6.4E-01**	-4.4E-04	-3.3E-02	-1.3E-05

Table 2.6. Sensitivity coefficients to Vmax's, defined by Eq. 2.10. Values in boldface have magnitude greater than 0.50.

	$V_{max,GK}$	$V_{max,G6pase}$	$V_{max,G6P\_GAP}$	$V_{max,PK}$	$V_{max,LDH}$	$V_{max,TCA}$	$V_{max,OxPhos}$	$V_{max,PC}$	$V_{max,PEPCK}$	V_{max,PEP_GAP}	V_{max,GAP_G6P}	V_{max,ATP_ADP}	V_{max,Glc,b_t}	V_{max,LAC,b_t}
Glc_{blood}	-4.9E-04	4.6E-03	-3.6E-03	-9.1E-03	2.3E-03	0.0E+00	-3.3E-04	1.0E-02	5.8E-05	4.6E-03	9.4E-03	-4.1E-03	1.6E-05	1.7E-03
Glc_{tissue}	-6.9E-04	6.4E-03	-5.0E-03	-1.3E-02	3.2E-03	0.0E+00	-4.5E-04	1.4E-02	6.0E-05	6.4E-03	1.3E-02	-5.8E-03	-3.0E-02	2.4E-03
LAC_{blood}	3.4E-03	-2.4E-02	2.4E-02	6.2E-02	-1.6E-02	0.0E+00	2.2E-03	-7.0E-02	6.9E-04	-3.1E-02	-6.4E-02	2.8E-02	-1.1E-04	-1.1E-02
LAC_{tissue}	1.2E-02	-8.3E-02	8.6E-02	2.1E-01	-5.5E-02	-7.4E-07	7.4E-03	-2.4E-01	6.9E-04	-1.1E-01	-2.3E-01	1.2E-01	-3.9E-04	2.9E-01
G6P	2.0E-01	**-9.5E+00**	-8.5E-02	-2.0E-01	3.9E-02	0.0E+00	-1.5E-02	1.7E-01	8.3E-05	1.0E-01	2.1E-01	-9.0E-02	-5.1E-03	2.8E-02
GLY	0.0E+00	0.0E+00	0.0E+00	0.0E+00	0.0E+00	0.0E+00	0.0E+00	0.0E+00	0.0E+00	0.0E+00	0.0E+00	0.0E+00	0.0E+00	0.0E+00
ATP	-5.5E-03	1.1E-02	-1.2E-02	-6.1E-03	-2.0E-02	0.0E+00	-1.4E-02	-8.6E-02	-4.3E-05	3.0E-03	6.7E-03	-8.8E-02	1.8E-04	-1.5E-02
NADH	-1.6E-02	3.6E-02	-3.7E-02	-1.9E-02	-6.4E-02	0.0E+00	-1.7E-01	-2.6E-01	-1.5E-04	9.5E-03	2.1E-02	-6.8E-02	5.7E-04	-4.6E-02
PYR	5.1E-02	-2.7E-01	2.7E-01	**6.2E-01**	3.5E-01	0.0E+00	**1.1E+00**	-3.5E-01	7.2E-04	-2.9E-01	**-7.0E-01**	**2.4E+00**	-1.6E-03	2.7E-01
AcCoA	-8.2E-03	1.8E-02	-1.8E-02	-9.5E-03	-3.2E-02	**-1.0E+00**	-7.7E-02	-1.3E-01	-7.3E-05	4.8E-03	1.0E-02	-3.9E-02	2.9E-04	-2.3E-02
PEP	4.4E-02	-4.3E-01	4.5E-01	**-6.8E-01**	2.8E-01	0.0E+00	**1.0E+00**	**1.5E+00**	6.0E-04	**-5.7E-01**	**-1.7E+00**	-1.7E-01	-1.4E-03	2.1E-01
OXA	5.1E-02	-2.7E-01	2.7E-01	**6.2E-01**	3.5E-01	0.0E+00	**1.1E+00**	**3.6E+00**	**-5.3E+01**	-2.9E-01	**-7.0E-01**	**2.4E+00**	-1.6E-03	2.7E-01
GAP	2.5E-02	-4.9E-01	**5.1E-01**	-4.2E-01	7.9E-02	0.0E+00	-2.8E-02	3.6E-01	1.5E-04	2.1E-01	**-2.4E+00**	-1.2E-01	-8.3E-04	5.9E-02
GK	4.3E-01	2.2E-02	-2.1E-02	-1.6E-02	-3.1E-02	0.0E+00	-2.2E-02	-1.3E-01	-4.3E-05	8.0E-03	1.7E-02	-1.0E-01	-1.4E-02	-2.3E-02
PK	3.0E-02	-2.2E-01	2.2E-01	5.6E-01	1.8E-01	7.2E-07	2.1E-01	**7.3E-01**	3.7E-04	-2.8E-01	-5.9E-01	-4.2E-02	-1.0E-03	1.3E-01
G6Pase	7.8E-02	5.5E-02	-4.4E-02	-1.0E-01	2.0E-02	0.0E+00	-7.6E-03	8.6E-02	4.3E-05	5.2E-02	1.1E-01	-6.7E-02	-2.5E-03	1.4E-02
TCA	0.0E+00	-3.4E-06	0.0E+00	0.0E+00	0.0E+00	0.0E+00	0.0E+00	0.0E+00	0.0E+00	0.0E+00	0.0E+00	8.5E-07	0.0E+00	0.0E+00
OxPhos	0.0E+00	-1.9E-05	0.0E+00	0.0E+00	0.0E+00	0.0E+00	0.0E+00	0.0E+00	-6.3E-06	0.0E+00	0.0E+00	2.2E-05	0.0E+00	0.0E+00
LDH	-3.9E-02	2.7E-01	-2.8E-01	**-7.0E-01**	1.8E-01	0.0E+00	-2.4E-02	**7.9E-01**	2.8E-04	3.6E-01	**7.4E-01**	-3.3E-01	1.3E-03	1.3E-01
PC	1.5E-02	-1.1E-01	1.1E-01	2.8E-01	1.4E-01	0.0E+00	1.4E-01	**6.1E-01**	2.9E-04	-1.4E-01	-2.9E-01	-7.6E-02	-4.9E-04	1.1E-01
PEPCK	1.5E-02	-1.1E-01	1.1E-01	2.8E-01	1.4E-01	0.0E+00	1.4E-01	**6.1E-01**	3.0E-04	-1.4E-01	-2.9E-01	-7.6E-02	-4.9E-04	1.1E-01
G6P_GAP	6.7E-02	**-8.9E-01**	**9.1E-01**	-1.1E-01	-1.3E-02	0.0E+00	-2.8E-02	-5.3E-02	-3.0E-05	5.7E-02	1.2E-01	-1.2E-01	-2.3E-03	-9.5E-03
GAP_G6P	1.2E-02	-2.2E-01	2.3E-01	-2.1E-01	4.1E-02	0.0E+00	-1.5E-02	1.8E-01	7.9E-05	1.1E-01	2.2E-01	-1.2E-01	-4.2E-04	3.0E-02
PEP_GAP	-1.7E-02	1.2E-01	-1.2E-01	-3.1E-01	8.0E-02	0.0E+00	-1.1E-02	3.5E-01	1.6E-04	1.6E-01	3.2E-01	-1.5E-01	5.7E-04	5.9E-02
ATPase	-8.9E-03	1.9E-02	-1.9E-02	-9.8E-03	-3.2E-02	0.0E+00	-2.1E-02	-1.4E-01	-6.9E-05	4.9E-03	1.1E-02	3.3E-02	2.9E-04	-2.4E-02
Glc,b_t_net	-6.9E-03	6.4E-02	-4.9E-02	-1.2E-01	3.2E-02	0.0E+00	-4.2E-03	1.4E-01	6.2E-05	6.2E-02	1.3E-01	-5.8E-02	1.9E-04	2.3E-02
LAC,b_t,net	-3.9E-02	2.7E-01	-2.8E-01	**-7.0E-01**	1.8E-01	0.0E+00	-2.4E-02	**7.9E-01**	2.5E-04	3.6E-01	**7.4E-01**	-3.3E-01	1.3E-03	1.3E-01

The model, without zonation, was modified to account for physiological changes during high-intensity exercise (0.195 kW), and the overall calculated glucose output and lactate uptake rates were compared to experimental values. Figure 2.10 contains simulation results representing the resting state and quasi-steady state at 20 minutes of exercise. During longer periods of exercise many other physiological changes occur which are not represented in the model. It is known that blood flow through the liver decreases by about 50% (Wahren et al. 1971) during high intensity exercise as nutrients and oxygen are diverted to the heart and muscle tissue. The results in Figure 2.10(ii) indicate that a 50% decrease in blood flow rate alone has negligible effect on glucose production and lactate uptake, and thus is not sufficient modification of the model to represent exercise. According to Wahren et al. (1971), arterial lactate concentration increases 5-fold in humans during exercise, and assuming negligible lactate uptake in the gut, the value for $C^{\infty}_{LAC,blood}$ was increased 5-fold to 6.0 mM. Figure 2.10(iii) shows that this increase in lactate concentration also has negligible effect on glucose output, although lactate uptake does increase by 30%. Glycerol uptake rate was then increased 3-fold and the glycogen degradation rate was increased to 2.2 umol/g/min, based on measurements in humans by (Wahren et al. 1971), and amino acid uptake (represented by alanine uptake) was increased 3-fold (Wasserman et al. 1991). These fluxes are assumed to be constant over the 20-minute simulation period. The incorporation of these changes into the model causes a doubling of hepatic glucose production (Figure 2.10iv), but the changes are still not enough to account for the 5-fold increase in observed glucose output during exercise (Wahren et al. 1971). Lactate uptake actually becomes negative, which is

an unrealistic resulting indicating that there is a bottleneck in the gluconeogenic reactions that keeps the extra substrate from exiting the tissue as glucose.

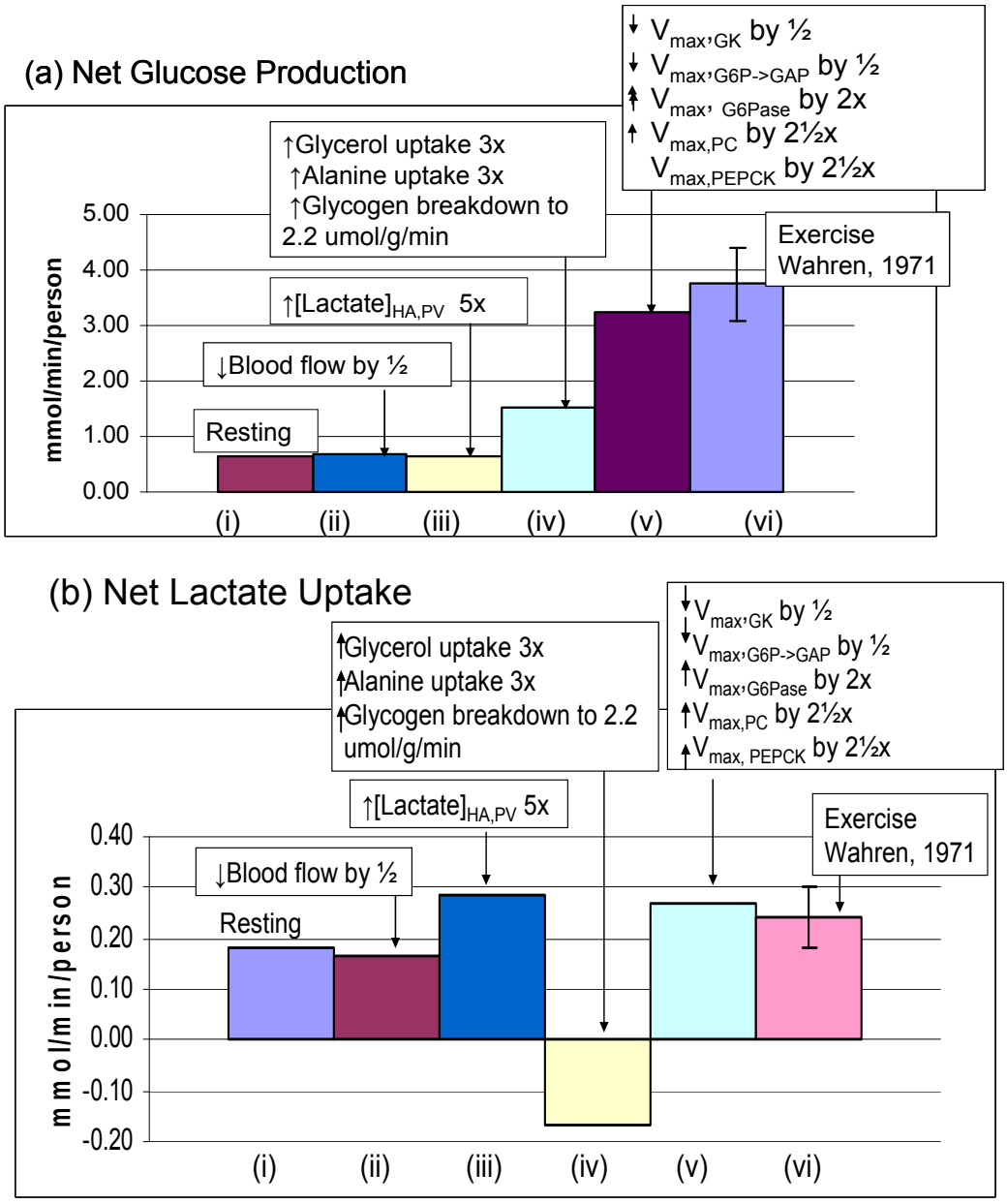

Figure 2.10. Net glucose production and lactate uptake by the liver, calculated at quasi-steady state at 20 minutes following transition from resting to high-intensity exercise. i) Resting, overnight fasted state (i.e. initial condition); ii) liver blood flow rate decreased by ½; iii) same parameters as in (ii), plus: 5-fold increase in lactate concentration in the combined hepatic artery/portal vein input to the liver ($C^{\infty}_{LAC,blood}$) to 6.0 mM; iv) same parameters as in (iii), plus: 3-fold increase in glycerol uptake, to 0.51 umol/g/min, increase in glycogen breakdown to 2.2 umol/g/min, and 3-fold increase in alanine uptake; v) same changes as in (iv), plus: changes in V_{max} of GK, G6Pase, PFK, PC, and PEPCK resulting from the decrease in insulin concentration and increase in glucagon during exercise; vi) measured value at high intensity exercise (Wahren, 1971).

It is known that exercise causes a 28% decrease in arterial insulin concentration (Wahren et al. 1971; Wahren et al.1974), which is already low because of the fasting state; more specifically, a 37% decrease occurs at high intensity exercise (Wharen et al. 1971). Exercise also causes an increase in glucagon concentration (Wahren et al.1974; Howlett et al. 1998). Additionally, the increased adrenergic activity during exercise causes an increase in adrenaline, noradrenaline (Enevoldsen et al. 2004), and epinephrine (Howlett et al. 1998). The insulin decrease and glucagon increase, together, cause the maximal enzyme activity of PK to decrease (Ito et al. 1998), and of G6Pase (Barzilai and Rossetti 1993), PEPCK and F1,6 bisphosphatase to increase (Ito et al. 1998). Glucagon induces the inhibition of PFK and PK via short-term allosteric action (Ito et al. 1998), while insulin acts conversely. Glucagon also induces PEPCK and F1,6 bisphosphatase activity over the long-term via gene expression, with inverse action by insulin. Simulations by El-Refai and Bergman (1976) have also suggested that the maximal activity of GK increases 100% upon insulin stimulation.

The hormonal changes during exercise described in the previous paragraph were incorporated into the model by decreasing $V_{max,GK}$ and $V_{max,G6P\rightarrow GAP}$ by 50%, increasing $V_{max,G6Pase}$ 2-fold, and increasing $V_{max,PC}$ and $V_{max,PEPCK}$ 2½ -fold immediately upon switching to the high-exercise state. As shown in Figure 2.10(v), these changes cause a 4-fold increase in hepatic glucose production, which compares favorably with experimental values (Figure 2.10vi). Calculated lactate uptake also increases, matching the experimental value.

2.4 Discussion

A model of reaction and transport in the liver that can describe the metabolite concentration and reaction flux dynamics separately within the tissue and blood domains was developed. The blood domain contains equations for convection, axial dispersion, and transport to the surrounding tissue; and the tissue domain consists of reactions representing key processes of glycolysis, gluconeogenesis, glycogenolysis, tricarboxylic acid cycle, oxidative phosphorylation, and fatty acid degradation and synthesis. The model includes the metabolic heterogeneity of the liver by incorporating spatial variation of key enzymatic maximal activities.

This model builds upon and integrates information from previous models of liver metabolism that have focused on either subsets of reactions, have included comprehensive set of metabolic pathways assuming well-mixed tissue, or have described the heterogenous nature of the liver in terms of a single species or reaction. Furthermore, the kinetic parameters and the data used for validation were based for the most part on human data, and to a lesser extent, on *in vivo* experiments with dogs or *in vitro* experiments with rats. We believe that this emphasis on use of *in vivo* data to obtain kinetic parameters circumvents the common criticism of complex models that use kinetic parameters that have been measured in environments that are very different from the intact system. Given that, there is still considerable uncertainty in parameter values, and assumptions made about K_m values then affected the values of V_{max}'s needed to be consistent with the *in vivo* data. Fortunately, our sensitivity analysis showed that the results were much less sensitive to the selection of K_m's than to V_{max}'s, and the V_{max}'s that were most influential belong to the regulatory reactions in glycolysis and

gluconeogenesis, for which there is substantial availability of *in vitro* experimental data. The kinetic parameters of the ATPase reaction also were among the most influential. Since this reaction represents many ATP-using reactions and the parameters have no direct physiological meaning, it may be better to consider this reaction flux as an adjustable parameter that has upper and lower limits derived from *in vivo* flux balance analysis.

Simulation results at the overnight fasted, resting state agree closely with experimental values of fluxes and concentrations, and overall glucose uptake and lactate output are confirmed with independent data. The incorporation of zonation of glycolytic and gluconeogenic enzyme activities causes the expected increase in glycolysis and decrease in gluconeogenesis along the sinusoid length. The results from simulations with and without zonation indicate that transport gradients are not sufficient to account for observed axial variations in gluconeogenesis and glycolysis, and that a distributed-in-space arrangement of enzyme activities is necessary to achieve this result. By incorporating the zonation of each enzyme separately in the model, we could ascertain the importance of each enzyme to the axial variation in glucose and lactate fluxes. While several enzymes were more influential, e.g. PK, F1,6BPase (represented by $R_{GAP \rightarrow G6P}$), and PC, no single enzyme alone with zonation caused a significant axial variation in fluxes. The zonation of all reactions combined served to increase the axial variations of glucose and lactate fluxes.

The physical causes of zonation, whether resulting from hormonal or oxygen gradients or differential innervation, as have been hypothesized (Jungermann 1983) have not been addressed in this work. While substantial evidence exists that enzymes of the fatty acid

metabolic pathways also exhibit distributed activities (Jungermann1988; Bederman et al. 2004), the analysis of enzymatic zonation presented here is strictly limited to the central carbohydrate pathways.

The model results are based on the assumption that the sinusoids are structured in parallel, and have uniform size and velocity. In reality, there is significant variation in both length and blood velocity, with a fraction of the sinusoids switching between having flow and no flow at any one time (MacPhee et al. 1995). Moreover, there is branching in some of the sinusoids, and some of the hepatic arterioles and portal venules may connect with the sinusoid at up to a third of the distance down the sinusoid. The effects of this complicated flow pattern and structure on the simulated metabolic results presented here are non-obvious, and will be subject of a future study.

During high-intensity exercise, the hepatic glucose production in humans increases nearly 5-fold, with a smaller increase in lactate uptake. The simulations shown here indicate that observed changes in arterial substrate concentrations and hepatic blood flow rate are not sufficient to shift the liver metabolism enough to account for this increased glucose output. Changes in gluconeogenic and glycolytic enzyme activities, whether caused by exercise-induced changes in insulin, glucagon, adrenaline, noradrenaline, or epinephrine, or even by direct adrenergic stimulation of the liver are needed to achieve the overall metabolic changes observed. The amounts of induction or inhibition of enzymatic activities that were incorporated into the model were based on extrapolation from information from the literature. The simulations have shown that hormonal effects on all the reactions analyzed are crucial for the physiologically realistic response of the

liver to exercise, and changes in individual enzyme activities (data not shown) were not sufficient to achieve this.

The changes in hormone concentrations, and the subsequent changes in enzyme activities, do not occur immediately at the onset of exercise. Since these changes in enzyme activities were incorporated in the model at the onset of exercise, the simulated transients are unrealistically fast (not shown), and thus only the steady state simulation results representing the physiological conditions expected at about 20 minutes of exercise were presented here. Several modifications to the model are needed to generate more realistic dynamics. Mass balance equations of hormones, especially insulin and glucagon, with upstream arterial concentrations that vary with time according to available experimental data, need to be added to the system. The influence of hormones will be especially visible in the distributed model, since hormone degradation occurs within the liver and significant gradients in hormone concentrations occur along the sinusoid length (Jungermann 1987). The allosteric effects on enzyme activity by the relevant local hormone concentrations (most likely the glucagon/insulin ratio), mediated by cAMP and phosphorylation or dephosphorylation reactions, need to be accounted for in the appropriate kinetic expressions. These changes can be expected to result in a more gradual response to the onset of exercise as well as to changes in dietary conditions.

Simulations were performed based on the fasted state, which is the condition under which many of the human exercise studies are performed. Since relatively simple kinetic expressions were used in the model, the response to exercise in the fed state will not closely match experimental data. Incorporation of allosteric regulatory mechanisms into

the key reactions in glycolysis and gluconeogenesis will result in a more robust model that is valid under a variety of nutritional states.

CHAPTER III

GLUCONEOGENESIS AND LIPID METABOLISM IN THE PERFUSED LIVER

3.1 Introduction

The maintenance of glucose homeostasis is one of the main functions of the liver in all mammals. It is accomplished through elegant regulation of the gluconeogenesis, glycolysis, glycogenolysis, fatty acid oxidation, and other pathways of intermediary metabolism. Gluconeogenesis in the liver has been studied extensively over the past four decades, resulting in a better understanding of the factors that regulate the rates of glucose synthesis from various substrates, and the effects of substances such as fatty acids and ethanol on this process.

Despite this wealth of experimental data, the challenge remains to be able to predict how alterations in specific physiological stimuli will affect gluconeogenic flux in the liver. This type of prediction will have potential benefit for designing therapeutic agents, both biochemical and genetic-based, for a variety of pathologies affecting the liver. An

in silico liver that is physiologically accurate can be a cost-effective method for screening potential therapeutic agents.

Metabolic models of the liver can be divided into two broad categories: *lumped models* that consider the organ as well-mixed, and *distributed-in-space models* that consider the heterogeneous nature of the organ. Garfinkel and colleagues (Achs et al. 1971; Anderson et al. 1971) developed the first well-recognized model of liver metabolism using detailed *in vitro*-based kinetic expressions. Their model of gluconeogenesis consisted of kinetic expressions for reactions taking place between phosphoenoylpyruvate (PEP) and glucose, with the net flux through enolase (interpreted from experimental data under a variety of substrates) taken as the input to the model. Since the reactions kinetics of pyruvate carboxylase (PC) and liver-type pyruvate kinase (PK-L) were not considered, the futile cycling that occurs through these reactions was neglected. Moreover, the model lacked ATP and redox balances, the ketogenic reactions and some of the dehydrogenase reactions that are critical to controlling the relationships between lipid metabolism and gluconeogenesis. Furthermore, this work was done prior to knowledge about important regulator effects, such as cAMP-mediated phosphorylation of key regulatory enzymes such as PK-L and fructose-1,6-bisphosphatase (FBPase) and the allosteric effects of fructose-2,6-bisphosphate (F2,6BP). Using a similar approach, Bergman and El Refai (1975) simulated glycogen (Glyc) synthesis and degradation and glucose output at fixed rates of gluconeogenesis. A subset of glycolytic and glycogenolytic reactions around glucose-1-phospahte (G1P), glucose-6-phosphate (G6P), and fructose-6-phosphate (F6P) was the subject of a power law formalism model applied to an *in vitro* experimental system, using tissue extracts (Torres 1994). Hepatic citric

acid cycle flux was modeled as an isolated subsystem, using parameter values that were time-dependent and adjusted for each substrate (Garfinkel 1971a, 1971b).

More recent modeling approaches have eschewed dynamic models for ones based on steady state, without the need for reaction kinetics. These include, the steady state flux balance analysis (FBA) approach with optimization of a presumed objective function (Nolan et al. 2006; Calik and Akbay 2000) (including energy constraints), FBA with Fischer discriminant analysis (Chan et al. 2003) and the FBA and thermodynamic constraint-based model (Beard and Qian 2004). All of these approaches consist of a comprehensive system of reactions describing hepatic metabolism and they provide insight into the distribution of fluxes at various steady states. The approach by Beard and Qian (2004) is particularly interesting, since it utilizes both FBA and thermodynamic constraints; even without kinetic parameters it can predict species concentrations at steady state and analyze the control structure. However, these FBA-based methods require the use of experimental measurements of fluxes as inputs to the model, and since they lack reaction kinetics, have limited predictive value.

The liver, in reality, has a very heterogeneous organization, and several published works have considered its distributed-in-space nature by representing the liver as a system of parallel tubular reactors (Saville et al. 1992; Roberts and Rowland 1985) for prediction of the elimination rates of specific drugs. In Chapter II of this dissertation, a distributed-in-space model, which employs a simplified reaction system representing gluconeogenesis and associated pathways and takes into account heterogeneity in enzyme distribution, i.e. “zonation”, (Jungermann et al. 1982) has been used to investigate the role of zonation in the relative rates of glycolysis and gluconeogenesis along the sinusoid

in the fasted, resting state, as well as to study the effect of high-intensity exercise on glucose production. While this distributed model uses available information concerning liver structure and enzyme distributions, there are few data available to validate the model's predictions at this level of detail. Most of the available data are derived from the entire organ, such as measurements of the concentrations of intermediates from tissue homogenates, metabolic flux determinations from arterial-venous differences (for *in vivo*), or input-perfusate concentrations (for perfused liver), with or without tracers. This makes it nearly impossible to thoroughly validate a distributed model. Furthermore, most measurements of enzymatic kinetic parameters in liver also represent the average value for the tissue.

In this chapter, we have developed a lumped model of hepatic metabolism, with an emphasis on gluconeogenesis and fatty acid metabolism. While the model was kept as simple as possible to achieve tractability, reactions are included as necessary to account for the relationship between gluconeogenesis and lipid metabolism. Additional reactions, such as those occurring mainly in glycolysis, are included to increase the flexibility of the model for future applications. Michaelis-Menten type kinetic expressions were used for many of the reactions. However, the exclusive use of these expressions was inadequate for achieving the expected physiological results. For key regulated reactions—FBPase, PFK, PC, PDC, and PK—rate expressions were used that incorporate allosteric effectors, specific substrate relationships (e.g. cooperative binding), and/or phosphorylation/dephosphorylation, and were developed using *in vitro* enzyme activity data and knowledge of the specific mechanisms.

The model is first used to represent the 24 hr fasted rat liver *in vivo*. Since many of the most well-controlled, data-rich experiments available in the literature have been performed with the perfused liver, we then modified the model to account for the conditions of the *ex vivo* liver in a recirculated perfusion system. With the same set of kinetic parameters, this model is used to predict the effect of fatty acid uptake on gluconeogenesis rates during separate lactate and pyruvate perfusions. Our simulations are then compared with experimental data available from the literature.

3.2 Model Development

3.2.1 Metabolic Pathways

The metabolic pathways considered in the model development are glycolysis, gluconeogenesis, the tricarboxylic acid cycle (TCA), fatty acid oxidation, fatty acid synthesis, ketogenesis, oxidative phosphorylation, and glycogen degradation (Fig. 3.1). Each pathway is represented by a few key reactions, mainly those essential for defining the relationships between lipid metabolism and gluconeogenesis.

The rate expressions are given in Table 3.1. The rate mechanism for transport between the blood and tissue domains is described by facilitated diffusion. The kinetic expressions for some of the relatively irreversible reactions are expressed by simple Michaelis-Menten kinetics, with modulation by ADP/ATP (PS) and NADH/NAD^+ (RS), as relevant. Reversible, near-equilibrium reactions (e.g. $R_{GAP \rightarrow PEP}$, R_{LDH}) are represented by a simplified form of a reversible, ping-pong mechanism, with the Haldane equation used to relate kinetic parameter values at near-equilibrium and to ensure consistency with thermodynamic constraints.

Table 3.1. Reaction rate stoichiometry, kinetic expressions, and parameter values used in the model. Definitions: $PS=C_{ADP}/C_{ATP}$; $RS_m=C_{NADH(m)}/C_{NAD(m)^+}$; (m):mitochondrial; (c): cytosolic; FBA: flux balance analysis, used to calculate some of the reaction rate fluxes from flux measurements of species entering and exiting the tissue at steady state. Steady state flux measurements are given in Table 3.2. Concentrations that are considered constant have been assigned the following values: C_{AMP}=0.125 μmol gww^{-1} hep (Garfinkel et al. 1979) ; C_{cAMP}=0.0094 μmol gww^{-1} hep (Pilkis et al. 1975); C_{Pi}=5.74 μmol gww^{-1} hep (Chan et al. 2003; Christian and Christain 1983); $C_{F2,6BP}$=0.00013 μmol gww^{-1} hep (Diem and Lentner 1970; Garfinkel et al. 1979); C_{NH4+}=0.7 μmol gww^{-1} hep (Achs et al. 1971; Calik and Akbay 2000); C_{CoA}=0.25 μmol gww^{-1} hep (Bracht et al. 1993); $(C_{ATP}+C_{ADP}+C_{AMP})_{total}$= 5.08 μmol gww^{-1} hep (Bergmeyer 1974; Hems et al. 1966)**;** $(C_{NADH} + C_{NAD+})_{total}$= 1.50 μmol gww^{-1} hep (Bergmeyer 1994; Stubs et al. 1972;Williamson et al. 1969a; Williamson et al. 1970)**.**

Steady state concentrations, used to estimate parameters values, are: $^aC_{NAD+\,(c),SS}$ from reference Williamson et al. 1969a**,** assuming 80-90% unbound; $^bC_{NADH\,(c),SS}$ calculated from $C_{NAD+\,(c),SS}$ and $(C_{NADH} + C_{NAD+})_{total}$. $K_{eq,RS}$ = 112, calculated from reference Achs et al. 1971.

*Reactions corrected from manuscript published from this chapter.

To reduce table space, superscripts in tables refer to the following references:

1 Agius and Alberti 1985
2 Bantenburg and Olson 1976
3 Bergmeyer 1994
4 Chien et al. 2000
5 Christian and Christian 1983
6 Diem and Lentner 1970
7 Ekdahl and Ekman 1983
8 Engela dn Dalziel 1967
9 Gross et al. 1967
10 Hems et al. 1966
11 Krebs 1967
12 Magnusson et al. 1991
13 McClure et al. 1971
14 Pusca and Belovich 2012
15 Reich and Selkov 1981
16 Scrutton and White 1972
17 Stubs et al. 1972
18 Van Schaftingen et al. 1980
19 Williamson et al. 1970
20 Exton and Park 1967
21 Huang 1997
22 Jin et al. 2004
23 Neese et al. 1995
24 Petersen et al. 1996
25 Rossetti et al. 1993
26 Salem et al. 2002
27 Torres 1994
28 Tucker and Dawson 1979
29 Williamson et al 1969b
30 Bode et al. 1973
31 Chp. II of this thesis
32 Pison et al. 1998

Rate	Kinetic Expression	Parameter Values	Method of determining parameters
		Parameters common to several reactions: PS_i=0.44	Set equal to steady state C_{ADP}/C_{ATP} [10]
		RS_i=0.2	Set equal to steady state $C_{NADH(m)}/C_{NAD^+(m)}$ [19]
A. Reaction Rates			
R_{GK} GLC + ATP → G6P+ ADP	$\frac{V_{\max,\,GK}\, C_{GLC\_t}}{K_{m,GK} + C_{GLC\_t}} \left(\frac{1/PS}{1/PS_i + 1/PS} \right)$	$V_{max,GK}$ = *2.19* µmol gww hep^{-1}min^{-1}	Calculated from R_{GK} flux (from FBA, assuming 30% cycling) and steady state GLC concentration[3]
		$K_{M,GK}$=*6.25* µmol/gww hep	Set equal to steady state GLC concentration[3]
R_{G6Pase} G6P→GLC	$\frac{V_{\max,\,G6Pase}\, C_{G6P}}{K_{m,G6Pase} + C_{G6P}}$	$V_{max,G6Pase}$= *3.65* µmol gww hep^{-1}min^{-1}	Calculated from R_{G6Pase} flux from FBA and steady state G6P concentration[3]
		$K_{m,G6Pase}$=*0.102* µmol/gww hep	Set equal to steady state G6P concentration[3]

R_{GI} G6P ↔ F6P	$\frac{\frac{V_{\max,G6P,GI}}{K_{m,F6P,GI}}\left(C_{F6P}-\frac{C_{G6P}}{K_{eq,GI}}\right)}{1+\frac{C_{F6P}}{K_{m,F6P,GI}}+\frac{C_{G6P}}{K_{m,G6P,GI}}}$	$V_{max,G6P,GI}$ = *32.8* µmol gww hep^{-1}min^{-1}	Calculated from R_{GI} flux from FBA and steady state F6P and G6P concentrations[3]
		$K_{m,F6P,GI}$ =*0.046* µmol/gww hep	Set equal to steady state F6P concentration[3]
		$K_{m,G6P,GI}$ =*0.10* µmol/gww hep	Set equal to steady state G6P concentration[3]
		$K_{eq,GI}$=*2.5*	Calculated from in vivo concentrations[3]
R_{FBPase} F1,6BP → F6P	$\frac{V_{\max,FBPase}\frac{\mu(1+\mu)^{n_{fgbp}}}{(1+\beta)^{n_{fbp}}(1+\sigma)^{n_{fbp}}}(1+\beta\gamma+\delta\gamma)^{n_{fbp}}}{L_{FBP}\frac{\left(1+\beta^{n_{fbp}}\right)}{(1+c_{FBP}\gamma)^{n_{fbp}}}+(1+\mu)^{n_{FBP}}}$ $\mu=\frac{C_{F1,6BP}}{K_{F1,6BP,FBPase}};\beta=\frac{C_{F2,6BP}}{K_{iF2,6BP,FBPase}};$ $\gamma=\frac{C_{cAMP}}{K_{icAMP,FBPase}};\delta=\frac{C_{AMP}}{K_{iAMP,FBPase}}$	$V_{max,FBPase}$=*20* µmol gww hep^{-1}min^{-1} $K_{F1,6BP,FBPase}$= *4.84E-04* µmol/gww hep* $K_{icAMP,FBPase}$= *9.23E-03* µmol/gww hep* $K_{iF2,6BP,FBPase}$ = *1.56E-02*µmol/gww hep $K_{iAMP,FBPase}$=*0.106* µmol/gww hep n_{FBP}=*5.52* L_{FBP}=*2.76E+06* C_{FBP}=*0.56*	Calculated from in vitro kinetic data[12,7] *modified 10- 20% from the original source.

R_{PFK} F6P + ATP → F1,6BP + ADP	$\frac{V}{V_{\max,PFK}} = \frac{C_{ATP} \cdot C_{F6P}^{\ 2}}{K_{PFK} + C_{ATP} \cdot C_{F6P}^{\ 2}}$ $K_{PFK} = K_{F6P,PFK}^{APP}\left(C_{ATP} + K_{ATP,PFK} + T_1^{n1}\frac{C_{ATP}^{\ 2}}{K_{iATP,PFK}}\right)^2\left(1 + T_2^{n2} + T_1^{n1}\right)$ $T_1 = \alpha\left(\frac{\cdot K_{iF2,6BP,PFK} + C_{F2,6BP}}{K_{iF2,6BP,PFK} + Q_1 C_{F2,6BP}}\right)$ $T_2 = \sigma\left(\frac{K_{iAMP,PFK} + C_{AMP}}{K_{iAMP,PFK} + Q_2 C_{AMP}}\right)$	$V_{max,PFK}$=*3.75* µmol gww hep^{-1}min^{-1} $K_{ATP,PFK}$=*2.91E-02* µmol/gww hep $Ki_{ATP,PFK}$=*0.058* µmol/gww hep $Ki_{AMP,PFK}$=*1.16* µmol/gww hep $K^{APP}_{F6P,PFK}$=*4.0E-04* µmol/gww hep $Ki_{F2,6BP,PFK}$=*1.7E-02* µmol/gww hep *α =2.0* *σ=3.5* *n1=3.0* *n2=3.0* *Q1=100* *Q2=50*	Calculated from in vitro kinetic data[7,18] .
R_{PK} PEP + ADP → PYR + ATP	$\frac{V_{\max,\,PK}\,\pi\left(1+\pi+\gamma\right)^{n_{PK}-1}}{L_p\,\frac{\left(1+\beta\right)^{n_{pk}}\left(1+\kappa_{ATP,PK}\,\gamma\right)^{n_{PK}}}{\left(1+\kappa_{ALA,PK}\,\beta\right)^{n_{PK}}\left(1+\phi\right)^{n_{PK}}} + \left(1+\pi+\gamma\right)^{n_{PK}}}$ $\pi = \frac{C_{PEP}}{K_{PEP,PK}};\ \gamma = \frac{C_{ATP}}{K_{ATP,PK}};$ $\beta = \frac{C_{ALA}}{K_{iALA,PK}};\ \phi = \frac{C_{FBP}}{K_{FBP,PK}}$	$V_{max,PK}$=*62.5*µmol gww hep^{-1}min^{-1} $K_{PEP,PK}$=*3.2E-02* µmol/gww hep $K_{ATP,PK}$=*0.435* µmol/gww hep $K_{iALA,PK}$=*1.16E-01*µmol/gww hep $K_{FBP,PK}$=*5.80E-04* µmol/gww hep* L_p=*1.60E+04* n_{PK}=*3.10* $\kappa_{ATP,PK}$=*2.0* $\kappa_{ALA,PK}$=*0.2*	Calculated from in vitro kinetic data[14]; modified from the original source.

R_{LDH} $LAC + NAD^+ \leftrightarrow PYR + NADH$	$\frac{\frac{V_{max,LDH}}{K_{m,LAC,LDH}}\left(C_{LAC}C_{NAD^+(c)} - \frac{C_{PYR}C_{NADH(c)}}{K_{eq,LDH}}\right)}{1 + \frac{C_{LAC}C_{NAD^+(c)}}{K_{m,LAC,LDH}} + \frac{C_{PYR}C_{NADH(c)}}{K_{m,PYR,LDH}}}$	$V_{max,LDH}$=*195* µmol gww hep^{-1}min^{-1}	in vitro[6]
		$K_{m,LAC,LDH}$=*1.43* µmol/gww hep	Set equal to product of steady state LAC [3,11,19] and $NAD^+(c)$ [a] concentrations
		$K_{m,PYR,LDH}$=*4.77E-05* µmol/gww hep	Calculated from in vivo LDH flux[5] and steady state LAC[3,11,19], PYR[3,11,17], $NAD^+_{(c)}$[a], and $NADH_{(c)}$[b] concentrations
		$K_{eq,LDH}$=*1.1E-04*	in vitro[19]
$R_{ALA\rightarrow PYR}$ $ALA + NAD^+ \rightarrow PYR + NADH$	$\frac{\frac{V_{max,ALA,PYR}}{K_{m,ALA,PYR}}\left(C_{ALA}C_{NAD^+(c)} - \frac{C_{PYR}C_{NADH(c)}}{K_{eq,ALA,PYR}}\right)}{1 + \frac{C_{ALA}C_{NAD^+(c)}}{K_{m,ALA,PYR}} + \frac{C_{PYR}C_{NADH(c)}}{K_{m,PYR,ALA}}}$	$V_{max,ALA,PYR}$= *300* µmol gww hep^{-1}min^{-1}	in vitro[6]
		$K_{mALA,PYR}$=*0.71* µmol/gww hep	Set equal to product of steady state ALA[3] and $NAD^+(c)$[a] concentrations
		$K_{m,PYR,ALA}$=*2.4E-07* µmol/ gww hep	Calculated from in vivo flux[5] and steady state ALA[3], $NAD^+_{(c)}$[a], PYR[3,11,17], and NADH(c)[b] concentrations
		$K_{eq,ALA,PYR}$=*2.5E-03*	In vitro[8]

$R_{PYR \rightarrow PEP}$ PYR + ATP + GTP → PEP + ADP + GDP + Pi + CO_2	$$\frac{V_{\max,PC}\frac{1}{\left(1+\frac{C_{ADP}}{K_{i,ADP,PYR,PC}}\right)}}{1+\frac{K_{ATP,PC}}{C_{ATP}^{n_{1PC}}}+\frac{K_{PYR,PC}}{C_{PYR}^{n_{2PC}}\left(1+\frac{C_{ADP}}{K_{i,ADP,PYR,PC}}\right)}\varpi}$$ $$\varpi=\left(\frac{1}{\left(1+\frac{C_{AcCoA}^{n_{3PC}}}{K_{a,AcCoA,PC}}\right)}+\frac{K_{ATP}}{K_{i,ADP,ATP,PC}}\frac{C_{ADP}}{C_{ATP}^{n_{1PC}}}\right)$$	$V_{max,PC}$=*12.4* µmol gww hep^{-1}min^{-1} $K_{ATP,PC}$=*0.034* (µmol/gww hep)$^{\wedge 1.03}$ $K_{PYR,PC}$=*7.1* (µmol/gww hep)$^{\wedge 0.8}$ $K_{iADP,PYR,PC}$=*1.74* µmol/gww hep $K_{iADP,ATP,PC}$=*0.521* µmol/gww hep $K_{a,AcCoA,PC}$=*2.28E-05* (µmol/gwwhep)$^{\wedge 1.65}$ $n_{1,PC}$ =*1.03* $n_{2,PC}$ =*0.80* $n_{3,PC}$ =*1.65*	Calculated from in vitro kinetic data for pyruvate carboxylase[13,16]
$R_{PEP \leftrightarrow GAP}$ PEP + ATP + NADH↔ GAP + ADP + NAD^+	$$\frac{\frac{V_{\max,PEP,GAP}}{K_{m,PEP,GAP}}\left(C_{PEP}C_{NADH(c)}C_{ATP}-\frac{C_{GAP}C_{Pi}C_{NAD^+(c)}C_{ADP}}{K_{eq,PEP,GAP}}\right)}{1+\frac{C_{PEP}C_{NADH(c)}C_{ATP}}{K_{m,PEP,GAP}}+\frac{C_{GAP}C_{Pi}C_{NAD^+(c)}C_{ADP}}{K_{m,GAP,PEP}}}$$	$V_{max,PEP,GAP}$ = *94.0* µmol gwwhep^{-1}min^{-1} $K_{m,PEP,GAP}$ =*4.3E-05* µmol/gww hep $K_{m,GAP,PEP}$=*9.13E-03* µmol/ gww hep $K_{eq,PEP,GAP}$=*4166*	In vitro[6] Set equal to product of PEP[3], NADH(c)[b], and ATP[3,10] concentrations'; modified during parameter estimation Calculated from $R_{PEP \leftrightarrow GAP}$ flux from FBA and steady state PEP[3], ATP[3,10], NAD^+(c)[a], NADH(c)[b], GAP[17,19], and ADP[3] In vitro[15]
*$R_{GAP \rightarrow F1,6BP}$ 2GAP→F1,6BP	$$\frac{V_{\max,GAP,F1,6BP}C_{GAP}}{K_{m,GAP,F1,6BP}+C_{GAP}}$$	$V_{max,GAP,F1,6BP}$ = *4.97* µmol gwwhep^{-1}min^{-1} $K_{m,GAP,F1,6BP}$ = *0.0194* µmol/gww hep	Calculated from $R_{GAP \leftrightarrow F1,6BP}$ flux from FBA and steady state GAP concentration[17,19] Set equal to steady state GAP concentration[17,19]

R_{PDC} PYR + NAD^+ → AcCoA + NADH	$\frac{V_{\max,PDC}C_{PYR}}{\left(1+\frac{\alpha_{PDC}}{PS}\right)\left(1+\beta_{PDC}\frac{C_{AcCoA}}{C_{CoA}}+\delta_{PDC}(RS_m)^2\right)(K_{PDC}+C_{PYR})}$	$V_{max,PDC}$ = *1.88* µmol gww hep^{-1}min^{-1} K_{PDC}=*0.20* µmol/gww hep $\alpha_{,PDC}$ = *0.9* $\beta_{,PDC}$ = *25;* $\delta_{,PDC}$ = *0.50*	Calculated from in vitro kinetic data[1,2]
$R_{FFA \rightarrow AcCoA}$ FFA + 2ATP + 7NAD^+ + 7FAD→ 8AcCoA + 7NADH + 7FADH + 2ADP	$\frac{V_{\max,FFA,AcCoA}C_{FFA}}{K_{m,FFA,AcCoA}+C_{FFA}}\left(\frac{1/RS_m}{1/RS_{i,}+1/RS_m}\right)\left(\frac{1/PS}{1/PS_{i,}+1/PS}\right)$	$V_{max,FFA,AcCoA}$= 6.76 µmol gww hep^{-1}min^{-1} $K_{m,FFA,AcCoA}$ =0.36 µmol/gww hep	Calculated from in vivo flux[5], steady state FFA[4], PS[10], and RS_m[19]concentrations Set equal to steady state FFA concentration[4]
$R_{TG \rightarrow FFA}$	$\frac{V_{\max,TG,FFA}C_{TG,t}}{K_{m,TG,FFA}+C_{TG,t}}$	$V_{\max,TG,FFA}$ = 3.67 µmol gww hep^{-1}min^{-1} $K_{m,TG,FFA}$ = 0.0071 µmol/gww hep	Calculated from $R_{TG \rightarrow FFA}$ flux from FBA and steady state TG,t[9] concentration Set equal to steady state TG,t[9] concentration
$R_{GLR\_t \rightarrow GR3P}$ GLR+ATP→GR3P+ADP	$\frac{V_{\max,GLR,GR3P}C_{GLR,t}}{K_{m,GLR,GR3P}+C_{GLR,t}}\left(\frac{1/PS}{1/PS_i+1/PS}\right)$	$V_{\max,GLR,GR3P}$ = 0.79 µmol gww hep^{-1}min^{-1} $K_{m,GLR,GR3P}$ = 0.125 µmol/gww hep	Calculated from in vivo flux[5] and steady state PS[10] and assumed GLR,t concentrations. Set equal to the assumed steady state GLR,t concentration
$R_{GR3P \leftrightarrow GAP}$ GR3P+$NAD^+ \leftrightarrow$GAP+NADH	$\frac{\frac{V_{\max,GR3P,GAP}}{K_{m,GR3P,GAP}}\left(C_{GR3P}C_{NAD^+(c)^+}-\frac{C_{GAP}C_{NADH(c)}}{K_{eq,GR3P,GAP}}\right)}{1+\frac{C_{GR3P}C_{NAD^+(c)}}{K_{m,GR3P,GAP}}+\frac{C_{GAP}C_{NADH(c)}}{K_{m,GAP,GR3P}}}$	$V_{max,GR3P,GAP}$= *115* µmol gww hep^{-1}min^{-1} $K_{m,GR3P,GAP}$=*0.47* µmol/gww hep $K_{m,GAP,GR3P}$= *7.06E-07* µmol/gww hep $K_{eq,GR3P,GAP}$=*1.3E-04*	in vitro[6] Set equal to product of steady state GR3P[3] and $NAD^+(c)$[a] concentrations Calculated from $R_{GR3P \leftrightarrow GAP}$ flux from FBA and steady state GR3P[3], $NAD^+(c)$[a], NADH(c)[b], and GAP[17,19] concentrations in vitro[15]

R_{FA_syn} $8AcCoA + 7ATP \rightarrow FFA_{c16} + 7ADP$	$\frac{V_{\max FA\_syn} C_{AcCoA}}{K_{m,FA\_syn} + C_{AcCoA}} \left(\frac{1/PS}{1/PS_i + 1/PS} \right)$	$V_{\max,FA\_syn}$ = 2.7 µmol gww hep^{-1}min^{-1} K_{m,FA_syn}=0.13 µmol/gww hep	Calculated from R_{FA_syn} flux from FBA and steady state AcCoA concentration[3] Set equal to the steady state AcCoA[3] concentration.
R_{TG_f} $3FFA_{c16} + 2ATP + GR3P \rightarrow TG + 2ADP$	$\frac{V_{\max,TG-f} C_{GR3P} C_{FFA}}{K_{m,TG-f} + C_{GR3P} C_{FFA}} \left(\frac{1/PS}{1/PS_i + 1/PS} \right)$	$V_{\max,TG-f}$ = 0.43 µmol gww hep^{-1}min^{-1} $K_{m,TG-f}$ =0.11 µmol/gww hep	Calculated from R_{TG_f} flux from FBA and steady state FFA concentration[4] Set equal to the product of steady state FFA[4] and GR3P[3] concentrations.
R_{TCA} $8AcCoA+ADP +3NAD^+ + FAD \rightarrow 16CO_2 + ATP + 3NADH +FADH$	$V_{mzx,TCA} C_{AcCoA} \left(\varepsilon \frac{1/RS_m}{1/RS_{i,} + 1/RS_m} + (1-\varepsilon) \frac{1/PS}{1/PS_{i,} + 1/P} \right.$	$V_{max,TCA}$= *22.33* µmol gww hep^{-1}min^{-1} ε *=0.75*	Calculated from in vivo flux[22] and steady state AcCoA[3] concentration. Derived previously.[26]
$R_{AcCoA \rightarrow AcAc}$ $2AcCoA \rightarrow AcAc+2CoA$	$\frac{V_{\max,AcCoA\_AcAc} C_{AcCoA}}{K_{m,AcCoA\_AcAc} + C_{AcCoA}}$	$V_{\max,AcCoA\_AcAc}$ = 9.28 µmol gww hep^{-1}min^{-1} $K_{m,AcCoA\_AcAc}$ = 0.124 µmol/gwwhep	Calculated from $R_{AcCoA \rightarrow AcAc}$ flux from FBA and steady state AcCoA concentration[3] Set equal to steady state AcCoA concentration[3]
R_{BHBdh} $AcAc + NADH \leftrightarrow BHB + NAD$	$\frac{\frac{V_{\max,AcAc\_BHB}}{K_{m,AcAc\_BHB}} \left(C_{AcAc} C_{NADH(m)} - \frac{C_{BHB} C_{NAD^+(m)}}{K_{eq,BHBdh}} \right)}{1 + \frac{C_{AcAc} C_{NADH(m)}}{K_{m,AcAc\_BHB}} + \frac{C_{BHB} C_{NAD^+(m)}}{K_{m,BHB\_AcAc}}}$	$V_{\max,AcAc\_BHB}$ = 60 µmol gww hep^{-1}min^{-1} $K_{m,AcAc\_BHB}$ = 0.0071µmol/gww hep K_{m,BHB_AcAc} = 0.0059µmol/gww hep $K_{eq,BHBdh}$=20	In vitro[28] Set equal to product of steady state concentrations of AcAc[3,11,19] and $NADH_m$ (assumed = 0.01 µmol gww^{-1} hep)[27,29] Calculated from R_{BHBdh} flux from FBA and steady state substrate concentrations in vitro[19]

R_{OxPhos} $O_2 + 5ADP + 2NADH \rightarrow 2H_20 + 5ATP + 2NAD^+$	$\frac{V_{\max,\ OxPhos}\ C_{O_2}}{K_{m,OxPhos}\ + C_{O_2}} \left(\frac{PS}{PS\ + PS_i} \right) \left(\frac{RS_m}{RS_i + RS_r} \right)$	$V_{max,OxPhos}$= *37.8* µmol gww hep^{-1}min^{-1} $K_{m,OxPhos}$=*7.3* µmol/gww hep	Calculated from R_{OxPhos} flux from FBA and steady state O_2[20] concentration Set equal to the steady state O_2[20] concentration
R_{urea} $2NH_4+HCO_3+3ATP \rightarrow$ urea+2ADP+2Pi+AMP+PPi	$\frac{V_{\max,urea} C_{NH4}}{K_{m,urea} + C_{NH4}} \left(\frac{1/PS}{1/PS_i + 1/PS} \right)$	$V_{max,urea}$=*2.57* µmol gww hep^{-1}min^{-1} $K_{m,urea}$=*0.70* µmol/gww hep	Calculated from R_{urea} flux from FBA and steady state NH_4^+[3] concentration Set equal to steady state NH_4^+[3] concentration
$R_{Glyc \rightarrow G6P}$ $(Glyc)_n \rightarrow (Glyc)_{n-1}$ + G6P	$R_{Glyc \rightarrow G6P}$= 0.0358 µmol gww hep^{-1}min^{-1}		Set equal to in vivo flux[24]
B. Transport Rates			
$J_{GLC,b\text{-}t,net}$	$\frac{V_{\max,Glc,b-t}(C_{Glc,b} - C_{Glc,t})}{(K_{m,Glc,b-t} + C_{Glc,b} + C_{Glc,t})}$	V_{max,Glc,b_t}= *17.8* µmol gww hep^{-1}min^{-1} K_{m,Glc,b_t}=*5.07* µmol/gww hep	Calculated from in vivo flux[22,23,25] and steady state GLC,b[5] concentration Set equal to steady state GLC,b[5] concentration
$J_{LAC,b\text{-}t,net}$	$\frac{V_{\max,Lac,b-t}(C_{Lac,b} - C_{Lac,t})}{(K_{m,Lac,b-t} + C_{Lac,b} + C_{Lac,t})}$	V_{max,LAC,b_t}= *22.5* µmol gww hep^{-1}min^{-1} $K_{m,\ LAC,b\_t}$=*1.2* µmol/gww hep	Calculated from in vivo flux [5]and steady state LAC,b[5]concentration Set equal to steady state LAC,b[5] concentration
$J_{FFA,b\text{-}t,net}$	$\frac{V_{\max,FFA,b-t}(C_{FFA,b} - C_{FFA,t})}{(K_{m,FFA,b-t} + C_{FFA,b} + C_{FFA,t})}$	V_{max,FFA,b_t}= *4.7* µmol gww hep^{-1}min^{-1} K_{m,FFA,b_t}=*0.67*µmol/gww hep	Calculated from in vivo flux [5]and steady state FFA,b[5]concentration Set equal to steady state FFA,b[5]concentration

$J_{GLR,b\text{-}t,net}$	$\frac{V_{max,GLR,b-t}(C_{GLR,b}-C_{GLR,t})}{(K_{m,GLR,b-t}+C_{GLR,b}+C_{GLR,t})}$	V_{max,GLR,b_t}= *2.53* µmol gww hep^{-1}min^{-1}	Calculated from in vivo flux [5] and steady state GLR,b[5] concentration
		K_{m,GLR,b_t}=*0.16* µmol/gww hep	Set equal to steady state GLR,b[5] concentration
$J_{TG,b\text{-}t,net}$	$\frac{V_{max,TG,b-t}(C_{TG,b}-C_{TG,t})}{(K_{m,TG,b-t}+C_{TG,b}+C_{TG,t})}$	V_{max,TG,b_t}= *0.044* µmol gww hep^{-1}min^{-1}	Calculated from flux from FBA and steady state TG,b concentration
		K_{m,TG,b_t}=*0.4* µmol/gww hep	Set equal to steady state TG,b concentration (assumed)
$J_{ALA,b\text{-}t,net}$	$\frac{V_{max,ALA,b-t}(C_{ALA,b}-C_{ALA,t})}{(K_{m,ALA,b-t}+C_{ALA,b}+C_{ALA,t})}$	V_{max,ALA,b_t}= *12* µmol gww hep^{-1}min^{-1}	Calculated from in vivo flux [5] and steady state ALA,b[5] concentration
		K_{m,ALA,b_t}=*0.56* µmol/gww hep	Set equal to steady state ALA,b[5] concentration
$J_{BHB,b\text{-}t,net}$	$\frac{V_{max,BHB,b-t}(C_{BHB,b}-C_{BHB,t})}{(K_{m,BHB,b-t}+C_{BHB,b}+C_{BHB,t})}$	V_{max,BHB,b_t}= *2.64* µmol gww hep^{-1}min^{-1}	Calculated from in vivo flux[5] and steady state BHB,b[5,21] concentration
		K_{m,BHB,b_t}=*0.85* µmol/gww hep	Set equal to steady state BHB,b[5,21] concentration
$J_{pyr,b\text{-}t,net}$	$\frac{V_{max,PYR,b-t}(C_{PYR,b}-C_{PYR,t})}{(K_{m,PYR,b-t}+C_{PYR,b}+C_{PYR,t})}$	V_{max,PYR,b_t}= *8* µmol gww hep^{-1}min^{-1}	Calculated from in vivo flux [5] and steady state PYR,b[5] concentration
		K_{m,PYR,b_t}=*0.062* µmol/gww hep	Set equal to steady state PYR,b[5] concentration
$J_{AcAc,b\text{-}t,net}$	$\frac{V_{max,AcAc,b-t}(C_{AcAc,b}-C_{AcAc,t})}{(K_{m,AcAc,b-t}+C_{AcAc,b}+C_{AcAc,t})}$	$V_{max,AcAc,b\_t}$= *34.8125* µmol gww hep^{-1}min^{-1}	Calculated from in vivo flux [5] and steady state AcAc,b[5] concentration
		$K_{m,AcAc,b\_t}$=*0.7* µmol/gww hep	Set equal to steady state AcAc,b[5] concentration

The kinetic parameters were generally obtained either by from *in vitro* kinetic studies with purified enzymes, by calculation from *in vivo* data and the assumed rate expression, or a combination of these methods. For reversible reactions, the equilibrium constants and Vmax's were obtained from the literature; the forward Km was set equal to the product of the substrate concentrations and the reverse Km was calculated based on the *in vivo* flux and concentrations. Michaelis-Menten kinetics were often used as simplifications for a series of reactions and do not necessarily represent a specific enzyme. Most often, parameters were calculated from *in vivo* data rather than from *in vitro* kinetic studies of purified enzymes. The Km was set equal to the approximate steady state concentration of the corresponding substrate, while the Vmax was calculated by setting the reaction expression equal to the corresponding *in vivo* flux expected during the 24-hour fasted state (given in Table 3.2). The specific approach used for each reaction is indicated in Table 3.1.

In some cases, Michaelis-Menten and reversible kinetics, as described above, were found to be inadequate for achieving the expected physiological responses during gluconeogenesis and lipid metabolism. Thus, the rate expressions were modified to take into account allosteric effectors, specific substrate relationships (e.g. cooperative binding), and phosphorylation/dephosphorylation. Detailed kinetic expressions were developed for five regulated reactions—FBPase, PFK, PC, PDC, and PK—using *in vitro* enzyme activity data and knowledge of the specific mechanisms gleaned from the literature (Table 3.1). The rate expression of FBPase includes the effect of phosphorylation and dephosphorylation by means of cAMP-dependent protein kinase, along with AMP as an uncompetitive inhibitor and F2,6BP as a competitive inhibitor.

Table 3.2. Steady state results, at the overnight fasted state, experimental and calculated using Eqns. 1 and 4, with upstream blood concentrations given here: C^*_{Glc}= 4.6 mM[3]; C^*_{LAC}=1.7 mM[3] ; C^*_{PYR}=0.12mM[3]; C^*_{FFA}=1.5 mM[3,30]; C^*_{AcAc}=0.43 mM[3,30]; C^*_{BHB}= 1.2 mM[30]; Physical parameters used in Eqn. 3.2 are: ; F_{blood} =6.57 ml/min ; V_{tissue}=5.25 cm^3, [12] ; V_{blood} =1.03 cm^3, [31] . Reaction rates (R_i) and transport rates ($J_{i,b\text{-}t}$) are given in Table 3.1 (+: production rate, -: uptake rate). Superscripts refer to citations given in Table 3.1.

Metabolite Concentrations μmol gww hep^{-1}			**Fluxes** μmol gww hep^{-1}min^{-1}		
	Calculated	**Experimental**		**Calculated**	**Experimental**
Glc,tissue	6.3	4.5-6[3]	$J_{GLC,b\text{-}t,net}$	1.11	1.2-1.9[22,23,25]
Glc,blood	5.55	5.07-5.48[5]	$J_{LAC,b\text{-}t,net}$	-1.38	-1.54[5]
F6P	0.039	0.046[3]	$J_{BHB,b\text{-}t,net}$	1.09	0.93[5]
F1,6BP	0.0023	0.016[3]	$J_{ALA,b\text{-}t,net}$	-0.59	-0.64[5]
G6P	0.087	0.102[3]	$J_{PYR,b\text{-}t,net}$	-0.12	-0.14[5]
glycogen	109	109-175[3]	$J_{FFA,b\text{-}t,net}$	-0.87	-0.8[5]
GAP	0.015	0.021[17,19]	$J_{GLR,b\text{-}t,net}$	-0.96	-0.14[5]
GR3P	0.25	0.31[3]	GK	0.57	
PEP	0.0061	0.05[3]	G6Pase	1.68	
PYR,blood	0.024	0.062[5]	GI	1.07	
PYR,tissue	0.023	0.059 [3,11,17]	GAP→F1,6BP	2.15	
LAC,blood	0.59	0.85-1.2[5]	FBPase	1.08	
LAC,tissue	0.46	0.35-0.95[3,11,19]	PFK	0.007	
AcAc,blood	1.47	0.68-0.99[5,21]	PEP→GAP	2.08	
AcAc,tissue	1.61	0.5-0.78[3,11,19]	PK	0.0003	5.56 [22]
BHB,blood	2.07	0.85-1.7[5,21]	PYR→PEP	2.09	3-3.6[32], 7.9[22]
BHB,tissue	5.6	2.23[3,11,19]	LDH	1.26	
ALA,blood	0.23	0.56[5]	GLR→GR3P	0.099	
ALA,tissue	0.18	0.475[3]	GR3P→GAP	0.06	
AcCoA	0.13	0.13[3]	FAT_syn	0.71	
ATP	3.46	3.43[3,10]	FFA→AcCoA	0.86	
ATP+ADP+AMP	5.07	3.68-5.2[3,10]	TG_f	0.11	
NADH(m)/NAD(m)$^+$	0.25	0.18[19]	AcCoa→AcAc	4.83	
NADH(c)/NAD(c)$^+$	0.0021	0 .0017[17,19]	OxPhos	8.20	
			TCA	1.37	1.75[22]
			$J_{TG,b\text{-}t,net}$	0.03	
			PDC	0.0023	

The PFK expression is based on the bi-bi mechanism, where ATP acts as substrate inhibitor while AMP and F2,6BP are activators. The kinetics of the lumped reaction $R_{PYR \rightarrow PEP}$ is represented by the kinetics of the PC reaction, with activation by acetyl CoA and inhibition by ADP, where ADP plays the role of uncompetitive inhibition with respect to pyruvate and competitive inhibition with respect to ATP. The PK expression reflects phosphorylation as an allosteric effect mediated by cAMP-dependent protein kinase, inhibition by both ATP and alanine and activation by F1,6BP. One of the PK model parameters ($K_{F1,6BP,PK}$) was modified significantly from the original kinetic model[23] to provide the expected fluxes at physiological concentrations of allosteric regulators not considered in the previous *in vitro* studies. The rate kinetics of PDC were developed to account for inhibition by acetyl CoA, ATP/ADP ratio, and NADH/NAD+ ratio and the effect of inhibition by phosphorylation of the enzyme by pyruvate dehydrogenase kinase that is mediated through ATP. Kinetic parameters were obtained by fitting the reaction expressions to *in vitro* kinetic data using least squares regression.

Although cytosolic-mitochondrial compartmentation is not considered specifically, the mitochondrial redox state is significantly different from the cytoplasmic redox state, and this difference between the two compartmental concentrations was found to significantly affect reaction rates involving NADH coupled enzymes. A pseudo-mitochondrial compartment was established only for NADH/NAD^+, with the assumption that the mitochondrial redox ratio, RS_m (defined as $C_{NADH(m)}/C_{NAD(m)+}$), is in equilibrium with the cytosolic ratio RS ($C_{NADH(c)}/C_{NAD(c)+}$); this assumption is expressed as $RS_m = K_{eq,RS} \cdot RS$. The equilibrium constant $K_{eq,RS}$ is calculated from the ratios of free cytosolic and

mitochondrial C_{NADH}/C_{NAD+} at the fasted steady state, obtained from measurements of C_{LAC}/C_{PYR} and C_{BHB}/C_{AcAc}, respectively, at equilibrium.

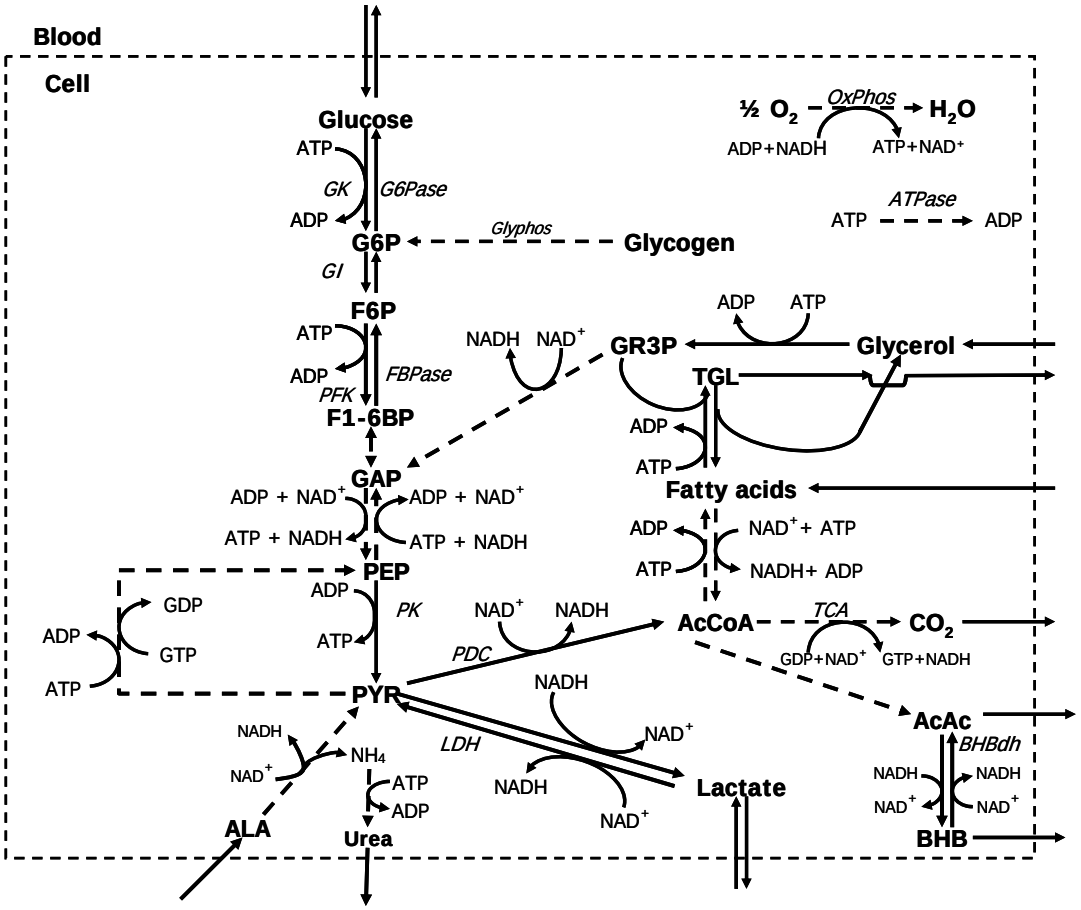

Figure 3.1. Reaction network considered in tissue model. Dashed lines indicate a series of reactions that have been lumped together. Detailed stoichiometry for each reaction shown here is given in Table 3.1. The ATPase reaction represents the total of all ATP-utilizing reactions that are not considered explicitly in the model. GK: glucokinase; G6Pase: glucose-6-phosphatase; Glyphos: glycogen phosphorylase; OxPhos: oxidative phosphorylation, PK: pyruvate kinase; PC: pyruvate carboxylase; PDC: pyruvate dehydrogenase complex; LDH: lactate dehydrogenase; BHBdh: :β -hydroxybutyrate dehydrogenase; GAP: glyceraldehyde-3-phosphate; GR3P: glycerol-3-phosphate; PEP: phosphoenyl pyruvate; AcAc: acetoacetate; BHB:β-hydroxybutyrate; AcCoA: acetyl CoA; ALA: alanine.

3.2.2 Model of the In Vivo Liver

The liver is represented by two well-mixed domains representing the tissue and blood compartments, with mass balances for each metabolite *i* given by:

$$\frac{dC_{i,tissue}}{dt} = J_{i,b-t} + \sum_j R_{i,j} \qquad (3.1)$$

$$\frac{dC_{i,blood}}{dt} = (C_i^* - C_{i,blood})\frac{F_{blood}}{V_{blood}} - J_{i,b-t}\left(\frac{V_{tissue}}{V_{blood}}\right) \qquad (3.2)$$

where C_i^* is the concentration of each species in the blood upstream of the liver (calculated from a weighted average of portal vein and hepatic artery concentrations; Table 3.2); $C_{i,tissue}$ and $C_{i,blood}$ are concentrations of species *i* in the tissue and blood domains, respectively; $J_{i,\text{b-t}}$ is the transport rate between the blood and tissue domains, in units of μmol g tissue^{-1} min^{-1}; $R_{i,j}$ is the reaction rate of each reaction *j* with species *i* as substrate or product; F_{blood} is the blood flow rate through the liver. The ratio of tissue volume to blood volume (V_{tissue}/V_{blood}) is used for conversion of units of $J_{i,b-t}$ from tissue volume units to blood volume units.

The mass balance equation of the tissue (Eq. 3.1) is written for each intermediate within the cell shown in the metabolic pathway in Fig. 3.1 (Glc, LAC, ALA, AcAc, BHB, Glyc, glycerol (GLR), TG, FA, PYR, ATP, NADH, G6P, F6P, F1,6BP, GAP, PEP, AcCoA, GR3P), using the stoichiometry given in Table 3.1. The mass balance for GTP is included within the balance for ATP by assuming a fast equilibration of neucleoside diphosphokinase. Eq. 3.2 is written for every intermediate that occurs in the blood, as shown in Figure 3.1 (i.e. Glc, LAC, ALA, AcAc, BHB, GLR, TG, FA, and PYR). Eqns.

3.1 and 3.2 were solved simultaneously at steady state. Since enzyme kinetic parameters were in general obtained from liver extracted from fasted rats, and the upstream blood concentrations (Ci*) were obtained from blood samples from fasted rats, this simulation represents the conditions *in vivo* for a liver from a 24-hour fasted rat.

3.2.3 Model of the Perfused Liver

The model was then modified to represent the liver perfused *ex vivo* in a recycle system, as used by Williamson et al. (1969a) and others (see Figure 3.2). The tissue mass balance is given by Eqn. 3.1. The mass balance in the blood domain is given by:

$$\frac{dC_{i,blood}}{dt} = (C_{i,perfusate} - C_{i,blood})\frac{F_{perfusate}}{V_{blood}} - J_{i,b-t}\left(\frac{V_{tissue}}{V_{blood}}\right) \qquad (3.3)$$

where $C_{i,perfusate}$ is the concentration of species *i* in the perfusion medium and $F_{perfusate}$ is the perfusate flow rate. Since the content of the blood domain is actually the saline perfusion medium rather than blood, Eqn. 3.3 is only written for those metabolic intermediates expected to occur in the perfusate (i.e. GLC, LAC, ALA, AcAc, BHB, PYR). The perfusion medium vessel, which we also assumed to be well-mixed, is represented by the following mass balance for each metabolic intermediate that exists in the blood domain:

$$\frac{dC_{i,perfusate}}{dt} = (C_{i,blood} - C_{i,perfusate})\frac{F_{perfusate}}{V_{perfusate}} \qquad (3.4)$$

where $V_{perfuate}$ is the volume of the perfusion medium. The quantities $F_{perfusate}$ and $V_{perfusate}$ in Eqn. 3.4 are assigned values that match the specific experimental conditions from the literature that are being simulated.

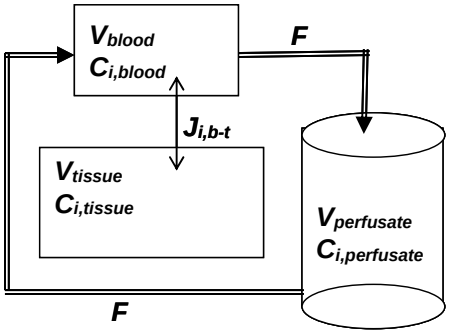

Figure 3.2. Schematic of perfusion system.

It is generally recognized that the *in vivo* environment of an enzyme may be different from the *in vitro* experimental conditions from which the parameters are determined. Thus, parameter values were fine-tuned to within ±10% of their original values using the parameter estimation method of generalized reduced gradient, nonlinear optimization (GRG2) to fit the dynamic solution of Eqns. 3.1, 3.3, and 3.4 to the experimental lactate perfusion data of Williamson, et al. (1969a) shown in Figure 3.3. These parameter values are given in Table 3.1. Three exceptions to this ±10% constraint were found to be necessary to achieve the expected physiological results: $K_{F1,6BP,FBPase}$ was decreased 16%, $K_{cAMP,FBPase}$ was decreased 20%, and $K_{m,PEP,GAP}$ was decreased 90%. This last parameter appears in the kinetic expression for the lumped reversible reaction $R_{PEP \leftrightarrow GAP}$. The large change in this parameter value indicates that the method of setting the Km equal to the substrate concentration does not yield the expected results at physiological conditions for this reaction.

3.3 Results

The model was first solved at conditions representing the *in vivo* 24-hr fasted stated, using the kinetic parameters in Table 3.1 and the physical parameters and upstream blood concentrations given in the caption of Table 3.2. The steady state results are shown in Table 3.2 in comparison with experimental values available from the literature. In general there is excellent agreement between calculated and experimental values, with the exceptions of F-1,6-BP and PEP, which are significantly lower than the *in vivo* measurements (which are already very low), and the flux through PK, which becomes completely inhibited in the model at this state.

Table 3.3. Initial conditions and input functions used in simulation of the perfused liver. ($R_{FA\text{-}endo}$=rate of endogenous fatty acid oxidation, normalized to µmol C_{16} (palmitate); $J^{*}_{FA\text{-}b\text{-}t}$ = the sum of the uptake rate of FFA and rate of endogenous fatty acid oxidation).
*Williamson et al. 1969b.

Lactate Perfusion			
Initial conditions used in Eqn. 3.4	**Saline pre-perfusion; $0 < t \leq 30$**	**Lactate infusion; $30 < t \leq 60$**	**Lactate + FA; $60 < t \leq 90$**
$C_{i,perfusate}$ (t=0) =0; *i*=Glc, LAC, BHB, AcAc (saline pre-perfusion contains no substrate)	$R_{FA\text{-}endo}$ = 0.105 µmol gww $hep^{-1}min^{-1}$, assumed to be equal to experimental measurements of ketone production during this period*.	$R_{FA\text{-}endo}$ = 0.0573 µmol gww $hep^{-1}min^{-1}$, as estimated* from ketone production. $C_{LAC,,perfusate}$ = 10(1-exp(-(t-30)/τ) mM (constant LAC concentration of 10 mM in perfusate); τ is time constant for achieving change in susbstrate concentration, set to 4 min.	$J^{*}_{FA\text{-}b\text{-}t}$= 0.0573+0.27(1-exp(-(t-60) /τ), τ=2.5 min; total rate of 0.33 µmol gww $hep^{-1}min^{-1}$ determined from experimental measurements of oleate infusion*. $C_{LAC,,perfusate}$ =10 mM
Pyruvate Perfusion			
Initial conditions used in Eqn. 3.4	**Saline pre-perfusion; $0 < t \leq 30$**	**Pyruvate infusion; $30 < t \leq 90$**	**Pyruvate + FA; $90 < t \leq 120$**
$C_{i,perfusate}$ (t=0) =0; *i*=Glc, LAC, BHB, AcAc, PYR (saline pre-perfusion contains no substrate)	$R_{FA\text{-}endo}$ = 0.105 µmol gww $hep^{-1}min^{-1}$	$R_{FA\text{-}endo}$ =0.0573 µmol gww $hep^{-1}min^{-1}$ $C_{PYR,,perfusate}$ = 2(1-exp(-(t-30)/ τ) mM (constant PYR concentration of 2 mM in perfusate); τ=3 min. $C_{LAC,,perfusate}$ calculated from Eqn. 3.3.	$J^{*}_{FA\text{-}b\text{-}t}$ = 0.0573+0.27(1-exp(-(t-60) / τ), τ=2.5 min; experimental FA uptake not reported; assumed equal to data from lactate perfusion. $C_{PYR,,perfusate}$ =2 mM

The model was then used to simulate the lactate perfusion protocol of Williamson, et al. (1969a), using the same set of kinetic parameters used in the *in vivo* model (Table 3.1, as described above), with input functions and initial conditions given in Table 3.3. The simulation results compared to their experimental data are shown in Figure 3.3. The first 30 min represents the liver, just removed from the animal, and perfused with saline. The replacement of the blood with saline, which contains no substrate, results in large concentration gradients of metabolites such as glucose, BHB, and AcAc; this leads to the very brief spikes in release of these substances from the tissue. Some of the glucose production also results from gluconeogenesis from endogenous substrates and a small amount from glycogenolysis. Lactate uptake drops quickly to zero because of the absence of substrate in the saline.

The simulated transition from saline perfusion to lactate perfusion begins at t>30 min. As expected, lactate uptake increases quickly and overshoots before settling to a steady state value. This overshoot results from stimulation of lactate transport by the large concentration gradient between the perfusate and tissue. At steady state, about 50% of the lactate (by mass) is converted to glucose, according to both the simulation and experimental data. According to the reported experimental data, the remaining carbon goes into the TCA cycle for oxidation. Our model underestimates TCA flux by about 50%, and instead overestimates total ketone body (BHB and AcAc) production. Futile cycling through the PFK-FBPase system accounts for 10% of the net gluconeogenic flux. While the exact amount of this futile cycling *in vivo* is difficult to quantify, it has been reported that in the fasted state, there is essentially no futile cycling (Hers and Shaftingen 1989).

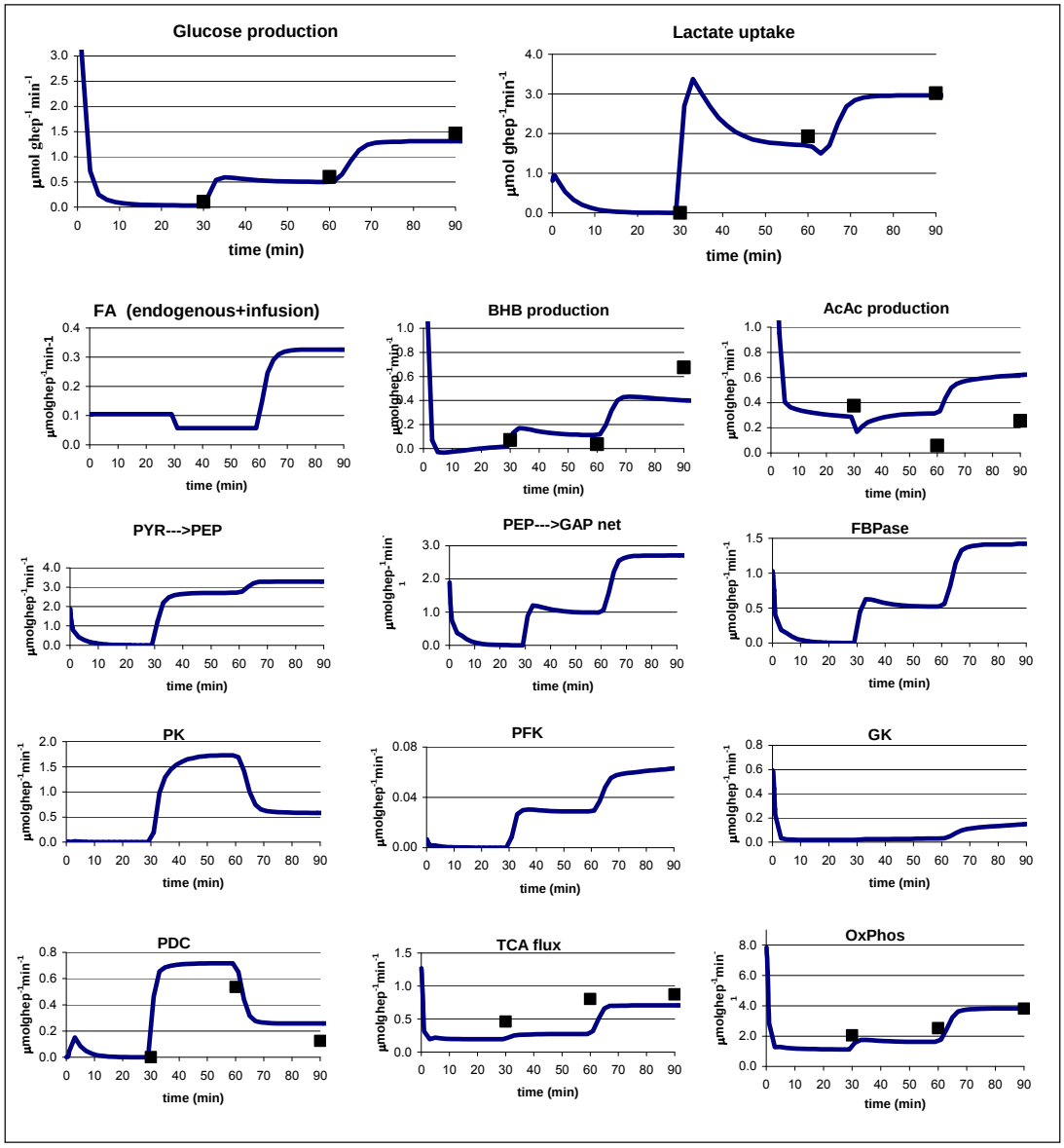

Figure 3.3. Fluxes calculated from perfusion model with lactate as substrate. Initial conditions represent the *in vivo* 24-hour fasted state; $0 < t \leq 30$ min: saline pre-perfusion (no substrate); $30 < t \leq 60$ min: lactate perfusion; $60 < t \leq 90$ min: lactate plus FA perfusion. Details given in Table 3.3. Symbols are experimental data from perfused fasted livers, from Williamson et al. 1969a, using a perfusion medium of Krebs-Henseleit bicarbonate buffer, with 4% bovine serum albumin, in a recirculated system; solid lines are simulations, using Eqns. 1,3 and 4, with $F_{perfusate}$=50 ml/min and $V_{perfusate}$=100 ml (corresponding to the experimental protocol), and all other parameters as given in Table 3.1. In order to view the details of the lactate and fatty acid perfusion, the y-axis scale was expanded, which cut off the initial peak values (in µmol gwwhep^{-1}min^{-1}), given here: glucose production: 7.4; BHB production: 2.1; AcAc production: 6.0.

Infusion with fatty acids is simulated beginning at t>60 min (Fig. 3.3). The additional energy generated by hepatic fatty acid oxidation increases the gluconeogenic flux, so that both glucose production and lactate uptake increase, with close correspondence to the experimental data. The increased AcCoA concentration, derived from the oxidation of exogenous fatty acids, inhibits flux through PDC and PK, while increasing flux through ketogenesis, as expected. The oxidative phosphorylation flux also increases, similar to reported values.

The sensitivity of the major outputs (glucose production and lactate uptake) was investigated for the four parameters ($K_{m,PEP,GAP}$, $K_{F1,6BP,PK}$, $K_{F1,6,BP,FBPase}$, and $K_{cAMP,FBPase}$) that needed to be modified significantly from the original values obtained from *in vitro* or *in vivo* data. Figure 3.4 shows the dynamic flux profiles during lactate perfusion, where each parameter is varied individually, while all other parameters are held constant at the values given in Table 3.1. The results are most sensitive to $K_{F1,6,BP,FBPase}$, $K_{cAMP,FBPase}$ and $K_{F1,6BP,PK}$, but sensitivity is still relatively low at these conditions, since a doubling of the parameter leads to, at most, a 10% change in glucose and lactate fluxes.

The model, with the same set of parameters as given in Table 3.1, was then used to simulate a variety of pyruvate, lactate, and fatty acid perfusion conditions, with the results compared to independent experimental data sets from the literature. Figure 3.5 shows the results of pyruvate perfusions. While the model underestimates both the pyruvate uptake and glucose production compared to the experiments, the yields of glucose from pyruvate calculated from the model are nearly the same as those measured, i.e. in Figure 3.5(a), 48% by mass of pyruvate is converted to glucose experimentally,

while the model predicts 45% conversion; in Figure 3.5(b), the experimental conversion is 50%, while the calculated conversion is 41%. The addition of fatty acids at t=90 min (Figure 3.5(b)) increases pyruvate uptake, glucose production, and lactate production, with trends similar to the published experimental data.

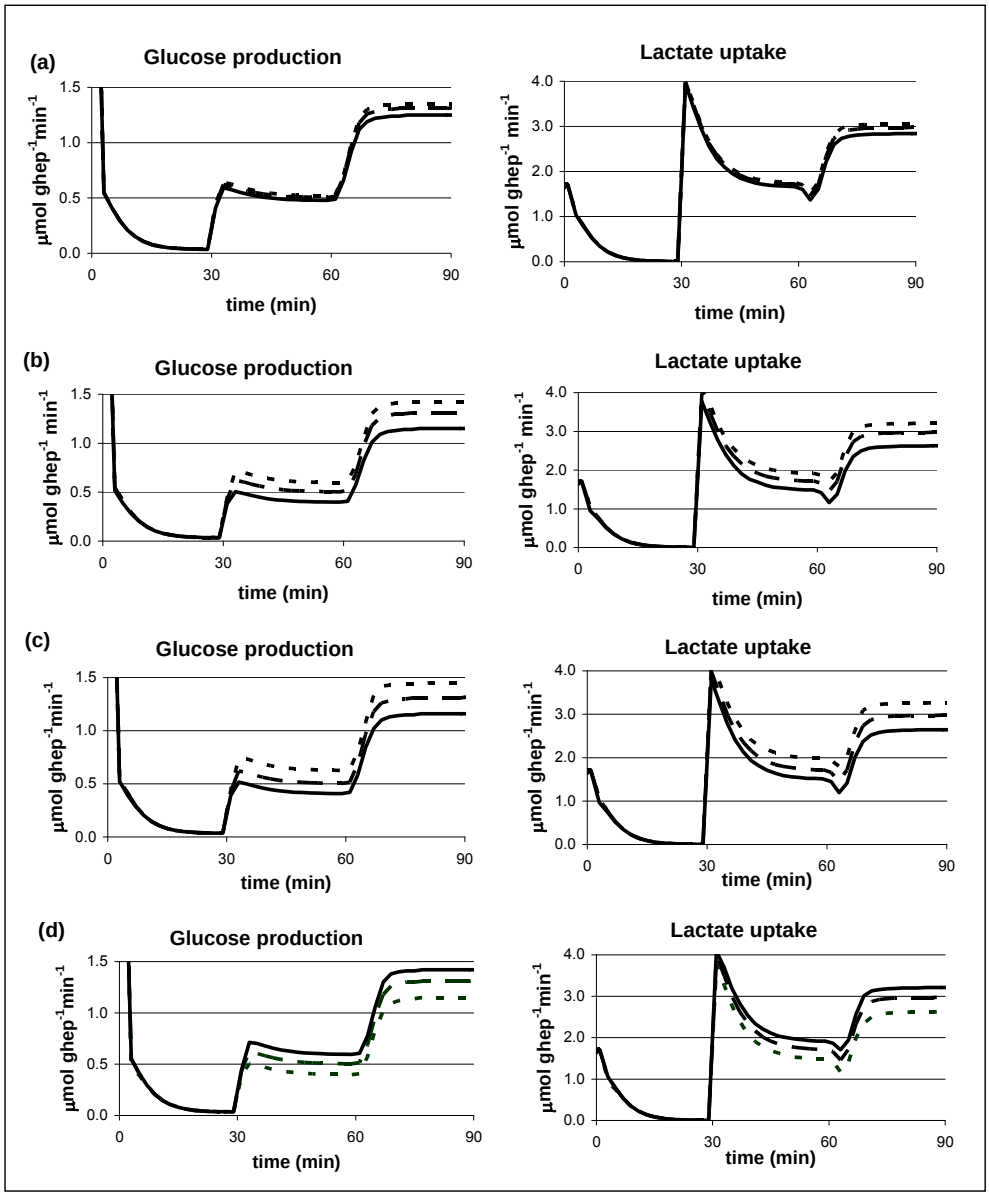

Figure 3.4. Simulations using the perfusion model, using parameters as given in Table 3.1, with the variations in a single parameter, as specified. Solid line: 2x Table 3.1 value; dashed line: Table 3.1 value; dotted line: 0.5x Table 3.1 value. (a) $K_{m,PEP,GAP}$; (b) K_{FBPase}; (c) $K_{F6P,PFK}$; (d) $K_{F1,6BP,PK}$.

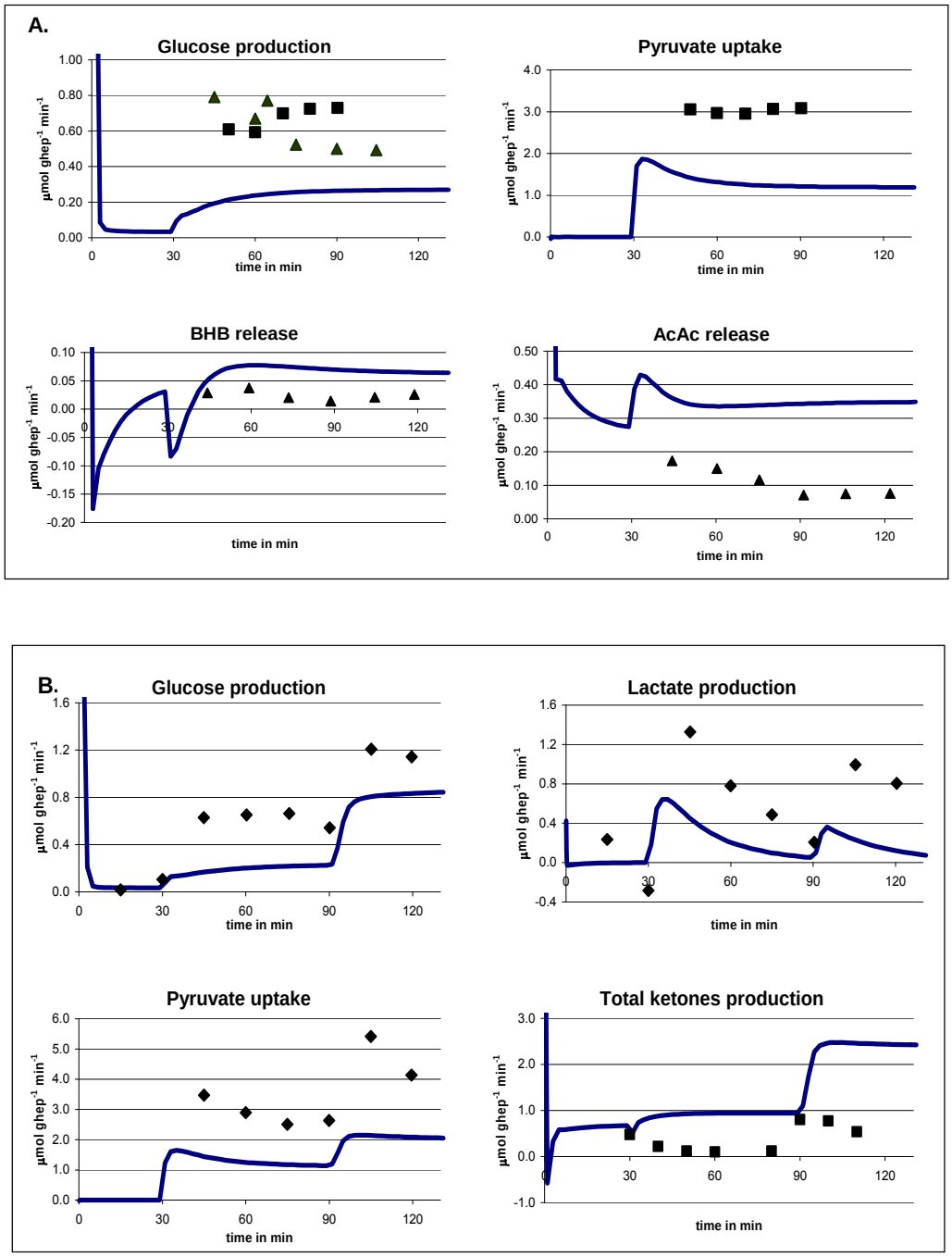

Figure 3.5. Fluxes calculated from perfusion model with pyruvate as substrate. Initial conditions represent the *in vivo* 24-hour fasted state. Symbols are experimental data from perfused fasted livers, using a perfusion medium of Krebs-Henseleit bicarbonate buffer, with 4% bovine serum albumin, in a recirculated system, with substrate added continuously to the medium. Solid lines are simulations, using Eqns. 3.1,3 and 4, with $F_{perfusate}$=50 ml/min, $V_{perfusate}$=100 ml; simulation details given in Table 3.3 and all other parameters given in Tables 3.1. (a) $0 < t \leq 30$ min: saline pre-perfusion (no substrate); $30 < t \leq 120$ min : PYR perfusion. Experimental data: ■ from Williamson et al. 1970b ; ▲ from Williamson et al. 1970a. (b) $0 < t \leq 30$ min: saline pre-perfusion (no substrate); $30 < t \leq 90$ min: PYR perfusion; $90 < t \leq 120$ min: PYR plus FA perfusion. Experimental data: ♦ from Williamson et al. 1969a**;** ■ from Williamson et al. 1970b.

Figure 3.6 shows the calculated glucose production compared to experimental data as reported in three separate published works using lactate as substrate. The simulations are again using the same parameters given in Table 3.1. While the model underestimates glucose production by about 40% in Figs. 3.6a and 3.6c, the prediction is nearly identical to experimental in Fig. 3.6b.

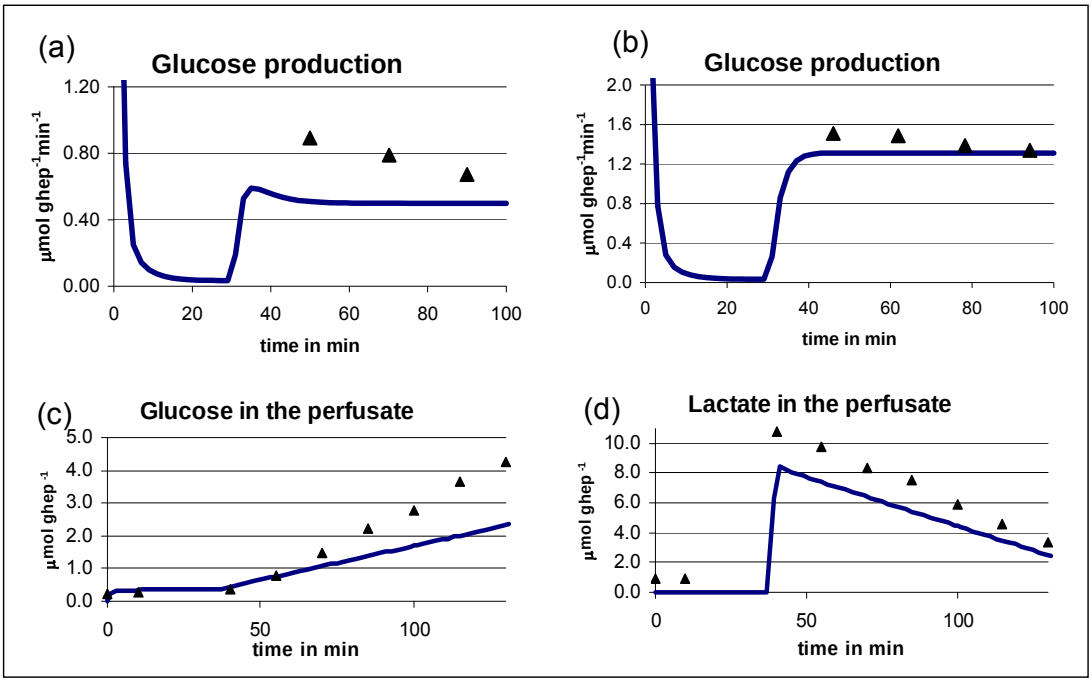

Figure 3.6. Fluxes calculated from perfusion model with lactate as substrate. Initial conditions represent the *in vivo* 24-hour fasted state. Symbols are experimental data from perfused fasted livers, using a perfusion medium of Krebs-Henseleit bicarbonate buffer, with bovine serum albumin, and washed human erythrocytes, in a recirculated system, with substrate added continuously to the medium. Solid lines are simulations, using Eqns. 1,3 and 4 and parameters as given in Tables 1. (a) $0 < t \leq 30$ min: saline pre-perfusion (no substrate); $30 < t \leq 100$ min: Lactate (10mM) perfusion. ▲ from Frohlich and Wieland 1972; simulations calculated with $F_{perfusate}$=7 ml/min, $V_{perfusate}$=100 ml. (b) $0 < t \leq 30$ min: saline pre-perfusion (no substrate); $30 < t \leq 100$ min: lactate (10mM) + FA perfusion. ▲ from Frohlich and Wieland 1972; simulations calculated with $F_{perfusate}$=9 ml/min, $V_{perfusate}$=100 ml. (c) $0 < t \leq 38$ min: saline pre-perfusion (no substrate); $30 < t \leq 100$ min: lactate (10mM). Symbols are experimental data from perfused fasted livers, using a perfusion medium of Krebs-Henseleit bicarbonate buffer, with bovine serum albumin, and with red blood cells, in a recirculated system, with substrate added as a single dose: ▲ from Hems et al. 1966; solid lines are simulations, using Eqns. 1,3 and 4, with $F_{perfusate}$=20 ml/min, $V_{perfusate}$=100 ml.

The accuracy of the model's dynamic response is evaluated in Fig. 3.7, for both lactate and pyruvate perfusions. In the retrograde perfusion data (Bracht et al. 1993), the time

constants for the glucose response was 2.5 – 4 min for both the addition and removal of substrate, with similar response times calculated by the model. The response time from the antegrade perfusions (Martins et al. 2006) were slower, with the steady state not achieved within 15 min of lactate perfusion.

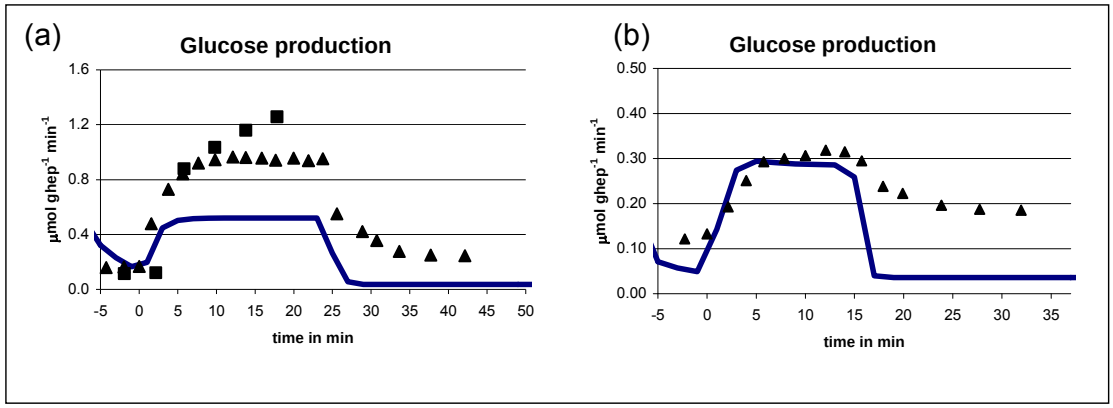

Figure 3.7. Glucose production dynamics. Solid lines are fluxes calculated from perfusion model using Eqns. 1 and 3, with $F_{perfusate}$=32 ml/min, and all other parameters as given in Tables 1. Symbols are experimental data from perfused fasted livers, using a perfusion medium of Krebs-Henseleit bicarbonate buffer saturated with a mixture of oxygen and carbon dioxide. (a) Liver was pre-perfused for 10 min, followed by lactate infusion for 24 min, followed by perfusion with buffer (no substrate) for another 20 min. ▲ from Bracht, et al. 1994, using a non-recirculated retrograde perfusion; ■ from Martins et al. 2006, using a a non-recirculated anterograde perfusion. (b) Liver was pre-perfused for 10 min, followed by pyruvate infusion for 14 min, followed by perfusion with buffer (no substrate) for another 20 min. ▲ from Bracht et al. 1994, using a non-recirculated retrograde perfusion.

3.4 Discussion

The aim of this study was to develop a model capable of representing the complexity of gluconeogenesis and lipid metabolism and their interactions in the liver. Parameter values were determined from a combination of in vitro enzyme kinetics and data obtained from in vivo fasted rats. One set of experimental perfusion data (Williamson et al. 1969a) was used for fine-tuning parameters (Fig. 3.3). This model was then independently validated by comparison of model predictions to data obtained from ten different experiments from seven different publications.

The glucose production and lactate uptake rates obtained from our simulation are in excellent agreement with the values reported by Williamson et al. (Fig. 3.3). These values are 50% lower than those reported by Ross et al. (1967a, 1967b) and Exton and Park (1967) with this difference partially attributed to the use of red blood cells in the perfusion medium by both of these groups. This could lead to higher rates of oxidative phosphorylation and thus energy availability for gluconeogenesis. The higher gluconeogenic rates have also been attributed by Exton and Park to the possible presence of an activator such as glucagon in the faction V albumin used in their perfusion medium (Williamson et al. 1969a; Exton and Park 1967). Furthermore, Exton and Park used a different, non-recycling perfusion system.

Conversion to glucose accounts for 60% of lactate uptake (Fig. 3.3); the remaining 40% is converted to AcCoA through PDC. This latter rate of conversion is in good agreement with the Williamson data, with the small difference due to the fact that our model assumes negligible pyruvate formation during perfusion with lactate. The endogenous fatty acid oxidation and the PDC flux constitute the source of AcCoA. In comparison to the experimental data (Williamson et al. 1969b; Ross et al. 1967a,b; Exton and Park 1967), our simulation overestimates AcCoA conversion to ketone bodies and underestimates its oxidation via the TCA cycle. The low ratio of TCA/ketogenesis could contribute to a shortage of NADH, however, it does not inhibit gluconeogenesis, since the NADH that is required for gluconeogenesis is provided by lactate dehydrogenase

A significant amount of futile cycling is calculated to occur through the PK-PC system during lactate perfusion, with 60% of the carbon through PC recycled through PK (Fig. 3.3). This probably overestimates the actual amount of recycling, but there is

considerable disagreement in the literature as to the actual extent of recycling. Experiments on livers from fasted rats, perfused with various labeled substrates (pyruvate, alanine, propionate) yielded PK recycling values of 26-45% (Freidman et al. 1971; Petersen et al. 1994; Jones et al. 1997). Earlier studies done on isolated hepatocytes incubated with lactate have reported PK recycling of less than 10% (Rognstad and Katz 1977). In vivo studies using ^{13}C-lactate or ^{13}C-propianate have reported higher PK recycling rates, 45-53% (Katz et al. 1993; Jones et al. 1997; Magnusson et al. 1991). More recently Jin et al. (2004) used a combination of ^{13}C-propianate and 3,4-^{12}C-glucose to determine an *in vivo* PK recycling of 70%; however this high PK recycling value could be attributed to the amount of glucose infused, which could reflect a change in nutritional state of the animal.

The addition of fatty acids to the perfusion medium stimulates gluconeogenesis from lactate, perfectly matching the experimental data (Fig. 3.3). Moreover, fatty acids also increase the activity of PC and inhibit the activity of PDC, presumably via generation of AcCoA and NADH. The inclusion of the regulatory terms for AcCoA in the kinetic expressions for these two enzymes is essential for achieving the correct rate of lactate uptake and gluconeogenesis.

In the pyruvate perfusions, the simulated glucose/pyruvate ratios (Fig. 3.5) are very similar to the average of 45% reported from various researchers (Williamson et al. 1969a,b; Menahan et al. 1969; Teufel et al. 1967; Ross et al. 1967a,b; Exton and Park 1967; Williamson et al. 1970), although the calculated pyruvate uptakes and glucose productions are generally about 50% lower than that observed experimentally. The rate of pyruvate uptake is determined by several factors, among them, the rate of endogenous

fatty acid oxidation. In the model, this rate ($R_{FA\text{-}endo}$) was set to the same values used for lactate perfusions, in the absence of information specific to the pyruvate perfusions. A simulated increase in $R_{FA\text{-}endo}$ does cause an increase in pyruvate uptake as well as glucose production (not shown), although not to the extent observed experimentally. The simulations yield 6% conversion of pyruvate to lactate; this value compares well with the 8% reported by Williamson, et al. (1969a).

Pyruvate oxidation through PDC plays a major role during the perfusion of pyruvate as the only substrate, since it provides the necessary NADH and ATP (along with endogenous fatty acid oxidation) required for conversion of pyruvate to glucose. Our simulation shows that 40% of pyruvate uptake is channeled through PDC in the absence of exogenous FA (not shown), which is in good agreement with an average of 30% reported previously (Menahan and Wieland 1969; Teufel et al. 1967; Ross et al. 1967a,b; Exton and Park 1967). The addition of fatty acids to the perfusion medium containing 2 mM pyruvate results in an inhibition of pyruvate oxidation to a value of 5% of pyruvate uptake, in agreement with the 9% measured experimentally (Menahan and Wieland 1969). This finding demonstrates again the importance of AcCoA, induced by the exogenous fatty acid addition, on the control of PDC and the subsequent control of hepatic gluconeogenesis.

As we noted during lactate perfusion, pyruvate alone does not inhibit ketogenesis in our model results, in contrast to most experimental results (Williamson et al. 1969b; Menahan and Wieland 1969; Teufel et al. 1967), while the addition of fatty acids stimulates ketogenesis both experimentally and in the simulation (Fig. 3.5b). The excessive rate of ketogenesis in the absence of exogenous fatty acids most likely results

from the representation of the formation of acetoacetate from AcCoA by means of Michaelis-Menten kinetics; this neglects the kinetic parameters of hydroxymethylglutaryl-CoA (HMG-CoA) synthase, the rate-limiting reaction in ketogenesis. Similarly, it may be necessary to include additional regulatory mechanisms and/or reactions in the representation of the TCA cycle. The rates of AcAc synthesis and TCA flux are closely linked via NADH, NAD+ and AcCoA, and inclusion of more physiologically-correct kinetic expressions are needed to correct this imbalance.

Our model also allows the prediction of dynamic as well as steady state responses of the liver to various substrates. As shown in Figure 3.7, the predicted transient responses to both lactate and pyruvate infusions are very similar to that observed experimentally by Bracht, et al. (1993), although in the former case, the model underestimated the steady state glucose production by about 45%. It is unclear why the results from Martins, et al. (2006) exhibit significantly slower dynamics than that of Bracht, et al. (1993). The calculated pyruvate response (Fig. 3.5b) is characterized by a rapid (1 min) response to pyruvate uptake and glucose and lactate production. However, after 5 min, the rate of lactate formation begins to decrease, accompanied by a slight reduction of the rate of pyruvate uptake and a gradual increase in glucose production over 30 min. Very similar dynamics have been observed in the experimental data of Williamson, et al. (1969a), also shown in Fig. 3.5b. This transient behavior results from the balance between a very fast transport rate (of both pyruvate and lactate), a fast LDH reaction, and relatively slower PC kinetics (not shown), which causes some of the initial pyruvate influx to drain out as lactate before the gluconeogenic rate has a chance to increase.

This work was limited to the effect of substrates in a fasted liver, and thus the kinetic parameters used are reflective of the hormonal concentrations present in the fasted state. While the effects of hormones are beyond the scope of this work, some of the effects of glucagon and insulin are included indirectly in the model via cAMP. cAMP concentration appears directly in the kinetic expressions for FBPase. Moreover, cAMP affects the concentration of F2,6BP, whose concentration is included in the expression for PFK and FBPase.

This model represents a promising tool to account for the relationship between gluconeogenesis and lipid metabolism and their role in various metabolic disorders. The model predicts with reasonable accuracy the effect of lipids on many of the metabolic fluxes in the liver tissue. The simulations clearly demonstrate that the liver function is an elegant balance among the numerous transport and reactions processes, with dependencies on both the mechanisms, represented by the structure of the kinetic equations, as well as the specific values of some key reaction parameters. Not surprisingly, the balance of NADH/NAD^+ is one of the key factors influencing the flux distribution. After modifying the kinetic expressions used for the TCA cycle and ketogenesis and the inclusion of a model for gluconeogenesis and urea formation from amino acids, such as alanine, this model should serve as an *in silico* representation of the healthy, fasted liver.

CHAPTER IV

CYTOSOLIC-MITOCHONDRIAL COMPARTMENTATION IN THE PERFUSED LIVER

4.1 Introduction

The redox ratio ($NADH/NAD^+$) is known to play a key role in the regulation of carbohydrate and lipid metabolism in the liver, in particular, the pathways of gluconeogenesis, tricarboxylic acid (TCA) cycle, ketogenesis, and oxidative phosphorylation. NADH stimulates gluconegensis mainly through the glyceraldehyde-3P dehydrogenase (GAPDH) reaction. The TCA cycle is influenced by the redox ratio primarily at two major sites: isocitrate dehydrogenase (Shepherd et al. 1969) and alpha-ketoglutarte dehydrogense (Smith et al. 1974), both being inhibited by NADH. Experiments with isolated hepatocytes have shown that an increase in the $NADH/NAD^+$ ratio caused by fatty acid oxidation is associated with a significant increase in the membrane potential, leading to increased oxidative phosphorylation (Nobes et al. 1990). The interactions between these major pathways are essential to consider in the investigation of energy metabolism regulation in the liver, and more specifically, to

quantify the role of the redox ratio in regulating these different pathways. Understanding of the interrelationship between these pathways and prediction of the fluxes, in response to environmental conditions, is thus predicated upon an accurate quantitative representation of the redox ratio and its influence on the reaction kinetics. The quantitative depiction of this system is complicated by three factors: the distribution of gluconeogenesis enzymes among both cytosolic and mitochondrial domains; the impermeability of the mitochondrial membrane to specific substrates (e.g. NADH, NAD^+, oxaloacetate (OAA)), which nonetheless exist in both compartments; and the significant difference in concentrations of some metabolites between the cytosol and mitochondria.

Lactate, pyruvate, and amino acids are the main precursors for hepatic gluconeogenesis, providing both the carbon skeleton as well as the necessary NADH for GAPDH in the cytosol. Lactate, as substrate, is converted to pyruvate, which is converted to OAA in the mitochondria via pyruvate carboxylase. Since the mitochondrial membrane is impermeable to OAA, the carbon skeleton of OAA is transferred to the cytosol as either aspartate or malate, where it is converted back to OAA for reaction by PEPCK. The transport of anions across the mitochondrial membrane is done by means of specific antiport or symport carriers (Chappell 1969; Klingenberg et al. 1970a,b; Meijer et al. 1974; Van Dan et al. 1971). The NADH requirement for GAPDH is provided by lactate dehydrogenase in the cytosol, therefore, no inter-compartmental transfer of reducing equivalents is necessary. Gluconeogenesis from lactate is said to be "NADH-neutral". In contrast with lactate, when pyruvate is the main precursor for gluconeogenesis, the NADH is generated inside the mitochondria and is transferred to the

mitochondria through malate which carries both the carbon skeleton and the reducing equivalents for gluconoegenesis. Gluconeogenesis from pyruvate is thus "NADH-demanding".

The concentrations of several metabolites common to the TCA cycle and the gluconeogenesis pathway differ significantly between the cytosolic and mitochondrial compartment. In particular, the cytoplasmic and mitochondrial redox ratios, which significantly affect the rates of NAD-linked dehydrogenase reactions, are more than an order-of-magnitude different from each other, with $NADH/NAD^+$ approximately equal to 0.001 in the cytosol and 0.05 in the mitochondria (Williamson et al. 1969a) after 24 h fasting. Other species with significant differences in cytosolic and mitochondrial concentrations include pyruvate, OAA, AcCoA, and MAL (Table 4.3).

The model described in Chapter III, which lumps the cytosolic and mitochondrial domains, approximately predicts the total rate of ketone production when perfused with lactate; however it overestimates the rate of ketogenesis with respect to pyruvate as a substrate. Inaccuracies in the ketone production rate, as well as the ratio of BHB/AcAc produced, are likely consequences of cytosolic values used for $NADH/NAD^+$, and to a lesser extent, OAA, in mitochondrial-located enzyme kinetics. It has been suggested that the availability of OAA for citrate synthase is the step determining the fate of acetylCoA-- to either proceed into the TCA cycle or into the ketogenesis pathway (Wieland et al. 1968). Thus the incorporation of a detailed and regulated TCA cycle was deemed necessary for a better representation of liver metabolism during gluconeogenesis from lactate and pyruvate, and during interaction between gluconeogenesis and fatty acid oxidation.

There are several published kinetic models of the TCA cycle, but few are specific to the liver. Garfinkel et al. (1970) presented a detailed model of the TCA cycle but the model lacked integration with other pathways such as gluconeogenesis, fatty acid oxidation, and intercompartmental transport. More recently, Beard et al. (2007) developed a comprehensive detailed model of the TCA cycle and metabolite transport across the mitochondrial membrane for heart and striated muscle. This model was further validated with additional data from *ex vivo* isolated mitochondria and *in vivo* data from skeletal muscle. The kinetic expressions and parameters are well-documented and the model accounts for enzyme regulation by different metabolites. The model is an excellent tool to represent the TCA cycle and metabolite transport across the mitochondrial membrane; however, as a representation of isolated mitochondria, it lacks the integration with glycolysis and gluconoegenesis. Moreover, their model is a representation of heart and muscle tissues, rather than liver tissue.

Several groups have developed relatively comprehensive models of intermediary metabolism in the liver. Orman et al. (2010, 2011, 2012, 2013) used flux balance analysis coupled with thermodynamic and futile cycle constraints and experimental data from perfused rat livers to analyze liver metabolism in response to burn injury and various oxygenation states. These models lack reaction kinetics, and therefore are limited in their ability to predict fluxes and species concentratins in novel situations.

Calvetti et al. (2008) modified our models presented in Chapters II and III with Bayesian Flux Balance Analysis (BFBA) to estimate the range of flux and transport rates at steady state, but as this is based on a single compartment, it is limited in its robustness. Konig et al. (2012) developed a kinetic model of glucose metabolism in human liver,

which includes representation of gluconeogenesis, glycolysis, and glycogen metabolism integrated with the hormonal control of these pathways. Even though this model considers cytosol-mitochondria compartmentation, it lacks the details of the TCA cycle and the shuttle mechanisms.

The aim of this work is, firstly, to accurately predict the cytoplasmic and mitochondrial redox ratios in a fasted rat liver model during perfusion with lactate, pyruvate, and fatty acids. The appropriate representation of the redox ratio can be expected to result in better estimation of key metabolic rates such as gluconoegenesis, TCA cycle, and ketogenesis. The second aim is to accurately represent the mechanisms for reducing equivalent and metabolite transfer across the mitochondrial membrane, with respect to different gluconoegenic precursors. These aims were met by building a comprehensive, detailed, and multidomain metabolic model of the perfused liver from the fasted rat. We modified the model described in Chapter III by incorporating distinct domains for cytosol and mitochondria, with metabolite transport across the mitochondrial membrane. The model was extended by featuring a detailed TCA cycle pathway, based on the work of Beard et al. (2007). The model was used to simulate the effects of lactate and pyruvate, with and without fatty acids, on the cytosolic and mitochondrial redox ratios and rates of gluconoegenesis, ketogenesis, TCA cycle, and oxidative phosphorylation, and on the rates and mechanisms of intercompartmental transport. These simulations were then validated by comparison to experimental data from different *ex vivo* studies in the literature.

4.2 Model Development

4.2.1 Metabolic Pathways

The model of gluconoegenesis in the perfused liver in Chapter III was modified by compartmentalizing the tissue into two separate cytosolic and mitochondrial domains. This was achieved by incorporating newly functional pathways and reaction fluxes that included a detailed tricarboxylic acid cycle, the malate-aspartate shuttle, and inter-compartmental transport for substrates exchange between the two domains. The complete set of pathways considered here is shown in Fig. 4.1. The kinetic expressions that have been added in the current model are shown in Table 4.1, while the remainder of the reactions are found in Table 3.1.

The mitochondrial compartment includes the following: eight reactions describing the detailed TCA cycle fluxes; two distinctive oxidative phosphorylation reactions; mitochondrial aspartate aminotransferase; glutamate dehydrogenase; and nucleoside diphosphokinase. The TCA cycle is regulated at three important sites: citrate synthase (CS), isocitrate dehydrogenase (IDH), and alpha-ketoglutarate dehydrogenase (AKGDH); therefore these reactions are modeled to appropriately account for activation and inhibition (e.g. by ATP, ADP, NADH). The kinetic expressions for the TCA cycle and some anionic transporters reactions were based on the work of Beard et al. (2007) with changes in some of the kinetic parameters to better fit and represent the nature of the liver tissue.

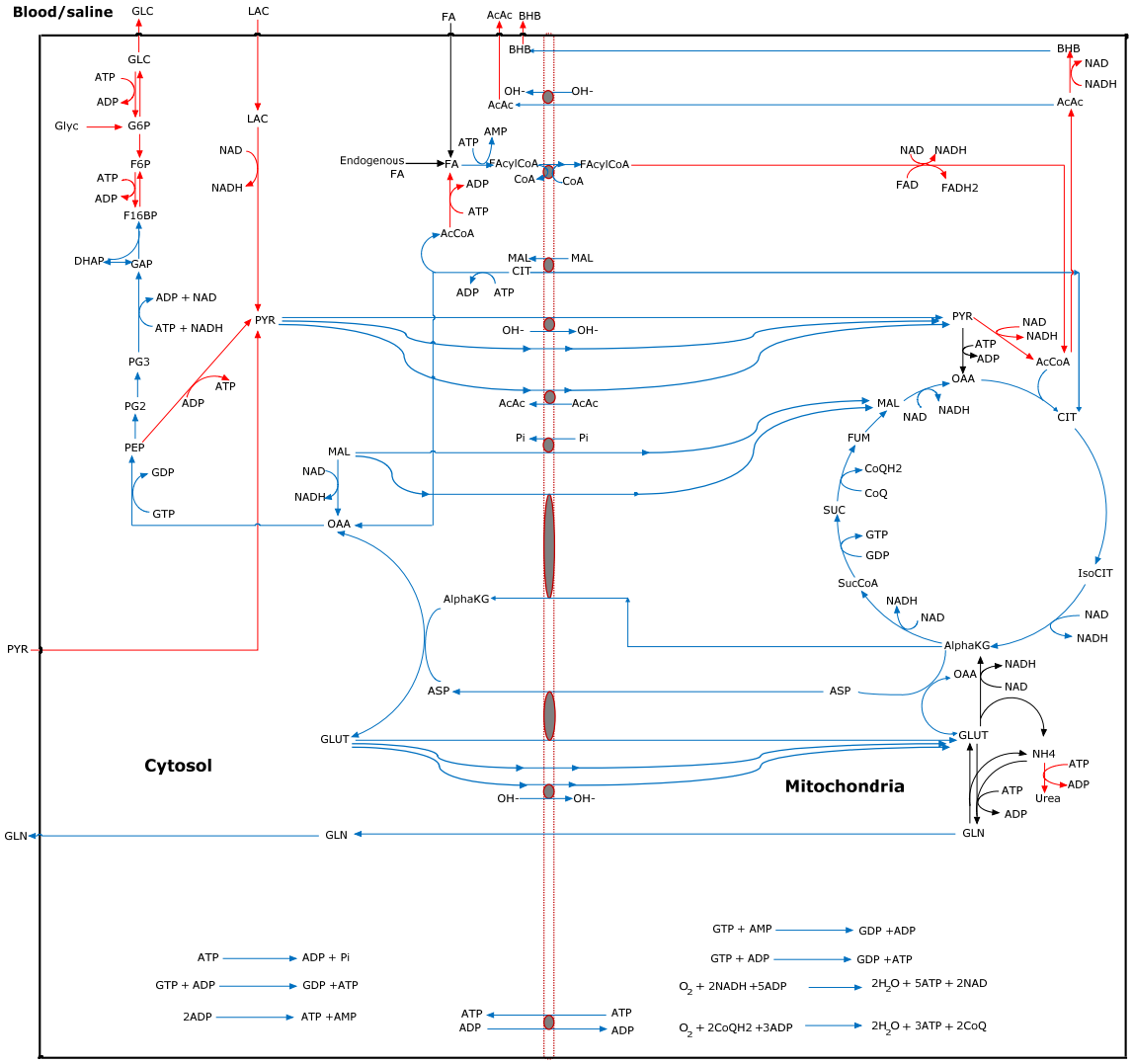

Figure 4.1. Reaction network considered in tissue model. Most transport and reaction fluxes are treated as reversible, but may be shown here as uni-directional to indicate the pred ominant direction. Tables 3.1 and 4.1 indicate whether a reaction is treated as reversible or irreversible. Detailed stoichiometry and the kinetic expression for each reaction shown here are given in Table 3.1 (for red reactions) and Table 4.1 (for blue reactions). Rates of endogenous FA degradation and FA uptake are given in Table 4.3. To simplify notation, NAD^+ is written as NAD. AcAc: acetoacetate; AcCOA: acetyl CoA; ASP: aspartate; BHB: β-hydroxybutyrate; CIT: citrate; DHAP: dihydroxyacetone phosphate; FA: fatty acid; FAcylCoA: fatty acyl CoA; F6P: fructose-6-phosphate; F16BP: fructose 1,6 bisphosphate; FUM: fumarate; GAP: glyceraldehyde-3-phosphate; GLUT: glutamate; GLN: glutamine; LAC: lactate; GLC: glucose; Glyc: glycogen; G6P: glucose-6-phosphate; IsoCIT: isocitrate; MAL: malate; PG3: 3-phosphoglycerate; PG2: 2-phosphoglycerate; PYR: pyruvate; OAA: oxaloacetate; AlphaKG: alpha-ketoglutarate; SucCoA: succinyl CoA; SUC: succinate..

The cytosolic compartment includes reaction kinetics for gluconoegenesis, glycolysis, and fatty acid synthesis (Table 3.1), plus added reaction for PEPCK, cytosolic nucleoside diphosphokinases (NDK), and cytosolic malate dehydrogenase (MDHc) (Table 4.1).

The exchange of substrates and cations across the mitochondrial membrane through specific transporters are modeled as facilitated diffusion processes. The following substrate transporters are included: the pyruvate-hydrogen co-transporter; the citrate-malate transporter; the malate-phosphate transporter; the glutamate-hydrogen co-transporter; the hydrogen-phosphate co-transporter; the ATP-ADP translocase; and the aspartate/glutamate and the malate/alpha-ketoglutarate exchangers that constitute the malate aspartate shuttle responsible for the transfer of NADH through the mitochondrial membrane.

The kinetic expressions for aspartate/glutamate and the malate/alpha-ketoglutarate exchangers are based on the work of Beard et al. (2007). The malate/alpha-ketoglutarate kinetic expression features the inhibition factors by the TCA cycle intermediates of glutamate, aspartate, and succinate.

The kinetic expressions of some reactions include modulation by coupled controllers. These controllers are the phosphorylation ratio ADP/ATP (PS) and redox ratio $NADH/NAD^+$ (RS). Since the mitochondrial membrane is impermeable to the NADH it was necessary to distinguish two different redox ratios, RSc and RSm, corresponding to the cytosolic and mitochondrial domains, respectively.

As described in Chapter III, reversible, near-equilibrium reactions (e.g. lactate dehydrogenase (LDH), MDH) are represented by a simplified form of a reversible, ping-

pong mechanism, with the Haldane equation used to relate kinetic parameter values at near-equilibrium and to ensure consistency with thermodynamic constraints. The rate mechanisms for transport between the blood and cytosol domains are described by facilitated diffusion.

The updated kinetic parameters for this model and the specific approach used for each reaction are listed in Table 4.2. The remaining kinetic parameters were kept the same as shown in Chapter III. In this chapter we explicitly accounted for the pH and the Pi (inorganic phosphate) concentrations in both cytosol and mitochondrial domains by assigning constant values consistent with data reported in the literature (Table 4.3).

The initial species concentrations in the cytosol, mitochondria, and blood were mostly taken from the literature and they were generally based on measurements from the livers of 24-hr fasted rats (Table 4.3). Subcellular distribution of metabolites between cytosol and mitochondria were determined from the literature when available.

Table 4.1 Reaction rates and kinetic expressions. Subscripts specify location of species or reaction; c: cytosol; m: mitochondria; b: blood; p: perfusate. Species that are located only in a single compartment (either cytosol or mitochondria) have no subscript. Species name abbreviations are given in the caption to Fig. 5.1. The "→" indicates that the reaction is treated as irreversible, while "↔" indicates that the reaction is treated as reversible, with the flux reported with positive values in the left-to-right direction.

Reaction rate name and stoichiometry	**Reaction rate kinetic expression**
Cytosolic-Mitochondrial Transport	
CIT:MAL Transport (m-c) CIT_c + MAL_m ↔ MAL_c + CIT_m	$V_{\max,c\_m\_cit}\left(\frac{C_{cit\_c}C_{mal\_m}-C_{cit\_m}C_{mal\_c}}{K_{m,c\_m\_cit}+C_{cit\_c}C_{mal\_m}+C_{cit\_m}C_{mal\_c}}\right)$
MAL:Pi Transport (c-m) MAL_c + pi_m ↔MAL_m + pi_c	$V_{\max,c\_m\_MAL}\left(\frac{C_{MAL\_c}C_{pi\_m}-C_{mal\_m}C_{pi\_c}}{K_{m,c\_m\_MAL}+C_{MAL\_c}C_{pi\_m}+C_{MAL\_m}C_{pi\_c}}\right)$
MAL-AlphaKG transport MAL_c + Alpha_KG_m ↔ MAL_m + Alpha_KG_c	$Ai_{MAL}=\frac{C_{MAL\_c}}{K_{i\_MAL\_c}}+\frac{C_{MAL\_m}}{K_{i\_MAL\_m}}, Ai_{AKG}=\frac{Alpha_{KG\_c}}{K_{i\_AKG\_c}}+\frac{Alpha_{KG\_m}}{K_{i\_AKG\_m}}$ $D=\left(\begin{array}{l}K_{i\_AKG\_c}K_{i\_MAL\_m}\left(2+Ai_{AKG}+Ai_{MAL}\right)+\\ \frac{Alpha_{KG\_c}C_{MAL\_m}}{K_{i\_AKG\_c}K_{i\_MAL\_m}}+\frac{Alpha_{KG\_m}C_{MAL\_c}}{K_{i\_AKG\_m}K_{i\_MAL\_c}}\end{array}\right)$ $N=X_{\_AKGMAL}\left(Alpha_{KG\_m}C_{MAL\_c}-Alpha_{KG\_c}C_{MAL\_m}\right)$ $rate=\frac{N}{D}$
GLUT:OH Transport (c-m) GLUT_c + OH_c ↔ GLUT_m + OH_m	$V_{\max,c\_m\_glut}\left(\frac{C_{glut\_c}C_{oh\_c}-C_{glut\_m}C_{oh\_m}}{K_{m,c\_m\_glut}+C_{glut\_c}C_{oh\_c}+C_{glut\_m}C_{oh\_m}}\right)$

Glut-ASP transport GLUT_c + ASP_m ↔ GLUT_m + ASP_c	$K = \left(K_{eq\_ASPGLUT} K_{i\_ASP\_c} K_{i\_GLUT\_m} K_{h\_ASPGLUT}\right)$ $N = X_{\_ASPGLUT}\left(C_{ASP\_m} C_{GLUT\_c} C_{OH\_c} - C_{ASP\_c} C_{GLUT\_m} C_{OH\_m} K_{eq\_ASPGLUT}\right)$ $D = \left(\begin{array}{l} K\left(2m + \left(\frac{C_{ASP\_c} C_{GLUT\_m} C_{OH\_m}}{K_{i\_ASP\_c} K_{i\_GLUT\_m} K_{h\_ASPGLUT}}\right)\right) + \\ \left(\frac{C_{ASP\_m} C_{GLUT\_c} C_{OH\_c}}{K_{i\_ASP\_m} K_{i\_GLUT\_c} K_{h\_ASPGLUT}}\right) + \\ m\left(\frac{C_{GLUT\_m} C_{OH\_m}}{K_{i\_GLUT\_m} K_{h\_ASPGLUT}}\right) + m\left(\frac{C_{GLUT\_c} C_{OH\_c}}{K_{i\_GLUT\_c} K_{h\_ASPGLUT}}\right) + \\ m\left(\frac{C_{ASP\_m} C_{OH\_c}}{K_{i\_ASP\_m} K_{h\_ASPGLUT}}\right) + m\left(\frac{C_{ASP\_c} C_{OH\_m}}{K_{i\_ASP\_c} K_{h\_ASPGLUT}}\right) + \\ m\left(\frac{C_{ASP\_m}}{K_{i\_ASP\_m}}\right) + m\left(\frac{C_{ASP\_c}}{K_{i\_ASP\_c}}\right) + \\ m\left(\frac{C_{OH\_c}}{K_{h\_ASPGLUT}}\right) + m\left(\frac{C_{OH\_m}}{K_{h\_ASPGLUT}}\right) \end{array} \right)$ $rate = \frac{N}{D}$
Glutamate transport (c-m) GLUT_c ↔ GLUT_m	$\left(\frac{V_{\max,c\_m\_GLUT}\left(C_{GLUT\_c} - C_{GLUT\_m}\right)}{\left(K_{m\_GLUT} + C_{GLUT\_c} + C_{GLUT\_m}\right)}\right)$
PYR:OH Transport (c-m) PYR_c + OH_c ↔ PYR_m + OH_m	$V_{\max c\_m\_pyr}\left(\frac{C_{pyr\_c} C_{oh\_c} - C_{pyr\_m} C_{oh\_m}}{K_{m,c\_m\_pyr} + C_{pyr\_c} C_{oh\_c} + C_{pyr\_m} C_{oh\_m}}\right)$

PYR transport (c-m) PYR_c ↔ PYR_m	$\left(\frac{V_{\max,c\_m\_PYR}\left(C_{PYR\_c}-C_{PYR\_m}\right)}{K_{m\_c\_m\_PYR}+C_{PYR\_c}+C_{PYR\_m}}\right)$
PYR:AcAc transport (c-m) PYR_c + AcAc_m ↔ PYR_m + AcAc_c	$\left(\frac{V_{\max,c\_m\_PYR}\left(C_{AcAc\_m}C_{PYR\_c}-C_{AcAc\_c}C_{PYR\_m}\right)}{K_{m\_c\_m\_PYR\_AcAc}+C_{AcAc\_m}C_{PYR\_c}+C_{AcAc\_c}C_{PYR\_m}}\right)$
AcAc:OH transport (m-c) AcAc_m + OH_m ↔ AcAc_c + OH_c	$\left(\frac{V_{\max,c\_m\_AcAc}\left(C_{AcAc\_m}C_{OH\_m}-C_{AcAc\_c}C_{OH\_c}\right)}{K_{m\_c\_m\_AcAc\_OH}+C_{AcAc\_c}C_{OH\_c}+C_{AcAc\_m}C_{OH\_m}}\right)$
BHB transport (m-c) BHB_m ↔ BHB_c	$\left(\frac{V_{\max,c\_m\_BHB}\left(C_{BHB\_m}-C_{BHB\_c}\right)}{K_{m\_c\_m\_BHB}+C_{BHB\_c}+C_{BHB\_m}}\right)$
FAcyl transport (c-m) FAcylCoA_c → CoA_c+ FA_m	$\left(\frac{V_{\max,FA\_a\_m}\left(C_{FAcylCoA\_c}\right)}{\left(K_{m\_FA\_a}+C_{FAcylCoA\_c}\right)}\right)$
Adenine translocase ADP_c + ATP_m ↔ ADP_m + ATP_c	$\left(\frac{V_{\max,ADP\_ATP}\left(C_{ADP\_c}C_{ATP\_m}-C_{ADP\_m}C_{ATP\_c}\right)}{K_{m,ADP\_ATP}+C_{ADP\_c}C_{ATP\_m}+C_{ADP\_m}C_{ATP\_c}}\right)$
GLN transport (m-c) GLN_m →GLN_c	$\frac{V_{\max\_c\_m\_GLN}\left(C_{GLN\_m}-C_{GLN\_c}\right)}{K_{m\_c\_m\_GLN}+C_{GLN\_m}+C_{GLN\_c}}$
Cytosolic-Blood Transport	
GLN transport (c-b) GLN_c →GLN_b	$\frac{V_{\max\_c\_b\_GLN}\left(C_{GLN\_c}-C_{GLN\_b}\right)}{K_{m\_c\_b\_GLN}+C_{GLN\_c}+C_{GLN\_b}}$

Cytosolic Reactions	
Aspartate aminotransferase (AST), cytosolic ASP_c+Alpha_KG_c $\leftrightarrow$ OAA_c +GLUT_c	$$V_{mrc,AsAT} = \left(\frac{V_{mfc,AsAT} K_{m,GLUT\_AsATc} K_{i,OAA\_m\_AsATc}}{K_{eq\_AsAT} K_{m,AKG\_AsATc} K_{i,ASP\_AsATc}} \right)$$ $$D = \left(\begin{array}{l} \left(V_{mrc,AsAT} K_{m,AKG\_AsATc} C_{ASP\_c} + V_{mrc,AsAT} K_{m,ASP\_AsATc} Alpha_{KG\_c} Alpha_{AsATc} \right) + \\ \left(\frac{V_{mfc,AsAT} K_{m,GLUT\_AsATc} C_{OAA\_c} \ Alpha_{AsATc}}{K_{eq\_AsAT}} \right) + \left(\frac{V_{mfc,AsAT} K_{m,OAA\_m\_AsATc} C_{GLUT\_c}}{K_{eq\_AsAT}} \right) + \\ \left(V_{mrc,AsAT} \ C_{ASP\_c} \ Alpha_{KG\_c} \right) + \left(\frac{V_{mfc,AsAT} K_{m,GLUT\_AsATc} C_{ASP\_c} C_{OAA\_c}}{K_{eq\_AsAT} K_{i,ASP\_AsAT}} \right) + \\ \left(\frac{V_{mfc,AsAT} C_{GLUT\_c} C_{OAA\_c}}{K_{eq\_AsAT}} \right) + \left(\frac{V_{mrc,AsAT} \ C_{GLUT\_c} Alpha_{KG\_c}}{K_{i,GLUT\_AsATc}} \right) \end{array} \right)$$ $$N = \left(V_{mfc,AsAT} V_{mrc,AsAT} \left(C_{ASP\_c} Alpha_{KG\_c} - \frac{C_{OAA\_c} C_{GLUT\_c}}{K_{eq\_AsAT}} \right) \right)$$ $$rate = \frac{N}{D}$$

Malate dehydrogenase (MDH), cytosolic MAL_c + NAD_c ↔OAA_c + NADH_c	$$V_{mr\_c,MDH} = \left(\frac{V_{mfc,MDH} K_{m,P} K_{i,q}}{K_{eq\_MDH\_c} K_{mb\_AsATc} K_{ia}} \right)$$ $$Alpha = \left(1 + \frac{C_{ATP\_c}}{K_{iATP\_MDH}} + \frac{C_{ADP\_c}}{K_{iADP\_MDH}} + \frac{C_{AMP\_c}}{K_{iAMP\_MDH}} \right)$$ $$D = \left(\begin{array}{l} \left(V_{mr\_c,MDH} K_{ia} K_{mb} Alpha + V_{mr\_c,MDH} K_{mb} \left(C_{NADH\_total\_c} - C_{NADH\_c} \right) + V_{mr\_c,MDH} \ K_{ma} C_{MAL\_c} Alpha \right) + \\ \left(\frac{V_{mf\_c,MDH} K_{mQ} C_{OAA\_c} \ Alpha}{K_{eq\_MDH\_c}} \right) + \left(\frac{V_{mf\_c\_MDH} K_{mP} C_{NADH\_c}}{K_{eq\_MDH\_c}} \right) + \\ \left(V_{mr\_c,MDH} \ \left(C_{NADH\_total\_c} - C_{NADH\_c} \right) C_{MAL\_c} \right) + \left(\frac{V_{mf\_c,MDH} K_{mQ}}{K_{eq\_MDH\_c} K_{ia}} \right) \left(C_{NADH\_total\_c} - C_{NADH\_c} \right) C_{OAA\_c} + \\ \left(\frac{V_{mr\_c\_MDH} K_{mA} C_{NADH\_c} C_{MAL\_c}}{K_{iQ}} \right) + \left(\frac{V_{mf\_c,MDH} \ C_{OAA\_c} C_{NADH\_c}}{K_{eq\_MDH\_c}} \right) + \\ \left(\frac{V_{mr\_c\_MDH} C_{NADH\_c} C_{OAA\_c} C_{MAL\_c}}{K_{iB} K_{eq\_MDH\_c}} \right) \end{array} \right)$$ $$N = \left(V_{mf\_c\_MDH} V_{mr\_c,MDH} \left(\left(C_{NADH\_total\_c} - C_{NADH\_c} \right) C_{MAL\_c} - \frac{C_{OAA\_c} C_{NADH\_c}}{K_{eq\_MDH\_c}} \right) \right)$$ $$rate = \frac{N}{D}$$
ATPase ATP_c → ADP_c + pi_c	$$\frac{V_{\max\_atp\_adp\_c} \, C_{ATP\_c} \Big/ C_{ADP\_c}}{C_{ATP\_c} \Big/ C_{ADP\_c} + K_{m\_atp\_adp\_c}}$$

Phosophoenylpyuvate carboxykinase (PEPCK) OAA_c + GTP_c → PEP + GDP_c	$\left(\frac{V_{\max,PEPCK} C_{OAA\_c}}{C_{OAA\_c} + K_{m\_PEPCK}}\right)\left(\frac{\frac{1}{C_{GDP\_c}/C_{GTP\_c}}}{\frac{1}{C_{GDP\_c}/C_{GTP\_c}} + \frac{1}{ps\_i\_ndk\_c}}\right)$
Enolase PEP ↔ PG2	$\left(\frac{V_{\max,Enolase}}{K_{\_Eno\_f}}\right)\left(\frac{C_{PEP} - \frac{C_{PG2}}{K_{eq\_Enolase}}}{1 + \frac{C_{PEP}}{K_{\_Eno\_f}} + \frac{C_{PG2}}{K_{\_Eno\_b}}}\right)$
Phosphogluomutase (PGM) PG2 ↔ PG3	$\left(\frac{V_{\max,PGM}}{K_{\_PGM\_f}}\right)\left(\frac{C_{PG2} - \frac{C_{PG3}}{K_{eq\_PGM}}}{1 + \frac{C_{PG2}}{K_{\_PGM\_f}} + \frac{C_{PG3}}{K_{\_PGM\_b}}}\right)$
Phosphoglycerate kinase/Glyceraldehyde-3-P dehydrogenase PG3 + ATP_c + NADH_c ↔ GAP + ADP_c + NAD_c + pi_c	$N = C_{PG3} C_{NADH\_c} C_{ATP\_c} - C_{GAP}(C_{NADH\_total\_c} - C_{NADH\_c}) C_{pi\_c} \frac{PS_c C_{ATP\_c}}{\mathrm{K}_{\mathrm{eq\_pep\_gap}}}$ $D = \mathrm{K}_{\mathrm{m\_pep\_gap}}(1 + C_{PG3} C_{NADH\_c} \frac{C_{ATP\_c}}{K_{m\_pep\_gap}}) +$ $C_{GAP} C_{pi\_c} C_{ATP\_c} PS\_c \frac{C_{NADH\_total\_c} - C_{NADH\_c}}{K_{m\_gap\_pep}}$ rate= $V_{\max\_pep\_gap} \frac{N}{D}$

Triose-phosphate isomerase (TPI) DHAP ↔ GAP	$\left(\frac{V_{\max,TPI}}{K_{\_TPI\_f}}\right)\left(\frac{C_{DHAP}-\frac{C_{GAP}}{K_{eq\_TPI}}}{1+\frac{C_{DHAP}}{K_{\_TPI\_f}}+\frac{C_{GAP}}{K_{\_TPI\_b}}}\right)$
Aldolase: GAP + DHAP → F16BP	$V_{\max\_gap\_f16bp}\frac{C_{GAP}C_{DHAP}}{K_{m\_gap\_f16bp}+C_{GAP}C_{DHAP}}$
Citrate lyase CIT_c + CoA_c + ATP_c → OAA_c + ADP_c + AcCoA_c + pi_c	$\left(\frac{V_{\max,CL}\ C_{CIT\_c}}{C_{CIT\_c}+K_{\_CL}}\right)\left(\frac{\frac{1}{C_{ADP\_c}/C_{ATP\_c}}}{\frac{1}{C_{ADP\_c}/C_{ATP\_c}}+\frac{1}{ps_{\_i\_cl}}}\right)$
FA activation FA_c + ATP_c +CoA→ FacylCoA_c + AMP_c + 2 pi_c	$\left(\frac{V_{\max,FA\_c\_m}\left(C_{FA\_c}C_{ATP\_c}\right)}{\left(K_{m\_FA\_c\_m}+C_{FA\_c}+C_{ATP\_c}\right)}\right)$
Nucleoside diphosphokinase (NDK), cytosolic GTP_c + ADP_c ↔ GDP_c + ATP_c	$\left(\frac{V_{\max,\_ndk\_C}\left(C_{GTP\_C}C_{ADP\_C}-C_{GDP\_C}C_{ATP\_C}\right)}{K_{m\_ndk\_C}\left(1+\frac{C_{GTP\_C}C_{ADP\_C}}{K_{m\_ndk\_C}}-\frac{C_{GDP\_C}C_{ATP\_C}}{K_{m\_ndk\_C\_r}}\right)}\right)$
Adenylate kinase, cytosolic 2 ADP_c ↔ ATP_c + AMP_c	$\left(\frac{V_{\max,\_\_AK\_c}\left(C_{ADP\_c}{}^{2}-\frac{C_{ATP\_c}C_{AMP\_c}}{K_{eq\_AK}}\right)}{K_{m\_AK\_c}\left(1+\frac{C_{ADP\_c}{}^{2}}{K_{m\_AK\_c}}-\frac{C_{ATP\_c}C_{AMP\_c}}{K_{m\_AK\_c\_r}}\right)}\right)$

Mitochondrial Reactions	
Oxidative phosphorylation of NADH O2 + 5 ADP_m + 2 NADH_m + 5 pi_m → 2 H2O + 5 ATP_m + 2 NAD_m	$\frac{V_{\max,\_oxd\_phosph}\,99.732\left(\frac{C_{ADP\_m}/C_{ATP\_m}}{C_{ADP\_m}/C_{ATP\_m}+ps\_i\_oxn}\right)\left(\frac{C_{NADH\_m}/\left(C_{NADH\_total\_m}-C_{NADH\_m}\right)}{C_{NAD\_m}/\left(C_{NADH\_total\_m}-C_{NADH\_m}\right)+rs\_i\_oxn}\right)}{\left(K_{m,\_oxd\_phosph}+99.732\right)}$
Oxidative phosphorylation of CoQH2 O2 + 3 ADP_m + 2 CoQH2 + 3 pi_m → H2O + 3 ATP_m + 2 CoQ	$\frac{V_{\max,\_oxd\_phosph}\,99.732\left(\frac{C_{ADP\_m}/C_{ATP\_m}}{C_{ADP\_m}/C_{ATP\_m}+ps\_i\_oxf}\right)\left(\frac{C_{CoQh2}/\left(C_{CoQ\_total}-C_{CoQh2}\right)}{C_{CoQh2}/\left(C_{CoQ\_total}-C_{CoQh2}\right)+rs\_i\_CoQ}\right)}{\left(K_{m,\_oxd\_phosph}+99.732\right)}$
Aspartate aminotransferase (AST), mitochondrial ASP_m + Alpha_KG_m ↔ OAA_m + GLUT_m	$V_{mr,AsAT}=\left(\frac{V_{mr,AsAT}K_{m,GLUT\_AsAT}K_{i,OAA\_m\_AsAT}}{K_{eq\_AsAT}K_{m,AKG\_AsAT}K_{i,ASP\_AsAT}}\right)$ $D=\left(\begin{array}{l}\left(V_{mr,AsAT}K_{m,AKG\_AsAT}C_{ASP\_m}+V_{mr,AsAT}K_{m,ASP\_AsAT}Alpha_{KG\_m}Alpha_{AsAT}\right)+\\ \left(\frac{V_{mf,AsAT}K_{m,GLUT\_AsAT}C_{OAA\_m}\ Alpha_{AsAT}}{K_{eq\_AsAT}}\right)+\left(\frac{V_{mf,AsAT}K_{m,OAA\_m\_AsAT}C_{GLUT\_m}}{K_{eq\_AsAT}}\right)+\\ \left(V_{mr,AsAT}\ C_{ASP\_m}\ Alpha_{KG\_m}\right)+\left(\frac{V_{mf,AsAT}K_{m,GLUT\_AsAT}C_{ASP\_m}C_{OAA\_m}\ Alpha_{AsAT}}{K_{eq\_AsAT}K_{i,ASP\_AsAT}}\right)+\\ \left(\frac{V_{mf,AsAT}C_{GLUT\_m}C_{OAA\_m}\ Alpha_{AsAT}}{K_{eq\_AsAT}}\right)+\left(\frac{V_{mr,AsAT}\ C_{GLUT\_m}Alpha_{KG\_m}}{K_{i,GLUT\_AsAT}}\right)\end{array}\right)$ $N=\left(V_{mf,AsAT}V_{mr,AsAT}K_{m,AKG\_AsAT}\left(C_{ASP\_m}Alpha_{KG\_m}-\frac{C_{OAA\_m}C_{GLUT\_m}}{K_{eq\_AsAT}}\right)\right)$ $rate=\frac{N}{D}$
FA_acylCoa formation FAcyl_m + CoA_m → FAcylCoA_m	$\left(\frac{V_{\max,FA\_CoA}\left(C_{FAcyl\_m}C_{CoA\_m}\right)}{\left(K_{m\_FA\_CoA}+C_{FAcyl\_m}+C_{CoA\_m}\right)}\right)$

FA β-oxidation FAacylCoA_m + 7 NAD_m + 7 CoQ + 7 CoA_m → 8 AcCoA_m + 7 NADH_m + 7 CoQh2 reaction:	$$\frac{V_{\max\_bo} C_{FAcylCoA\_m}}{K_{m\_bo} + C_{FA\_acylCoA}} \left(\frac{1/RS_m}{1/RS_{i,} + 1/RS_m} \right) \left(\frac{1/PS}{1/PS_{i,} + 1/PS} \right)$$
Citrate synthase (CS) AcCoA_m + OAA_m ↔ CIT_m+CoA_m	$$AlphaI1 = \left(1 + \frac{C_{CIT\_m}}{K_{i\_CIT\_CitSase}} \right)$$ $$AlphaI2 = \left(\begin{array}{l} 1 + \frac{C_{ATP\_m}}{K_{i\_ATP\_CitSase}} + \frac{C_{ADP\_m}}{K_{i\_ADP\_CitSase}} + \frac{C_{AMP\_m}}{K_{i\_AMP\_CitSase}} + \\ \frac{C_{CoA\_m}}{K_{i\_CoA\_CitSase}} + \frac{C_{SucCoA}}{K_{i\_SucCoA\_CitSase}} \end{array} \right)$$ $$rate = \left(\begin{array}{l} \frac{V_{\max,CitSase} \left(C_{OAA\_m} C_{AcCoA\_m} \right)}{\left(K_{ia\_CitSase} K_{m\_AcCoA\_CitSase} AlphaI1 \right) + \left(C_{AcCoA\_m} K_{m\_OAA\_CitSase} AlphaI1 \right) + \left(C_{OAA\_m} K_{m\_AcCoA\_CitSase} AlphaI2 \right) + \left(C_{AcCoA\_m} C_{OAA\_m} \right)} \\ \left(1 - \frac{C_{CoA\_m} C_{CIT\_m}}{C_{AcCoA\_m} C_{OAA\_m} K_{eq\_CitSase}} \right) \end{array} \right)$$
Aconitase CIT_m ↔ IsoCIT	$$\left(\frac{V_{\max,aconitase} \left(C_{CIT\_m} - \frac{C_{IsoCIT}}{K_{eq\_aconitasee}} \right)}{\left(K_{CIT} \left(1 + \frac{C_{CIT\_m}}{K_{CIT}} \right) + \frac{C_{IsoCIT}}{K_{IsoCIT}} \right)} \right)$$

Isocitrate dehydrogenase (IDH) Iso_cit + NAD_m ↔Alpha_KG_m + NADH_m + CO2	$$Alpha\_ICDH = \frac{\left(1+\frac{C_{ADP\_m}}{K_{a\_ADPm\_ICDH}}\right)}{\left(1+\frac{C_{ADP\_m}}{a_{\_ICDH}K_{a\_ADPm\_ICDH}}\right)}$$ $$D = \left(\begin{array}{l}\left(1+\frac{K_{m\_nad\_ICDH}}{\left(C_{NADH\_total\_m}-C_{NADH\_m}\right)}\right)\left(1+\frac{C_{NADH\_m}}{K_{i\_nadh\_ICDH}}\right)+ \\ \left(\frac{K_{m\_ICIT\_ICDH}}{C_{ISO\_CIT}}\right)^{n\_ICDH} Alpha\_ICDH + \\ \left(\frac{K_{m\_ICIT\_ICDH}}{C_{ISO\_CIT}}\right)^{n\_ICDH} \frac{K_{i\_nad\_ICDH}}{\left(C_{NADH\_total\_m}-C_{NADH\_m}\right)} \\ \left(1+\left(1+\frac{C_{NADH\_m}}{K_{i\_nadh\_ICDH}}\right)Alpha\_ICDH\right)\end{array}\right)$$ $$N = V_{mf\_ICDH}\left(1-\frac{1}{K_{eq\_ICDH}}\left(\frac{C_{Alpha\_KG\_m}C_{NADH\_m}}{C_{ISO\_CIT}\left(C_{NADH\_total\_m}-C_{NADH\_m}\right)}\right)\right)$$ $$rate = \frac{N}{D}$$

alpha-ketoglutarate dehydrogenase (AKGDH) Alpha_KG_m + NAD_m + CoA_m ↔ SucCoA + NADH_m + CO2	$$Alpha_{AKGDH} = \frac{\left(1+\frac{K_{a\_ADPm\_AKGDH}}{C_{ADP\_m}}\right)}{\left(1+\frac{C_{ATP\_m}}{K_{i\_ATP\_AKGDH}}\right)}$$ $$D = \left(\begin{array}{l} 1+\frac{K_{m\_AKG\_AKDH}}{\left(ALPHA_{KG\_m}\right)}ALPHA_{AKGDH} + \\ \left(\frac{K_{m\_CoA\_AKGDH}}{C_{CoA\_m}}\right)\left(1+\frac{C_{SucCoA\_m}}{K_{i\_SucCoA\_AKGDH}}\right) + \\ \frac{K_{m\_nad\_AKGDH}}{\left(C_{NADH\_total\_m}-C_{NADH\_m}\right)}\left(1+\frac{C_{NADH\_m}}{K_{i\_nadh\_AKGDH}}\right) \end{array}\right)$$ $$N = V_{mf\_AKGDH}\left(1-\frac{1}{K_{eq\_AKGDH}}\left(\frac{C_{SucCoA\_m}C_{NADH\_m}}{C_{CoA\_m}ALPHA_{KG\_m}\left(C_{NADH\_total\_m}-C_{NADH\_m}\right)}\right)\right)$$ $$rate = \frac{N}{D}$$
Succinate dehydrogenase (SDH) SUC + CoQ ↔ FUM + CoQH2	$$V_{\max\_SDH}\left(\left(\frac{C_{Suc}\left(C_{CoQ\_total}-C_{CoQh2}\right)-C_{FUM}\left(\frac{C_{CoQh2}}{K_{eq\_SDH}}\right)}{\left(K_{m\_SDH}\left(1+\frac{C_{Suc}\left(C_{CoQ\_total}-C_{CoQh2}\right)}{K_{m\_SDH}}+C_{FUM}\left(\frac{C_{CoQh2}}{K_{m\_SDH\_r}}\right)\right)\right)}\right)$$

Fumarase FUM ↔ MAL_m	$V_{\max\_Fumarase}\left(\left(\frac{C_{FUM}-\left(\frac{C_{MAL}}{K_{eq\_Fumarase}}\right)}{\left(K_{FUM}\left(1+\frac{C_{FUM}}{K_{FUM}}+\left(\frac{C_{MAL}}{K_{MAL}}\right)\right)\right)}\right)\right)$
Succinyl-CoA synthetase SucCoA + GDP_m + pi_m ↔ SUC + GTP_m + CoA_m	$\left(\left(\frac{V_{\max\_SCoA\_synt}\frac{C_{SucCoA}C_{GDP\_m}C_{pi\_m}-\left(\frac{C_{Suc}C_{GTP\_m}C_{CoA\_m}}{K_{eq\_SCoA\_synt}}\right)}{K_{m\_SCoA\_synt}}}{\left(\left(V_{mr}K_{mA}AlphaC_{MAL\_m}+\frac{V_{mf}K_{mQ}AlphaC_{OAA\_m}}{K_{eq\_MDH\_m}}+\frac{V_{mf}K_{mP}C_{NADH\_m}}{K_{eq\_MDH\_m}}+V_{mr}C_{NADH\_m}\left(1+\frac{C_{SucCoA}C_{GDP\_m}C_{pi\_m}}{K_{m\_SCoA\_synt}}+\left(\frac{C_{Suc}C_{GTP\_m}C_{CoA\_m}}{K_{m\_SCoA\_synt\_r}}\right)\right)\right)\right)}\right)\right)$

Malate dehydrogenase (MDH), mitochondrial

MAL_m + NAD_m $\leftrightarrow$ OAA_m + NADH_m

$$V_{mr} = \frac{V_{mf} K_{mP} K_{iq}}{K_{mB} K_{ia} K_{eq\_MDH\_m}}$$

$$Alpha = 1 + \frac{\left(C_{ATP\_m}\right)}{K_{ia\_ATP\_MDH}} + \frac{\left(C_{ADP\_m}\right)}{K_{ia\_ADP\_MDH}} + \frac{\left(C_{AMP\_m}\right)}{K_{ia\_AMP\_MDH}}$$

$$D = \left(\begin{array}{l} V_{mr} K_{ia} K_{mB} ALPHA + V_{mr} K_{mB} \left(C_{NADH\_total\_m} - C_{NADH\_m}\right) C_{MAL\_m} + \\ \frac{V_{mf} K_{mQ} \left(C_{NADH\_total\_m} - C_{NADH\_m}\right) C_{OAA\_m}}{K_{ia} K_{eq\_MDH\_m}} + \\ \frac{V_{mr} K_{mA} \left(C_{NADH\_m}\right) C_{MAL\_m}}{K_{iq}} + \frac{V_{mf} \left(C_{NADH\_m}\right) C_{OAA\_m}}{K_{eq\_MDH\_m}} + \\ \frac{V_{mr} \left(C_{NADH\_total\_m} - C_{NADH\_m}\right) C_{OAA\_m} C_{MAL\_m}}{K_{ip}} + \\ \frac{V_{mf} \left(C_{NADH\_m}\right) C_{OAA\_m} C_{MAL\_m}}{K_{ib} K_{eq\_MDH\_m}} \end{array} \right)$$

$$N = V_{mf} V_{mr} \left(C_{NADH\_total\_m} - C_{NADH\_m}\right)\left(C_{MAL\_m}\right) - \frac{\left(C_{OAA\_m} - C_{NADH\_m}\right)}{K_{eq\_MDH\_m}}$$

$$rate = \frac{N}{D}$$

Glutamate dehydrogenase GLUT_m + NAD_m ↔ Alpha_KG_m + NADH_m + NH4	$\left(\frac{V_{\max,GDH} \left(C_{GLUT\_m} \left(C_{NADH\_total\_m} - C_{NADH\_m} \right) - \frac{Alpha\_KG\_m \, C_{NADH\_m}}{K_{eq\_GDH}} \right)}{K_{m\_GDH} \left(\frac{C_{GLUT\_m} \left(C_{NADH\_total\_m} - C_{NADH\_m} \right)}{K_{m\_GDH}} \right) + \frac{Alpha\_KG\_m \, C_{NADH\_m}}{K_{m\_GDH\_r}}} \right)$
Glutamine synthetase GLUT_m + NH4 + ATP_m →GLN_m + ADP_m + Pi_m	$\left(\frac{V_{\max\_GLS} \; C_{GLUT\_m} C_{NH4} C_{ATP\_m}}{K_{m\_GLS} + C_{GLUT\_m} C_{NH4} C_{ATP\_m}} \right)$
Glutaminase GLN_m → GLUT_m + NH4	$\left(\frac{V_{\max\_GLas} \; C_{GLN\_m}}{K_{m\_GLas} + C_{GLN\_m}} \right)$
Urea synthesis 2ATP_m + NH4 → urea + 2ADP_m + pi_m	$\left(\frac{V_{\max\_urea} C_{NH4}}{K_{m\_urea} + C_{NH4}} \right) \left(\frac{\frac{1}{C_{ADP\_m} / C_{ATP\_m}}}{\frac{1}{C_{ADP\_m} / C_{ATP\_m}} + \frac{1}{ps\_i\_urea}} \right)$
Nucleoside diphosphokinase (NDK), mitochondrial GTP_m + ADP_m ↔GDP_m + ATP_m	$\left(\frac{V_{\max,\_ndk\_m} \left(C_{GTP\_m} C_{ADP\_m} - C_{GDP\_m} C_{ATP\_m} \right)}{K_{m\_ndk\_m} \left(1 + \frac{C_{GTP\_m} C_{ADP\_m}}{K_{m\_ndk\_m}} - \frac{C_{GDP\_m} C_{ATP\_m}}{K_{m\_ndk\_m\_r}} \right)} \right)$
GTP:AMP Phosphotransferase GTP_m + AMP_m ↔ GDP_m + ADP_m	$\left(\frac{V_{\max,\_\_GTP\_AMP} \left(C_{GTP\_m} C_{AMP\_m} - \frac{C_{GDP\_m} C_{ADP\_m}}{K_{eq\_GTP\_AMP}} \right)}{K_{m\_GTP\_AMP} \left(1 + \frac{C_{GTP\_m} C_{AMP\_m}}{K_{m\_GTP\_AMP}} - \frac{C_{GDP\_m} C_{ADP\_m}}{K_{m\_GTP\_AMP\_r}} \right)} \right)$

Table 4.2 Kinetic parameters. Ratio of cytosol to mitochondrial volume is set to 9.52(Reich and Selkov, 1981)

Kinetic parameter	Parameter value	Source
Vmax_pdh	25.51 mM/min	Chalhoub et al. 2007
Alpha	0.9	
Beta	25	
Kp	0.35 mM/min	
Gama	0.5 mM/min	
Vmax_pc	168.67 mM/min	Chalhoub et al. 2007
Ki_adp_pyr_pc	3 mM/min	
K_atp_pc	0.06 mM	
n1_pc	1.03	
n2_pc	0.8	
n3_pc	2.75	
K_pyr_pc	11 mM	
K_accoa_pc	5.10E-05 mM	
Ki_adp_atp_pc	0.9 mM	
Vmax_ldh_b	348.21 mM/min	Reich and Selkov, 1981
Keq_ldh	0.00011	Reich and Selkov, 1981
Km_ldh_b	1.0857 mM	Set equal to steady state product of LAC and NAD^+ concentrations
Km_ldh_f	3.39E-06 mM	Calculated from in vivo LDH flux (Christian and Christian, 1983) and steady state product of LAC, NAD^+ (c), NADH (c) and PYR concentrations
Vmax_pk	89.28 mM/min	Chalhoub et al. 2007
K_pep_pk	0.055 mM	
K_atp1_pk	0.0075 mM	
n_pk	3.1	
L_pk	16000	
c_atp	2	
K_ala_pk	0.2 mM	
c_ala_pk	0.2	
K_f16bp_pk	0.0001 mM	
Vmax_fbpase	20 mM/min	Chalhoub et al. 2007
K_f16bp	0.000827586 mM	
n_fbpase	5.524	
K_f26bp	0.0269 mM	
K_amp	1.82759 mM	
K_cAMP	0.0159138 mM	
L_fbpase	2.76E+06	
c_fbpase	0.5597	
Vmax_PFK	5.3571 mM/min	Chalhoub et al. 2007
Kapp_f6p_pfk	0.0007 mM	
K_atp_pfk	0.05 mM	
Alpha_pfk	2	
q1_pfk	100	
n1_pfk	3	

Kiatp_pfk	1 mM	
Sigma_pfk	3.5	
n2_pfk	3	
Ki_f26bp_pfk	0.03 mM	
Kiamp_pfk	2 mM	
q2_pfk	50	
Vmax_pep_gap	167.857 mM/min	Reich and Selkov, 1981
Keq_pep_gap	16666.7	Reich and Selkov, 1981
Km_pep_gap	0.00061 mM	Set equal to product of steady state PG3 and NADH(c), and ATP(c) concentrations
Km_gap_pep	0.00487 mM	Calculated from R_{pep_gap} and steady state product of PG3, NAD^+ (c), NADH (c) and GAP concentrations
Vmax_g6p_f6p	46.873 mM/min	Calculated from R_{GI} flux from FBA flux analysis and steady state F6P and G6P
Keq_g6p_f6p	2.5	Reich and Selkov, 1981
K_f6p	0.0665714 mM	Set equal to steady state F6P concentration
K_g6p	0.145714 mM	Set equal to steady state G6P concentration
Vmax_g6p	5.2132 mM/min	Calculated from R_{GI} flux from FBA flux analysis and steady state G6P, Reich and Selkov, 1981
Km_g6pase	0.145714 mM	Set equal to steady state G6P concentration
Vmax_gk	3.1279 mM/min	Calculated from R_{GI} flux from FBA flux analysis and steady state GLC and Shonk and Boxer, 1964
Km_gk	8.9286 mM	Set equal to steady state GLC concentration
ps_i_gk	0.3012	Set equal to steady state C_{ADP_c}/C_{ATP_c} Seis 1982
Vmax_gap_f16bp	42.8571 mM/min	Reich and Selkov, 1981
Km_gap_f16bp	0.0007 mM	Set equal to steady state product of GAP and DHAP concentrations
Vmax_gr3p_gap	205.357 mM/min	Shonk and Boxer, 1964
Keq_gr3p_gap	0.00013	Reich and Selkov, 1981
Km_gr3p_gap	0.3571 mM	Set equal to product of steady state of GR3P and NAD^+ concentrations
Km_gap_gr3p	1.12E-07 mM	Calculated from R_{Gr3p_gap} and steady state product of GR3P, NAD^+ (c), NADH (c) and DHAP concentrations
Vmax_glr_gr3p	1.1279 mM/min	Calculated from in vivo flux (Christian and Christian, 1983) and steady state product of GLR, and ps_i_glr_gr3p concentrations
Km_glr_gr3p	0.1786 mM	Set equal to steady state GLR concentration
ps_i_glr_gr3p	0.3012	Set equal to steady state C_{ADP_c}/C_{ATP_c} Seis 1982
Vmax_enolase	30.3571 mM/min	Reich and Selkov, 1981
Keq_enolase	0.25	Reich and Selkov, 1981
K_eno_f	0.0708929 mM	Set equal to steady state PEP concentration
K_eno_b	0.2679 mM	Set equal to steady state PG2 concentration
Vmax_PGM	178.571 mM/min	Shonk and Boxer, 1964; Hannon and Vaughan, 1960
Keq_PGM	6.66667 mM	Reich and Selkov, 1981
K_PGM_f	0.2679 mM	Set equal to steady state PG2 concentration

K_PGM_b	0.1357 mM	Set equal to steady state PG3 concentration
Vmax_TPI	8.92857 mM/min	Reich and Selkov, 1981
Keq_TPI	0.04545	Reich and Selkov, 1981
K_TPI_f	0.0232 mM	Set equal to steady state DHAP concentration
K_TPI_b	0.0303571 mM	Set equal to steady state GAP concentration
Vmax_PEPCK	17.6857 mM/min	Reich and Selkov, 1981; Shonk and Boxer, 1964
Km_PEPCK	0.0040179 mM	Set equal to steady state OAA (c) concentration
ps_i_ndk_c	0.278287	Set equal to steady state C_{GDP_c}/C_{GTP_c} Seis 1982
Km_accoa_AcAc	0.981 mM	Set equal to steady state AcAc (m) concentration
Vmax_accoa_AcAc	126.327 mM/min	Calculated from in vivo flux and steady state product of AcAc (m) AcCoA (m), and CoA(m) concentrations
Vmax_bhb	1020.41 mM/min	Reich and Selkov, 1981
Keq_bhb	20	Reich and Selkov, 1981
Km_bhb	0.2846 mM	Calculated from R_{BHB} and steady state product of AcAc(m), NAD^+ (m), NADH (m) and BHB(m) concentrations
Km_bhb_r	4.2857 mM	Set equal to product of steady state of AcAc(m) and NADH(m) concentrations
Vmax_bo	91.9048 mM/min	Calculated from in vivo flux and steady state of FA_acylCoA (m), rs_i_b0, and ps_i_b0 concentrations
rs_i_b0	0.25	Set close to steady state C_{NADH_m}/C_{NAD_m} (Reich and Selkov, 1981)
ps_i_b0	0.7514	Set equal to steady state C_{ADP_m}/C_{ATP_m} Seis 1982
Vmax_fat_syn	3.8603 mM/min	Reich and Selkov, 1981
ps_i_fat_syn	0.3012	Set equal to steady state C_{ADP_c}/C_{ATP_c} Seis 1982
Km_fat_syn	0.0809 mM	Set equal to steady state AcCoA(c)
Vmax_urea	34.0136 mM/min	Reich and Selkov, 1981
Km_urea	9.52 mM	Set equal to steady state NH4 (m) concentration
ps_i_urea	0.7514	Set equal to steady state C_{ADP_m}/C_{ATP_m} Seis 1982
ps_i_ndk_c	0.278287	Set equal to steady state C_{GDP_c}/C_{GTP_c} Seis 1982
Vmax_CL	22.3214 mM/min	Reich and Selkov, 1981
Km_CL	2.52812 mM	Calculated from in vivo flux, in vitro Vmax_CL and steady state of CIT(c), CoA(c), and ps_i_CL concentrations
ps_i_CL	0.3012	Set equal to steady state C_{ADP_c}/C_{ATP_c} Seis 1982
Vmax_ADP_ATP	154.286 mM/min	Hanson and Mehlman, 1981
Km_ADP_ATP	0.00126 mM	Hanson and Mehlman, 1981, Seis 1982
Vmax_oxd_phosph	514.22 mM/min	Calculated from R_{oxPhos} flux from FBA and steady state O_2 concentration
Km_oxd_phosph	99.7732 mM	Set equal to steady state O_2 concentration
ps_i_oxn	0.7514	Set equal to steady state C_{ADP_m}/C_{ATP_m} Seis 1982
rs_i_oxn	0.2	Set close to steady state C_{NADH_m}/C_{NAD_m} (Reich

		and Selkov, 1981)
Vmax_oxd_phosph_f	514.612 mM/min	Calculated from R_{oxPhos} flux from FBA and steady state O_2 concentration
Km_oxd_phosph_f	99.7732 mM	Set equal to steady state O_2 concentration
ps_i_oxf	0.7514	Set equal to steady state C_{ADP_m}/C_{ATP_m} (Seis 1982)
rs_i_CoQ	0.391753	Set equal to steady state C_{CoQH2_m}/C_{CoQ_m} (Seis 1982)
Vmax_CitSase	190 mM	Reich and Selkov, 1981
Keq_CitSase	1.10E+06	Reich and Selkov, 1981
KmOAA_CitSase	0.002 mM	Sheperd and Garland, 1969
KmAcCoA_CitSase	0.016 mM	Sheperd and Garland, 1969
KiCIT_CitSase	16 mM	Smith and Williamson, 1971
KiCoA_CitSase	0.675 mM	Smith and Williamson, 1971
KiATP_CitSase	0.55 mM	Sheperd and Garland, 1969
KiADP_CitSase	1.4 mM	Sheperd and Garland, 1969
KiAMP_CitSase	6.7 mM	Sheperd and Garland, 1969
KiSucCoA_CitSase	0.14 mM	Smith and Williamson, 1971
Kia_CitSase	0.00333 mM	Kohn et al. 1981
Vmax_aconitase	255.102 mM/min	Reich and Selkov, 1981
Keq_aconitase	0.05555	Reich and Selkov, 1981
K_CIT	1.43224 mM/min	Calculated from in vivo TCA flux (Jin et al. 2004), in vitro Vmax_aconitase and steady state of CIT(m), and Iso_cit concentrations
K_Iso_cit	0.15306 mM/min	Set equal to steady state Iso_cit concentration
Vmf_icdh	51.02 mM/min	Reich and Selkov, 1981
Ki_nad_icdh	0.0776 mM	Kohn et al. 1979; Kohn and Garfinkel, 1983
Ki_nadh_icdh	0.475 mM	---
Km_nad_icdh	0.5 mM	---
Km_icit_icdh	0.1489 mM	---
n_icdh	3	Kohn et al. 1979; Kohn and Garfinkel, 1983
a_icdh	0.0004	---
Ka_ADPm_icdh	61.3 mM	Plaut et al. 1979
Keq_ICDH	1200	Reich and Selkov, 1981
Vmf_akgdh	204.082 mM/min	Reich and Selkov, 1981
Ki_succoa_akgdh	0.0069 mM	Kohn et al. 1979; Kohn and Garfinkel, 1983
Ki_nadh_akgdh	0.0006 mM	Wu et al. 2007
Km_akg_akgdh	0.08 mM	Kohn et al. 1979; Kohn and Garfinkel, 1983
Km_coa_akgdh	0.055 mM	Kohn et al. 1979; Kohn and Garfinkel, 1983
Km_nad_akgdh	0.021 mM	Kohn et al. 1979; Kohn and Garfinkel, 1983
Ka_ADPm_akgdh	0.1 mM	Kohn et al. 1979; Kohn and Garfinkel, 1983
Ki_atp_akgdh	0.05 mM	Kohn et al. 1979; Kohn and Garfinkel, 1983
Keq_AKGDH	60000	Reich and Selkov, 1981
Vmax_SCoAsynt	255.102 mM/min	Reich and Selkov, 1981
Km_SCoAsynt	61.4484 mM	Set equal to +50% of product steady state of GDP(m), SucCoA(m) and Pi(m) concentrations
Km_SCoAsynt_r	1.21102 mM	Calculated from in vivo flux of TCA (Jin et al. 2004), and steady state GDP(m), TP(m), SucCoA(m) CoA(m) and Pi(m) concentrations
Keq_SCoAsynt	3.7037	Reich and Selkov, 1981

Vmax_SDH	510.204 mM/min	Reich and Selkov, 1981
Km_SDH	12.2075 mM	Kohn et al. 1981
Km_SDH_r	0.0199182 mM/min	Kohn et al. 1981
Keq_SDH	1.1	Reich and Selkov, 1981
Vmax_Fumase	3061.22 mM/min	Reich and Selkov, 1981
K_FUM	1.27551 mM	Set equal to steady state FUM concentration
K_MAL	95.4716 mM	Calculated from in vivo TCA flux (Jin et al. 2004), in vitro Vmax_CL and steady state of MAL(m), FUM(m) concentrations
Keq_Fumase	12	Reich and Selkov, 1981
Vmf	4591 mM/min	Reich and Selkov, 1981; Shonk and Boxer, 1964
KmA	0.09055 mM	Kohn et al. 1979; Kohn and Garfinkel, 1983
KmB	0.25 mM	Kohn et al. 1979; Kohn and Garfinkel, 1983
KmP	0.00613 mM	Kohn et al. 1979; Kohn and Garfinkel, 1983
KmQ	0.00258 mM	Kohn et al. 1979; Kohn and Garfinkel, 1983
Kia	0.279 mM	Kohn et al. 1979; Kohn and Garfinkel, 1983
Kib	0.36 mM	Kohn et al. 1979; Kohn and Garfinkel, 1983
Kip	0.0055 mM	Kohn et al. 1979; Kohn and Garfinkel, 1983
Kiq	0.00318 mM	Kohn et al. 1979; Kohn and Garfinkel, 1983
KiATP_MDH	0.1832 mM	Kohn et al. 1979; Kohn and Garfinkel, 1983
KiADP_MDH	0.3944 mM	Kohn et al. 1979; Kohn and Garfinkel, 1983
KiAMP_MDH	0.42 mM	Kohn et al. 1979; Kohn and Garfinkel, 1983
Vmf_c	892 mM/min	Reich and Selkov, 1981; Shonk and Boxer, 1964
KmA	0.09055 mM	Kohn et al. 1979; Kohn and Garfinkel, 1983
KmB	0.25 mM	Kohn et al. 1979; Kohn and Garfinkel, 1983
KmP	0.00613 mM	Kohn et al. 1979; Kohn and Garfinkel, 1983
KmQ	0.00258 mM	Kohn et al. 1979; Kohn and Garfinkel, 1983
Kia	0.279 mM	Kohn et al. 1979; Kohn and Garfinkel, 1983
Kib	0.36 mM	Kohn et al. 1979; Kohn and Garfinkel, 1983
Kip	0.0055 mM	Kohn et al. 1979; Kohn and Garfinkel, 1983
Kiq	0.00318 mM	Kohn et al. 1979; Kohn and Garfinkel, 1983
KiATP_MDH	0.1832 mM	Kohn et al. 1979; Kohn and Garfinkel, 1983
KiADP_MDH	0.3944 mM	Kohn et al. 1979; Kohn and Garfinkel, 1983
KiAMP_MDH	0.42 mM	Kohn et al. 1979; Kohn and Garfinkel, 1983
Keq_MDH_c	2.80E-05	Reich and Selkov, 1981
Vmfc_AsAT	803.571 mM/min	Reich and Selkov, 1981
Km_ASP_AsATc	3.9 mM	Henson and Cleland, 1964
Km_AKG_AsATc	0.43 mM	Henson and Cleland, 1964
Km_OAAm_AsATc	0.0088 mM	Henson and Cleland, 1964
Km_GLUT_AsATc	8.9 mM	Henson and Cleland, 1964
Ki_ASP_AsATc	3.48 mM	Henson and Cleland, 1964
Ki_AKG_AsATc	0.71 mM	Henson and Cleland, 1964
Ki_OAAm_AsATc	0.05 mM	Henson and Cleland, 1964
Ki_GLUT_AsATc	8.4 mM	Henson and Cleland, 1964
KIn_AKG_AsATc	16.6 mM	Henson and Cleland, 1964
Vmf_AsAT	7653.06 mM/min	Reich and Selkov, 1981
Km_ASP_AsAT	3.9 mM	Henson and Cleland, 1964
Km_AKG_AsAT	0.43 mM	Henson and Cleland, 1964
Km_OAAm_AsAT	0.0088 mM	Henson and Cleland, 1964

Km_GLUT_AsAT	8.9 mM	Henson and Cleland, 1964
Ki_ASP_AsAT	3.48 mM	Henson and Cleland, 1964
Ki_AKG_AsAT	0.71 mM	Henson and Cleland, 1964
Ki_OAAm_AsAT	0.05 mM	Henson and Cleland, 1964
Ki_GLUT_AsAT	8.4 mM	Henson and Cleland, 1964
KIn_AKG_AsAT	16.6 mM	Henson and Cleland, 1964
Keq_AsAT	0.151515	Reich and Selkov, 1981
X_AKGMAL	21798 mM/min	Wu et al. 2007
KiAKG_c	0.03 mM	Indiveri et al. 1991
KiAKG_m	0.17 mM	Indiveri et al. 1991
KiMAL_c	1.4 mM	Indiveri et al. 1991
KiMAL_m	0.07 mM	Indiveri et al. 1991
KiASP_c	0.028 mM	Dierks et al. 1988
KiASP_m	2.8 mM	Dierks et al. 1988
KiGLUT_c	0.18 mM	Dierks et al. 1988
KiGLUT_m	1.6 mM	Dierks et al. 1988
Kh_ASPGLUT	3.16E-07 mM	Dierks et al. 1988
Keq_ASPGLUT	0.1	Dierks et al. 1988
m	1.8	Dierks et al. 1988
Vmax_AK_c	142.85 mM/min	Reich and Selkov, 1981
Km_AK_c	1.0042 mM	Set equal to steady state ADP(c) concentration
Km_AK_c_r	0.297066 mM	Set equal to product steady state of ATP(c) and AMP(c) concentrations
Keq_AK_c	1.2	Reich and Selkov, 1981
Vmax_ndk_c	75.8929 mM/min	Reich and Selkov, 1981
Km_ndk_c	0.3277 mM/min	Set equal to product steady state of GTP(c) and ADP(c) concentrations
Km_ndk_c_r	0.30277 mM	Set equal to product steady state of GDP(c) and ATP(c) concentrations
Vmax_ndk_m	127.551 mM/min	Reich and Selkov, 1981
Km_ndk_m	4.35839 mM	Set equal to product steady state of GTP(m) and ADP(m) concentrations
Km_ndk_m_r	5.51728 mM	Set equal to product steady state of GDP(m) and ATP(m) concentrations
Vmax_GDH	170.068 mM/min	Reich and Selkov, 1981
Km_GDH	17.9592 mM	Set equal to product steady state of NAD^+(m) and GLUT(m) concentrations
Km_GDH_r	0.176327 mM	Set equal to product steady state of NADH(m) and AKG(m) concentrations
Keq_GDH	0.004	Reich and Selkov, 1981
Vmax_FA_a_m	4.825 mM/min	Calculated from $R_{FA\_a\_m}$ flux (Christian and Christian, 1983) from FBA and steady state FA_a concentration
Km_FA_a	0.516071 mM	Set equal to steady state of FA_a concentration
Vmax_FA_CoA	7.0068 mM/min	Reich and Selkov, 1981
Km_FA_CoA	0.5126 mM	Set equal to product steady state of FA(m) and CoA(m) concentrations
Vmax_GTP_AMP	51 mM/min	Reich and Selkov, 1981
Km_GTP_AMP	0.33 mM	Set equal to product steady state of AMP(m) and ATP(m) concentrations
Km_GTP_AMP_r	4.14 mM	Set equal to product steady state of GDP(m) and

		ADP(m) concentrations
Keq_GTP_AMP	0.8	Reich and Selkov, 1981
Vmax_b_c_lac	73.1455 mM/min	Calculated from in vivo flux (Christian and Christian, 1983) and steady state of LAC(b) concentration
Km_b_c_lac	1.5 mM	Set equal to steady state LAC (b) concentration
Vmax_b_c_glc	9.07893 mM/min	Calculated from in vivo flux (Christian and Christian, 1983) and steady state of GLC(b) concentration
Km_b_c_glc	5.07 mM	Set equal to steady state GLC (b) concentration
Vmax_b_c_PYR	8.375 mM/min	Calculated from in vivo flux (Christian and Christian, 1983) and steady state of PYR(b) concentration
Km_b_c_PYR	0.075 mM	Set equal to steady state PYR (b) concentration
Vmax_c_b_BHB	50.0085 mM/min	Calculated from in vivo flux (Christian and Christian, 1983) and steady state of BHB(b) concentration
Km_c_b_BHB	0.85 mM	Set equal to steady state BHB (b) concentration
Vmax_c_b_AcAc	23.6504 mM/min	Calculated from in vivo flux (Christian and Christian, 1983 and steady state of AcAC(b) concentration
Km_c_b_AcAc	0.7 mM	Set equal to steady state Ac Ac(b) concentration
Vmax_c_m_PYR	42.85 mM/min	*adjusted to maintain Pyruvate flux
Km_c_m_PYR_PYR	0.175 mM	*adjusted to maintain Pyruvate flux
Km_c_m_PYR_OH	1.58E-05 mM	Set equal to product steady state of PYR(c) and OH(m) concentrations
Km_c_m_PYR_AcAc	0.61 mM	Set equal to product steady state of PYR(c) and AcAc(m) concentrations
Vmax_c_m_CIT	2.25633 mM/min	Calculated from $R_{CIT\_c\_m}$ flux from FBA and steady state CIT(c) CIT(m), MAL(c), and MAL(m) concentrations
Km_c_m_CIT	0.019425 mM	Seis 1982
Vmax_c_m_MAL	257.143 mM/min	Hanson and Mehlman, 1981
Km_c_m_MAL	0.02415 mM	Hanson and Mehlman, 1981; Seis 1982
Vmax_c_m_GLUT	99.6429 mM/min	Hanson and Mehlman, 1981
Km_c_m_GLUT	0.4725 mM	Hanson and Mehlman, 1981; Seis 1982
Vmax_FA_c_m	4.825 mM/min	Calculated from $R_{FA\_a\_m}$ flux from FBA and steady state FA_a concentration
Km_FA_c_m	0.5161 mM	Set equal to steady state of FA_a concentration
Vmax_c_m_AcAc	43.0581 mM/min	*adjusted to maintain AcAc flux
Km_c_m_AcAc	10.7143 mM	Set equal to steady state of AcAc(m) concentration
Vmax_c_m_pi	209.184 mM/min	Hanson and Mehlman, 1981
Km_c_m_pi	0.168 mM	Hanson and Mehlman, 1981

Table 4.3. Initial cytosolic, mitochondrial and blood concentrations, representing 24 hour fasted state. The following concentrations were set as constants: NADH_total_c= 0.801361mmol/L cyt water[1,4,5,7,9]; NADH_total_m= 2.4 mmol/L mit water[1,4,5,7,9]; F26BP=0.000143 mmol/L cyt water[1]; cAMP=0.0075 mmol/L cyt water; Pi_c= 8.5 mmol/L cyt water[1]; Pi_m=9.5 mmol/L mit water[1]; OH_c= 0.00016 mmol/L cyt water[1]; OH_m= 0.000251mmol/L mit water[1]; CoQ_total= 1.35 mmol/L mit water[1].
*: subcellular metabolie distribution in isolated hepatocytes from 48 hr starved rats incubated with lactate

Cytosolic metabolite concentrations mmol/L cyt water	
PYR_c	0.0696[1,3,4,7*]
OAA_c	0.000417[1c7*]
AcCoA_c	0.08093[1,7*]
CIT_c	0.2534[1,7*]
MAL_c	0.1843[1,7*]
Alpha_KG_c	0.1465[1,7*]
ASP_c	1.1536[1,7*]
GLUT_c	3.7714[1,7*]
ATP_c	3.3271[1,8,7*]
ADP_c	1.0021[1,8,7*]
AMP_c	0.0893[1,8,7*]
GTP_c	0.327[7,7*]
GDP_c	0.091[7,7*]
BHB_c	2.6786[1,3,5]
AcAc_c	0.8929[1,3,5]
NADH_c	0.00136[1,4,5,7,9]
CoA_c	0.0564[1,7*]
LAC_c	1.3571[2]
PEP	0.0709[1]
PG2	0.2679[1]
PG3	0.1357[1]
DHAP	0.0232[1]
GAP	0.03036[4,5]
F16BP	0.02321[1]
F6P	0.06607[1]
G6P	0.1464[1]
GLC_c	8.9285[1]
GR3P	0.4464[1]
GLR_c	0.1785[1]
FA_c	0.5161[1]
glycogen	157.143[1]

Mitochondrial metabolite concentrations mmol/L mit water	
PYR_m	0.1358[1,3,4,x*]
OAA_m	0.0011[1]
AcCoA_m	0.9809[1]
CIT_m	3.1989[1]
MAL_m	1.2346[1]
Alpha_KG_m	0.4408[1]
ASP_m	1.9387[1]
GLUT_m	8.9795[1]
ATP_m	14.9116[1,8]
ADP_m	11.2041[1,8]
AMP_m	0.8503[1,8]
GTP_m	0.389[7]
GDP_m	0.37[7]
BHB_m	30.4421[1,3,5]
AcAc_m	10.7142[1,3,5]
NADH_m	0.4[1,4,5,7,9]
CoA_m	2.8214[1,7*]
Iso_cit	0.153[1,7]
SucCoA	12.5850[1,7]
SUC	12.5850[1,7]
FUM	1.2755[1,7]
FA_m	0.1871[1,7]
FA_acylCoa	0.1871[1,7]
CoQh2	0.38[c,7]
CoQ	0.97[1,7]

Blood metabolite concentrations mM	
FA_b	0.673[2c]
LAC_b	1.5[1,3,5]
ALA_b	0.7[2]
GLC_b	5.07[2]
BHB_b	0.85[2,6]
AcAc_b	0.7[2,6]
PYR_b	0.075[2]

Citations:

1: Bergmeyer 1994
2: Christian and Christian 1983
3: Krebs 1967
4: Stubs et al. 1972
5: Williamson et al. 1970
6: Huang 1997
7: Sies 1982
8: Hems et al. 1966
9:Williamson et al. 1969a

4.2.2 Model of the Perfused Liver

The liver tissue is represented by four distinct compartments, representing the cytosol, the mitochondria, the blood, and the perfusate. Each compartment is assumed to be well-mixed. The dynamic mass balance for each species *i* in the blood domain is given by:

$$\frac{dC_{i,blood}}{dt} = (C_{i,perfusate} - C_{i,blood})\frac{F_{perfusate}}{V_{blood}} - J_{i,b-c}\left(\frac{V_{cytosol}}{V_{blood}}\right) \qquad (4.1)$$

The content of the blood domain is actually the saline perfusion medium rather than blood, and Eqn. 4.1 is only written for those metabolic intermediates expected to occur in the blood/saline perfusate (i.e. GLC, LAC, ALA, AcAc, BHB, GLR, PYR, FA).

In the cytosol the dynamic mass balance equation for species *i* is decribed as:

$$\frac{dC_{i,cytosol}}{dt} = J_{i,b-c} + J_{i,c-m} + \sum_j R_{i,j,c} \qquad (4.2)$$

In the mitochondrial domain, the dynamic mass balance equation for species *i* is given by:

$$\frac{dC_{i,mitochondria}}{dt} = J_{i,c-m}\left(\frac{V_{cytosol}}{V_{mitochondria}}\right) + \sum_j R_{i,k,m} \qquad (4.3)$$

The perfusion medium is represented by the following mass balance for each metabolic intermediate that exists in the blood domain:

$$\frac{dC_{i,perfusate}}{dt} = (C_{i,blood} - C_{i,perfusate})\frac{F_{perfusate}}{V_{perfusate}} \qquad (4.4)$$

$C_{i,cytosol}$, $C_{i,mitochondria}$, $C_{i,blood}$, and $C_{i,perfusate}$ are concentrations of species *i* in the cytosol, mitochondria, blood, and perfusate domains, respectively; $J_{i,b\text{-}c}$ is the transport rate between the blood and cytosol domains, while $J_{i,c\text{-}m}$ is the transport rate between the

cytosol and the mitochondria domains. $J_{i,\text{b-c}}$ and $J_{i,\text{c-m}}$ are both expressed in units of mM(cytosol) min^{-1}; $R_{i,j,c}$ is the rate of each reaction *j*, with species *i* as substrate or product, taking place in the cytosol; $R_{i,k,m}$ is the rate of each reaction *k*, with species *i* as substrate or product, taking place inside the mitochondrial compartment; F_{blood} is the flow rate through the liver. The ratio of cytosol volume to blood volume ($V_{cytosol}/V_{blood}$) is used for conversion of units of $J_{i,b\text{-}c}$ from cytosol volume units to blood volume units, whereas ($V_{cytosol}/V_{mitochondria}$) is used for conversion of units *of* $J_{i,c\text{-}m}$ from cytosol volume units to mitochondria volume units.

The model consisted of a total of 108 mass balances (Equations 4.1-4.4), representing 40 different species distributed among the four different compartments (Table 4.3). The set of differential equations were solved simultaneously using ODE 45 in Matlab.

4.2.3 Parameter Estimation and Simulation Strategy

Since there are few experimental data compared to the large amount of model parameters, it is infeasible to perform a complete parameter estimation process. As determined in Chapter III, the distribution of NADH and NAD^+ between the cytosol and mitochondria is a critical aspect in controlling gluconeogenesis and predicting more accurate flux distributions. To reconcile the simulated redox ratios with experimental ones during gluconeogenesis, the sensitivities of concentrations of NADHc and NADHm to each kinetic parameter were calculated at the overnight fasted *in vivo* steady state condition, using:

$$S_{NADHc,j} = \frac{\partial[NADHc]/[NADHc]}{\partial K_j / K_j}; \qquad S_{NADHm,j} = \frac{\partial[NADHm]/[NADHm]}{\partial K_j / K_j} \qquad (4.5)$$

Partial derivatives were estimated by central finite differences. The parameters with the greatest sensitivities, shown in Fig. 4.2, were then manually tuned such that the model simulations yielded the best fit for both cytosolic and mitochondrial NADH concentrations at the quasi steady states representing overnight fasted (Table 4.3), lactate perfusion, and lactate plus oleate perfusion (Fig 4.3A). In addition, several other parameters were found to significantly affect the predicted redox ratios and important fluxes. Altogether, a total of nine parameters were adjusted from the original values (from either *in vitro* data or from use in previous models). These nine parameter values are given in Table 4.4.

Table 4.4 Parameters with the largest magnitude of sensitivity to NADHc and NADHm, with original values and after model tuning. Units are given in Table 4.2.

Kinetic parameters	Original kinetic values	Kinetic values after tuning
n3_pc	1.65	2.75
Vmax_atp_adp_c	35.4104	55.41
Km_atp_adp_c	3.32	17.2
Keq_MDH_m	0.000028	0.00028
Km_PEPCK	0.00040179	0.0040179
X_ASPGLUT	44.88	448.8
Km_bhb	2.846003	0.2846
K_amp	0.182758621	1.8759
K_atp1_pk	0.75	0.0075

The mathematical model, with the fine tuned parameters as described above, was then used to simulate the perfused rat liver, with additions of lactate and pyruvate, without and with fatty acids, according to different perfusion protocols. These perfusion protocols

with input functions are summarized in Table 4.5. The initial conditions for the variables in Eqns. 4.1-4.3 are given in Table 4.3. Initial conditions for Eq. 4.4 are:

$$C_{i,perfusate}(0) = 0 \text{ for } i\text{=Glc, LAC, PYR, BHB, AcAc} \qquad (4.6)$$

(i.e. the saline pre-perfusion contains no substrate). The simulations were used to investigate the effects of lactate, pyruvate, and fatty acids on the dynamics of cytosolic and mitochondrial NADH and a wide range of fluxes reflecting rates of gluconoegenesis, TCA cycle, ketogenesis, and specific carbon shuttles. No parameters were changed between all the subsequent simulations, unless explicitly stated.

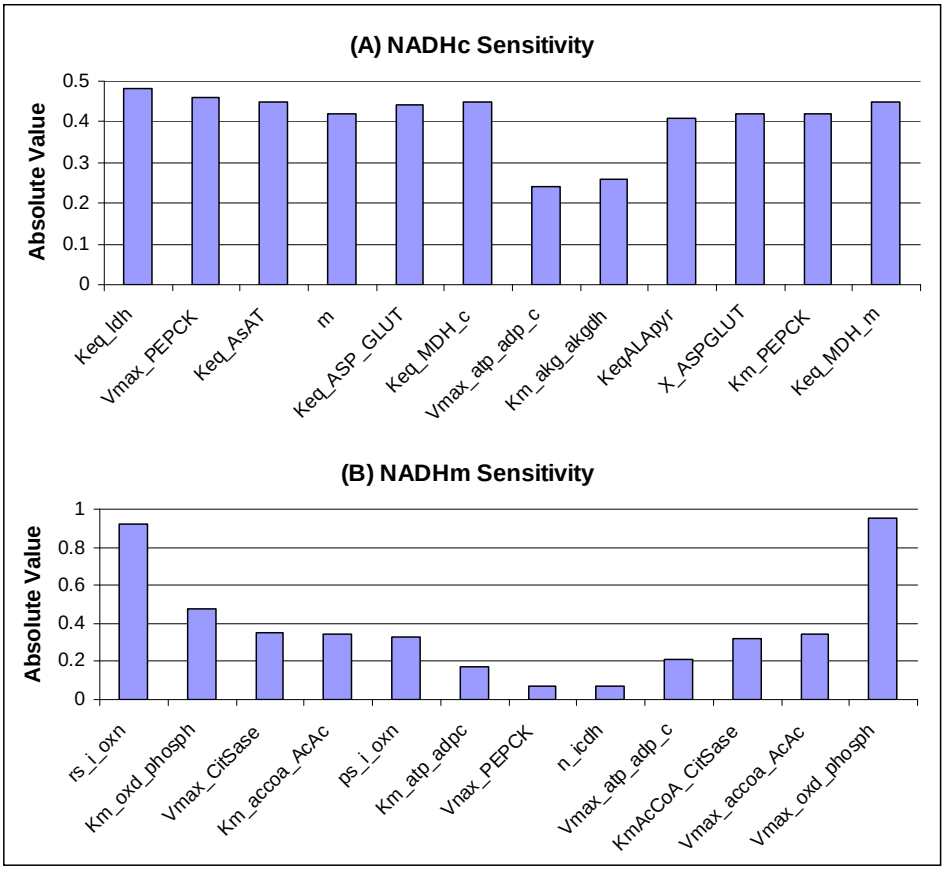

Figure 4.2. Absolute values of the normalized sensitivities of the most sensitive parameters to NADH for the lactate perfusion model; (A) cytosolic NADH; (B) midochondrial NADH.

Table 4.5. Input functions used in simulation of the perfused liver. $R_{FA\text{-}endo}$=rate of endogenous fatty acid oxidation, normalized to µmol C_{16} (palmitate); $J^*_{FA\text{-}b\text{-}t}$ = the sum of the uptake rate of FFA and rate of endogenous fatty acid oxidation

Lactate Perfusion		
Saline pre-perfusion; $0 < t \leq 30$	Lactate infusion; $30 < t \leq 120$	Lactate + FA; $90 < t \leq 120$
$R_{FA\text{-}endo} = 0.15$ µmol(Lcyt water $)^{-1}min^{-1}$, assumed to be equal to experimental measurements of ketone production during this period[26].	$R_{FA\text{-}endo} = 0.08178$ µmol(Lcyt water $)^{-1}min^{-1}$, as estimated[26] from ketone production. $C_{LAC,,perfusate}$ = $10(1-\exp(-(t-30)/\tau)$ mM (constant LAC concentration of 10 mM in perfusate); τ is time constant for achieving change in susbstrate concentration, set to 4 min.	$J^*_{FA\text{-}b\text{-}t}$= $0.08178+0.466(1-\exp(-(t-90)/\tau)$, τ=2.5 min; total rate of 0.5874 µmol(Lcyt water $)^{-1}min^{-1}$ determined from experimental measurements of oleate infusion[26]. $C_{LAC,,perfusate}$ =10 mM
Pyruvate Perfusion		
Saline pre-perfusion; $0 < t \leq 30$	Pyruvate infusion; $30 < t \leq 120$	Pyruvate + FA; $90 < t \leq 120$
$R_{FA\text{-}endo} = 0.15$ µmol(Lcyt water $)^{-1}min^{-1}$	$R_{FA\text{-}endo}$ =0.08178 µmol(Lcyt water $)^{-1}min^{-1}$ $C_{PYR,,perfusate}$ = $2(1-\exp(-(t-30)/\tau)$ mM (constant PYR concentration of 2 mM in perfusate); τ=3 min. $C_{LAC,,perfusate}$ calculated from Eqn. 3.	$J^*_{FA\text{-}b\text{-}t}$ = $0.08178+0.466(1-\exp(-(t-90)/\tau)$, τ=2.5 min; total rate of 0.5874 µmol(Lcyt water $)^{-1}min^{-1}$ determined from experimental measurements of oleate infusion[26]. $C_{PYR,,perfusate}$ =2 mM

4.3 Results

Fig. 4.3A shows that the predicted redox ratios in both the cytoplasm and the mitochondria are in very good agreement with the experimental results with lactate and fatty acids (Williamson et al. 1969). The simultaneous shift in the mitochondrial and the cytosolic redox ratios are obvious upon stimulation with fatty acid, and these correlate extremely well with the experimental observations. Also note that the order-of-

magnitude difference between cytosol and mitochondria ratios is predicted accurately by the model. The results with 2 mM pyruvate in place of lactate (Fig. 4.3B) further confirm that the model gives results in general agreement with the physiological findings, both before and after addition of fatty acids. This reflects an improvement from the single-tissue compartment model (Chapter III), which could not distinguish between cytoslic and mitochondrial redox ratios.

While the lumped-tissue model of Chapter III closely predicted the gluconeogenesis flux during simulation with lactate and fatty acid, the rates of glucose production, ketogenesis, and several other metabolic rates were underestimated under pyruvate simulation (Fig. 3.5). We attributed the discrepancy of these results between lactate and pyruvate to a different scheme for metabolite and reducing equivalent transport across the mitochondrial membrane in each case. While lactate provides directly the reducing equivalent to the GAPDH in the cytosol through LDH, pyruvate, on the other hand, needs to use a specific shuttling mechanism to provide the necessary reducing equivalents for GAPDH.

The calculated net malate transport in the pyruvate perfusion agrees closely with experimental value and transport direction from the mitochondria to the cytosol (Fig. 4.3B). Moreover the model predicts a larger transport rate through the malate-phosphate shuttle compared to malate alpha-ketoglutarate exchange (Fig. 4.4B). This latter result corresponds well with experimental observations (Robinson et al., 1967; Meijer et al. 1969) on the important role of malate-phosphate exchange in malate efflux and its relative role in driving the gluconoegenesis pathway.

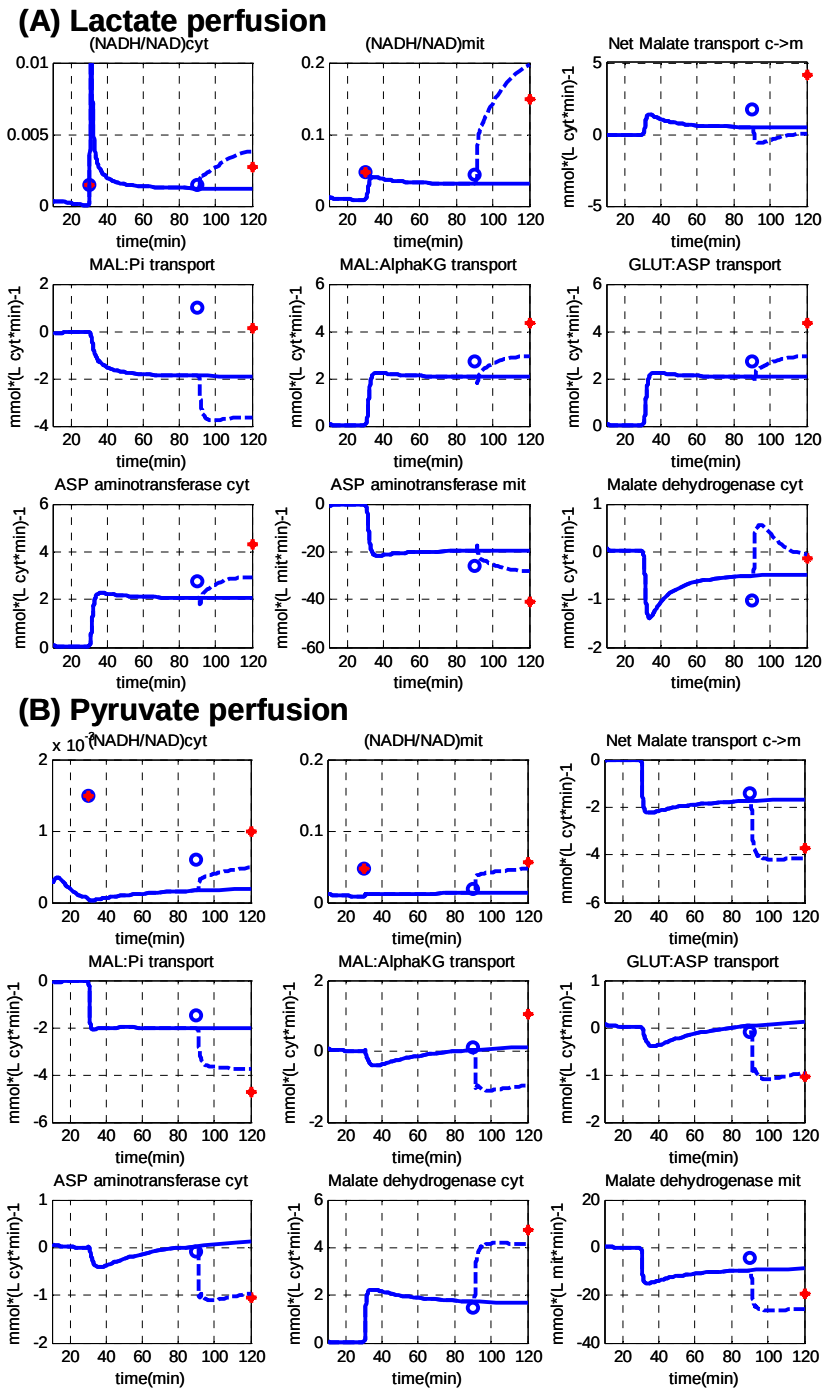

Figure 4.3. Redox ratio (NADH/NAD) and fluxes calculated from perfusion model with (A) lactate and (B) pyruvate as substrate. Initial conditions represent the *in vivo* 24-hour fasted state. Symbols are experimental data from perfused fasted livers, from Williamson, et al. 1969a, 1969b, 1970a, using a perfusion medium of Krebs-Henseleit bicarbonate buffer, with 4% bovine serum albumin, in a recirculated system. Closed circle: pre-perfusion with no substrate; open circle: perfusion with (A) 10 mM lactate or (B) 2 mM pyruvate; star (*, at 120 min): perfusion with 1.5 mM oleate added to previous substrate. Solid and dashed lines are simulations, using Eqns. 4.1,3 and 4, with $F_{perfusate}$=50 ml/min and $V_{perfusate}$=100 ml (corresponding to the experimental protocol), and all other parameters as given in Tables 4.1. Solid lines: $10 < t \leq 30$ min: saline pre-perfusion (no substrate); $30 < t \leq 120$ min: perfusion with 10 mM lactate or 2 mM pyruvate. Dashed lines: $90 < t \leq 120$ min: lactate or pyruvate plus 1.5 mM FA perfusion.

Aspartate efflux from the mitochondria was found to be negligible during pyruvate perfusion alone (Fig. 4.3B, GLUT:ASP transport), while the GLUT:ASP exchange is four-fold greater than net malate transport during lactate perfusion (Fig. 4.3A), in good agreement with several studies (Wieland 1968; Krebs et al. 1967; Williamson et al. 1968, 1969a, 1969b, 1969c, 1969d). The movement of aspartate into and out of the mitochondria is tightly linked to the rate of transamination between aspartate and glutamate on both sides of the membrane. As Fig. 4.3A indicates for lactate perfusion, the OAA formed in the mitochondria is converted to aspartate, and after being transported to the cytosol, aspartate is converted back to OAA, by the mitochondrial and cytosolic aspartate aminotransferases, respectively. Therefore the carbon requirements for gluconoegenesis are met by the transport of asparate to the cytosol. Note that the value of the flux in the mitrochondria appears to be 10 times that of the cytosolic flux; this results from the different compartment volume units used, since the mitochondrial volume is about 1/10 that of the cytosolic volume. However, during pyruvate simulation, malate acts both as transporter of the carbon and the reducing equivalents from the mitochondria to the cytosol. The computed rates and directions of the cytosolic and mitochondrial MDH agree with the estimated rates provided by Williamson et al. (1970) during the lactate and pyruvate perfusions with and without oleate (Fig. 4.3A,B).

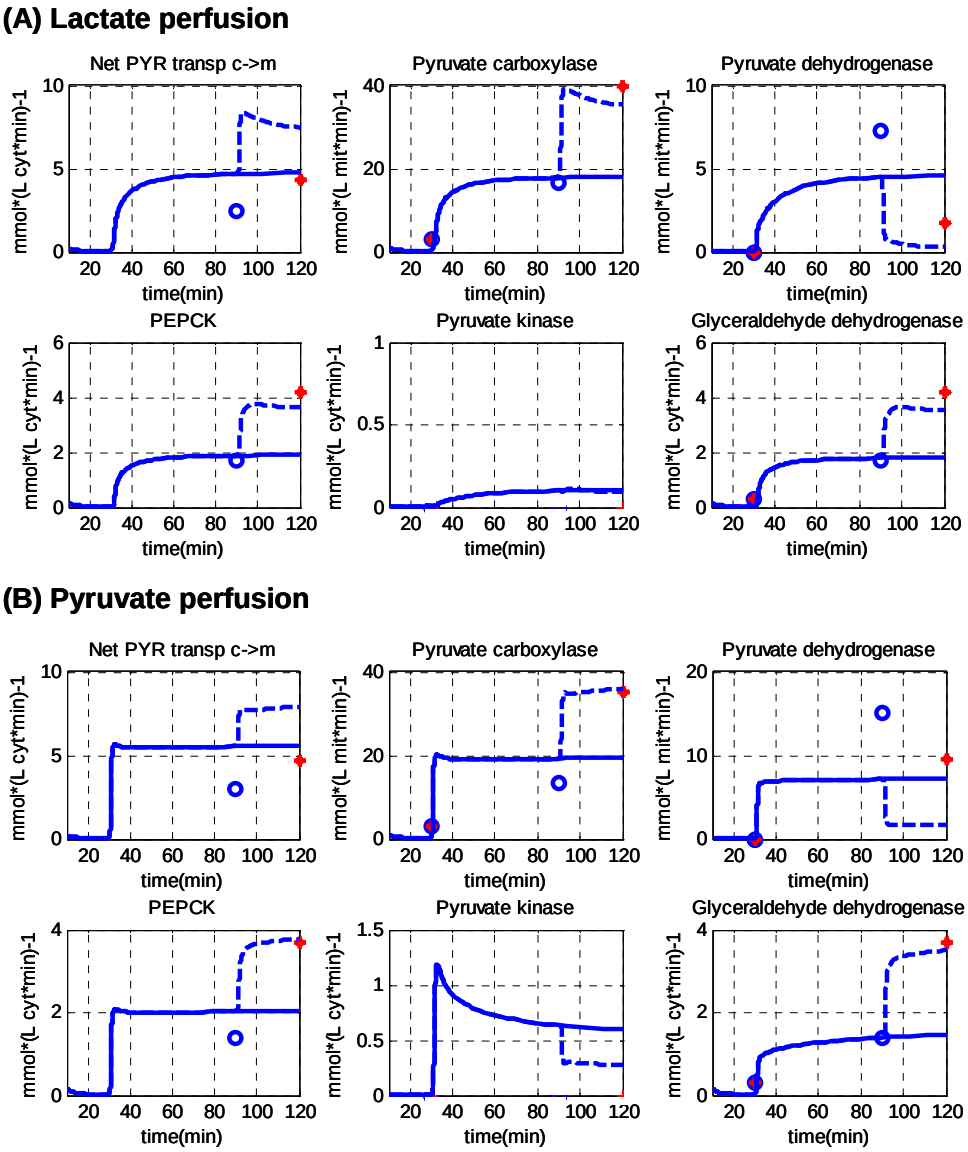

Figure 4.4. Fluxes calculated from perfusion model with (A) lactate and (B) pyruvate as substrates. Simulation and experimental details given in Figure 4.3 caption.

Cytosolic pyruvate, whether from the perfusion medium, or from oxidation of lactate by LDH, is transported to the mitochondria by specific carriers, the most notable one being the pyruvate-hydroxyl ion carrier (Brouwer et al. 1973; Halestrap, 1975; Halestrap et al. 1974; Papa et al. 1974, 1971; Mowbray, 1975). Fig. 4.4 shows a net transport of

pyruvate from cytosol to mitochondria during lactate and pyruvate simulations. The subsequent addition of fatty acids to either lactate or pyruvate further increased the rate of pyruvate transport to the mitochondria, agreeing well with fluxes estimated by Williamson. A continuous supply of pyruvate to the mitochondria is necessary for many metabolic rates, most importantly the pyruvate carboxylase which is an important intermediate step in gluconoegenesis.

The rate of pyruvate carboxylase (PC) increases upon addition of oleate to lactate and pyruvate (Fig. 4.4), in coordination with the increase in the rate of pyruvate entry from the cytoplasm to the mitochondria. However, this increase in PC flux is not primarily due to the greater availability of pyruvate. Instead, the current model (as did the Chp III model) accounts for the activation of PC by AcCoA. The addition of exogenous oleate enhances the rate of fatty acid oxidation in the mitochondria, subsequently increasing the mitochondrial redox ratio and the concentration of the mitochondrial AcCoA (not shown). Conversely, the rate of pyruvate dehydrogenase (PDC) is inhibited during the addition of fatty acids in both the lactate and pyruvate scenarios, due to inhibition of PDC by mitochondrial redox ratio and AcCoA.

The rates of gluconoegenesis produced under the two different gluconoegenic substrates correspond well with the experimental data (Fig. 4.5). The glucose production rate approximately doubles in response to oleate addition. The conversions, by mass, of pyruvate and lactate to glucose are 80 % and 70% respectively, compared to 55 and 65% found by Williamson et al. (1970, 1969). However, a higher conversion of pyruvate to glucose (around 80%) was reported when oleate was added to the perfusion medium.

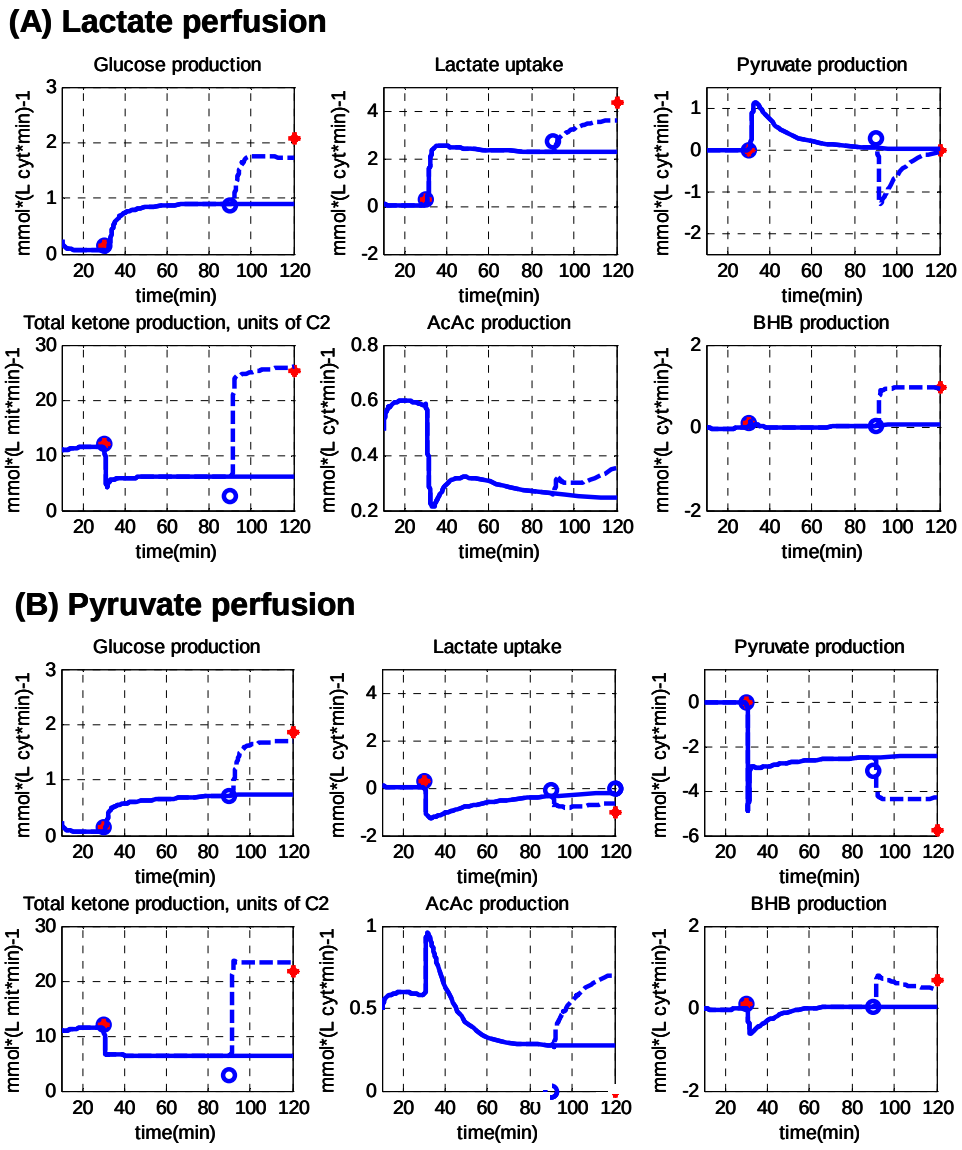

Figure 4.5. Fluxes calculated from perfusion model with (A) lactate and (B) pyruvate as substrates. Simulation and experimental details given in Figure 4.3 caption.

The rates of ketogenesis (i.e. total ketones, as measured by the rate of synthesis of AcAc, and BHB production) agree very closely with the experimental data (Fig. 4.5), showing a reduction during the perfusion period of pyruvate or lactate and a rapid increase upon stimulation with fatty acids.

The citric acid cycle estimated in the model appears to be less active than the experimental results during lactate and pyruvate perfusions; however these results are still consistent with the directional change of the cycle, especially during enhanced fatty acid oxidation (Fig. 4.6). The simulations overestimate the activation of the TCA cycle by oleate compared to the data as measure by citrate synthase (i.e. lactate: 117% simulated vs. 9% data; pyruvate: 105% simulated vs.40% data). It is worth noting that the TCA fluxes in Williamson et al. were not measured directly; rather, they were calculated from measurements of the respiratory activity and the metabolic balance of substrates across the liver, and involved several assumptions that might alter the estimates of the fluxes. Moreover, the authors themselves mentioned the need for reinterpretation of their TCA cycle flux calculation, especially in the case of lactate perfusion, where oleate addition appeared to cause only a small increase in the TCA cycle rate.

The calculated rate of oxygen consumption matches closely the data during the lactate plus oleate perfusion (Fig. 4.6), however the calculated baseline after the pre-perfusion is lower than the data; therefore the model seems to overestimate the stimulation of oxygen uptake by lactate and oleate. The model predicts an increase in oxygen consumption by 115% upon lactate addition compared to a measured 23% increase. The subsequent addition of oleate caused a 50% increase as reported by Williamson, while our model predicts an increase of 130%.

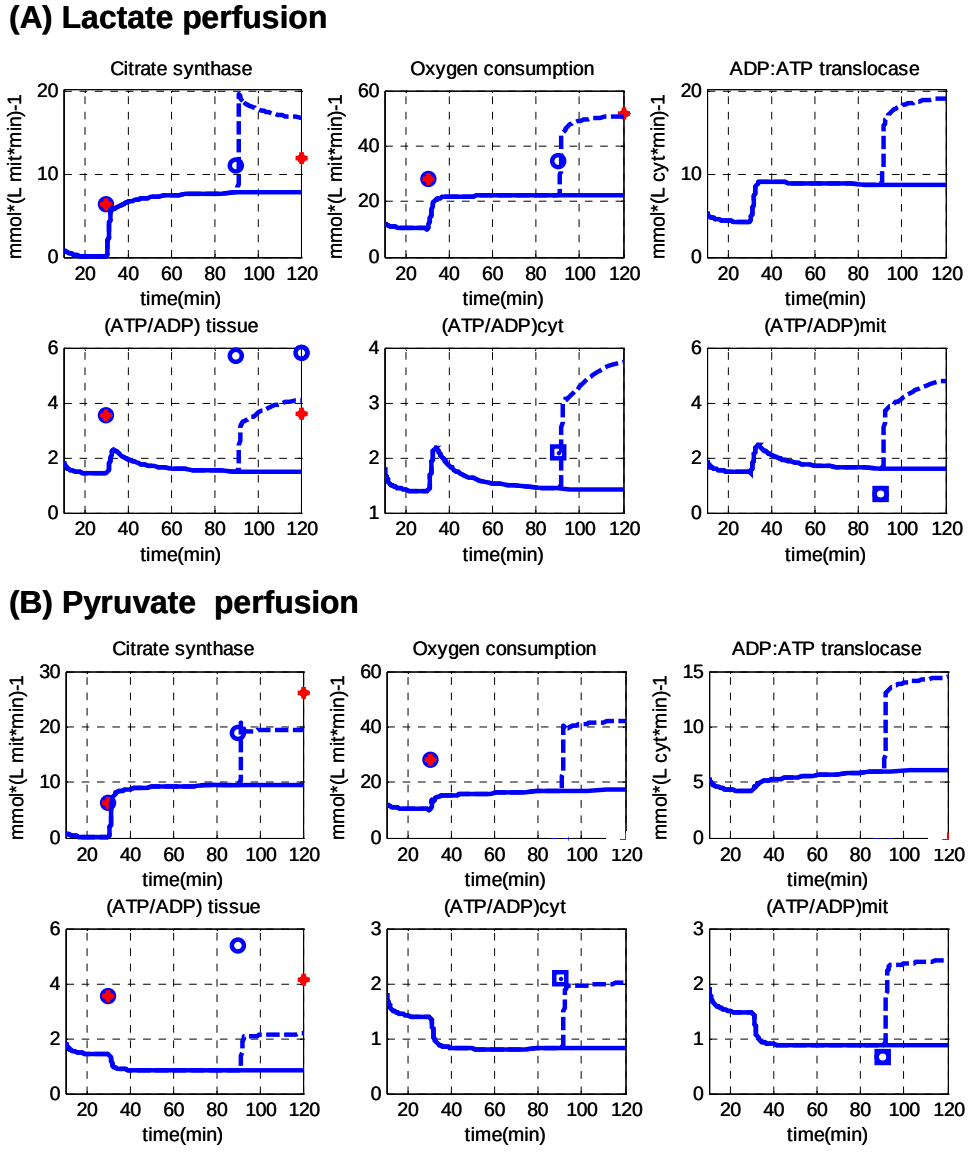

Figure 4.6. Fluxes and ATP/ADP ratios calculated from perfusion model with substrates: (A) lactate and (B) pyruvate. Simulation and experimental details given in Figure 4.3 caption.

The ADP:ATP transport across the mitochondrial membrane requires a carrier known as the ADP:ATP translocase. It is highly specific and permits the efflux of ATP synthesized in the mitochondria in exchange for ADP. The simulated translocation flux (Fig. 4.6) indicates a clear transport of ADP from the cytosol into the mitochondria in

exchange for ATP, in accordance with various experimental results. The addition of oleate increases the rate of respiration, increasing the amount of mitochondrial ATP, therefore increasing the rate of ADP:ATP translocase. The model results agree well with this expected chain of events. The model supports the non-uniform distribution of adenine nucleotides between the cytosol and the mitochondria, with 40% of the overall tissue adenine nucleotides found in the mitochondria, compared with 27% reported experimentally (Soboll et al. 1978). The overall tissue ATP/ADP ratio predicted by the model (Fig. 4.6) is equal to 1.5 and 0.84 for lactate and pyruvate perfusion, respectively. The ratio was significantly lower than the one found by Williamson et al. We then examined the cytosolic and mitochondrial ATP/ADP ratios. Our model predicts the cytosolic and mitochondrial ATP/ADP ratios to be similar, at 1.4 and 1.6, respectively, (Fig. 4.6) during lactate perfusion, while most studies show an asymmetry between the two ratios, with higher cytosolic ratio compared to the mitochondrial ratio. Experiments with hepatocytes showed a much higher mitochondrial ATP/ADP ratio of about 2.0, compared to perfused tissues or intact animals (Akerboom et al. 1978; Sies and Wieland 1976; Sobol et al, 1980). It is generally known that during the state of low-energizing, or even de-energized mitochondria, the mitochondrial ATP/ADP ratio is increased and the difference between cytosolic and mitochondrial ATP/ADP ratios is greatly decreased. Livers from starved animals are unable to meet their ATP requirements due to lack of glycogen, and the energization of their mitochondria is much lower than in fed animals, and thus one may expect a reduced difference in ATP/ADP ratios between the cytosol and the mitochondrial compartment.

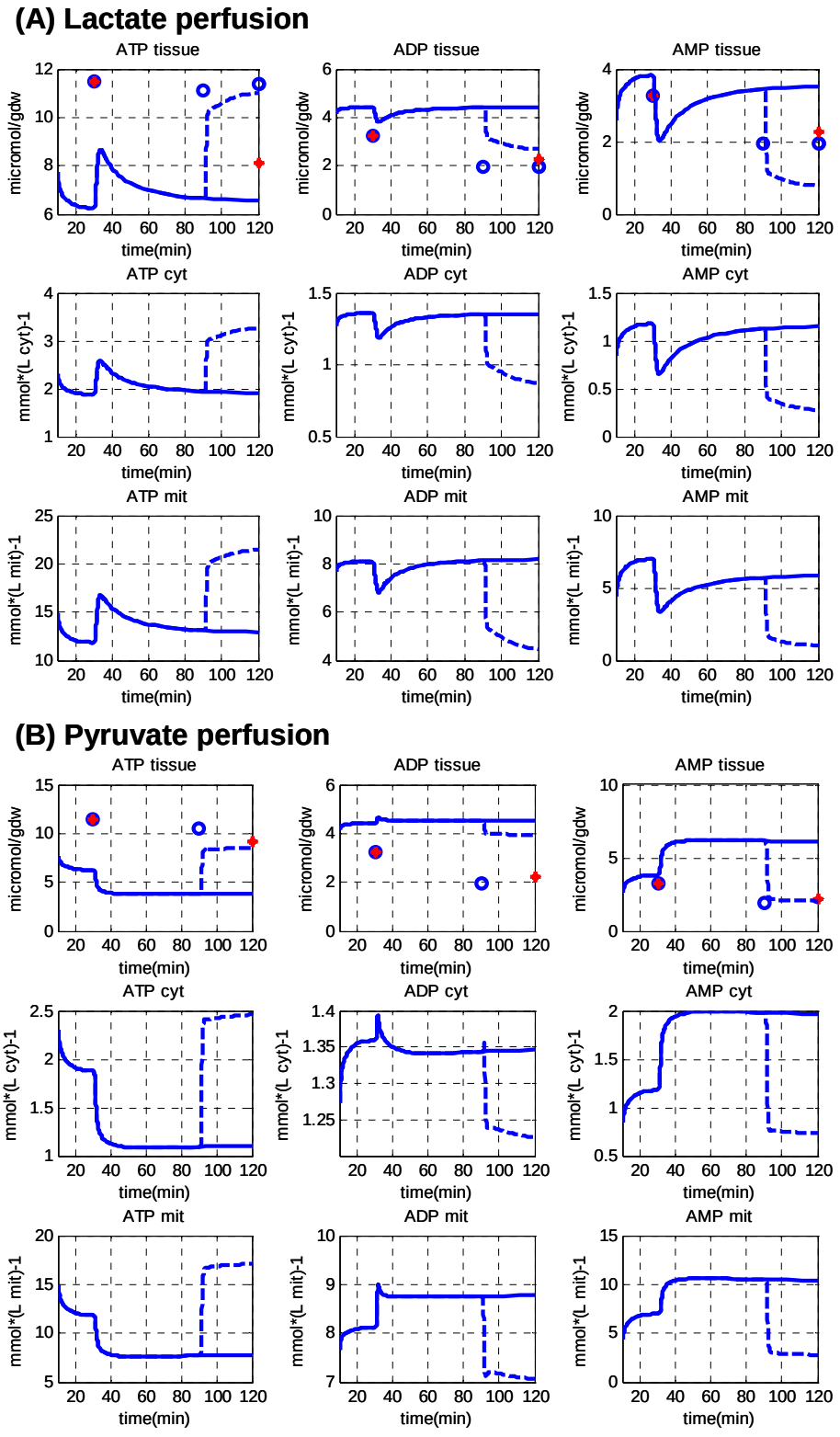

Fig. 4.7 Adenine nucleotide concentrations calculated from perfusion model with lactate as substrate. Details given in Fig. 4.3 caption.

The addition of oleate to either lactate or pyruvate causes an increase in the tissue ATP concentration, and a rapid decrease in the AMP concentration and a decrease in the ADP concentration (Fig. 4.7); this seems to be in contrast to the experimental data which shows insensitivity to the addition of oleate to substrate.

The model was then used to simulate perfusions with both lactate and pyruvate simultaneously, with total concentration of lactate and pyruvate from 1 to 10 mM, and the lactate to pyruvate ratio maintained at 9.0. Fig. 4.8 compares the predicted rates of glucose production and ketone formation to that found in different studies from 24 to 48-hour-starved isolated liver cells. The results are in good agreement with experimental data, further validating our computational model's ability to predict metabolic rates of the liver near physiological level conditions.

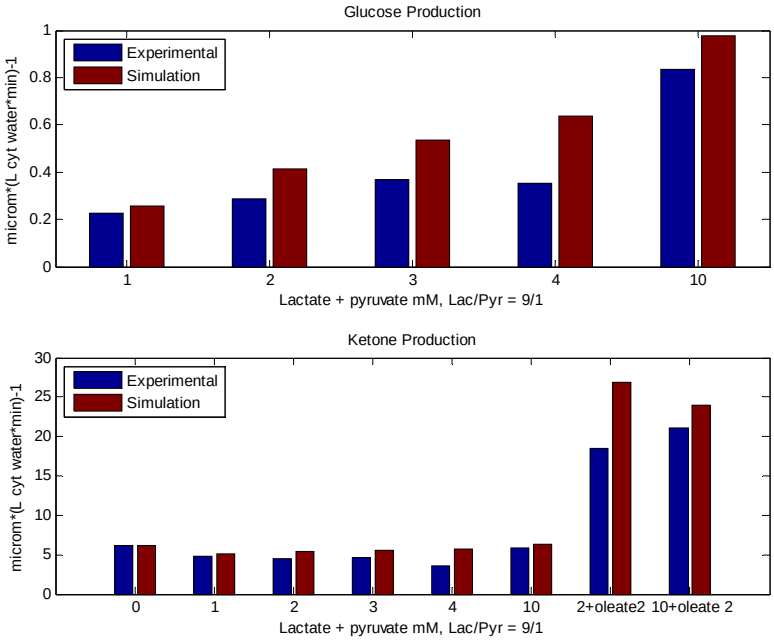

Figure 4.8. Rates of glucose production and ketogenesis at different total concentrations of lactate and pyruvate in perfusion medium, with lactate/pyruvate ratio constant at 9/1. Red bars are experimental data from starved liver slices incubated with lactate and pyruvate (Soling et al., Kuhn et al., Janson et al). Blue bars are simulations, using Eqns. 4.1,3 and 4, with $F_{perfusate}$=50 ml/min and $V_{perfusate}$=100 ml and all other parameters as given in Tables 4.1. The x-axis represents the total concentration of lactate and pyruvate in the perfusion medium, with a lactate/pyruvate ratio of 9/1 at all times.

4.4 Discussion

The compartmental model developed in this work successfully simulates the perfusion of a starved rat liver with substrates of lactate, perfusion, and oleate. It mimics the key metabolic rates involved in the liver metabolism and provides predictions of all the intermediate steps and their interactions. The model successfully predicts the preferred mechanisms for anion transport and the indirect transfer of reducing equivalents across the mitochondrial membrane with respect to the perfused substrate. When lactate is the gluconoegenic substrate, the model predicts that NADH is formed directly in the cytosol by oxidation of lactate to pyruvate, and aspartate is used to transport the carbon backbone from the mitochondria to the cytosol. This is consistent with the experimental observations (Williamson et al 1968; Krebs et al 1976). The pyruvate model predicts the following scheme: transport of pyruvate to the mitochondria, formation of OAA through the pyruvate carboxylase, conversion of OAA to malate through the mitochondrial MDH, a net malate efflux toward the cytosol, and reconversion of malate to OAA in the cytosol. Therefore malate transport from the mitochondria provides both the carbon and reducing equivalents to support the gluconeogenesis metabolism in the rat liver, in accordance with several experimental observations (Meijer et al. 1974; Rongstad et al. 1972; Soling et al.1973).

The model serves as a tool to monitor the values of intermediate fluxes which are difficult to measure directly. Transamination between glutamate and aspartate was noted in both perfusion models. However these rates are higher with lactate than with pyruvate, while the net malate efflux is obviously higher with pyruvate than with lactate. Malate exchange can be accomplished through specialized carriers, such as MAL:Pi,

MAL:AKG, and Mal:CIT. The efflux through MAL:Pi was predominant over the other carriers with pyruvate as substrate. This is consistent with observations on the role of MAL:Pi in supporting gluconoegenesis, where the use of MAL:Pi inhibitors lead to inhibition of gluconeogenesis from pyruvate and alanine in rat liver (Chamalaun et al. 1971; Williamson et al. 1970). Thus, the model can provide insight into the function and directional movement of the cytosol-mitochondrial transporters in other situations where direct measurements are not available.

The simulation with fatty acids results in an increase in the rate of malate transport from the mitochondria. The NADH generated by the cytsolic malate dehydrogenase increases the redox ratio and allows the glyceraldehyde dehydrogenase reaction to use the extra NADH to drive further the rate of gluconoegenesis. It is evident that the addition of fatty acid has increased both the cytosolic and mitcochondrial redox ratios; these ratios in turn increase the rates of gluconoegenesis and ketogenesis, respectively. In addition, simulations of fatty acid perfusion with either lactate or pyruvate resulted in an appropriate increase in oxidative phopsphorylation and the TCA cycle fluxes.

The model was able to predict a cytosolic ATP/ADP ratio which reflects the tissue-average ATP/ADP ratio according to Soboll et al. (1978). The major limitations of the model are: its inability to mimic an asymmetry in ATP/ADP between the mitochondria and cytosol; and its underestimation of the ratio compared to experimental data (Fig. 4.6). A simplification of the oxidative phosphorylation mechanism representation which lumps the ATPase reaction with the oxygen consumption rate is possibly responsible for the mismatch between the simulations and the expected experimental data. Furthermore, it has been suggested that the rate of respiration of isolated mitochondria is controlled by

the external phosphate potential (Davis et al. 1974, 1975; Owen and Wilson, 1974; Slater et al, 1973). It has also been shown that the mitochondrial ATP/ADP ratio is independent of the cytosolic ATP/ADP ratio and the respiratory rate (Klingenberg, 1972 and Davis et al., 1974, 1975). The model predicts higher concentrations of ADP and AMP in the mitochondria than in the cytosol, which correspond well with Soboll et al. The difficulty in accurately predicting ATP and ADP levels in each compartment indicates the need for a better representation of the ADP translocase.

The ADP translocase reaction is partially electroneutral and partially electrogenic with a 50 to 70 % proportion for the latter. This implies that the membrane potential plays an important role in the transport of the nucleotides and results in a higher ATP/ADP ratio on the outside of the membrane than on the inside of the mitochondria (Klingenberg 1970, 1972, 1973). The cytosolic and mitochondrial Pi concentrations in the model were assigned constant values, with the mitochondrial value slightly higher than in the cytosolic (Table 4.3).

The model is able to account for the rate of pyruvate recycling through the pyruvate kinase without affecting the overall rate of gluconoegenesis, therefore giving more credibility to the model. The estimated rate of pyruvate kinase during the pyruvate simulation constituted 30% of the rate of gluconeogenesis (Fig. 4.4), which agrees well with various observations from (Friedman et al .1971; Petersen et al. 1994; Jones et al. 1997). The incorporation of pyruvate kinase in our model predicts higher rates of PC and PEPCK when compared to Williamson et al. since these authors neglected the presence of recycling in their calculations.

The computer simulation predicted a lower rate of TCA cycle than that reported in the experimental results from Williamson et al (1969) for either lactate or pyruvate perfusion; however, many uncertainties accompanied their method of TCA estimation, as admitted by the authors.

This enhanced version of the model of liver metabolism solidifies our ability to represent the interrelationship between the gluconoegenesis and lipid metabolism under different substrates and with varying concentrations by using a single set of parameters and reactions to simulate all these different conditions. More importantly the model gives a reliable source for estimating the redox ratio in the cytosolic and the mitochondrial compartment allowing for better estimation of dependent metabolic rates. While the model does not explicitly account for hormonal regulation, many of the regulated enzyme kinetic expressions account for regulation by cAMP, which is an indirect signal for insulin and glucagon effects. The model successfully represents the elegant and specific transport mechanisms of metabolites, reducing equivalents, and anions across the mitochondrial membrane which is deemed essential for mammalian metabolism. The model will allow us to explore the specific distribution of metabolites in the different compartments and bridge the gap in the experimental data. Moreover modeling these specific carriers will provide us a tool to predict the effect of transport of other metabolites or ions, such as those involved in calcium metabolism, which plays an important role in mitochondrial activities as an inhibitor and activator of PC and PDH, respectively. Also, the modeling of these carriers is important for modeling the interactions of various pharmaceutical agents with carbohydrate and lipid metabolism in the liver.

CHAPTER V

ETHANOL OXIDATION IN THE PERFUSED LIVER

5.1 Introduction

Fourteen million Americans meet the criteria for alcohol abuse and/or dependence (Kim et al. 2002) and over 90% of these suffer from some aspect of alcoholic liver disease (ALD) (Stickel et al. 2003). Ten thousand Americans die each year from ALD (Kim et al. 2002). The risk of being affected by ALD depends on a wide variety of factors and differs greatly between individuals, even when consuming similar amounts of alcohol. Genetic factors, gender, and the existence of hepatitis C are some of the factors that influence a patient's susceptibility to liver damage.

Dietary factors can influence the development and treatment of ALD. It has been shown that a high-fat, low-carbohydrate diet promotes liver damage in alcohol-fed rats (French et al.1995; Badger et al. 1998). In humans, high amounts of polyunsaturated fats positively correlated with development of cirrhosis in humans, while cholesterol and saturated fats were negatively correlated (Nanjii et al. 1986). Diets high in carbohydrates and protein and supplements of branched-chain amino acids have been shown to ameliorate ALD (Stickel et al. 2003).

Pharmaceutical agents such as metadoxine and S-adenosyl-l-methionine have shown success in treatment of ALD (Stickel et al. 2003). Therapeutic use of antibodies to eliminate inflammatory cytokines have resulted in decreased liver injury in rats. The suppression of endotoxins in alcohol-fed rats has reduced the signs of liver damage (Nanji et al. 1994; Adachi et al. 1995).

Alcohol consumption also affects the liver and other organs indirectly by interfering with the metabolism of various drugs, and thus decreasing their effectiveness and increasing the risk of side effects. The most common alcohol-medication interaction is with acetaminophen. Ethanol is known to activate the CYP2E1 enzyme which is responsible for transforming acetaminophen into toxic products which can lead to serious liver damage (Whitcomb 1998).

An *in silico* model of ethanol metabolism in the liver can provide a tool to test potential nutritional and pharmaceutical therapies for ALD, and to predict ethanol-related side effects of various drugs in the liver, thus accelerating research results and reducing costs for clinical trials. Moreover, this model can be modified to represent specific sub-population genotypes, leading to more personalized drug and dosage guidelines.

Ethanol is primarily metabolized in the liver by means of two separate pathways. The predominant pathway involves two enzymes: alcohol dehydrogenase (ADH) and acetaldehyde dehydrogenase (ALDH). ADH is expressed in high concentrations in the liver and is localized in the cytosol. The oxidation of ethanol by ADH results in the formation of acetaldehyde, a highly toxic and carcinogenic substance. The acetaldehyde is oxidized into a less active byproduct, acetate, by the mean of ALDH, which exists in both cytosolic and mitochondrial form. The majority of the acetaldehyde is oxidized by

the mitochondria ALDH. The second major pathway for ethanol metabolism is the microsomal ethanol oxidizing system (MEOS) which involves mainly the cytochrome P450 and CYP2E1. This pathway becomes more active in individuals with chronic alcohol consumption.

Individual variations in ADH and ALDH structures and rates of expression are significant, leading to variations among populations and individuals with regard to tolerance to alcohol (Pastino et al. 2000). Several ADH isoforms (ADH1A, ADH1B, AQDH1C, ADH5, ADH6, ADH7), with various Km's for ethanol, and two primary ALDH isoforms (ALDH1, ALDH2) exist in the liver (Ehrig et al. 1990).

Since the liver is the major organ for metabolizing alcohol, it is most vulnerable to damage from excessive alcohol consumption. The acute effects of ethanol metabolism are mainly the consequences of alterations in the $NADH/NAD^+$ ratio, resulting from the oxidation of ethanol and acetaldehyde by ADH and ALDH respectively. The fate of the cytosolic NADH is dependent on the capacity of the malate-aspartate shuttle or the glycerol-phosphate shuttle to convert the NADH back to NAD^+, which in turn is affected by the rate of the TCA cycle. The additional amount of mitochondrial NADH produced by ALDH reduces the TCA cycle activity. The increased amount of cytosolic NADH production affects the direction of lactate dehydrogenase, resulting in production of lactate, mainly by diverting pyruvate from gluconeogenesis, and leading to reduction in glucose production (Kreisberg 1967; Kreisberg et al. 1971).

Another consequence of ethanol-induced elevated $NADH/NAD^+$ is liver hypoxia, especially in the perivenous hepatocytes. Some of the NADH produced by mitochondrial ALDH is oxidized through the oxidative phosphorylation pathway, causing an increase in

the uptake rate of oxygen from the circulating blood in the pericentral region, and thus leading to hypoxia in the perivenous region. It has been found that the expression rates of certain genes are dependent on the redox state of the cell, where NAD^+ may act as sensor in up-regulating their level of expression. The NAD^+-regulated genes have been demonstrated to extend the life span of some organisms, and reduce the frequency of some diseases, notably diabetes, some cancers, and immune deficiencies (Bordone and Guarente 1995)

Liver diseases related to chronic alcohol consumption usually progress through three conditions: fatty liver syndrome, associated with fat deposits in the liver; alcoholic hepatitis, associated with the widespread inflammation and destruction of healthy liver tissues and replacement by scar tissue known as fibrosis; and alcoholic cirrhosis, the last and most fatal stage of liver disease. While the first two disorders can be reversed by stopping drinking, the latter is irreversible.

Fatty liver syndrome results from the redirection of AcCoA and glycerol 3-phosphate towards triglyceride synthesis. Acetaldehyde oxidation in the mitochondria leads to an increase in the level of acetyl-CoA, which is diverted to the fatty acid synthesis due to the NADH-inhibition of the TCA cycle. The reduction of cytosolic NAD^+, as a consequence of ethanol metabolism, leads to a reduction in glycerol-3 phosphate dehydrogenase activity, resulting in a greater amount of glycerol 3-phospahate being transformed into triglycerides. Acetaldehyde also interacts with specific proteins to form the so-called acetaldehyde-protein adducts. These adducts are recognized by the immune system as foreign bodies, resulting in a cascade of antibody production leading to prolonged inflammation and the destruction of hepatocytes.

Mathematical models of ethanol metabolism in the mammalian organism have primarily been restricted to simple pharmacokinetic models (Levitt and Levitt 2000) and physiological-based pharmacokinetic models (Pastino and Conolly 2000) of alcohol clearance in the organism. More recently, a physiologically-based multi-organ compartmental model has been developed which includes simplified kinetic expressions for ADH and ALDH (Umulis 2005). None of these models are capable of investigating the interactions of ethanol with carbohydrate and lipid metabolism in the liver.

Previous models presented in Chapters III and IV demonstrate the complex interplay between gluconoegenesis and lipid metabolism in the liver. The most recent model in Chapter IV considers cytosolic and mitochondrial compartmentation by including kinetics for the malate-aspartate shuttle, inter-compartmental transports, and a detailed citric acid cycle. The model successfully predicts the effects of various gluconeogenic precursors such as lactate and pyruvate in combination with fatty acids on the cytosolic and mitochondrial redox ratios. The model also predicts the directional movement of the complex malate-aspartate shuttle.

In the present chapter we present a model of ethanol metabolism in the fasted, perfused, rat liver, based on the model presented in Chapter IV. The production of the extra NADH by ethanol metabolism can significantly shift the redox state, resulting in changes in gluconeogenesis, ketogenesis, and citric acid cycle rates. The reactions representing the ethanol metabolism are based in part on an earlier model developed by Pande (2001). The model is then used to represent the *ex vivo* liver in a recirculated perfusion system. The model predicts the effects of ethanol in the liver perfused with either lactate or pyruvate, with and without oleate, on the redox ratio both in the cytosol

and the mitochondria. In addition, the model is used to predict the interrelationships between ethanol oxidation and pathways of gluconeogenesis, the citric acid cycle, and the shuttle mechanisms between cytosol and mitochondria. The simulations are compared to experimental data when available in the literature.

5.2 Model Development

The ethanol model is built upon the liver model presented in Chapter IV with the same set of kinetic parameters presented there, and using the general mass balance equations given by Eqns. 4.1-4.4. Figure 5.1 shows the metabolic pathway of ethanol in the liver and its interaction with the other metabolic pathways. Species abbreviations are defined in the caption of Fig. 5.1. The ethanol-related metabolic reactions (Table 5.1) and kinetic parameters (Table 5.2) were obtained from the literature from *in vitro* experiments. The reversibility of each reaction is indicated in Table 5.1. The effects of ethanol on the fasted rat liver, perfused with lactate, pyruvate and oleate in multiple scenarios as described in Table 5.3, were simulated. The set of differential equations were solved using ODE 45 in Matlab. No additional parameter tuning was performed. The initial conditions for the variables in Eqns. 4.1-4.3 are given in Table 4.3. Initial conditions for Eq. 4.4 are:

$$C_{i,perfusate}(0) = 0 \text{ for all species } i \qquad (5.1)$$

i.e. the saline pre-perfusion contains no substrate.

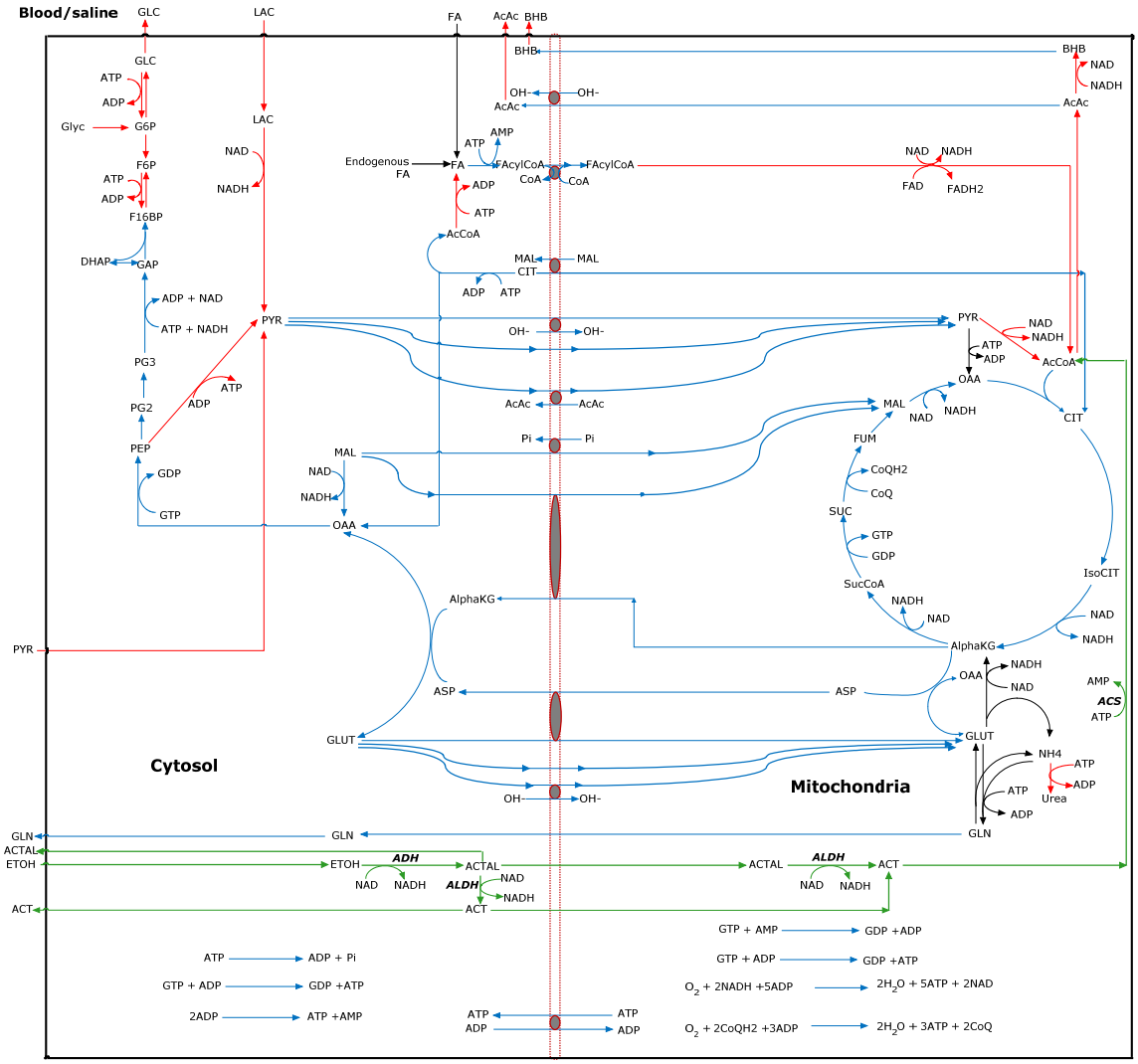

Fig. 5.1 Metabolic pathway of the liver including ethanol metabolism. Most transport and reaction fluxes are treated as reversible, but may be shown here as uni-directional to indicate the predominant direction. Tables 3.1, 4.1, and 5.1 indicate whether a reaction is treated as reversible or irreversible. Detailed stoichiometry and the kinetic expression for each reaction shown here are given in Tables 3.1, 4.1, and 5.1. To simplify notation, NAD^+ is written as NAD. Reactions in green are new to this chapter. Species abbreviations: ACTAL: acetaldehyde; ACT: acetate; AcAc: acetoacetate; AcCOA: acetyl CoA; ALA: alanine; AlphaKG: alpha-ketoglutarate; ASP: aspartate; BHB: β-hydroxybutyrate; CIT: citrate; ETOH: ethanol; FA: fatty acid; F6P: fructose-6-phosphate; F16BP: fructose 1,6 bisphosphate; FUM: fumarate; GLC: glucose; GLN: glutamine; GLR: glycerol; GAP: glyceraldehyde-3-phosphate; G6P: glucose-6-phosphate; GLUT: glutamate; Glyc: glycogen; GR3P: glycerol-3-phosphate; IsoCIT: isocitrate; LAC: lactate; MAL: malate; PYR: pyruvate; OAA: oxaloacetate; SucCoA: succinyl CoA; SUC: succinate. Reaction abbreviations: ADH: Alcohol dehydrogenase; ALDH: aldehyde dehydrogenase; ACS: acetyl CoA synthetase.

Table 5.1. Kinetic reactions for the ethanol model. Subscripts specify location of species or reaction; c: cytosol; m: mitochondria; b: blood; p: perfusate. Species name abbreviations are given in the caption to Fig. 5.1. The "→" indicates that the reaction is treated as irreversible, while "↔" indicates that the reaction is treated as reversible, with the flux reported with positive values in the left-to-right direction.

Alcohol dehydrogenase (ADH) ETOH_c + NAD_c ↔ ACTAL_c + NADH_c	$\frac{V_{\max,\_ADH\_f} V_{\max,\_ADH\_r} C_{ACTAL\_c}\left(C_{NADH\_c} C_{ETOH\_c} - \frac{C_{NADH\_total\_c} C_{ACTAL\_c}}{Keq_{ADH}}\right)}{K_{iNAD\_ADH} K_{ETOH\_ADH} + K_{ETOH\_ADH} C_{ATOH\_c} + C_{NADH\_c} C_{ETOH\_c} + \frac{K_{iNAD\_ADH} K_{ETOH\_ADH} K_{NAFH\_ADH\_c} C_{ACTAL\_c}}{K_{ACTAL\_ADH\_c} K_{iNADH\_ADH\_c}} + \frac{K_{iNAD\_ADH} K_{ETOH\_ADH} C_{NADH\_c}}{K_{iNADH\_ADH\_c}} + \frac{K_{iNAD\_ADH} K_{ETOH\_ADH} C_{NADH\_total\_c} C_{ACTAL\_c}}{K_{ACTAL\_ADH\_c} K_{iNADH\_ADH\_c}} + \frac{K_{NADH\_ADH} K_{ETOH\_ADH} C_{NADH\_c} C_{ACTAL\_c}}{K_{ACTAL\_ADH\_c} K_{iNADH\_ADH\_c}} + \frac{K_{NAD\_ADH} C_{NADH\_c} C_{ETOH\_c}}{K_{iNADH\_ADH\_c}} + \frac{K_{iNAD\_ADH} K_{ETOH\_ADH} C_{NADH\_c} C_{ETOH\_c}}{K_{i\_ADH\_c} K_{iNADH\_ADH\_c}} + \frac{K_{NAD\_ADH} C_{NADH\_c} [C_{ETOH\_c}][C_{ETOH\_c}]}{K_{i\_ADH\_c} K_{iNADH\_ADH\_c}} + \frac{C_{NAD\_c} [C_{ETOH\_c}][C_{ETOH\_c}]}{K_{i\_ADH\_c}}}$
Acetaldehyde dehydrogenase (ALDH_c) ACTAL_c + NAD_c → ACT_c + NADH_c	$\left(\frac{V_{\max,\_ALDH\_c} C_{ACTAL\_c}\left(C_{NADH\_total\_c} - C_{NADH\_c}\right)}{\left(K_{m\_ACTAL\_ALDH\_c} + C_{ACTAL\_c}\right)\left(K_{m\_nad\_ALDH\_c} + \left(C_{NADH\_total\_c} - C_{NADH\_c}\right)\right)}\right)$

ACTAL c↔b ACTAL_c ↔ ACTAL_b	$\left(\frac{V_{\max,\_b\_t\_ACT}\left(C_{ACTAL\_c}-C_{ACTAL\_b}\right)}{\left(K_{m\_b\_t\_ACT}+C_{ACTAL\_c}+C_{ACTAL\_b}\right)}\right)$
Acetaldehyde dehydrogenase, mitochondrial (ALDH_m) ACTAL_m + NAD_m → ACT_m + NADH_m	$\left(\frac{V_{\max,\_ALDH\_m}\ C_{ACTAL\_m}\left(C_{NADH\_total\_m}-C_{NADH\_m}\right)}{\left(K_{m\_ACTAL\_ALDH\_m}+C_{ACTAL\_m}\right)\left(K_{m\_nad\_ALDH\_m}+\left(C_{NADH\_total\_m}-C_{NADH\_m}\right)\right)}\right)$
Acetyl CoA synthetase (ACS) ACT_m + ATP_m + CoA_m → AcCoA_m + AMP_m + 2 pi_m	$\left(\frac{V_{\max,\_ACS}\left(C_{ACT\_m}C_{ATP\_m}\right)}{\left(K_{m\_ACS}+C_{ACT\_m}+C_{ATP\_m}\right)}\right)$
ACTAL p↔b 0.0104 ACTAL_p ↔ ACTAL_b	$\left(\frac{F\left(C_{ACTAL\_p}-C_{ACTAL\_b}\right)}{\left(Volume\_simusoid\_comp*Sinusoid\_no\right)}\right)$
ACTAL_c ↔ ACTAL_m	$\left(\frac{V_{\max,\_c\_m\_ACTAL}\left(C_{ACTAL\_c}-C_{ACTAL\_m}\right)}{\left(K_{m\_c\_m\_ACTAL}+C_{ACTAL\_m}+C_{ACTAL\_c}\right)}\right)$
ETOH_b ↔ ETOH_c	$\left(\frac{V_{\max,\_b\_t\_ETOH}\left(C_{ETOH\_b}-C_{ETOH\_c}\right)}{\left(K_{m\_b\_t\_ETOH}+C_{ETOH\_b}+C_{ETOH\_c}\right)}\right)$
ACT_c ↔ ACT_b	$\left(\frac{V_{\max,\_b\_t\_ACT}\left(C_{ACT\_c}-C_{ACT\_b}\right)}{\left(K_{m\_b\_t\_ACT}+C_{ACT\_b}+C_{ACT\_c}\right)}\right)$
ACT_c ↔ ACT_m	$\left(\frac{V_{\max,\_c\_m\_ACT}\left(C_{ACT\_c}-C_{ACT\_m}\right)}{\left(K_{m\_c\_m\_ACT}+C_{ACT\_b}+C_{ACT\_m}\right)}\right)$
ETOH_p ↔ETOH_b	$\left(\frac{F\left(C_{ETOH\_p}-C_{ETOH\_b}\right)}{\left(Volume\_simusoid\_comp*Sinusoid\_no\right)}\right)$
ACT_p ↔ ACT_b	$\left(\frac{F\left(C_{ACT\_p}-C_{ACT\_b}\right)}{\left(Volume\_simusoid\_comp*Sinusoid\_no\right)}\right)$

Table 5.2 Kinetic parameters used in the ethanol model.

Kinetic parametrs	Kinetic values	Units	Source
Vmax_b_c_ETOH	6.14286	mM/min	From *in vivo* study (Huang et al. 1993)
Km_b_c_ETOH	0.142857	mM	Assumed based on expected ethanol concentration *in vivo*
Vmax_b_c_ACT	5.77143	mM/min	From *in vivo* study (Huang et al. 1993)
Km_b_c_ACT	0.142857	mM	Assumed based on expected ethanol concentration *in vivo*
Vmax_c_m_ACT	5.77143	mM/min	From *in vivo* study (Huang et al. 1993)
Km_c_m_ACT	0.142857	mM	Assumed based on expected ethanol concentration *in vivo*
Vmax_c_m_ACTAL	5.77143	mM/min	From *in vivo* study (Huang et al. 1993)
Km_c_m_ACTAL	0.142857	mM	Assumed based on expected ethanol concentration *in vivo*
Vmax_ACS	5.4	mM/min	Reich and Selkov, 1981
Km_ACS	0.15	mM	Assumed based on expected ethanol concentration *in vivo*
Vmax_ADH_f	9.58571	mM/min	Crabb et al. 1983
Vmax_ADH_r	48.0286	mM/min	
Km_ETOH_ADH	0.685714	mM	
Km_nad_ADH	0.0471429	mM	
Km_ACTAL_ADH	0.0528571	mM	
Km_nadh_ADH	0.00571429	mM	
Ki_ETOH_ADH	1.15714	mM	
Ki_nad_ADH	0.0828571	mM	
Ki_ACTAL_ADH	0.0171429	mM	
Ki_nadh_ADH	0.00128571	mM	
Ki_ADH	242.857	mM	
Keq_ADH	0.0003		Reich and Selkov, 1981
Vmax_ALDH	72.1088	mM/min	Svanas and Weiner, 1985
Km_ACTAL_ALDH	0.00462585	mM	
Km_nad_ALDH	0.126259	mM	
Vmax_ALDH_c	1.5028	mM/min	Svanas and Weiner, 1985
Km_ACTAL_ALDH_c	0.00462585	mM	
Km_nad_ALDH_c	0.126259	mM	

Table 5.3. Input functions used in simulations of the perfused liver. ($R_{FA\text{-}endo}$=rate of endogenous fatty acid oxidation, normalized to µmol C_{16} (palmitate); $J^{*}_{FA\text{-}b\text{-}t}$ = the sum of the uptake rate of FA and rate of endogenous fatty acid oxidation).

Lactate Perfusion		
Saline pre-perfusion; $0 < t \leq 30$	Lactate infusion; $30 < t \leq 120$	Lactate + Ethanol; $90 < t \leq 120$
$R_{FA\text{-}endo} = 0.15$ µmol(Lcyt water)$^{-1}$min^{-1}, assumed to be equal to experimental measurements of ketone production during this period[26].	$R_{FA\text{-}endo} = 0.08178$ µmol(Lcyt water)$^{-1}$min^{-1}, as estimated[26] from ketone production. $C_{LAC,,perfusate}$ = 10(1-exp(-(t-30)/τ) mM (constant LAC concentration of 10 mM in perfusate); τ is time constant for achieving change in susbstrate concentration, set to 4 min.	$R_{FA\text{-}endo} = 0.08178$ µmol(Lcyt water)$^{-1}$min^{-1}, as estimated[26] from ketone production. $C_{ETOH,,perfusate}$ = 10(1-exp(-(t-90)/τ) mM (constant ETOH concentration of 10 mM in perfusate); τ is time constant for achieving change in susbstrate concentration, set to 4 min. $C_{LAC,,perfusate}$ =10 mM
Pyruvate Perfusion		
Saline pre-perfusion; $0 < t \leq 30$	Pyruvate infusion; $30 < t \leq 120$	Pyruvate + Ethanol $90 < t \leq 120$
$R_{FA\text{-}endo} = 0.15$ µmol(Lcyt water)$^{-1}$min^{-1}	$R_{FA\text{-}endo}$ =0.08178 µmol(Lcyt water)$^{-1}$min^{-1} $C_{PYR,,perfusate}$ = 2(1-exp(-(t-30)/ τ) mM (constant PYR concentration of 2 mM in perfusate); τ=3 min. $C_{LAC,,perfusate}$ calculated from Eqn. 4.3.	$R_{FA\text{-}endo} = 0.08178$ µmol(Lcyt water)$^{-1}$min^{-1}, as estimated[26] from ketone production. $C_{ETOH,,perfusate}$ = 10(1-exp(-(t-90)/τ) mM (constant ETOH concentration of 10 mM in perfusate); τ is time constant for achieving change in susbstrate concentration, set to 4 min. $C_{PYR,,perfusate}$ =2 mM

Table 5.4 Input functions used in simulation of the perfused liver, with fatty acids. ($R_{FA\text{-}endo}$=rate of endogenous fatty acid oxidation, normalized to µmol C_{16} (palmitate); $J^*_{FA\text{-}b\text{-}t}$ = the sum of the uptake rate of FFA and rate of endogenous fatty acid oxidation).

Lactate + Fatty Acid Perfusion			
Saline pre-perfusion; $0 < t \leq 30$	Lactate infusion; $30 < t \leq 60$	Lactate + FA $60 < t \leq 120$	Lactate + FA+ Ethanol; $90 < t \leq 120$
$R_{FA\text{-}endo} = 0.15$ µmol(Lcyt water)$^{-1}$min^{-1}, assumed to be equal to experimental measurements of ketone production during this period[26].	$R_{FA\text{-}endo} = 0.08178$ µmol(Lcyt water)$^{-1}$min^{-1}, as estimated[26] from ketone production. $C_{LAC,,perfusate}$ = 10(1-exp(-(t-30)/τ) mM (constant LAC concentration of 10 mM in perfusate); τ is time constant for achieving change in susbstrate concentration, set to 4 min.	$J^*_{FA\text{-}b\text{-}t}$= 0.08178+0.466(1-exp(-(t-60) /τ), τ=2.5 min; total rate of 0.5874 µmol(Lcyt water)$^{-1}$min^{-1}determined from experimental measurements of oleate infusion[26]. $C_{LAC,,perfusate}$ =10 mM	$R_{FA\text{-}endo} = 0.08178$ µmol(Lcyt water)$^{-1}$min^{-1}, as estimated[26] from ketone production. $C_{ETOH,,perfusate}$ = 10(1-exp(-(t-90)/τ) mM (constant ETOH concentration of 10 mM in perfusate); τ is time constant for achieving change in susbstrate concentration, set to 4 min. $C_{LAC,,perfusate}$ =10 mM
Pyruvate + Fatty Acid Perfusion			
Saline pre-perfusion; $0 < t \leq 30$	Pyruvate infusion; $30 < t \leq 60$	Pyruvate + FA $60 < t \leq 120$	Pyruvate + FA+ Ethanol ; $90 < t \leq 120$
$R_{FA\text{-}endo} = 0.15$ µmol(Lcyt water)$^{-1}$min^{-1}	$R_{FA\text{-}endo}$ =0.08178 µmol(Lcyt water)$^{-1}$min^{-1} $C_{PYR,,perfusate}$ = 2(1-exp(-(t-30)/ τ) mM (constant PYR concentration of 2 mM in perfusate); τ=3 min. $C_{LAC,,perfusate}$ calculated from Eqn. 4.3.	$J^*_{FA\text{-}b\text{-}t}$= 0.08178+0.466(1-exp(-(t-60) /τ), τ=2.5 min; total rate of 0.5874 µmol(Lcyt water)$^{-1}$min^{-1}determined from experimental measurements of oleate infusion[26]. $C_{pyr,,perfusate}$ =2 mM	$R_{FA\text{-}endo} = 0.08178$ µmol(Lcyt water)$^{-1}$min^{-1}, as estimated[26] from ketone production. $C_{ETOH,,perfusate}$ = 10(1-exp(-(t-90)/τ) mM (constant ETOH concentration of 10 mM in perfusate); τ is time constant for achieving change in susbstrate concentration, set to 4 min. $C_{PYR,,perfusate}$ =2 mM

5.3 Results

5.3.1 Lactate Perfusions

Figs. 5.2-3 show the results from the simulation of 10 mM lactate perfusion with subsequent addition of 10 mM ethanol at 90 minutes (Table 5.3). The addition of ethanol causes 6-fold increases in both cytosolic and mitochondrial redox ratios (Fig. 5.2), due to increased supply of NADH by the oxidation of ethanol through ADH and oxidation of acetaldehyde by ALDH. A high cytosolic redox ratio is expected to drive the transfer of reducing equivalents to the mitochondria through various mechanisms, of which the malate-aspartate cycle is hypothesized to be the main mechanism. The first step in this process is seen with the increase in the rate of conversion of OAA to malate in the cytosol (MDH reaction, Fig. 5.2), driven by the high cytosolic redox ratio. This surplus in cytosolic malate drives its transport into the mitochondria, causing a 4-fold increase in the forward flux of mitrochondrial MDH.

Fig. 5.2 shows that ethanol perfusion causes an approximate seven-fold increase in net malate transport from cytosol to mitochondria, correlating well with the increase in the cytosolic redox ratio. Inter-compartmental transport of malate can be accomplished via three transporters: MAL:AlphaKG (as part of the malate-aspartate shuttle), MAL:Pi, and MAL:CIT. Fig. 5.2 shows that the transporters MAL:AlphaKG and MAL:Pi have different directions, with MAL:AlphaKG predominating, while the flux through MAL:CIT is very low. This is accompanied by two-fold increase in the concentration of malate in both compartments (not shown). Thus the net malate transport into the mitochondria is responsible for the transport of reducing equivalents from the cytosol to the mitochondria, with the carbon returned to the cytosol in the form of AlphaKG. The

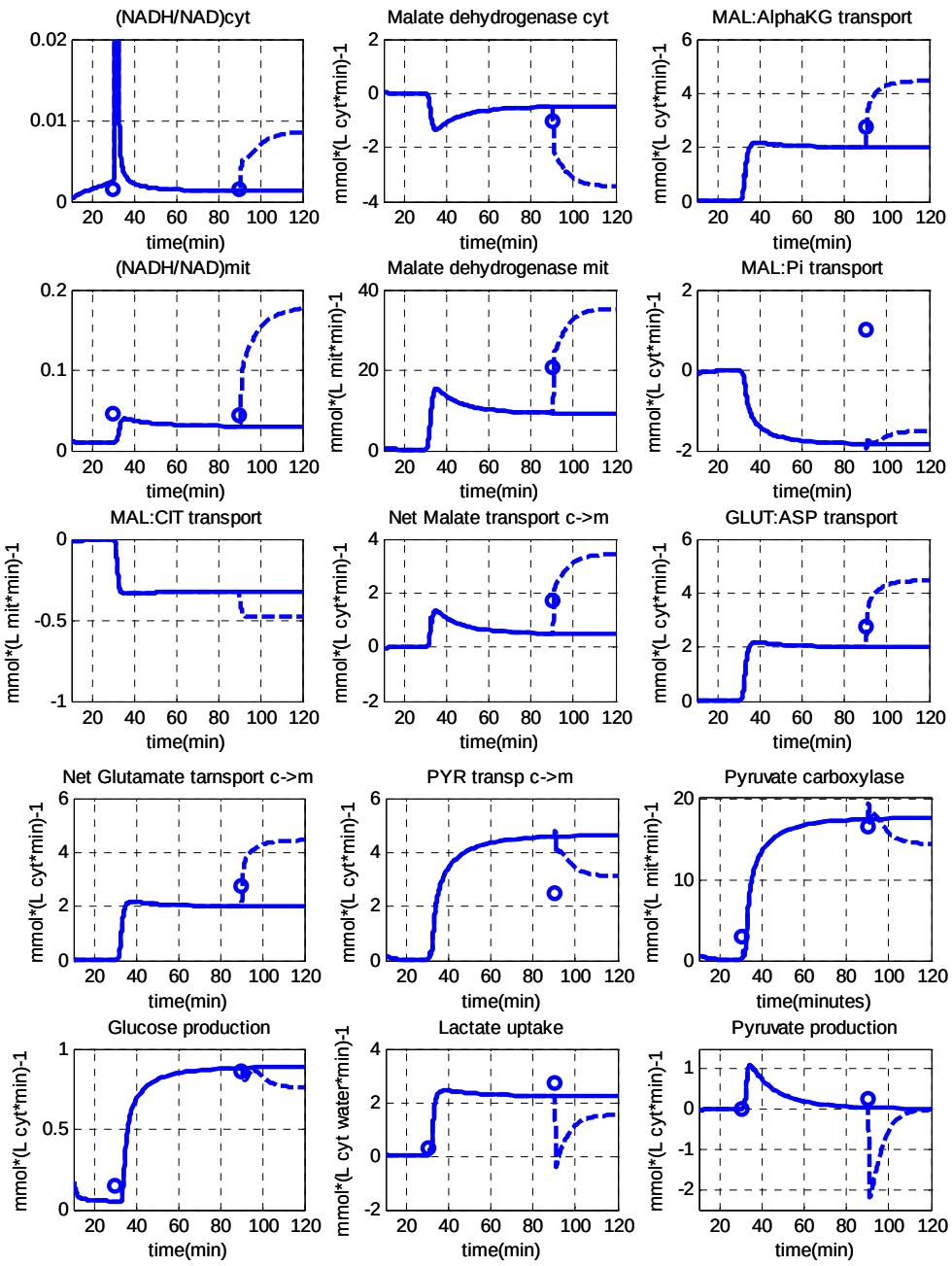

Figure 5.2. Redox ratios and fluxes calculated from perfusion model with lactate, and lactate + ethanol as substrates. Initial conditions represent the *in vivo* 24-hour fasted state. Symbols are experimental data from perfused fasted livers, from Williamson, et al. 1969b, using a perfusion medium of Krebs-Henseleit bicarbonate buffer, with 4% bovine serum albumin, in a recirculated system. Lines are simulations, using Eqns. 4.1-4, with $F_{perfusate}$=50 ml/min and $V_{perfusate}$=100 ml (corresponding to the experimental protocol), and all other parameters as given in Tables 4.2 and 5.2. Solid lines: $10 < t \leq 30$ min: saline pre-perfusion (no substrate); $30 < t \leq 120$ min: 10 mM lactate perfusion. Dashed lines: $90 < t \leq 120$ min: 10 mM lactate plus 10 mM ethanol perfusion. To view details of the lactate and ethanol perfusions, the x-axis scale was started at 10 min. Net malate transport and net glutamate transport are each calculated from the sum of their three respective transporters.

other part of the MAL-ASP cycle, the glutamate-aspartate exchange, increases over two-fold (Fig. 5.2) in response to ethanol. These simulations indicate the important role of the malate-aspartate cycle during ethanol metabolism and are corroborated qualitatively by experimental observations from various researchers (Williamson et al. 1974a, 1974b; Meijer et al. 1975a), whose studies revealed an increase in ethanol uptake by isolated liver cells from starved rats upon addition of external MAL and alphaKG. Moreover the use of aminooxyacetate, an inhibitor of the malate-aspartate cycle, inhibited the increase in ethanol uptake, showing a clear relationship between the malate-aspartate cycle and ethanol oxidation.

Other than the rate of transfer of reducing equivalents, the simulations show, in general, that ethanol decreases the metabolic rates of the liver. Ethanol causes a 32% reduction in the rate of pyruvate transport to the mitochondria (Fig. 5.2) with a simultaneous reduction of the mitochondrial pyruvate concentration (data not shown). Ethanol reduces the TCA cycle flux by 41% (as measured by IDH, Fig. 5.3), gluconeogenesis by 15 % (as measured by glucose production, Fig. 5.2), and lactate uptake and oxidation by 33% (Fig. 5.2). Conversely, the rate of ketogenesis is stimulated by the addition of ethanol (Fig. 5.3), due to the increase in the AcCoA production from acetate.

The rate of ethanol uptake by the liver is predicted by the model to be 2.2 μmol (L cyt water)$^{-1}$ min^{-1} at 10 mM ethanol and 10 mM lactate (Fig. 5.3), which agrees well with the maximum rate of ethanol utilization of 3.5 μmol (L cyt water)$^{-1}$ min^{-1} found at ethanol concentrations above 2 mM in fed rats but with no added lactate (Lindros et al. 1972).

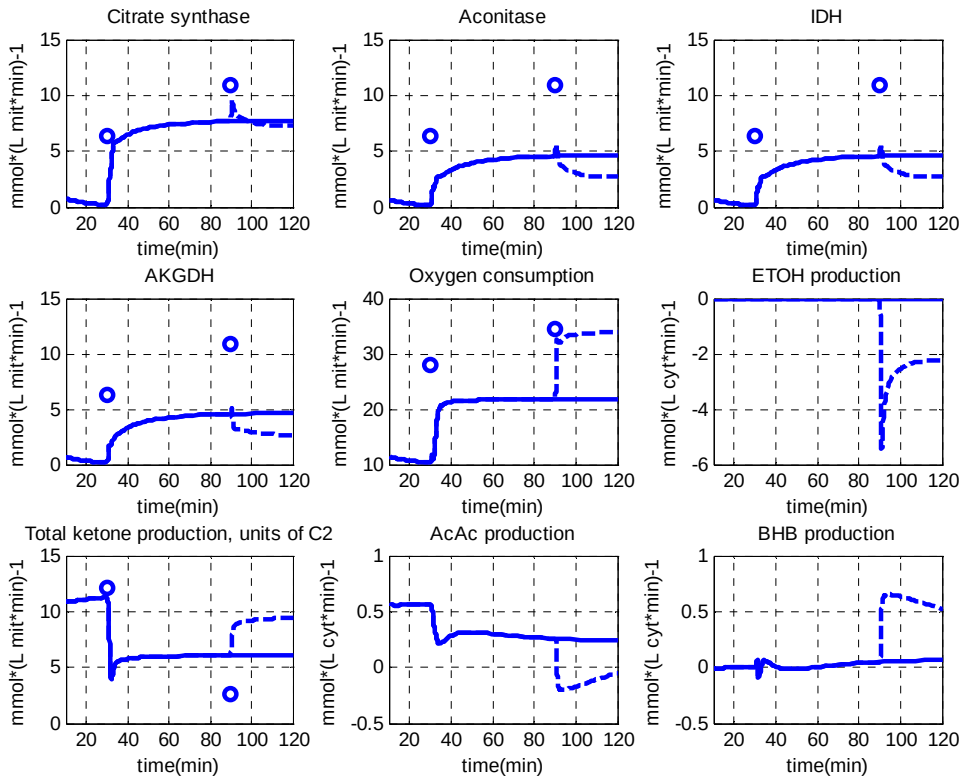

Figure 5.3. Metabolic fluxes calculated from perfusion model with lactate, and lactate + ethanol as substrates. Simulation and experimental details are the same as in Fig. 5.2.

The results from the addition of ethanol to perfusion medium containing both oleate and lactate are shown in Figs. 5.4-5, with simulation conditions described in Table 5.4. The simulated results indicate a 6- and 4-fold increase in the cytoplasmic and the mitochondrial redox ratios, respectively, upon addition of ethanol to the lactate-oleate mixture (Fig. 5.4). Inhibition of gluconeogenesis by ethanol is much more pronounced in the presence of oleate, with 50% reduction (Fig. 5.4), compared to 20% reduction in the absence of oleate (Fig. 5.2).

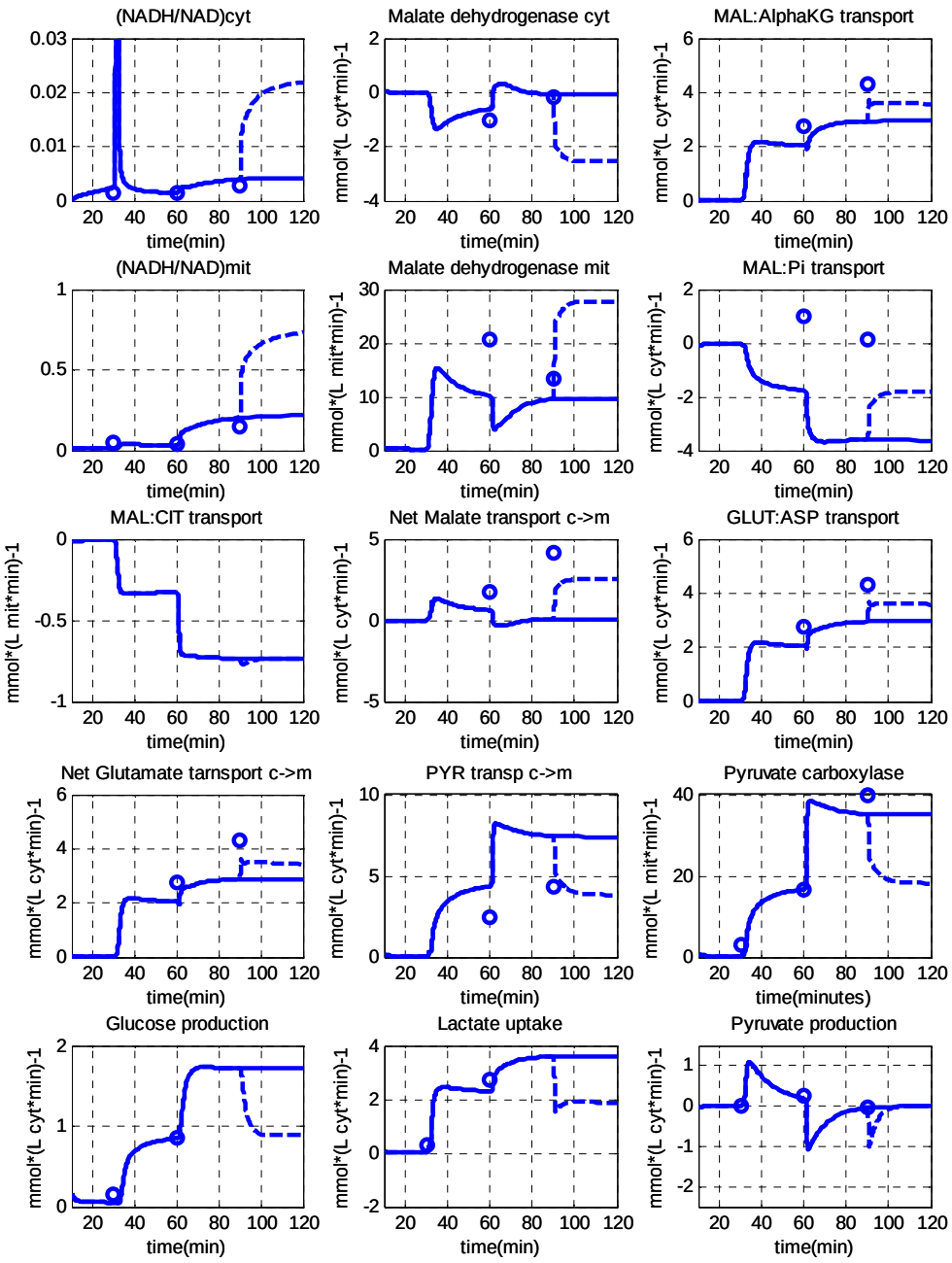

Figure 5.4 Redox ratio ($NADH/NAD^+$) and fluxes calculated from perfusion model with lactate, lactate + oleate, and lactate + oleate + ethanol as substrates. Initial conditions represent the *in vivo* 24-hour fasted state. Symbols are experimental data from perfused fasted livers, from Williamson, et al. 1969b, using a perfusion medium of Krebs-Henseleit bicarbonate buffer, with 4% bovine serum albumin, in a recirculated system: preperfusion with no substrate; and perfusion with 10 mM lactate and 1.5 mM oleate respectively. Solid and dashed lines are simulations, using Eqns. 4.1- 4, with $F_{perfusate}$=50 ml/min and $V_{perfusate}$=100 ml (corresponding to the experimental protocol), and all other parameters as given in Tables 4.1 and 5.2. Solid lines: $10 < t \leq 30$ min: saline pre-perfusion (no substrate); $30 < t \leq 60$ min: 10 mM lactate; $60 < t \leq 120$ min: 10 mM lactate and 1.5 mM oleate perfusion. Dashed lines: $90 < t \leq 120$ min: 10 mM lactate, 1.5 mM oleate and 10 mM ethanol perfusion. Details given in Table 5.4.

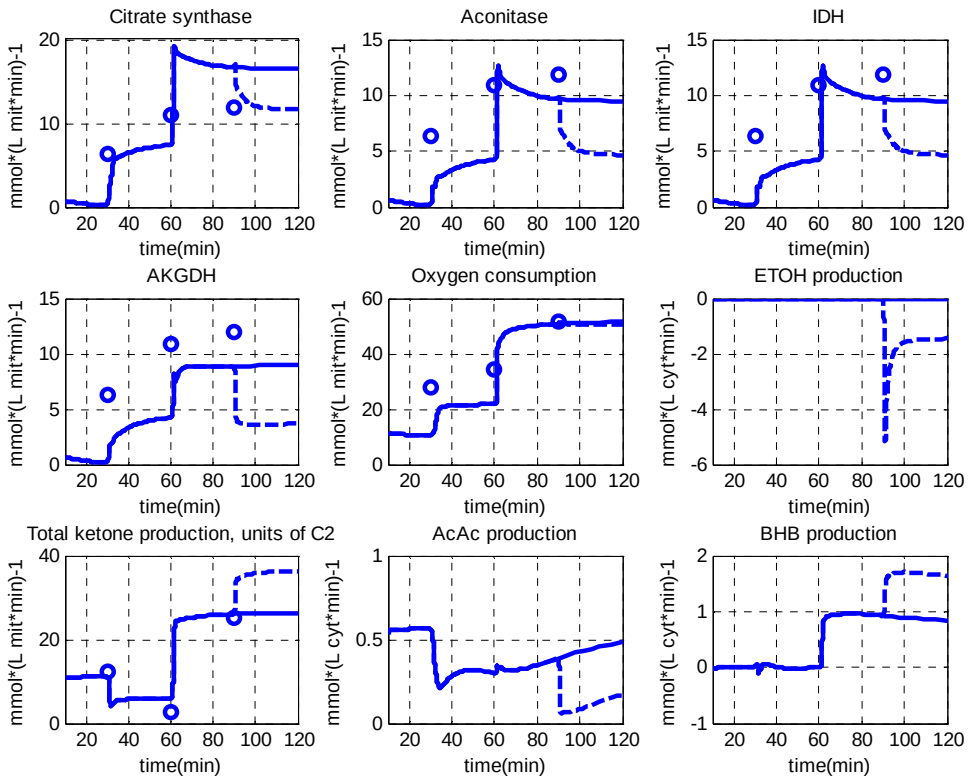

Figure 5.5. Rates of TCA cycle, oxygen consumption, ethanol production (-uptake), and ketone production calculated from perfusion model with lactate, lactate + oleate, and lactate + oleate + ethanol as substrates respectively. Simulation and experimental details are the same as in Fig. 5.4.

5.3.2 Pyruvate Perfusions

The effect of ethanol on pyruvate metabolism was examined using the same model with the same set of kinetic parameters as described above, with initial conditions and inputs described in Table 5.3. As expected, the addition of 2 mM ethanol to the pyruvate perfusion significantly increases both cytosolic and mitochondrial redox ratios (Fig. 5.6). In contrast with the results from lactate perfusion, gluconoegenesis from pyruvate is not inhibited by ethanol addition (Fig. 5.6); on the contrary, significant stimulation of glucose production is observed. This is corroborated by Williamson et al. (1969c) who observed that ethanol stimulated gluconeogenesis

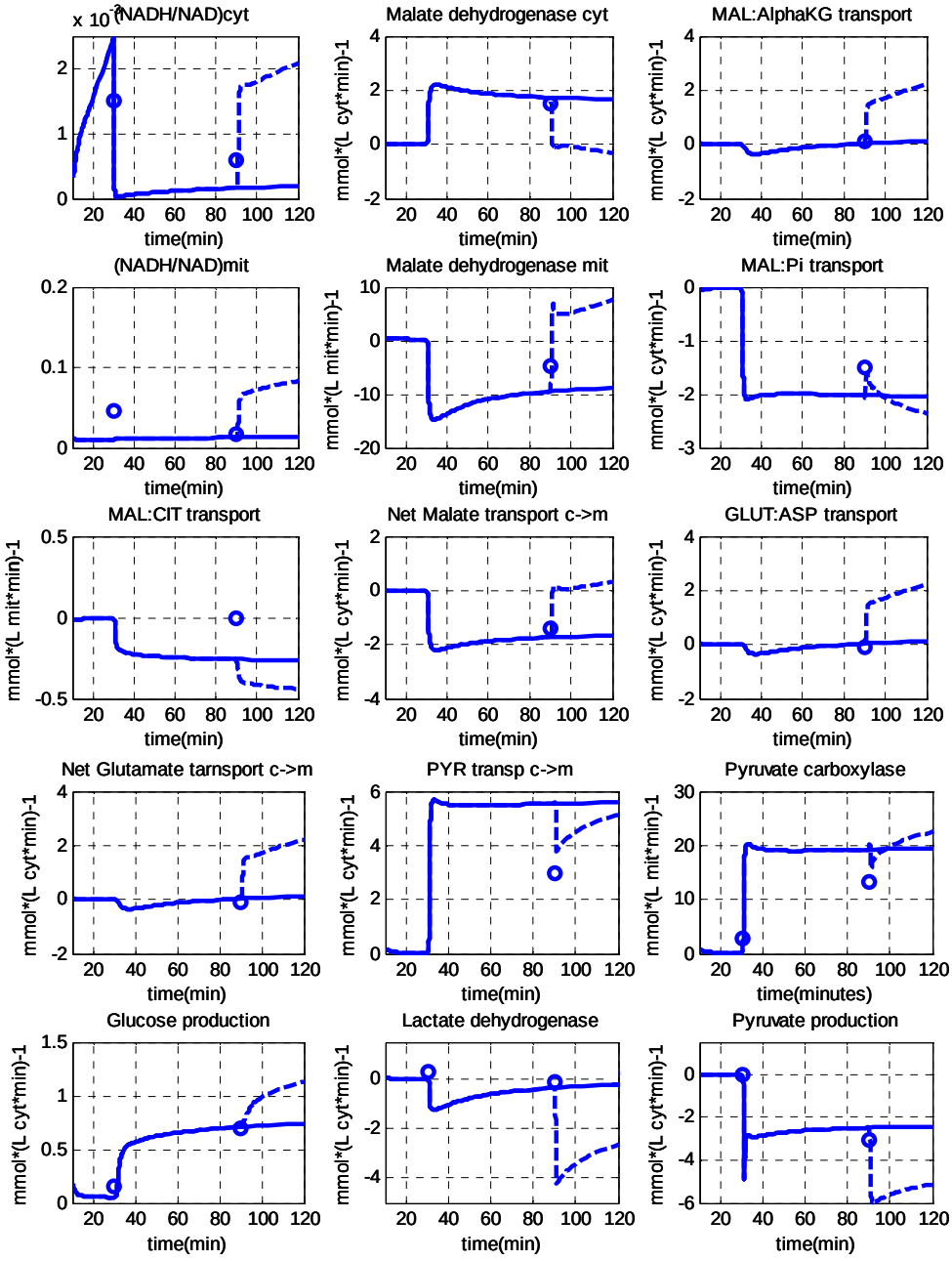

Figure 5.6. Redox ratio (NADH/NAD$^+$) and fluxes calculated from perfusion model with pyruvate, and pyruvate + ethanol as substrates. Initial conditions represent the *in vivo* 24-hour fasted state. Symbols are experimental data from perfused fasted livers, from Williamson, et al.1970a, using a perfusion medium of Krebs-Henseleit bicarbonate buffer, with 4% bovine serum albumin, in a recirculated system; open circle-0: Preperfusion with no substrate; and perfusion with 2 mM pyruvate respectively. Solid and dashed lines are simulations, using Eqns. 4.1-4, with $F_{perfusate}$=50 ml/min and $V_{perfusate}$=100 ml (corresponding to the experimental protocol), and all other parameters as given in Tables 4.1 and 5.2. Solid lines: $10 < t \leq 30$ min: saline pre-perfusion (no substrate); $30 < t \leq 120$ min: 2 mM pyruvate perfusion. Dashed lines: $90 < t \leq 120$ min: 2 mM pyruvate plus 10 mM ethanol perfusion. Details given in Table 5.3. In order to view the details of the pyruvate and ethanol perfusion, the x-axis scale was started at 10 min.

when alanine (which produces pyruvate via alanine aminotransferase) was the substrate. The extra cytosolic NADH produced by ethanol oxidation is used to drive the reduction of pyruvate to lactate by mean of LDH, as shown in Fig. 5.6.

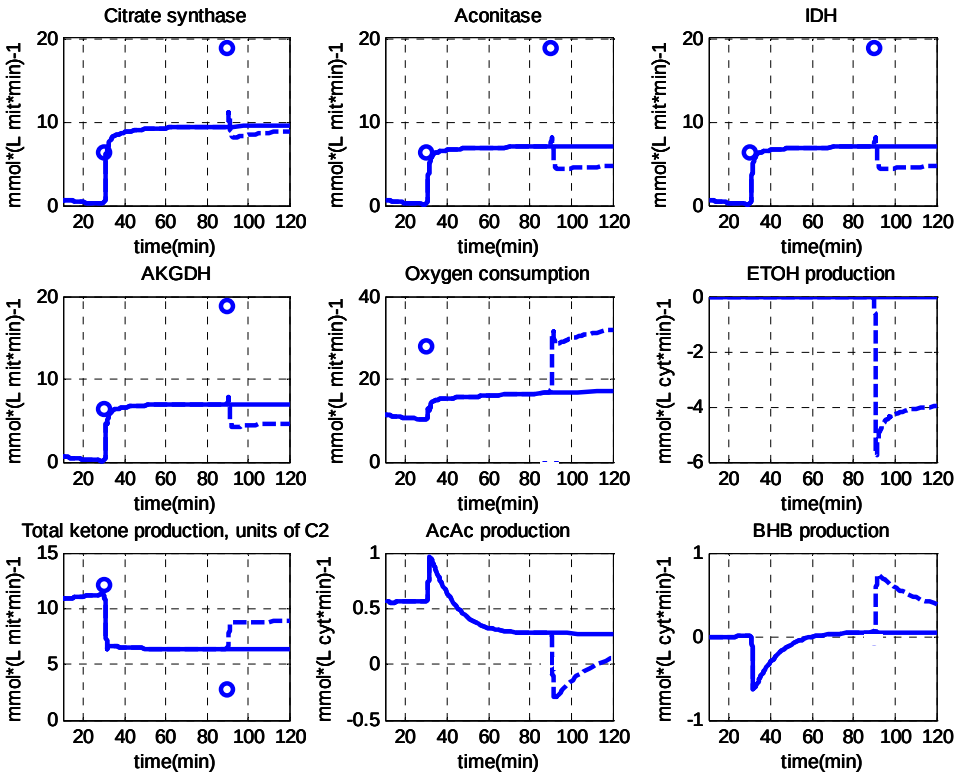

Fig. 5.7. TCA cycle fluxes, oxygen uptake, ethanol uptake (-production), and ketogenesis, calculated from perfusion model with pyruvate, and pyruvate + ethanol as substrates. Simulation and experimental details are the same as in Fig. 5.6.

The effects of ethanol after prior addition of oleate to pyruvate are illustrated in Figs 5.8-9. In contrast with lactate perfusion, pyruvate perfusion causes a net efflux of MAL out of the mitochondria (Fig. 5.8). Ethanol oxidation causes a further increase in the cytoplasmic and mitochondrial redox ratios, which significantly reduces the MAL efflux.

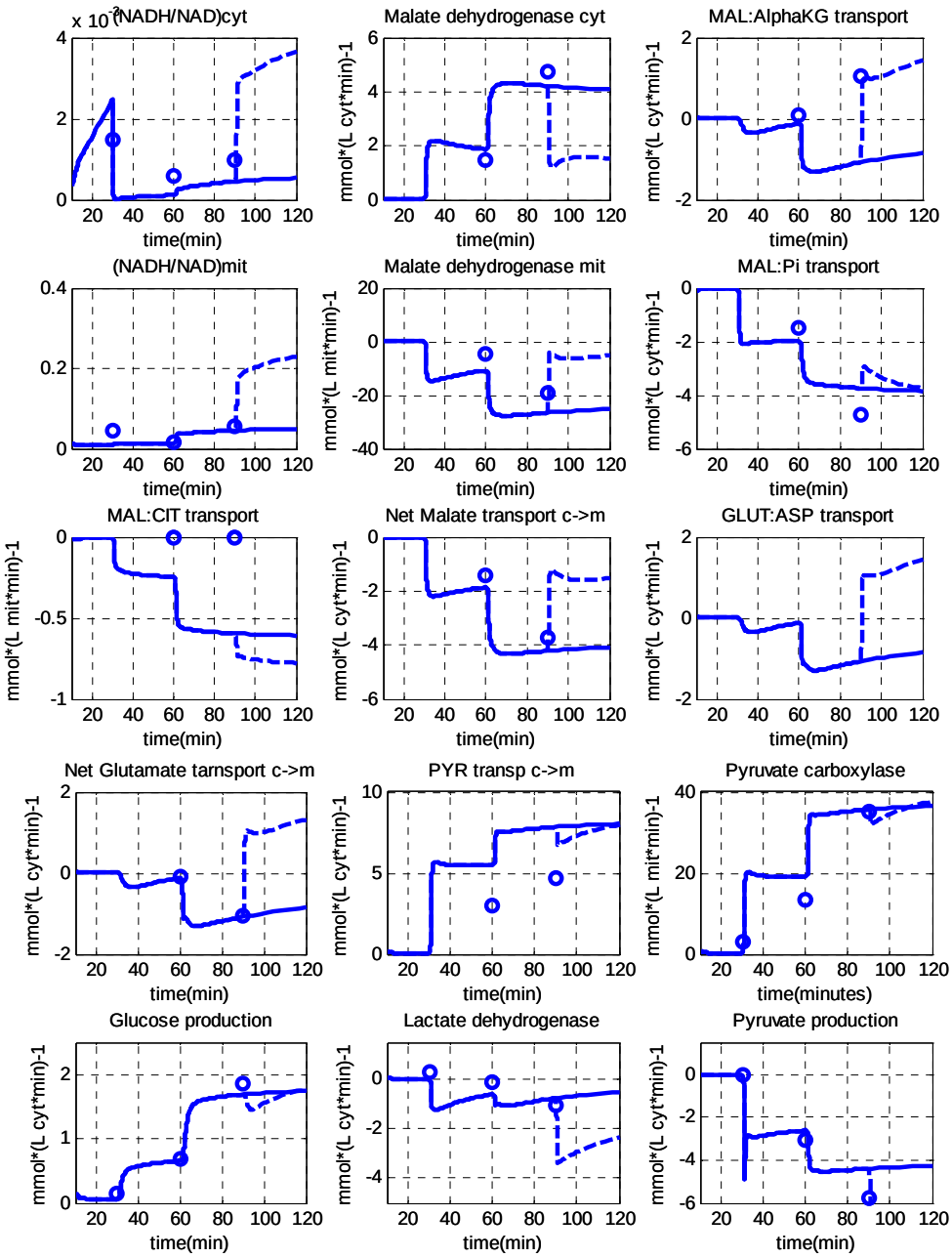

Figure 5.8. Redox ratio (NADH/NAD), intercompartmental fluxes, and gluconeogenesis rates calculated from perfusion model with pyruvate, pyruvate + oleate, and pyruvate + oleate + ethanol as substrates respectively. Initial conditions represent the *in vivo* 24-hour fasted state. Symbols are experimental data from perfused fasted livers, from Williamson, et al. 1970a, using a perfusion medium of Krebs-Henseleit bicarbonate buffer, with 4% bovine serum albumin, in a recirculated system; open circle-0: Preperfusion with no substrate; and perfusion with 2 mM pyruvate and 1.5 mM oleate respectively. Solid and dashed lines are simulations, using Eqns. 1,3 and 4, with $F_{perfusate}$=50 ml/min and $V_{perfusate}$=100 ml (corresponding to the experimental protocol), and all other parameters as given in Tables 4.1. Solid lines: $10 < t \leq 30$ min: saline pre-perfusion (no substrate); $30 < t \leq 120$ min: 2 mM pyruvate and 1.5 mM oleate perfusion. Dashed lines: $90 < t \leq 120$ min: 2 mM pyruvate, 1.5 mM oleate and 10 mM ethanol perfusion. Details given in Table 5.3. In order to view the details of the pyruvate and ethanol perfusion, the x-axis scale was started at 10 min.

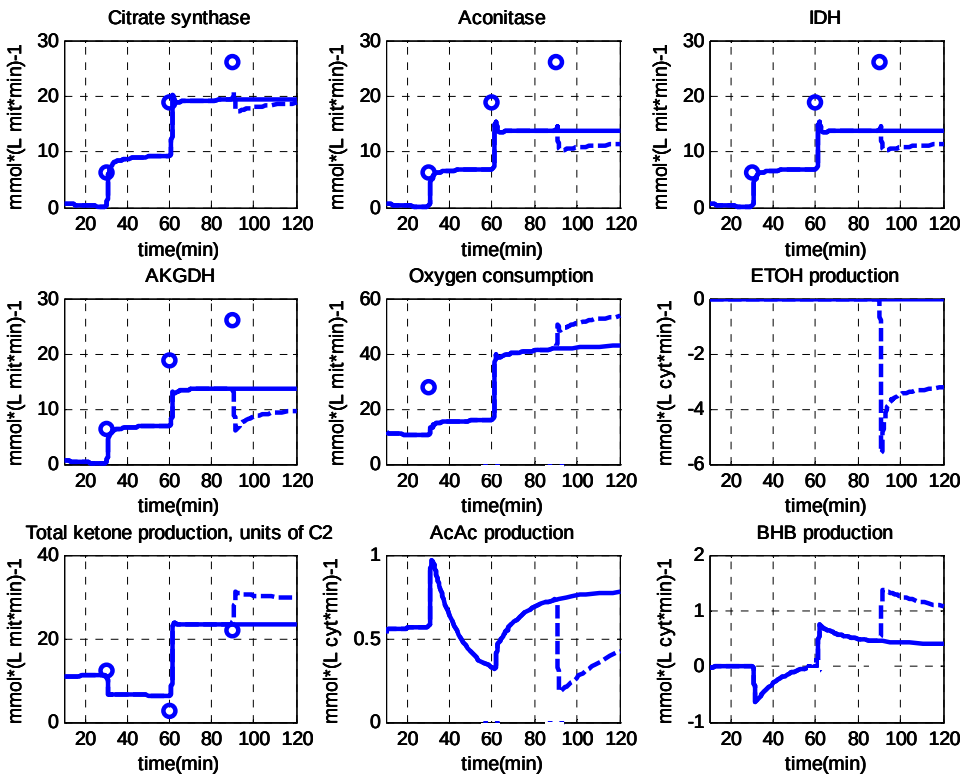

Fig. 5.9. TCA cycle fluxes, oxygen uptake, ethanol production (-uptake), and ketogenesis, calculated from calculated from perfusion model with pyruvate, pyruvate + oleate, and pyruvate + oleate + ethanol as substrates. Simulation and experimental details are the same as in Fig. 5.8.

Simulations using near-physiological pyruvate concentration of 0.1 mM in combination with oleate are shown in Fig. 5.10. Ethanol increases the rate of pyruvate reduction to lactate (in LDH) and thus decreases glucose production. As expected, the rate of ketogenesis (Fig. 5.10) is further increased by the expected increase in the mitochondrial redox ratio (not shown).

The model was further validated with dynamic data in which fasted rat livers were perfused with 2.5 mM lactate and 10 mM ethanol in a non-recirculated perfusion system (Lopez et al. 2009). Using the same parameters as in all the previous results, the model underestimates both glucose production and the ethanol-induced inhibition of glucose production (Fig. 5.11A). However, when the rate of endogenous fatty acid oxidation is

increased from 0.085 to 0.15 micromol/(L cyt water*min), the steady state and dynamic glucose production agrees more closely with the experimental data (Fig. 5.11B). The rate of inhibition of glucose production by ethanol is predicted to be 41%, compared to measured inhibition of 60%. The larger FA rate also increases the BHB production rate, to better match the data, especially during ethanol perfusion. Since endogenous FA oxidation is not directly measurable, and can vary depending on the state of the liver, it can be considered an adjustable parameter that closely correlates with ketone production. The dynamic responses to ethanol of AcAc and BHB production correspond well with the experimental data, with an increase of BHB production and a decrease in AcAc formation.

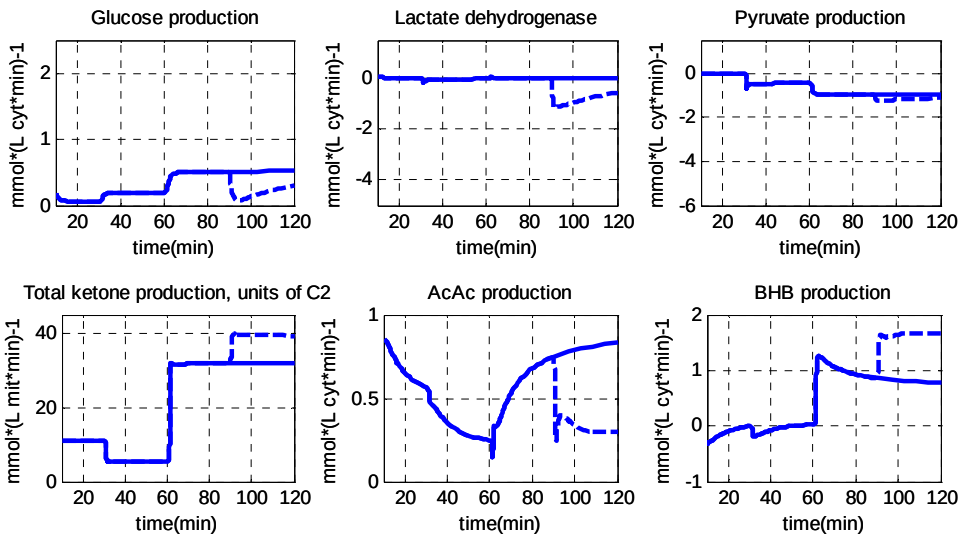

Figure 5.10. Fluxes calculated from perfusion model with near physiological level of pyruvate (0.1 mM), pyruvate + oleate, and pyruvate +oleate+ ethanol as substrates, respectively. Initial conditions represent the *in vivo* 24-hour fasted state. Solid and dashed lines are simulations, using Eqns. 5.1,3 and 4, with $F_{perfusate}$=50 ml/min and $V_{perfusate}$=100 ml (corresponding to the experimental protocol), and all other parameters as given in Tables 4.1. Solid lines: $10 < t \leq 30$ min: saline pre-perfusion (no substrate); $30 < t \leq 120$ min: 0.1 mM pyruvate and 1.5 mM oleate perfusion. Dashed lines: $90 < t \leq 120$ min: 0.1 mM pyruvate, 1.5 mM oleate and 10 mM ethanol perfusion

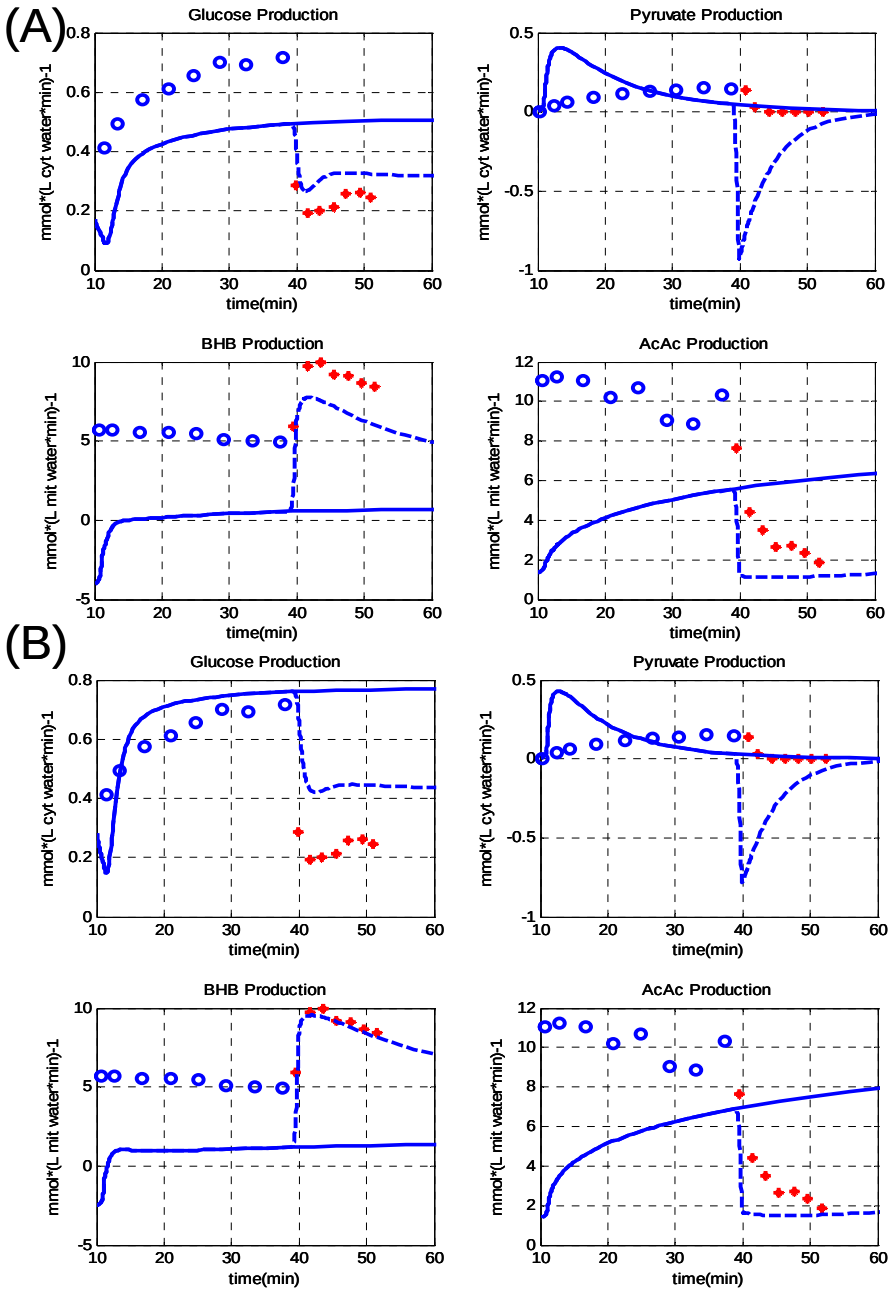

Figure 5.11. Dynamics of glucose, pyruvate, and ketone production calculated from perfusion model with lactate and lactate + ethanol as substrates. Symbols are experimental data from perfused fasted livers, from Lopez, et al. 2009, using a perfusion medium of Krebs-Henseleit bicarbonate buffer, with 25% bovine serum albumin, in a non-recirculated system; open circle-o: Pre-perfusion with no substrate; and perfusion with 2.5 mM lactate respectively. Star-*: Perfusion with 2.5 mM lactate and 10mM ethanol. Solid and dashed lines are simulations, using Eqns. 4.1-4, with $F_{perfusate}$=24.5 ml/min and $V_{perfusate}$=100 ml (corresponding to the experimental protocol), and all other parameters as given in Tables 4.1 and 5.2. Solid lines: $10 < t \leq 60$ min: perfusion with 2.5 mM lactate. Dashed lines: $40 < t \leq 60$ min: 2.5 mM lactate and 10 mM ethanol perfusion. (A) Rate of endogenous fatty acid oxidation set to 0.085 micromol/(L cyt water*min). (B) Rate of endogenous fatty acid oxidation set to 0.15 micromol/(L cyt water*min).

5.4 Discussion

While the literature contains a vast amount of information on ethanol metabolism in perfused rat livers, especially in the fed state, specific data related directly to the fasted rat liver is lacking. In particular, there is shortage of data with respect to lactate and pyruvate perfusion with ethanol in the fasted liver. For instance, Lindros et al. 1972 conducted experiments on rat livers perfused with combinations of lactate and pyruvate, but with additions of glucose. Forsander et al. (1965) studied the effect of ethanol on liver metabolism in fed and starved rats, but their medium contained 5 to 6 mM of glucose in bovine blood. Krebs et al. (1969) also used red blood cells (causing high rates of gluconeogenesis). All of these experimental setups are incompatible with our perfusion model conditions. However, alanine and ethanol have been widely studied in both fasted and fed rat livers. Alanine constitutes one of the three main gluconeogenic precursors *in vivo.* Alanine is expected to affect the liver metabolism in a manner similar to that of lactate and pyruvate, since they share many pathways and transporters. Within the cytosol, alanine is transaminated to pyruvate, which can then be reduced to lactate and exported from the cell, or transferred to the mitochondria for oxidation or as substrate for gluconeogenesis. Thus, we used data on alanine and ethanol perfusions in starved rats from Williamson et al. (1969c) to qualitatively validate some of the responses of our model to lactate and pyruvate with ethanol in the starved state.

We have demonstrated earlier (Chapter IV) the validity of the liver model in terms of transferring reducing equivalents and carbon via the malate shuttle. Ethanol oxidation in the liver provides an enhanced supply of reducing equivalents in the cytosol as has been observed experimentally from different studies (Forsander et al. 1965, 1966;

Freinkel et al. 1965). Since the mitochondrial membrane is impermeable to the NADH generated in the cytosol, the evidence indicates that reducing equivalents are transferred to the mitochondria by a specialized shuttle mechanism (Williamson et al. 1969a, 1969b; Chappell et al. 1968; Borst et al. 1963). The most prominent shuttle is the malate-aspartate cycle which involves the influx of malate and glutamate to the mitochondria and efflux of aspartate and alphaKG coupled to aspartate aminotransferase on both sides of the membrane. Our model successfully predicts that ethanol added to lactate causes the following sequence of events: an increase in the rate of NADH supply in the cytoplasm; malate transport to the mitochondria predominantly via the MAL:alphaKG transporter coupled with stoichiometric glutamate transport via the GLUT:ASP shuttle (Fig. 5.2); transamination of OAA to aspartate; efflux of aspartate, which then undergoes a reverse transamination.

Williamson et al. (1969c) reported an increase of oxygen uptake, upon separate ethanol and oleate addition to alanine in fasted perfused rat liver, of 1.2-fold and 1.5-fold, respectively. The model predicts this enhancement of oxygen uptake by ethanol and oleate, but to a somewhat larger extent-- 1.5 fold (Fig. 5.7) and 2.3 fold (Fig. 5.9), respectively. On the other hand, the addition of ethanol following oleate addition during lactate perfusion causes no additional rise in the oxygen consumption rate; instead a small decrease was estimated by the model (Fig. 5.5), which correlates well with the small decrease observed from Williamson et al. 1969c when ethanol was added to alanine+oleate perfusions (5% reduction).

The model demonstrates the inhibitory effect of ethanol on the TCA cycle. The model predicts a 42% inhibition by ethanol addition to lactate (IDH, Fig. 5.3). The oleate

addition prior to ethanol causes a further inhibition of the TCA cycle by 60% (Fig. 5.5, AKGDH, IDH). These model estimates seem to match closely with the data from Williamson et al. (1969c) of 75% reduction in TCA cycle with alanine perfusion. The three enzymes-- CS, IDH, and AKGDH --are generally considered the main regulatory points of the TCA cycle, and all thee are inhibited when ethanol is added to lactate plus oleate (Fig. 5.5). However, the model illustrates that ethanol inhibition of the TCA cycle occurs primarily at the sites of IDH and AKGDH, since there is no change in the rate of CS (Fig.5.3, 7,9), during all other perfusions. In the presence of oleate, ethanol seems to counteract the oleate-induced enhancement of CS, resulting in reduction in the rate of citrate synthase (CS) in addition to significant reduction in the rate of IDH and AKGDH (Fig. 5.5). These flux inhibitions are most likely caused both by reductions in substrate concentrations, as observed from experimental decreases in citrate, alphaKG, and succinate during alanine-oleate-ethanol perfusions (Williamson, et al. 1969c), and increased mitochondrial NADH, which cause inhibition of these three reactions, as represented in the *in vitro* kinetics (Tables 4.1 and 5.1).

The rise in the rate of ketone production by ethanol in both lactate and pyruvate perfusion scenarios is attributed mainly to the increase in the mitochondrial redox ratio, rather than a surplus of AcCoA, since CS is not inhibited significantly in most circumstances. The addition of ethanol to lactate causes a 6-fold increase in the rate of BHB production, at the expense of AcAc production, which settles at essentially zero (Fig.5.3). Although these experimental measurements are not available for lactate-ethanol perfusions, these predictions are corroborated by alanine-ethanol perfusion data

(Williamson et al. 1969c), of approximately 11-fold increase in the BHB flux with the addition of ethanol to alanine.

Due to the dearth of experimental data with ethanol and pyruvate and lactate in fasted rat livers, data from ethanol and alanine perfusions were used to qualitatively validate many of the results presented here. However, alanine metabolism is more complicated than lactate and pyruvate metabolism, since the alanine degradation pathway interacts with ureagenesis pathway, which was not modeled in detail in this work. Thus some differences will be expected between simulations using alanine compared to lactate or pyruvate as substrate. One of the future directions of this study be to include the interaction between ureagenesis and gluconeogenesis.

This model of ethanol oxidation in the fasted perfused rat liver successfully predicts the expected trends as well the actual rates of most metabolic reactions. This will allow us in the future to study disease states of the liver related to alcohol, such as fatty liver alcohol syndrome and liver cirrhosis, and to investigate the usefulness of potential nutritional and pharmaceutical therapies.

CHAPTER VI

CONCLUSIONS AND FUTURE DIRECTIONS

6.1 Summary of Results

The study presented here uses mathematical models to represent the metabolism of a fasted liver and to predict the intermediate fluxes and concentrations in response to different combinations of nutrients and exercise. Two main modeling approaches were explored: modeling the carbohydrate metabolism in human liver using a distributed approach, and modeling a detailed regulated gluconoegenic model of the fasted perfused rat liver.

6.1.1 Distributed Model

The distributed model consists of reaction and transport equations to represent carbohydrate metabolism, tissue heterogeneity, and axial concentration gradients. The model features the metabolic zonation concept by incorporating the spatial variation of key enzymatic reactions. This model reliably predicts the rate of gluconeogenesis and lactate uptake by the liver, and the effect of high intensity exercise on the various hepatic fluxes.

The incorporation of zonation of glycolytic and gluconeogenic enzyme activities causes the expected increase in glycolysis and decrease in gluconeogenesis along the sinusoid length from periportal to perivenous regions, while fluxes are nearly constant along the sinusoid length in the absence of enzyme zonation. These results confirm that transport limitations are not sufficient to account for the observed tissue heterogeneity of metabolic fluxes. Modeling results indicate that changes in arterial substrate concentrations and hepatic blood flow rate, which occur in the high-intensity exercise state, are not sufficient to shift the liver metabolism enough so as to account for the five-fold increase in hepatic glucose production measured during exercise. Changes in maximal enzyme activities, whether caused by exercise-induced changes in insulin, glucagon, or other hormones, are responsible for observed glucose output. The distributed model was expected to offer the opportunity to examine and test the effect and the importance of liver structure hetrogeneity on its metabolic functions. However the distributed model could not be conclusively validated, since few experimental data are available that are capable of representing the complex structure of the liver and its enzyme heterogeneity.

6.1.2 G**luconeogenesis and Lipid Metabolism in the Perfused Liver**

The need for a robust and predictive model led us to develop a lumped model of hepatic metabolism that incorporates all the significant metabolic pathways needed to represent the variety of substrates (e.g: lactate, pyruvate, alanine, fatty acids) under variable concentrations in well-controlled experiments, such as use of perfused livers. In general, the predicted steady state glucose production and substrate uptake rates, and

especially the ratio of glucose/substrate, are in good agreement with the experimental results. The simulations predict the same trends, in terms of stimulation of substrate uptake by fatty acid addition, as observed experimentally. The model also predicts the dynamic response to lactate and pyruvate perfusions with good accuracy. This model represents an encouraging step toward developing a comprehensive model for carbohydrate metabolism, especially representing the complex interplay between gluconeogenesis and the lipid metabolism. One of the limitations of this model was its inability, even after numerous attempts at parameter estimation, to correctly predict the $NADH/NAD^+$ ratio. This caused discrepancies in the reactions that involved reducing equivalents and indicated the need for consideration of cytosolic-mitochondrial compartmentation.

6.1.3 Cytosolic-Mitochondrial Compartmentation in the Pefused Liver

Developing a computational model of metabolic compartmentation and inter-compartmental transport between the cytosol and the mitochondria allowed the successful prediction of the redox ratio, in both the cytosolic and the mitochondrial compartments, and major metabolic fluxes. The model also predicts the directional movement of the carbon shuttle across the mitochondrial membrane during lactate, pyruvate, and oleate perfusions. The model represents a tool to generate much needed time course data on different metabolites and their relative distribution. All simulation results were obtained using a single set of parameters. Parameter estimations were primarily performed for matching redox ratios, confirming the central importance of this ratio in regulating metabolism.

6.1.4 Ethanol Metabolism in the Perfused Liver

The effects of ethanol on different metabolic rates, such as gluconoegenesis, ketogenesis, and TCA cycle, were simulated by using the model developed in Chapter IV. The ethanol simulations constitute a further validation for the model. In general the model predicts that ethanol oxidation alters the level of redox ratio in both the cytoplasm and the mitochondrial compartment causing inhibition of the gluconoegenesis and TCA cycle rates while increasing the rate of ketogenesis in accordance with experimental data. The ethanol model can establish a base for studying disease states such as fatty liver disease.

6.2 Recommendations for Future Directions

To achieve the overall goal of developing an *in silico* liver capable of accurately predicting the *in vivo* state of the fasted rat liver, we developed a model that simulated the gluconoegenesis from pyruvate and lactate. We now suggest a plan to include the effect of alanine and the urea cycle, therefore integrating the effect of the three main gluconeogenic precursors. This model will allow for a complete representation and detailed pathways interaction.

6.2.1 Oxidative Phosphorylation and the Inner Mitochondrial Membrane Space

The model of oxidative phosphorylation developed in this work is a simplification that lumps different steps of the oxidation process and the ATPase reaction into two simple reactions. The ADP: ATP translocase also plays a role in regulating the transport of ADP

from the cytosol to the mitochondria in exchange of ATP synthesized in the mitochondria. Moreover the exchange of ATP for ADP is electrogenic and controlled by the high membrane potential of the inner membrane. The model developed in Chapter IV predicts the rate of oxygen consumption well within the expected experimental data; however the model fails to predict the asymmetry of the ATP/ADP ratio between the cytosol and the mitochondria.

One possible solution to these shortcomings is to account for the potential energy of the inner membrane in the rate of ADP:ATP translocase and to also model separately the rate of oxidative phosphorylation and the rate of ATPase. This approach could also lead into the consideration of modeling the matrix separately from the intermembrane space. We suggest that the detailed model of the oxidative phosphorylation built by Beard et al. be used to try to remediate the discrepancies in cytsolic and mitochondrial ATP/ADP ratios.

6.2.2 Alanine Metabolism

Gluconeogenesis constitutes the main source for glucose production during periods of fasting or starvation. The main precursors for gluconeogenesis are lactate, pyruvate, and the amino acids. The amino acids are especially important substrates for hepatic gluconeogenesis during fasting compared to lactate and pyruvate. Studies involving fasted rat livers which were perfused with normal physiological levels of gluconeogenesis precursor have indicated that amino acids contributed to more than 50% of glucose production (Exton and Park 1967). The amino acids are obtained from the breakdown of protein, mostly from skeletal muscle. However experimental data from arteriovenous data from human muscle (Felig and Wahren 1974) and from isolated rat

muscle indicate that alanine and glutamine are released into the blood stream to a greater extent compared to other amino acids. Alanine constitutes the principal amino acid for liver gluconeogenesis whereas glutamine is considered the main gluconeogenic precursor for the kidney.

Alanine from the muscle and peripheral tissue passes into the blood and travels to the liver. Once inside the cytosol alanine transaminase transfers the amino group from alanine to α-ketoglutarate, forming pyruvate and glutamate. Pyruvate is the port of entry for alanine into the gluconeogenesis pathway. Glutamate enters the mitochondria and releases the ammonia through glutamate dehydrogenase. Ammonia is a very toxic component for the human body and its accumulation can cause serious risks such as brain damage. The urea cycle provides the liver with a specific mechanism to transform the toxic ammonia resulting from the catabolism of the alanine into urea, which is then released into the urine. Parallel increases in gluconeogenesis and ureagenesis have been observed during prolonged starvation in the rat (Parrilla 1978). Hormonal stimulation was found to stimulate gluconeogenesis rate along with an increase in the rate of urea production (Ayuso-Parrilla et al. 1976). Moreover, in pathological conditions it has been observed that inhibition of gluconeogenesis was accompanied by hyperammonemia (Rosenberg 1982) giving further evidence about the relationship between these two pathways. These two pathways are linked through the sharing of many enzymes such as aspartate and malate dehydrogenase, and through mitochondrial metabolite transport such as: glutamate, aspartate and α-ketoglutarate. Experiments (Kashiwagura et al. 1984; Meijer et al. 1978; Ohtake and Clemens 1991) with rat livers perfused with NH_4^+ or isolated hepatocytes demonstrated a close relationship between ureagenesis and

gluconeogenesis . It has been suggested that the availability of aspartate in the cytosol plays a major role in controlling the flux rate through argininosuccinate synthetase (Meijer et al. 1978) which could be considered to be the rate limiting steps for ureagenesis from NH_4^+. Moreover pyruvate has been found to increase the rate of ureagenesis from NH_4^+ (Meijer et al. 1978). In addition, ureagenesis is responsible for malate production in the cytosol, hence different effects are expected, depending on whether lactate or pyruvate is used as gluconeogenic precursor. Interactions between the two pathways are highly expected; therefore a model of urea cycle is necessary to represent the disposal of ammonia, account for the energy requirement in form of ATP needed to fuel the urea cycle, and in regulating the transfer of metabolites responsible for maintaining the reducing equivalents balance.

The urea cycle is subject to short-term regulation by three essential factors: the availability of substrate (NH_4^+), the intramitochondrial concentration of N-acetylglutamate (AGA) and the availability of ornithine, which is critical for the process of the urea cycle. AGA is synthesized in the mitochondria from AcCoA and glutamate by N-acetylglutamate synhase. Carbamoyl-phospahte synthetase, the slowest step in the urea cycle, is regulated by AGA, therefore exerting an important role in the control of the urea cycle (Shigesada et al. 1978; Shigesada and Tatibana 1971). The rate expression for carbamoyl-phosphate synthetase should incorporate the activation by AGA and inhibition by products (carbamoyl phosphate, and ADP) (Elliott and Tipton 1974; Lusty 1978). The ornithine carbamoyl transferase, argininosuccinate synthetase, and lyase are reversible and they should be represented by Haldane relation. The arginase kinetic expression should also incorporate the inhibition effect by ornithine.

The urea cycle is partly located in the cytosol and partly in the mitochondria, making the compartmentation model developed in Chapter IV of this dissertation a useful platform for this model. Inter-compartmental transport for ornithine and citrulline should also be added. We suggest that the integration of the alanine and urea cycle models with the compartmental of Chapter IV to be used to simulate the effects of alanine, fatty acid, ethanol, and NH_4^+, and their various combinations, on the rates of gluconeogenesis, uregenesis, TCA cycle, and ketogenesis. Upon validation with experimental data, this model will constitute a good representation of the *in vivo* fasted state of a rat liver.

6.2.3 Insulin and Glucagon Control

The model developed in this work accounts for many allosteric and substrate effectors on different enzyme kinetics such as PC, PK, FBPase, and PFK. The role of glucagon is of great importance especially in controlling the rate of gluconoegenesis. Glucagon stimulates the rate of gluconoegenesis from lactate and pyruvate by raising the intracellular level of cAMP, which stimulates FBPase a critical intermediate step for glucose production.

We suggest that the model be modified to include the effects of glucagon on the different pathways and regulatory enzymes. The model could be tested and validated with the vast data in the literature on glucagon effects during gluconoegenesis. This hormonal signaling pathway modeling can constitute the foundation for a model with future physiological application.

BIBLIOGRAPHY

1. Achs MJ, Anderson JH, and Garfinkel D. Gluconeogenesis in rat liver cytosol. I. Computer analysis of experimental data. *Comput Biomed Res* 4:65-106, 1971.
2. Adachi Y**,** Moore LE, Bradford BU, Gao W, and Thurman RG. Antibiotics prevent liver injury in rats following long-term exposure to ethanol.*Gastroenterology* 108:218-224, 1995.
3. Agius L, Alberti KG. Regulation of flux through pyruvate dehydrogenase and pyruvate carboxylase in rat hepatocytes. Effects of fatty acids and glucagons. *Eur J Biochem/FEBS* 152(3):699-707, 1985.
4. Ahmad AB, Bennett PN, and Rowland M. Models of hepatic drug clearance: discrimination between the 'well stirred' and 'parallel-tube' models. *The Journal of Pharmacy and Pharmacology* 35:219-224, 1983.
5. Alberty RA. *Thermodynamics of Biochemical Reactions*. Wiley: Hoboken, NJ, 2003.
6. Anderson JH, Achs MJ, and Garfinkel D. Gluconeogenesis in rat liver cytosol. II. Computer simulation of control properties. *Comput Biomed Res* 4:107-125, 1971.
7. Aubert A. Modelling of the coupling between brain electrical activity and metabolism. *Acta Biotheoretica*. 49:301-326, 2001.
8. Ayuso-Parrilla MS, Martin-Requero A, Perez-Dias J, and Parrilla R. Role of glucagon on the control of hepatic protein synthesis and degradation in the rat in vivo. *Journal of Biological Chemistry* 251:7785-7790, 1976.
9. Badger TM**,** Korourian S, Hakkak R, Ronis MJJ, Shelnutt SR, Ingelman-Sundberg M,

and Waldron J. Carbohydrate deficiency as a possible factor in ethanol-induced hepatic necrosis. *Alcoholism: Clinical and Experimental Research* 22(3):742, 1998.

10. Bantenburg JJ, Olson MS. Regulation of pyruvate dehydrogenase by fatty acid in isolated rat liver mitochondria. *J Biol Chem* 251(5):1364-1370, 1976.
11. Barzilai N and Rossetti L. Role of Glucokinase and Glucose-6- Phosphatase in the acute and chronic regulation of hepatic glucose fluxes by insulin. *J Biol Chem* 268:25019-25025, 1993.
12. Bassingthwaite JB, Knopp TJ, and Hazerlig JB. A concurrent model of capillary tissue exchange, in: C*apillary permeability. The transfer of molecules and ions between capillary blood and tissue. Proceedings of the Alfred Benzon Symposium II, Copenhagen 22-26 June 1969,* Crone C and Lassen NA, eds**.** New York: Academic Press, 1970.
13. Beard DA and Qian H. Thermodynamic-based computational profiling of cellular regulatory control in hepatocyte metabolism. *American Journal of Physiology* 288:E633-644, 2005.
14. Bederman IR, Kasumov T, Reszko AE, David F, Brunengraber H, Kelleher JK. In vitro modeling of fatty acid synthesis under conditions simulating the zonation of lipogenic[^{13}C]acetyl-CoA enrichment in the liver. *J Biol Chem* 279(41): 43217-26, 2004.
15. Bergman RN and El-Refai M. Dynamic control of hepatic glucose metabolism: studies by experiment and computer simulation. *Biomedical Engineering* 3:411-432, 1975.
16. Bergmeyer HU (Ed.). *Methods of Enzymatic Analysis, 2nd Ed.*. Williamson DH and

Brosnan JT, Concentrations of metabolites in animal tissue. New York: Academic Press, 2266-2290, 1974.

17. Bjorkman O, Eriksson LS, Nyberg B, and Wahren J. Gut exchange of glucose and lactate in basal state and after oral glucose ingestion in postoperative patients. *Diabetes* 39:747-751, 1990.
18. Bode JC, Zelder O, Rumpelt HJ and Wittkamp U. Depletion of liver adenosine phospahtes and metabolic effects of intravenous infusion of fructose or sorbitol in man and in the rat. *European Journal of Clinical Investigation* 3:436-441, 1973.
19. Boesiger P, Buchli R, Meier D, Steimann B, and Gitzelmann R. Changes of liver metabolite concentrations in adults with disorders of fructose metabolism after intravenous fructose by 31P MRS. *Pediatric Research* 36:436-440, 1994.
20. Bohnensack R and Fritz S. Stimulation of alanine metabolism by ammonia in the perfused rat liver. Quantitative analysis by means of a mathematical model. *Biochimica et biophysica acta* 1073:347-356, 1991.
21. Bordone L, and Guarrente L. Calorie restriction, SIRT1 and metabolism: Understanding longevity. *Nature* 6:298–305, 2005.
22. Borst P, In *Fiunctionelle und Morphologische Organization der Zelle* (P.Karlson ed.) Springer -Verlag , Berlin 137-162.
23. Bracht A, Constantin J, Ishii-Iwamoto EL, Suzuki-kemmelmeir F. Zonation of gluconeogenesis from lactate and pyruvate in the rat liver studied by means of anterograde and retrograde bivascular perfusion. *Biochim. Biophys. Acta* 1199:298-304, 1993.

24. Brouwer A, Smits GG, Tas J, Meijer AJ, and Tager JM. Substrate anion transport in mitochondria. *Biochimie*. 55:717-725, 1973.

25. Brundin T and Wahren J. Influence of a mixed meal on splanchnic and interscapular energy expenditure in humans. *American Journal of Physiology - Endocrinology and Metabolism* 260:232-237, 1991.

26. Brundin T and Wahren J. Whole body and splanchnic oxygen consumption and blood flow after oral ingestion of fructose or glucose. *American Journal of Physiology* 264:504-513, 1993.

27. Calik P and Akbay A. Mass flux balance-based model and metabolic flux analysis for collagen synthesis in the fibrogenesis process of human liver. *Medical Hypotheses* 55:5-14, 2000.

28. Calvetti D, Kuceyeski A, and Somersalo E. A mathematical model of liver metabolism: from steady state to dynamic. *J. Phys: confer ser* 124 012012, 2008.

29. Chalhoub E, Hanson RW, and Belovich JM. A computer modelofgluconeogenesis and lipid metabolism in the perfused liver. *Am J Physiol Endocrinol* Metab 293:E1676-E1686, 2007.

30. Chan C, Hwang D, Stephanopoulos GN, Yarmush M, Stephanopoulos G. Application of multivariate analysis to optimize function of cultured hepatocytes. *Biotechnol Prog* 19:580-598, 2003.

31. Chappell JB. In *Inhibitors: Tools in Cell Research. Twentieth Colloquium of te Gesellshaft Fur Biologishe Chemie. Mosbach/Baden* (T. Bucher and H. Seis, eds), Springer-Verlag, Heidelberg. 335-350, 1969.

32. Chappell, JB. Systems used for the transport of substrates into mitochondria. *Brit*

Med Bull 24: 150-157, 1968.

33. Chiandussi L, Greco G, Sardi G, Vaccarino A, Ferraris CM, and Curti B. Estimation of hepatic arterial and portal venous blood flow by direct catheterization of the vena porta through the umbilical cord in man. Preliminary results. *Acta Hepato-splenol* 15:166, 1968.
34. Chien D, Dean D, Saha AK, Flatt JP, Ruderman NB. Malonyl-CoA content and fatty acid oxidation in rat muscle and liver in vivo. *Am J Physiol* 279(2):E259-265, 2000.
35. Christian R, Christian D. Changes in availability of glucogenic and ketogenic substrates and liver metabolism in fed and starved states. *Ann Nutr Metab* 27:57-70, 1983.
36. Cohen SM. Effects of insulin on perfused liver from streptozotocin-diabetic and untreated rats: ^{13}C NMR assay of pyruvate kinase flux. *Biochemistry* 26:573-580, 1987.
37. Crabb DW, Borson WF, Li TK. Steady-state kinetic properties of purified rat liver alcohol dehydrogenase: application to predicting alcohol elimination rates in vivo. Arch Biochem Biophys 224(1):229-309, 1983.
38. Davis EJ and Lumeng L. *J Bio Chem* 250:2275-2282, 1975.
39. Davis E.J, Lumeng L, and Bottoms D. On the relationships between the stoichiometry of oxidative phosphorylation and the phosphorylation potential of rat liver mitochondria as functions of respiratory state. *FEBS Let* 39:9-12, 1974.
40. Deussen A and Bassingthwaighte JB. Modeling [^{15}O]oxygen tracer data for estimating oxygen consumption. *Am J Physiol Heart Circ Physiol* 270:H1115-H1130, 1996.

41. Diem K and Lentner C, eds. *Documenta Geigy Scientific Tables*, 7th Edition, Geigy, Basel, 1970, p. 585.

42. Dierks T, Riemer E, and Kramer R. Reaction mechanism of the reconstituted aspartate/glutamate carrier from bovine heart mitochondria. *Biochem Biophys Acta* 92: 233-244, 1988.

43. Ehrig T, Borson WF, and Li TK. Alcohol and ethanol oxidation in vivo and in hepatocytes. Pharmacol Biochem Behav. 25(2-3):105:116, 1990

44. Ekdahl KN, Ekman P. The effect of fructose-2,6-bisphosphate and AMP on the activity of phosphorylated and unphosphorylated fructose-1,6-bisphosphatase from rat liver. *FEBS* 167(2):203-209, 1983.

45. Elliott KR and Tipton KF**.** Product inhibition studies on bovine liver carbamoyl phosphate synthetase. *Biochem J* 141:817-824, 1974.

46. El-Refai M and Bergman RN. Simulation study of control of hepatic glycogen synthesis by glucose and insulin. *The American journal of Physiology* 231:1608-1619, 1976.

47. Enevoldsen LH, Simonsen L, Macdonald IA, and Bulow J. The combined effects of exercise and food intake on adipose tissue and splanchnic metabolism. *Journal of Physiology* 561(3):871-872, 2004.

48. Engel PC, Dalziel K. The equilibrium constants of the glutamate dehydrogenase systems. *Biochem J* 105, 691-695, 1967.

49. Exton JH and Park CR. Control of gluconeogenesis in liver. I. General features of gluconeogenesis in the perfused livers of rats. *J Biol Chem* 242:2622-2636 ,1967.

50. Felig P and Wahren J. Protein turnover and amino acid metabolism in the regulation

of gluconeogenesis. *Federation Proceedings* 33: 1092-1097, 1974.

51. French SW, Morimoto M. and Tsukamoto H. Animal models of alcohol-associated liver injury. In: Hall, P., ed. Alcoholic Liver Disease: *Pathology and Pathogenesis. 2d ed. London: Edward Arnold*, 1995. pp. 279-296.
52. Fogler S. *Elements of Chemical Reaction Engineering*. New Jersey: Prentice Hall, 3 rd edition, 880-881, 2001.
53. Forsander OA, Raiha M, Salaspuro M, and Maenpaa P. Influence of ethanol on the lactate/pyruvate ratio of rat-liver slices. *Biochem J*. 98:244-247, 1966.
54. Forsander OA. Influence of ethanol on the liver metabolism of fed and starved rats. *Biochem. J*. 94:259-265, 1965.
55. Fournier RL *Basic Transport Phenomena in Biomedical Engineering*. New York: Taylor and Francis, 27- 48, 1998.
56. Freidman B, Goodman EH, Saunders HL, Kostos V, and Weinhouse S. An estimation of pyruvate recycling during gluconeogenesis in the perfused rat liver. *Arch Biochem Biophys* 143:566-578, 1971.
57. Freinkel R, Cohen AK, Arky RA, Foster AE. Alcohol Hypoglycemia: II. A postulated mechanism of action based on experiments with rat liver slices. *The Journal of Clinical Endocrinology and Metabolism*. 25:76-94, 1965.
58. Frohlich J and Wieland O. Different actions of glucagon and fatty acids on gluconeogenesis from lactate in the perfused rat liver. *Horm Metab Res* 4:171-175, 1972.
59. Galassetti P, Coker RH, Lacy DB, Cherrington AD, Wasserman DH. Prior exercise increases net hepatic glucose uptake during a glucose load. *Am J Physio* 276: E1022-

E1029, 1999.

60. Gannon MC, Ercan-Fang N, Ratth VL, Treadway JL, Taylor MR, Nuttall FQ. Integrated effects of multiple modulators on human liver glycogen phosphorylase a. *American Journal of Physiology - Endocrinology and Metabolism* 283:29-37, 2002.
61. Garfinkel D. Simulation of the Krebs cycle and closely related metabolism in perfused rat liver. I. Construction of a model. *Comput Biomed Res* 4:1-17, 1971a.
62. Garfinkel D. Simulation of the Krebs cycle and closely related metabolism in perfused rat liver. II. Properties of the model. *Comput Biomed Res* 4:18-42, 1971b.
63. Garfinkel L, Kohn MC, Garfinkel D. Computer simulation of the fructose bisphosphatase / phosphofructokinase couple in rat liver. *Eur J Biochem* 96:183-192, 1979.
64. Goresky CA and Nadeau BE. Uptake of materials by the intact liver, the exchange of glucose across the cell membrane. *J Clin Invest* 53:634-646, 1974.
65. Goresky CA, Bach GG, and Nadeau BE. Uptake of materials by the intact liver. The transport and net removal of galactose. *J Clin Invest.* 52:991-1009, 1973.
66. Goresky CA. Uptake in the liver: the nature of the process, in *International Review of Physiology*, 21:65-79, 1980.
67. Gray MR and Tam YK. The series- compartment model for hepatic elimination. *Drug Metabolism and Disposition*. 15:27-31, 1986.
68. Gross RC, Eigenbrodt EH, Farguhar JW. Endogenous triglyceride turnover in liver and plasma of the dog. *Journal of Lipid Research* 8:114-125, 1967.
69. Guder WG, Schmidt U. Liver cell heterogeneity: The distribution of pyruvate kinse and phosphoenolpyruvate carboxykinase (GTP) in the liver lobule of fed and starved

rats. *Hoppe-Seyler's Z Physiol Chem* 357:1793-1800, 1976.

70. Gyorgy B, Yang Z-J, Meguid M, Laviano A, Szeverenyi N. Effects of fasting, intermittent feeding, or continous parenteral nutrition on rat liver and brain energy metabolism as assessed by 31P-NMR. *Physiology and Behavior* 58:521-527, 1995.
71. Halestrap AP and Denton RM. Specific inhibition of pyruvate transport in rat liver mitochondria and human erythrocytes by α-cyano-4-hydroxycinnamate**.** *Biochem J* 138:313-316, 1974.
72. Halestrap A.P. The mitochondrial pyruvate carrier. Kinetics and specificity for substrates and inhibitors**.** *Biochem J*. 148:85-96, 1975.
73. Hannon JP and Vaughan DA. *Am J Physiol* 198: 375, 1960.
74. Hanson RW and Mehlman MA. *Gluconeogenesis: Its Regulation in Mammalian Species. Role of Anion Transport in the Regulation of Metabolism* (John R Williamson*)* John Wiley & Sons, New York, 1981.
75. Hems R, Ross BD, Berry MN and Krebs HA. Gluconeogenesis in the perfused rat liver. *Biochem J* 101:284-290, 1966.
76. Henson CP and Cleland WW. Kinetic studies of glutamic oxaloacetic transaminase isozymes. *Biochemistry* 3:338-345, 1964.
77. Hers HG, Shaftingen V. The fructose 6-phosphste / fructose 1,6-bisphosphate cycle. *Curr Top Cell Reg* 18, 199-209, 1989.
78. Hiroshi M, Shulman G, Peters EJ, Wolfe MH, Elahi D, Wolfe RR. Hormonal control of substrate cycling in humans. *Journal of Clinical Investigation* 81:1545-1555, 1988.
79. Howlett K, Angus D, Proietto J, Hargeaves M. Effect of increased blood glucose

availability on glucose kinetics during exercise. *Journal of Applied Physiology* 84: 1413-1417,1998.

80. http://arbl.cvmbs.colostate.edu/hbooks/pathphys/digestion/liver/histo_hcytes.html
81. Huang M. Saturating concentration for the uptake of free fatty acids and release of ketone bodies in vivo in rat liver. *Life Sciences* 60:1915-1922, 1997.
82. Huang MT, Huang CC, Chen MY. In vivo uptake of ethanol and release of acetate in rat liver and GI. *Life Sci.* 53(10): 165-170, 1993.
83. Hultman E, Nilson LH, and Sahlin K. Adenine nucleotide content of human liver. *Scandinavian Journal of Clinical Investigation* 35:245-251, 1975.
84. Indiveri C, Dierks T, Kramer R, and Palmieri F. Reaction mechanism of the reconstituted oxoglutarate carrier from bovine heart mitochondria. *Eur J Biochem* 198:339-347, 1991.
85. Ito J, Kuzumaki T, Otsu K, Iuchi Y, Ishikawa K. Hormonal regulation of aldolase B gene expression in rat primary cultured hepatocytes. *Archives of Biochemistry and Biophysics* 350 :291-297, 1998.
86. Jensen MD. Gender differences in regional fatty acid metabolism before and after meal ingestion. *Journal of Clinical Investigation* 96:2297-2303, 1995.
87. Jensen MD. Regional glycerol and free fatty acid metabolism before and after injestion. *Am J Phsiol* 276:E863-E869, 1999.
88. Jin ES, Jones JG, Merritt M, Burgess SC, Malloy CR, Sherry AD. Glucose production, gluconeogenesis, and hepatic tricarboxylic acid cycle fluxes measured by nuclear magnetic resonance analysis of a single glucose derivative. *Analytical Biochemistry*, 327:149-155, 2004.

89. Jones JG, Naidoo R, Sherry DA, Jeffrey FMH, Cottam GA, and Malloy CR. Measurements of gluconeogenesis and pyruvate recycling in the rat liver: a simple analysis of glucose and glutamate isotopomers during metabolism of [1,2,3-$^{13}C^{3}$] propionate. *FEBS Letters*, 412:131-137, 1997.

90. Jones JG, Solomon MA, Cole SM, Sherry AD, Malloy CR. An integrated (2)H and (13)C NMR study of gluconeogenesis and TCA cycle flux in humans. *Am J Physiol Endocrinol Metab* 281(4):E848-56, 2001.

91. Jungermann K, Teutsch HF, Katz N, and Sasse D. Heteregeneous reciprocal localization of fructose 1, 6 bisphosphatase and of glucokinase in micro dissected periportal and perivenous rat liver tissue. *FEBS Letters* 83:272-276, 1977.

92. Jungermann K, Heilbronn R, Katz N, and Sasse D. The Glucose/Glucose - 6-Phosphate cycle in the periportal and perivenous zone of rat liver. *Eur J Biochem* 123:429-436, 1982.

93. Jungermann K. Functional significance of hepatocyte heterogeneity for glycolysis and gluconeogenesis. *Pharmacology Biochemistry & Behavior* 18(Suppl. 1):409-414, 1983.

94. Jungermann K. Metabolic zonation of liver parenchyma. *Seminars in Liver Disease* 8(4):329-341, 1988.

95. Jungermann K. Metabolic zonation of liver parenchyma: significance for the regulation of glycogen metabolism, gluconeogenesis and glycolysis, *Diabetes/Metabolism Reviews* 3(1):269-293, 1987.

96. Jungermann K. Role of intralobular compartmentation in hepatic metabolism. *Diabete & Metabolisme (Paris)* 18:81-86, 1992.

97. Kashiwagura T, Deutsch CJ, Taylor J, Erecinska M, and Wilson DF. Dependence of gluconeogenesis, urea synthesis, and energy metabolism of hepatocytes on intracellular pH. *Journal of Biological Chemistry* 259: 237-243, 1984.

98. Katz J, Wals P, and Lee WNP. Isotopomer studies of gluconeogenesis and the Krebs cycle with 13C- labeled lactate. *J Biol Chem* 268: 25509-25521, 1993.

99. Katz N, Teutsch HR, Sassee D, Jungermann K. Heterogeneous distribution of glucose-6-phosphatase in microdissected periportal and perivenous rat liver tissue. *FEBS Letters* 72(2):226-230, 1977.

100. Kim WR, Brown RS, Terrault NA, El-Serag H. Burden of Liver Disease in the United States: Summary of a Workshop. *Hepatology*, 36(1) 227-242, 2002.

101. King RB, Raymond GM, and Bassingthwaighte JB. Modeling blood flow heterogeneity. *Ann Biomed Eng* 24: 352-372, 1996.

102. Klingenberg M, and Buchholz M. On the mechanism of bongkrekate effect on the mitochondrial adenine-nucleotide carrier as studied through the binding of ADP**.** *Eur J Biochem* 38:346-358, 1973.

103. Klingenberg M, Buchholz M, Erdelt H, Falkner G, Grebe K, Kadner H, Scherer B, Stengel-Rutkowski L, and Weidman J. In *Biochemistry and Biophysics of Mitochondrial Membranes* (GF Azzone, E Carafoli, AL Lehninger, E Quagliariello, and N Siliprandi, eds), Academic Press New York. 465-486, 1972b.

104. Klingenberg M. In *Mitochondria: Biogenesis and Bioenergetics/Biomembranes: Molecular Arrangements and Transport Mechanisms,* Federation of European Biochemical Societies Proceedings of the Eighth Meeting, Amsterdam (SG Van Den Bergh, P Borst, LLM Van Deenen, JC Riemersma, EC Slater and JM Tager, eds),

North Holland Publishing Co., Amsterdam 28:147-162, 1972a.

105. Klingenberg M. Metabolite transport in mitochondria: an example for intracellular membrane function**.** *Essays in Biochem*. 6:119-154, 1970b.

106. Klingenberg M. Mitochondria metabolite transport**.** *FEBS Lett*. 6:145-154, 1970a.

107. Kohn MC, Achs MJ, Garfinkel D. Computer simulation of metabolism in pyruvate-perfusate rat heart. II. Krebs cycle. *Am J Physiol 237*: R159-166, 1979.

108. Kohn MC, Achs MJ, and Garfinkel D. *BioSSIM*. 1981.

109. Kohn MC and Garfinkel D. Computer simulation of metabolism in palmitate-perfusate rat heart. II. Behavior of complete model. *Ann Biomed Eng* 11:361-384, 1983.

110. Konig M, Bulik S, and Holzhutter HG. Qunatifying the contribution of the liver to glucose homeostatis: A detailed kinetic model of human hepatic glucose metabolism. PLOS Computational Biology 8(6):e1002577, 2012

111. Koo A, Liang IY. Microvascular filling pattern in rat liver sinusoids during vagal stimulation**.** *J Physiol* 295:191-199, 1979.

112. Krebs HA. The redox state of nicotinamide adenine dinucleotide in the cytoplasm and mitochondria of rat liver. *Advances in Enzyme Regulation* 5:409-434, 1967.

113. Krebs HA and Veech RL. In *The Energy Level and Metabolic Control in Mitochondri*a. (S.Papa, J.M Tager, E.Quagliariello, and E.C Slater eds.). Adriatica Editrice, Bari, Italy 329-382, 1969.

114. Krebs HA, Freedland RA, Hems R, and Stubbs M. Inhibition of hepatic gluconeogenesis by ethanol. *Biochem J* 112:117-124, 1969.

115. Kreft A, and Zuber A. On the physical meaning of the dispersion equation and its

solutions for different initial and boundary conditions. *Chemical Engineering Science* 33:1471-1480, 1978.

116. Kreisberg RA. Effect of ethanol on glucose production and lactate, pyruvate and ketone body metabolism by the isolated perfused rat liver. *Diabetes* 16:784-790, 1967

117. Kreisberg RA, Siegal AM, and Owen WC. Glucose-lactate interrelastionships: Effect of ethanol. *The journal of clinical investigation*. 50:175-185, 1971

118. Kurland IJ and D'Argenio DZ. A minimal model of liver glycogen metabolism; feasibility for predicting flux rates. *J Theor Biol* 135:343-358, 1988.

119. Lardy, HA. *The Harvey Lectures*, 261, 1964-1965.

120. LeCouteur, D. Liver research team, Concorde RG hospital, University of Sydney, Sydney, Australia. http://www.chmeds.ac.nz/research/liversievefl/background.htm, retrieved 2004.

121. Levitt MD and Levitt DG. Use of a two-compartment model to predict ethanol metabolism. *Alcoholism-Clinical and Experimental Research* 24(4): 409-410, 2000.

122. Lindros KO, Vihma R, and Forsander OA. Utilization and metabolic effects of acetaldehyde and ethanol in the perfused rat liver. Biochem J. 126:945-952, 1972

123. Lopez CH, Kemmelmeier FS, Constantin J, and Bracht A. Zonation of the action of ethanol on gluconeogenesis and ketogenesis studied in the bivascularity perfused rat liver. *Chemico-Biological Interactions* 177:89-95, 2009.

124. Lusty CJ. Carbamoylphosphate synthetase I of rat-liver mitochondria. Purification, properties, and polypeptide molecular weight. *European Journal of Biochemistry / FEBS* 85: 373-383, 1978.

125. MacPhee PJ, Schmidt EE, Groom AC. Intermittence of blood flow in liver sinuoids,

studied by high-resolution in vivo microscopy. *Am J Physiol* 269:G692-G698, 1995.

126. Magnusson I, Schumann WC, Bartsch GE, Chandramouli V, Kumaran K, Wahren J, Landau BR. Noninvasive tracing of Krebs cycle metabolism in liver. *J Biol Chem* 266(11):6975-84, 1991.

127. Martins AG, Constantin J, Bracht F, Kelmer-Bracht AM, Bracht A. The action of extracellular NAD+ on gluconeogenesis in the perfused rat liver. *Mol Cell Biochem* 286:115-124, 2006.

128. Matsumura T, Kashiwagi T, Meren H, and Thurman RG. Gluconeogenesis predominates in periportal regions of the liver lobule. *Eur J Biochem* 144:409-415, 1984.

129. McClure WR, Hardy H, Wagner M, Cleland WW. Rat liver pyruvate carboxylase II. Kinetic studies of the forward reaction. *J Biol Chem* 246: 3579-3583, 1971.

130. Meijer AJ and Tager JM. *Biochim Biophys Acta* 189:136-138, 1969.

131. Meijer AJ and Williamson JR. Transfer of reducing equivalents across the mitochondrial membrane. I. Hydrogen transfer mechanisms involved in the reduction of pyruvate to lactate in isolated liver cells**.** *Biochim Biophys Acta* 333:1-11, 1974.

132. Meijer AJ, DeLeeuw G, Gimpel J, and Williamson JR. Role of anion translocation across the mitochondrial membrane in the regulation of urea synthesis from ammonia by isolated rat hepatocytes. *J Biol Chem* 250:7728-7738, 1975.

133. Meijer AJ, Gimpel JA, Deleeuw G, Tischler ME, Tager JM, and Williamson JR. Interrelationships between gluconeogenesis and ureogenesis in isolated hepatocytes. *The Journal of Biological Chemistry* 253: 2308-2320, 1978.

134. Menahan LA and Wieland O. The role of endogenous lipid in gluconeogenesis and

ketogenesis of perfused rat liver. *Eur J Biochem* 9:182-188, 1969.

135. Morikawa S, Inubushu T, Takahashi K, Ishii H, and Ozawa K. Gluconeogenesis and phosphoenergetics in rat liver during endotoxemia. *Journal of Surgical Research* 74, 179-186, 1998.

136. Mowbray JA. Mitochondrial monocarboxylate transporter in rat liver and heart and its possible function in cell control. *Biochem J* 148:41-47, 1975.

137. Nanji AA**,** and French SW. Dietary factors and alcoholic cirrhosis. *Alcoholism: Clinical and Experimental Research* 10(3):271-273, 1986.

138. Nanji AA**,** Khettry U, and Sadrzadeh SMH. Lactobacillus feeding reduces endotoxemia and severity of experimental alcoholic liver (disease).*Proceedings of the Society for Experimental Biology and Medicine* 205(3):243-247, 1994.

139. Nanji AA. Dietary fatty acids and alcoholic liver disease: Pathogenic mechanisms**.** *Alcoholism: Clinical and Experimental Research* 22(3):747-748, 1998

140. Neese RA, Schwarz JM, Faix D, Turner S, Letscher A, Vu D, and Hellerstein MK. Gluconeogenesis and intrahepatic triose phosphate flux in response to fasting or substrate loads. *Journal of Biological Chemistry*, 270:14452-14463, 1995.

141. Nobes CD, Brown GC, Olive PN, Brand MD. Non-ohmic proton conductance of the mitochondrial inner membrane in hepatocytes. *J. Biol. Chem*. 265:12903-12909, 1990

142. Nolan RP, Fenley AP, and Lee K. Identification of distributed metabolic objectives in the hypermetabolic liver by flux and energy balance analysis. *Metab Eng* 8:30-45, 2006.

143. Ohtake Y and Clemens MG. Interrelationship between hepatic ureagenesis and gluconeogenesis in early sepsis. *The American Journal of Physiology* 260: E453-458, 1991.

144. Orman MA, Arai K, Yarmush ML, Androulakis IA, Berthiaume F, and Ierapetritou MG. Metabolic flux determination in perfused livers by mass balance analysis: Effect of fasting. *Biotechnology and Bioengineering 107(5):825-835*, 2010

145. Orman MA, Ierapetritou MG, Androulakis IA, and Berthiaume F. Metabolic response of perfused livers to various oxygenation conditions. *Biotechnology and Bioengineering 108(12):2947-2957*, 2011.

146. Orman MA, Androulakis IA, Berthiaume F, and Ierapetritou MG. Metabolic network analysis of perfused livers under fed and fasted states: Incorporating thermodynamic and futile-cycle-associated regulatory constraints. *JTB 293:101-110*, 2012

147. Orman MA, Ierapetritou MG, Androulakis IA, and Berthiaume F. Effect of fasting on the metabolic response of liver to experimental burn injury. *PLOS one* 8(2): e54825, 2013.

148. Owen CS and Wilson DF. Control of respiration by the mitochondrial phosphorylation state. *Arch. Biochem. Biophys*. 161:581-591, 1974.

149. Pande P. Mathematical Model of Ethanol Metabolism in Liver. MS thesis, Cleveland State University, 2001.

150. Papa S, and Paradies G. On the mechanism of translocation of pyruvate and other monocarboxylic acids in rat-liver mitochondria. *Eur J Biochem* 49:265-274, 1974.

151. Papa S, Francavilla A, Paradies G, and Meduri B. The transport of pyruvate in rat liver mitochondria. *FEBS Lett*. 12:285-288, 1971.

152. Parrilla R. The effect of starvation in the rat on metabolite concentrations in blood, liver and skeletal muscle. *Pflugers Arch* 374: 9-14, 1978.

153. Pastino GM and Conolly RB. Application of a physiologically based pharmacokinetic

model to estimate the bioavailability of ethanol in male rats: Distinction between gastric and hepatic pathways of metabolic clearance. *Toxicological Sciences* 55(2): 256-265, 2000.

154. Pastino GM, Flynn EJ, Sultatos LG. Genetic polymorphisms in ethanol metabolism: Issues and goals for physiologically based pharmacokinetic modeling. *Drug and Chemical Toxicology* 23(1):179-201, 2000.

155. Petersen K, Cline GW, Blair J, and Shulman G. Substrate cycling between pyruvate and oxaloacetate in awake normal and 3,3'-5-triodo-L- thyronine-treated rats. *Am J Phys* 267:E273-E277, 1994.

156. Petersen K, Price T, Cline GW, Rothman DL, Shulman GI. Contribution of net hepatic glycogenolysis to glucose production during the early postprandial period. *American Journal of Physiology* 270:186-191, 1996.

157. Pilkis S J, Claus TH, Johanson RA. Hormonal control of cyclic 3's'-amp levels and gluconeogenesis in isolated hepatocytes from fed rats. *J Biol Chem*, 250:6328-6336, 1975.

158. Pison CM, Chauvin C, Perrault H, Lafond JL, Boujet C, Levere CM. In Vivo hypoxic exposure impairs adaptations to a 48 hour fast in rats. *Eur Respir J* 12:658-665, 1998.

159. Plaut GW, Cheung CP, Suhadolnik RJ, and Aogaichi T . Cosubstrate and allosteric modifier activities of structural analogues of NAD and ADP for NAD-specific isocitrate dehydrogenase from bovine heart. *Biochemistry* 18: 3430-3438, 1979.

160. Pusca F, Belovich J. Unpublished data.

161. Rappaport AM. Observations on the pathophysiology of liver structure. *Klinische Wochenschrift* 38:561-577, 1960.

162. Rappaport AM. The microcirculatory acinar concept of normal and pathological hepatic structure. *Beitrage zur Pathologie* 157:215-243, 1976.

163. Rappaport, A.M. Hepatic blood flow: morphologic aspects and physiologic regulation. *Int Rev Physiolo* 21:1-63, 1980.

164. Reich JG and Selkov EE. *Energy metabolism of the cell: a theoretical treatise*. London ; New York : Academic Press, 1981.

165. Reinhart GD, Hartleip SB. Influence of fructose 2,6-bisphosphate and MgATP on rat liver phosphofructokinase at pH 7: evidence for a complex interdependence. *Arch Biochem Biophy* 296, 224-230, 1992.

166. Renkin EM. Multiple pathways of capillary permeability, *Circulation Research*. 41:735-743, 1977.

167. Roberts MS and Rowland M. Correlation between in-vitro microsomal enzyme activity and whole organ hepatic elimination kinetics: analysis with a dispersion model. *J Pharm Pharmacol* 38:177-181, 1985.

168. Robinson BH, and Chappell JB. The Inhibition of malate, tricarboxylate and oxoglutarate entry into mitochondria by 2-n-butylmalonate**.** *Biochem Biophys Res Commun* 28:249-255, 1967.

169. Rognstad R and Katz J. Role of pyruvate kinase in the regulation of gluconeogenesis from L-Lactate. *J Biol Chem* 252:1831-1833, 1977.

170. Rongstad R, and Katz J. Gluconeogenesis in the kidney cortex. quantitative estimation of carbon flow**.** *J Biol Chem* 247:6047-6054, 1972.

171. Rosen F, Roberts NR and Nichol CA. *J Biol Chem* 234:437, 1959.

172. Rosenberg LE. Disorders of propionate and methylmalonate metabolism, in The

Metabolic Basis of Inherited Disease (5th ed.), pp 474-497, JB Stanbury et al., editors. New York: McGraw-Hill, 1982.

173. Ross BD, Hems R, and Krebs HA. The rate of gluconeogenesis from various precursors in the perfused rat liver. *Biochem J* 102:942-951, 1967a.

174. Ross BD, Hems R, Freedland RA, and Krebs HA. Carbohydrate metabolism of the perfused rat liver. *Biochem J* 105:869-875, 1967b.

175. Rossetti L, Giaccari A, Barzilai N, Howard K, Sebel G, Hu .Mechanism by which hyperglycemia inhibits hepatic glucose production in conscious rats. Implications for the pathophysiology of fasting hyperglycemia in diabetes. *J Clin Invest* 92:1126-1134, 1993.

176. Rowland M, Ahmad AB, Bennett PN, Roberts MS. Models of hepatic drug clearance: discrimination between the 'well stirred' and 'parallel-tube' models, *J Pharm Pharmacol* 35(4):219-24, 1983.

177. Salem J, Saidel G, Stanley W, and Cabrera M. Mechanistic model of myocardial energy metabolism under normal and ischemic conditions. *Ann Biomed Eng* 30: 202-216, 2002.

178. Saville BA, Gray MR, and Tam YK. Models of hepatic drug elimination. *Drug Metabolism Reviews* 24:49-88, 1992.

179. Scrutton M, White D. Pyruvate carboxylase from rat liver: catalytic properties in the absence, and at low concentrations of acetyl-CoA. *Biochemical and Biophysical Research Communications* 48:85-93, 1972.

180. Shepherd D, and Garland PB. The kinetic properties of citrate synthase from rat liver mitochondria. *Biochem J* 114:597-610, 1969

181. Shigehiro M, Inubushi T, Takahashi K, Ishii H, Ozawa K. Gluconeogenesis and phosphoenergetics in rat liver during endotoxemia. *Journal of Surgical Research* 74:179:186, 1998.

182. Shigesada K and Tatibana M. Role of acetylglutamate in ureotelism. I. Occurrence and biosynthesis of acetylglutamate in mouse and rat tissues. *Journal of Biological Chemistry* 246: 5588-5595, 1971.

183. Shigesada K, Aoyagi K, and Tatibana M. Role of acetylglutamate in ureotelism. Variations in acetylglutamate level and its possible significance in control of urea synthesis in mammalian liver. *European Journal of Biochemistry / FEBS* 85: 385-391, 1978.

184. Shonk, CE and Boxer GE *Cancer Res*. 24, 709, 1964.

185. Shulman GI, Ladenson PW, Wolfe MH, Ridgway EC, Wolfe RR. Substrate cycling between gluconeogenesis and glycolysis in euthyroid, hypothyroid, and hyperthyroid man. *Journal of Clinical Investigation* 76:757-764, 1985.

186. Shorten PR and Upreti GC. A mathematical model of fatty acid metabolism and VLDL assembly in human liver. Biochim. Biophys. Acta. 1736:94-108, 2005.

187. Sies H (Ed.) *Metabolic compartmention.* Siess EA, Brocks DG, and Wieland OH, Subcelluar Distribution of Adenine Nucleotides and of Metabolites of Tricarboxylate Cycle and Gluconeogenesis in Hepatocuytes (), Academic Press, 1982.

188. Siess EA and Wieland OH. Phosphorylation state of cytosolic and mitochondrial adenine nucleotides and of pyruvate dehydrogenase in isolated rat liver cells**.** *Biochem. J*. 156:91-102, 1976.

189. Sindelar DK, Chu CA, Venson P, Donahue EP, Neal DW, Cherrington AD. Basal

hepatic glucose production is regulated by the portal vein insulin concentration. *Diabetes* 47:523-529, 1998.

190. Slater E.C, Rosing J, and Mol A. The phosphorylation potential generated by respiring mitochondria. *Biochim Biophys. Acta*. 292:534-553, 1973.

191. Smith CM, Bryla J, and Williamson JR. Regulation of alpha-ketoglutarate metabolism by product inhibition at alpha_ketoglutarate dehydrogenase. *J. Biol Chem* 249:1497-1505, 1974.

192. Smith CM and Williamson JR. Inhibition of citrate synthase by succinyl-CoA and other metabolites. *FEBS Lett* 18: 35-38, 1971.

193. Soboll S, Akerboom T. P, Schwenke W. D, Haase R, and H Siess. Mitochondrial and cytosolic ATP/ADP ratios in isolated hepatocytes. A comparison of the digitonin method and the non-aqueous fractionation procedure. *Biochem J* 192:951-954, 1980.

194. Soboll S, Scholz R, Heldt HW. Subcellular metabolite concentrations. dependence of mitochondrial and cytosolic ATP systems on the metabolic state of perfused rat liver. *Eur J Biochem* 87:377-390, 1978.

195. Soling HD, Kleineke J, Willms B, Janson G, and Kuhn A. Relationship between intracellular distribution of phosphoenolpyruvate carboxykinase, regulation of gluconeogenesis, and energy cost of glucose formation. *Eur J Biochem* 37:233-243, 1973.

196. Soling HD, Janson G, Kuhn A, and Heinz. In *Gluconeogenesis: Its Regulation in Mammalian Species*. (Hanson R.W, and Mehlman M.A. eds,) John Wiley & Sons, New York. p:393, 1976.

197. Song SD. Department of Biological Sciences, Kyungpook National University,

Korea. http://bh.knu.ac.kr/~sdsong/images/HB16-Liver.gif

198. Stickel F, Hoehn B, Schuppan D, Seitz HK. Nutritional therapy in alcoholic liver disease. Aliment Pharmacol Ther 18:357-373, 2003.

199. Stubbs M, Veech RL, Krebs HA. Control of the redox state of the nicotinamide-adenine dinucleotide couple in rat liver cytoplasm. *Biochem J* 126:59-65, 1972

200. Stucki J. Union Schweizerischer Gesellschaften für Experimentelle Biologie. *Cellular and Molecular Life Sciences*. 29:739-780, 1973.

201. Svanas GW, Weiner H. Aldehyde dehydrogenase activity as the rate-limiting factor for acetaldehyde metabolism in rat liver. *Arch Biochem Biophys* 236(1):36-46, 1985.

202. Teufel H, Menahan LA, Shipp JC, Boning S, and Wieland O. Effect of oleic acid on the oxidation and gluconeogenesis from 1-^{14}C pyruvate in the perfused rat liver. *Eur J Biochem* 2:182-186, 1967.

203. Torres NV. Modelizaton and experimental studies on the control of the glycolytic-glycogenolytic pathway in rat liver. *Molecular and Cellular Biochemistry*, 132:117-126, 1994.

204. Tsuji A, Yoshikawa T, Nishide K, Minami H, Kimura M, Tersaki T, Miyamoto E, Nightingale C, and Yamana T. Physiologically based pharmacokinetic model, Tissue distribution and elimination in rats, *J Pharm Sci* 72(11):1239-1252, 1983.

205. Tucker GA, Dawson AP. The kinetics of rat liver and heart mitochondrial -hydroxybutyrate dehydrogenase. *Biochem J* 179:579-581, 1979.

206. Umulis DM, Gurmen NM, Singh P, Fogler HS. A physiologically based model for ethanol and acetaldehyde metabolism in human beings. *Alcohol* 35:3-12, 2005.

207. Uyeda K, Furuya E, Luby IJ. The effect of natural and synthetic D-fructose 2,6-

bisphosphate on the regulatory kinetic properties of liver and muscle phosphofructokinases . *J Biol Chem* 256:8394-8399, 1981.

208. Van Dam K, and Meijer AJ. Oxidation and energy conservation by mitochondria. *Ann Rev Biochem*. 40:115-160, 1971.

209. Van Schaftingen E, Hue L, Hers HG. Study of the fructose 6-phosphate/fructose 1,6-bi-phosphate cycle in the liver in vivo. *Biochem J* 192(1):263-71, 1980.

210. Wahren J, Felig P, Ahlborg G, Hendler R, Hagenfeldt L. Substrate turnover during prolonged exercise in man. *The Journal of Clinical Investigation* 53:1080-1090, 1974.

211. Wahren J, Felig P, Ahlborg G, Jorfeldt L. Glucose metabolism during leg exercise in man. *Journal of Clinical Investigation* 50:2715-2725, 1971.

212. Wasserman DH, Geer RJ, Williams PE, Becker T, Brooks Lacy D, Abumrad NN. Interaction of gut and liver in nitrogen metabolism during exercise. *Metabolism* 40: 307-314, 1991.

213. Wieland O and Weiss L. Increase in liver acetyl-coenzyme A during ketosis. *Biochemical and Biophysical Research Communications* 10:333-339, 1963.

214. Wieland O, Weiss L, and Eger-Neufeldt I. Enzymatic regulation of liver acetyl-CoA metabolism in relation to ketogenesis. *Advances in Enzyme Regulation* 2:85-99, 1964.

215. Wieland O**.** Ketogenesis and its regulation. *Advances in metabolic disorders* 3: 1-47, 1968.

216. Williamson DH, Lund P, Krebs HA. The redox state of free nicotinamide-adenine dinucleotide in the cytoplasm and mitochondria of rat liver. *Biochem* J 103, 514-527, 1967a.

217. Williamson JR, Anderson J, and Browning ET. Inhibition of gluconeogenesis by butylmalonate in perfused rat liver. *J Biol Chem*. 245:1717-1726, 1970.

218. Williamson JR, Browning ET, and Olson MS. Interrelations between fatty acid oxidation and the control of gluconeogenesis in perfused rat liver. *Ad Enzyme Regul* 6:67-100, 1968.

219. Williamson JR, Meijer AJ, and Ohkawa K. In *Regulation of Hepatic Metabolism (Alfred Benzon Symposium VI) (F. Lundquist and N. Tygstrup, eds)*, Munkgaard Copenhagen. 457-479, 1974a.

220. Williamson JR, Ohkawa K and Meijer AJ. In *Alcohol and Aldehyde Metabolizing Systems (RG Thurman, T Yonetani, JR Williamson and B Chance, eds)*, Academic Press, New York. 365-381, 1974b.

221. Williamson JR, Scholz R, Browning ET, Thurman RG, and Fukami RH. Metabolic effects of ethanol in perfused rat liver. *J Biol Chem* 244:5044-5054, 1969c.

222. Williamson JR, Anderson J, Browning ET. Inhibition of gluconeogenesis by butymalonate in perfused rat liver. *J Biol Chem* 245:1717-1726, 1970a.

223. Williamson JR, Browning ET, and Scholz R. Control mechanisms of gluconeogenesis and ketogenesis. I. Effects of oleate on gluconeogenesis in perfused rat liver. *Journal of Biological Chemistry* 244:4607-4616, 1969a.

224. Williamson JR, Browning ET, Scholz R. Control mechanisms of gluconeogenesis and ketogenesis. II. Interactions between fatty acid oxidation and the citric acid cycle in perfused rat liver. *J Biol Chem* 244:4617-4627, 1969b.

225. Williamson JR, Rostand SG, Peterson MJ. Control factors affecting gluconeogenesis in perfused rat liver. *J Biol Chem*, 245:3242-3251, 1970b.

226. Whitcomb D.C. Acetaminophen hepatotoxicity: The rest of the story. *Gastroenterology* 114(5):1105-1106, 1998

227. Wu F, Yang F, Vinnakota KC, and Beard DA. Computer modeling of mitochondrial tricarboxylic acid cycle, oxidative phosphorylation, metabolite transport, and electrophysiology. *Journal of Biological Chemistry* 282:24525-24537, 2007.

APPENDIX

Codes for the different models are available in the following directories:

1) Chapter II (Distributed model):
    a. Liver_model/distributed_model/ **Dist-model.FOR** (Fortran code).
    b. Also need the following Fortran subroutines:
        i. DLSODE.FOR
        ii. DSS1.FOR

2) Chapter III (Gluconeogenesis and lipid metabolism in the perfused liver):
    a. Liver_model/Gluconeogenesis_lipid_model/**Estimation6.for**
    b. Also need the following Fortran subroutines and text files:
        i. GCOMP6.FOR
        ii. Constraints6.FOR
        iii. Diffeqns6.FOR
        iv. Gcomp6.FOR
        v. Opkdomain.FOR
        vi. Opkda1.FOR
        vii. Opkda2.FOR
        viii. Subint.FOR
        ix. Grg2-1.FOR
        x. Grg2-2.FOR
        xi. Initial condition-n3m.txt
        xii. Initial parameters-n3m.txt
        xiii. Initial parameters orig.txt
        xiv. Initial condition.txt

3) Chapter IV (Cytosolic-mitochondrial compartmentation in the perfused liver):
    a. The simbiology core code model:
    Liver_model/Compartmentation_model/
    gluc_v18_tca_comp_eapperf(vt163.2.5).sbproj
    b. The simbiology code is only compatible with R2007
    c. Executable codes:
        i. lactate+oleate:
        Liver_model/Compartmentation_model/**lac_oleate.m**
        ii. pyruvate+oleate:
        Liver_model/Compartmentation_model/**pyr_oleate.m**
        iii. These are Matlab executable code, compatible with R2007 and 2008 versions.

4) Chapter V (Ethanol oxidation in the perfused liver):
    a. The simbiology core code model:
       Liver_model/Compartmentation_model/
       gluc_v18_tca_comp_eapperf(vt163.2.5).sbproj
    b. The simbiology code is only compatible with R2007
    c. Executable codes:
        i. Lactate+ethanol:
           Liver_model/Compartmentation_model/**lac_etoh.m**
        ii. Pyruvate+ethanol:
           Liver_model/Compartmentation_model/**pyr_etoh.m**
        iii. Lactate+oleate+ethanol:Liver_model/Compartmentation_model/**lac_etoh_ol**.m
        iv. Pyruvate+oleate+ethanol:Liver_model/Compartmentation_model/**pyr_etoh_ol.m**
        v. These are Matlab executable code, compatible with R2007 and 2008 versions.